



**University of
Nottingham**

UK | CHINA | MALAYSIA

Department of Mechanical, Materials & Manufacturing
Engineering
University of Nottingham

**R&D of carbon nanotubes based nanocomposites for
self-heating and de-icing applications**

Francesco Zangrossi
4285172

Thesis submitted to the University of Nottingham
for the degree of Doctor of Philosophy

April 2021

Then, in the name of democracy, let us use that power - let us all unite. Let us fight for a new world - a decent world that will give men a chance to work - that will give youth a future and old age a security. By the promise of these things, brutes have risen to power. But they lie! They do not fulfil that promise. They never will!

Dictators free themselves but they enslave the people! Now let us fight to fulfil that promise! Let us fight to free the world - to do away with national barriers - to do away with greed, with hate and intolerance. Let us fight for a world of reason, a world where science and progress will lead to all men's happiness. Soldiers! In the name of democracy, let us all unite!

Charlie Chaplin

Abstract

Icing is a problem that aerospace environment has to face. Ice accretion on aircraft surfaces can cause serious problems on flight safety, performances and efficiency. Several ice protection strategies have been developed to overcome the icing hazards in the aerospace industry. The electro-thermal method is one of the popular approaches to prevent ice accretion and accumulation on aircraft surfaces. Given the increasing requirement of composites on aircraft structures, metal frameworks/fibre reinforced composites have been developed as a de-icing solution for the new generation aircraft. Next-generation aircraft structures require increased strength and lightweight composite materials, which pushes a high interest in nanomaterial based composite. In this project it was proposed to fabricate self-heating nanocomposites from carbon nanotubes, as an effective de-icing approach in aerospace. Due to the natural advances of nanomaterials, the nanocomposite electro-thermal structures are also expected to offer enhanced mechanical properties. Carbon nanotubes have been used to fabricate carbon nanotube films (carbon nanotube buckypaper, CNP) that have been integrated into composite structures. The novelties of the project were the chemicals treatments used to improve the electrical conductivity of the carbon nanotubes buckypaper and the mechanical tests used to analyse the mechanical behaviour of the nanocomposites. Due to static and dynamic loads during the flight conditions, it is essential to understand the mechanical characteristics of the CNP-based composites. This work was focused, in accordance with the industrial partner, on improving the electrical characteristics of the nanocomposite without compromising the mechanical properties. Once the optimal electrical characteristics will be reach, the future work should be focused on improving the thermal properties of the nanocomposite to further increase the ice protection efficiency.

The results showed that acid treatments of CNTs with nitric acid lead to an electrical conductivity improvement of CNT papers. The CNP showed promising electrical characteristics and heating performances for possible application in self-heating composites. Carbon nanotubes buckypapers embedded in fibre reinforced polymer composites have been fabricated by different processing approaches. Mechanical tests and the study of heating performance demonstrated that the CNP-based composite is a promising self-heating material candidate for ice protection of the aircraft surfaces.

Acknowledgements

This work is funded by the INNOVATIVE doctoral programme. The INNOVATIVE programme is partially funded by the Marie Curie Initial Training Networks (ITN) action (project number 665468) and partially by the Institute for Aerospace Technology (IAT) at the University of Nottingham. The work was supported by Dr Xianghui Hou, Dr Xu Fang, Prof. Nicholas Warrior and all the colleagues of the laboratory. Special thanks go to Dr Smith Emily, that helped to carry out the XPS characterization experiments, and to Dr Fay Michael, that helped to carry out the TEM characterization the experiments.

Meggitt Airframe Systems Division, UK, is acknowledged for the supply of the materials and the instruments used in the placement. The placement was supported by Mr Mark Hancock, Mr Michael Sanders, Mr Peter Karapapas and all the colleagues of the laboratory. Special thanks go to Mr Nick Thompson that helped to carry out the mechanical test on the composite samples.

Kyoto Institute of Technology is acknowledged for the supply of the instruments used in the placement. The placement was supported by Prof. Pezzotti Giuseppe, Prof. Marin Elia and all the colleagues of the laboratory.

PUBLISHED ARTICLE

Title: Electro-thermal and mechanical performance of multiwall carbon nanotubes buckypapers embedded in fibre reinforced polymer composites for ice protection applications

Authors: Francesco Zangrossi, Fang Xu, Nick Warrior, Petros Karapappas and Xianghui Hou

Journal: Journal of Composite Materials (SAGE)

Details: Vol 54, Issue 23, 2020

Link: <https://doi.org/10.1177/0021998320915639>

MANUSCRIPT UNDER PREPARATION

Title: Improvement in electrical characteristics by surface modification of multiwall carbon nanotube based buckypaper for de-icing application.

Authors: Francesco Zangrossi, Ghosh Barun, Fang Xu, Nick Warrior and Xianghui Hou

CONFERENCE

46th International Conference on Metallurgical Coatings and Thin Films, May 19 – 24, 2019, San Diego, CA, USA.

Poster: Surface modification of multiwall carbon nanotubes for de-icing application.

Contents

Chapter 1	Introduction	1
Chapter 2	Literature review	7
2.1	Aircraft icing hazards and ice protection systems.....	7
2.2	High electrical conductive nanomaterials	13
2.2.1	Carbon nanotubes - CNTs.....	14
2.2.2	Silver nanowires.....	34
2.2.3	Graphene	41
2.3	Electro-thermal properties improvements of nanocomposites.....	46
2.4	Materials for electro thermal ice protection systems	48
Chapter 3	Methodologies.....	54
3.1	Raw materials and chemicals	57
3.2	Fabrication of CNT network	59
3.2.1	Fabrication of CNT network by spray technique.....	59
3.2.2	Buckypaper production	62
3.3	Acid treatments of CNTs.....	63
3.4	Enhancements of CNT and CNP electrical characteristics using zinc oxide coatings	66
3.4.1	Spray technique for ZnO coatings	68
3.4.2	Spin coating.....	69
3.4.3	Atomic layer deposition	70
3.4.4	ZnO coatings by filtration	72
3.5	Enhancements by electrical conductive particles.....	73
3.5.1	Silver decoration	73
3.5.2	Doping agents.....	76
3.6	Self-heating composite preparation.....	80
3.6.1	One layer configuration	81
3.6.2	Two layers configuration	82
3.7	Microstructure and characterization.....	84
3.7.1	Scanning Electron Microscope	84
3.7.2	Transmission Electron Microscope.....	85
3.7.3	X-Ray Diffraction	86
3.7.4	X-ray Photoelectron Spectroscopy	86
3.7.5	Raman spectroscopy	87
3.7.6	Laser scanning microscope	88
3.8	Tests and properties.....	89
3.8.1	Electrical resistance.....	89
3.8.2	Heating performance.....	92
3.8.3	Ice melting test	92

3.8.4	Mechanical tests	93
Chapter 4	Chemical oxidation of CNTs and electrical conductivity improvements by ZnO coatings	98
4.1	Acid treatments effects on nanotubes.....	99
4.1.1	Characteristics of high temperature acid treated CNTs	99
4.1.2	Characteristics of low temperature acid treated CNTs	109
4.1.3	Ice protection evaluation of acid treated CNP	114
4.2	Electrical resistance reduction with ZnO coatings.....	118
4.2.1	Electrical characteristics and morphological analysis	118
4.2.2	Results for ZnO coated CNP.....	124
4.3	Summary.....	126
Chapter 5	Effects of metal decoration and doping agents on CNT network	128
5.1	Doping using pre-formed nano/micro particles	129
5.1.1	Graphene and copper as doping agents.....	129
5.1.2	Silver particles as doping agents.....	134
5.2	Effect of silver decoration	138
5.2.1	Comparison between magnetic stirring and ultrasound for NaOH method.....	139
5.2.2	Silver quantification.....	141
5.2.3	Phase analysis and distribution	146
5.2.4	Electrical resistance.....	151
5.3	Electrical conduction and fracture mechanisms in doped CNP.....	152
5.4	Summary.....	156
Chapter 6	Analysis of self-heating composites characteristics	158
6.1	CNP based self-heating composites	160
6.1.1	Electrical resistance.....	160
6.1.2	Heating performance.....	166
6.1.3	Ice melting test.....	170
6.1.4	Mechanical test.....	173
6.2	Combination of super-hydrophobic resin with CNP based self-heating composites	184
6.2.1	Morphology and electrical characteristics	184
6.2.2	Electro-thermal test in icing environment	189
6.3	Summary.....	193
Chapter 7	Technical discussion	195
7.1	Acid treatment effects on CNT network	195
7.2	ZnO coatings results.....	196
7.3	Effects of doping agents on CNP characteristics	197
7.4	Overall results of CNP based composites	199

Chapter 7	Conclusions	202
Chapter 8	Future work	205
References	207

Acronym

1000 N-Ag CNTs	: nitric acid treated CNTs silver decorated with NaOH method (1000 μ l of NaOH)
10GPH-CNP	: doped CNP with 10 mg of grahpene powder
150Ag-CNP	: doped CNP with 150 ml of silver flakes suspension
20AgNWs-CNP	: doped CNP with 20 ml of silver nanowires suspension
250 N-Ag CNTs	: nitric acid treated CNTs silver decorated with NaOH method (250 μ l of NaOH)
2AgNWs-CNP	: doped CNP with 2 ml of silver nanowires suspension
2-CNP	: double layer of carbon nanotubes buckypapers
3 μ Cu-CNP	: doped CNP with 300 mg of copper micropowder
3nCu-CNP	: doped CNP with 300 mg of copper nanopowder
500 N-Ag CNTs	: nitric acid treated CNTs silver decorated with NaOH method (500 μ l of NaOH)
50Ag-CNP	: doped CNP with 50 ml of silver flakes suspension
50GPH-CNP	: doped CNP with 50 mg of grahpene powder
750 N-Ag CNTs	: nitric acid treated CNTs silver decorated with NaOH method (750 μ l of NaOH)
9 μ Cu-CNP	: doped CNP with 90 mg of copper micropowder
9nCu-CNP	: doped CNP with 90 mg of copper nanopowder
A-CNT	: acid treated carbon nanotube
Ag	: silver
AgNW	: silver nanowire
AgNWs	: silver nanowires
ALD	: atomic layer deposition
AT-T-CNTs	: nitric acid treated CNTs silver decorated with Tollen method
CNP	: carbon nanotubes buckypaper
CNT	: carbon nanotubes
CNTs	: carbon nanotubes
-COOH	: carboxylic group
EDS	: energy dispersive X-ray analysis
EF-MWCNP	: untreated buckypaper soaked in Silikopon resin
EF-NA-CNP	: nitric acid treated buckypaper soaked in Silikopon resin
EL2-MWCNP	: untreated buckypaper soaked in EL2 laminating resin
EL2-NA-CNP	: nitric acid treated buckypaper soaked in EL2 laminating resin
EMEDS	: electro-mechanical expulsion deicing system
EMI	: electromagnetic interference
EMS	: electromagnetic shielding
ESD	: electrostatic dissipation
fcc	: face-cubic centred
FPD	: flat panel display
FTIR	: Fourier transform infrared spectroscopy
GKN	: GKN group
GNR	: graphene nanoribbon
GO	: graphene oxide
GPH	: graphene
H ₂ O ₂	: hydrogen peroxide
H ₂ SO ₄	: sulphuric acid
HCl	: cloridric acid

HF	:	fluoridric acid
HNO ₃	:	nitric acid
ILSS	:	interlaminar shear strength
ITO	:	indium tin oxide
LSM	:	laser scanning microscopy
MWCNP	:	multiwall carbon nanotube paper
MWCNT	:	multiwall carbon nanotubes
NA-CNP	:	nitric acid treated buckypapers
NH ₄ OH	:	ammonium hydroxide
Ni	:	nickel
NO ₂	:	Nitrogen dioxide
-OH	:	hydroxyl group
OLED	:	organic light emitting diode
PEEK	:	polyether ether ketone
PET	:	polyethylene terephthalate
PP	:	pre-preg pressure method
PP-CNP	:	CNP modified composite with PP method
PTFE	:	polytetrafluoroethylene
PTT	:	poly(trimethylene terephthalate)
PV	:	pre-preg vacuum method
PV-CNP	:	CNP modified composite with PV method
RP	:	resin impregnation pressure method
RP-2-SCNP	:	2 soaked CNP layers in RP composite
RP-CNP	:	CNP modified composite with RP method
RP-ref	:	reference sample for RV method
RV	:	resin impregnation vacuum method
RV-2-SCNP	:	2 soaked CNP layers in RV composite
RV-CNP	:	CNP modified composite with RV method
RV-ref	:	reference sample for RV method
SCNP	:	soaked (in thermosetting resin) carbon nanotubes buckypaper
SDS	:	sodium dodecyl sulphate
SEM	:	scanning electron microscope
SO ₃	:	sulphur trioxide
SWNT	:	single wall nanotube
SWNTs	:	single wall nanotubes
TEM	:	transmission electron microscope
Tenv	:	environment temperature
TS	:	touch screen
U-T-CNTs	:	untreated CNTs silver decorated with Tollen method
WPU	:	waterborne polyurethane
ZnO	:	zinc oxide

List of Tables

Table 2.1 - Features comparison of EMEDS technology and traditional Pneumatic Boots [11]	10
Table 2.2 – Measured electrical conductivities of WBPU films, CNT and A-CNT sheets [35, 36]	22
Table 3.1 - Suspension volumes utilised for spray technique	59
Table 3.2 - Acid treatment parameter: volume utilised and relative ratio of nitric and sulphuric acid	62
Table 3.3 - Chemicals used for Zinc oxide coating	67
Table 3.4 - Quantities of chemicals used	67
Table 3.5 - Quantities of chemicals used	71
Table 3.6 - Samples name and characteristics for silver flakes doped CNP	77
Table 3.7 - Samples name and characteristics for silver nanowires doped CNP	77
Table 3.8 - Samples name and characteristics for CNP doped with copper micro-powder	77
Table 3.9 - Samples name and characteristics for CNP doped with copper nano-powder	78
Table 3.10 - Samples name and characteristics for CNP doped with graphene powder	79
Table 4.1 - Quantitative results for C1s scan	103
Table 4.2 - Electrical sheet resistance values for HT mixed acid treated coatings compared to the untreated	107
Table 4.3 - Electrical sheet resistance values and their relative standard deviation of 90 ml suspension coatings: pure, nitric and sulphuric acid treated	108
Table 4.4 - Quantitative results for C1s scan	109
Table 4.5 - Carbon nanotube buckypapers characteristics	111
Table 4.6 - Electrical properties of carbon nanotubes buckypaper	112
Table 4.7 - Electrical properties for two-layered carbon nanotubes buckypapers	113
Table 4.8 - Power densities of the ice protection test	115
Table 4.9 - Electrical sheet resistance values and their relative standard deviation of 90 ml suspension coated with ZnO	117
Table 4.10 - Quantitative results from XPS scans of ZnO coatings	119
Table 4.11 - Zn signals and Auger parameter from XPS scan	119
Table 5.1 - Electrical characteristics of buckypaper doped with graphene and copper (micro and nano) powders	128
Table 5.2 - Electrical characteristics of buckypaper doped with silver flakes and nanowires	133
Table 5.3 – Surface roughness values and their standard deviation	136
Table 5.4 - XPS results: Ag, C and O atomic percentages of each sample	140

Table 5.5 - Ag 3d electron binding energy, Ag Auger electron kinetic energy and Auger parameter of respective U-T-CNTs and AT-T-CNTs samples	143
Table 6.1 - Electrical resistance values for the composite samples	159
Table 6.2 - Electrical characteristics of CNP: soaked in resin and not	164
Table 6.3 - Heating performance and testing characteristics of RV-samples	166
Table 6.4 - Heating performance and testing characteristics of RP-samples	166
Table 6.5 - De-icing tests characteristics for RV and RP samples	171
Table 6.6 - Buckypaper weight percentage in the composite structure	175
Table 6.7 – Three-point flexural tests results	176
Table 6.8 - Interlaminar Shear Strength results	178
Table 6.9 - Composite samples characteristics	184
Table 6.10 - Electrical properties of composite samples	187
Table 6.11 - Power densities of the ice protection test	191

List of Figures

Fig. 2.1 – Schematic representation of superhydrophobic coating effect on water drop: a) water drop on an un-coated surface; b) superhydrophobic coating reduces the angle of contact of the water drop	8
Fig. 2.2 – a) Cross section of a pneumatic de-icing boot uninflated (top) and inflated (bottom); b) de-icing boot deflated (left) and inflated (right) [4]	9
Fig. 2.3 – Electro-Mechanical Expulsion Deicing System (EMEDS) [11]	10
Fig. 2.4 – Hot air bleed duct systems scheme [4]	11
Fig. 2.5 – Heated wing leading edge [4]	12
Fig. 2.6 - Electro-thermal heating system representation	12
Fig. 2.7 - CNT geometric structures: armchair (top), zig-zag (middle) and chiral (bottom) [13]	15
Fig. 2.8 - a) π -orbitals of graphene; b) rearrangement of π -orbitals in a nanotube; c) rehybridization of a carbon nanotube [18]	15
Fig. 2.9 - Transmittance vs. resistivity plot for sprayed CNT layers and ITO. Each curve represents different CNT material (black curves: MWCNT; grey curves: SWCNT; dark grey: ITO). [21]	16
Fig. 2.10 - Required surface resistivity in typical applications for transparent conductive coatings compared to the performance of thin conductive CNT networks [24]. EMI: electromagnetic interference (10 kHz–1 MHz); FPD: flat panel display (PET: polyethylene terephthalate); TS: touch screen; EMS: electromagnetic shielding for cathode ray tubes; ESD: electrostatic dissipation [25]	19
Fig. 2.11 - Functionalisation of MWCNTs by carboxylic (-COOH), carbonyl (>C=O) and hydroxyl group (-OH)[37]	19
Fig. 2.12- Scheme of MWCNTs acid treatments [33]	22
Fig. 2.13 - SEM images of the treated MWCNTs at two different magnifications: (a) after purification with HCl; (b) after nitric acid oxidation; (c) after oxidation with piranha; (d) after oxidation with ammonium hydroxide and hydrogen peroxide mixture; TEM images after modification with (e) ammonium hydroxide and hydrogen peroxide mixture and (f) after nitric acid. [33]	21
Fig. 2.14 – The graph shows the changing of the electrical conductivity in function of carbon nanotubes content. Curve (a) WBPU/CNT and curve (b) WBPU/A-CNT composite films [34]	22
Fig. 2.15 - Schematic representation of electron transfer between nanotubes before (a) and after (b) the nitric acid treatment. The contact resistance was reduced by the low resistance path created by the functional groups	24
Fig. 2.16 - TEM images of MWCNTs decorated with Ag nanoparticles: a) x340000; b) x125000 [57]	26
Fig. 2.17 - SEM image of the Ag-CNT products [58]	27
Fig. 2.18 - Silver decorated MWNTs sheet [69]	30
Fig. 2.19 - Thermal cycles from environment temperature (T_{env}) and maximum temperature (T_{max}) reachable with 5, 6, 7V of input voltages: stage I, ramping up, stage II: stable-state and stage III: cooling down [69]	31

Fig. 2.20 - The fabricating process of CNP/glass fibre/epoxy composite. Magnified areas are the schematic drawing of the CNP at different stages [71]	32
Fig. 2.21 - (a) Scanning electron microscopy (SEM) image of drawable CNT forests (b,c) CNT webs (d) GF/CNT/GF epoxy composite (e) Cross-section SEM of the sample with 10 layers of CNT web (f) GF/CF/GF epoxy composite [72]	32
Fig. 2.22 - SEM images of super-hydrophobic coating combined with electric heating coating (a), super-hydrophobic coating surface (b) and electric heating coating surface (c) and the insets are the contact angles of 10 μ l of water droplets on the surfaces [73]	33
Fig. 2.23 - Silver nanowire structure representation: a) three dimensional and b) cross section	34
Fig. 2.24 - a) & b) SEM images of air dried AgNW; c) & d) SEM images of AgNW heat treated at 200°C: melting and fusion of AgNWs (inside circles) and reduction of solvent residues help to decrease the electrodes sheet resistance [89]	36
Fig. 2.25 - a) Top-view laser scanning microscopy (LSM) images of AgNW films derived from unformulated AgNW ink and formulated AgNW ink with clay platelets (middle). b) Top-view SEM images of AgNW-coated films with different densities, in which the AgNWs are shown to be a continuous network [98]	38
Fig. 2.26 - Defrosting test results of GO/AgNW hybrid film heater: optical photo before (a) and after (b) frost formation, and (c) after the defrosting test operated at 10 V [102]	39
Fig. 2.27 - (a) Ultimate thermal performance of heaters based on pure AgNWs, GO/AgNWs/GO, and rGO/AgNWs/GO, respectively. (b) Heating and cooling tests of heaters under current on/off interval of 60 s, and (c) long-time working stability of them. (d) Defrosting performance and working stability of different heaters. Inset images in (a) are infrared images of heaters working at the highest temperature [103]	40
Fig. 2.28 - Thermal performance of 10 cm \times 10 cm SWCNT/AgNW THFs with a sheet resistance of (a) 9 Ohm/sq, (b) 30 Ohm/sq on PET, (c) thermal stability at 80 °C for 360 h [104]	41
Fig. 2.29 - Graphene structure: single layer of graphite	42
Fig. 2.30 - Wing with electro-thermal protection system [108]	43
Fig. 2.31 - Schematic of the coating of a rotor blade segment with the graphene nanoribbons-epoxy composite [110]	44
Fig. 2.32 - Electrical current intensity (black square symbol) and increase of temperature (red triangle symbol) as a function of the electrical voltage applied for coatings doped with (a) 8, (b) 10, and (c) 12 wt%. Experimental data fitting with equation (blue solid line) and with Ohm's law at low and high voltage (black dotted lines) [111]	45
Fig. 2.33 - The change of (a) current and (b) temperature of graphene-based glass rovings at various voltages; (c) the power consumption per unit length of graphene-based glass rovings shows linear relationship with the increase of temperature [117]	45
Fig. 2.34 - GKN leading edge heating element for the Boeing 787 [124]	49
Fig. 2.35 - De-icing test with the ice protection system carbon nanotube based developed by Fraunhofer Institute for Structural Durability and System [127]	51
Fig. 3.1 - Flow chart of overall steps	55
Fig. 3.2 - Spray gun supplied by Clark Air	59

Fig. 3.3 – Automated spray system: a) adjustable spray nozzle; b) rotating hot plate; c) fluid pump; d) automated arm. This last is connected to (e) liquid intake and f) air intake tubes. (e) is connected to the fluid pump (c); (f) is connected to (g) air supply	60
Fig. 3.4 - Automated spray gun pattern to cover the samples area	61
Fig. 3.5 - Example of carbon nanotube buckypaper (CNP)	62
Fig. 3.6 - Flow chart of the overall steps for acid treatments experiments: a) acid treatments procedure: for the left branch the first batch of nanotubes have been used, for the right branch the second batch of nanotubes have been used; b) acid treatments experiments description	63
Fig. 3.7 - Whatman® Anodisc inorganic filter membrane used in the vacuum filtration system: diam. 47 mm, pore size 0.02 μm ; high purity alumina matrix manufactured electrochemically	64
Fig. 3.8 - a) Flow chart of the overall steps for ZnO coatings experiments; b) flow chart of the overall steps for ZnO coatings preparation	66
Fig. 3.9 – a) Chemat KW-4A spin coater; b) scheme of spin coating process	69
Fig. 3.10 - Schematic process of atomic layer deposition: a) first precursor layer (blue circle); b) second precursor layer (red circle); c) repetition of the two previous step until desired thickness	70
Fig. 3.11 - Example of ALD software from CambridgeNanotech	71
Fig. 3.12 - a) Flow chart of the overall steps for silver decoration experiments; b) flow chart of the overall steps for silver decoration procedures	73
Fig. 3.13 - Flow chart of the overall steps for doping agents experiments. The second batch of nanotubes have been used	76
Fig. 3.14 - Flow chart of the overall steps for self-heating nanocomposite production and characterization	80
Fig. 3.15 - Schematic diagram of the mold layer structure	81
Fig. 3.16 - Composite samples of two layers configuration class: a) reference material for mechanical tests; b) CNP-composite for mechanical tests; c) CNP-composite for electrical resistance, ice protection and heating performance tests	83
Fig. 3.17 - SEM schematic representation	84
Fig. 3.18 - Jandel HM21 system (a) and head of 4-point probe (b)	88
Fig. 3.19 – a) Four point resistance measurement scheme. A: current applied. V: voltage control. 1, 2, 3 and 4: probes. b) Geometry of the ideal film	89
Fig. 3.20 - Device for electrical resistance and heating performance tests: a) schematic diagram of layer structure; b) photo of the assembled device	90
Fig. 3.21 - a) composite samples in the cold chamber (on the right) connected to the water nebulizer; b) composite sample connected to the power supply	92
Fig. 3.22 - Schematic representation of: a) DMA test sample; b) three point flexure test sample; c) ILSS test sample	93
Fig. 3.23 - TA Instruments Q800 DMA	95

Fig. 4.1 - Raman spectra comparison of MWCNTs of first (blue line) and second (green line) batch	99
Fig. 4.2 - TEM images of : a) 1°MWCNT; b) HT-SA c) HT-NA	100
Fig. 4.3 - Example of deconvolution C1s orbital scan component (XPS C1s orbital scan of HT-NA)	102
Fig. 4.4 - XPS C1s orbital scans of high temperature treated samples: a) pure acid solutions treated MWCNTs; b) mixed acid solution treated MWCNTs	104
Fig. 4.5 - Normalized Raman spectra of high temperature treated samples: a) pure acid solutions treated MWCNTs; b) mixed acid solution treated MWCNTs	106
Fig. 4.6 - Pictures of CNTs coatings on glass substrates. The respective volumes (ml) of used suspensions are labelled in the picture	108
Fig. 4.7 - Normalized Raman spectra for 2°MWCNT (blue line) and NA-CNT (green line)	109
Fig. 4.8 - TEM images of: a) untreated multiwall carbon nanotubes; b) formed defects (red circles) on MWCNTs walls after nitric acid treatment; c) magnified image of one acid attacked position	110
Fig. 4.9 - SEM images of: a) x10000 MWCNP; b) x30000 MWCNP; c) x10000 NA-CNP; d) x30000 NA-CNP	112
Fig. 4.10 - Ice formed on the sample surface in a cold environment (-20°C)	113
Fig. 4.11 - Example of temperature versus heating time during the de-icing test for one 2-MWCNP sample and one 2-NA-CNP sample	114
Fig. 4.12 - Photos (left column) and thermal images (right column) of the de-icing test: a, d) at the beginning of the test; b, e) during ice melting; c, f) at the end of ice melting	116
Fig. 4.13 - SEM images of a) sand blasted glass; b) ZnO ALD coating c) ZnO spray coating; d) ZnO spin coating	118
Fig. 4.14 - XPS result for CNT spin coated with ZnO: a) Zn 2p orbital scan; b) Zn Auger peaks	120
Fig. 4.15 - SEM images of carbon nanotubes: 1st-MWCNT	121
Fig. 4.16 - SEM images of Untreated CNTs sprayed using 90 ml suspension: a) ZnO spin coated, x4000; b) ZnO spin coated, x120000; c) ZnO sprayed coating, x1000; d) ZnO sprayed coating, x4000	122
Fig. 4.17 - SEM images of Untreated CNT, ZnO coated with ALD technique, sprayed using 90 ml suspension: a) x9500; b) x80000; c) x130000; d) x160000	123
Fig. 4.18 - Example of cracked CNP coated with ZnO (a) and SEM images of ZnO coated CNP: b) the red dotted circle highlights an area in which ZnO coated the nanotubes; c) CNT bundle coated by ZnO	124
Fig. 4.19 - Schematic representation of uneven ZnO coated CNP	125
Fig. 5.1 - Pictures of cracked buckypaper doped with: a) graphene (50GPH-CNP); b) copper nanopowder (3nCu-CNP). The yellow arrows highlights the crack on the surface	129

Fig. 5.2 - a, b) SEM images of 10GPH-CNP (x10000). The yellow arrows highlight the area where graphene plates should be. c) TEM image of graphene plate covered with MWCNTs (highlighted by the yellow dotted circle)	130
Fig. 5.3 - SEM images of 9nCu-CNP: a, b) x10000; c) x30000	131
Fig. 5.4 - a) SEM images of 9 μ Cu-CNP (x1000); b) copper micropowder (x250). The yellow arrows and the yellow dotted circles indicate the copper microparticles	132
Fig. 5.5 – a) XPS results for μ Cu powder; b) photo of copper micropowder	132
Fig. 5.6 - Picture of 150Ag-CNP (50 mm x 50 mm)	133
Fig. 5.7 - SEM images of: a) 150Ag-CNP cross section (x250); b, c) 150Ag-CNP surface (x1000, x5000)	134
Fig. 5.8 - SEM images (x1000, x10000) of: a, b) 20AgNWs-CNP cross section; c) 2AgNWs-CNP cross section	135
Fig. 5.9 - Comparison between Ag 3d/5 orbital scans of: (a) 500 N-Ag CNTs and (b) 500 N-US-Ag CNTs	139
Fig. 5.10 - Comparison between Ag 3d/ 5 orbital scans of: (a) 750 N-Ag CNTs and (b) 750 N-US-Ag CNTs	140
Fig. 5.11 - XPS wide scans of: a) U-T-CNTs; b) AT-T-CNTs; c) 250 N-Ag CNTs; d) 500 N-Ag CNTs; e) 750 N-Ag CNTs; f) 1000 N-Ag CNTs	141
Fig. 5.12 - XPS O 1s/4 orbital scans of: a) U-T-CNTs; b) AT-T-CNTs; c) 250 N-Ag CNTs; d) 500 N-Ag CNTs; e) 750 N-Ag CNTs; f) 1000 N-Ag CNTs	142
Fig. 5.13 - XPS Ag 3d/5 orbital scans of: a) U-T-CNTs; b) AT-T-CNTs; c) 250 N-Ag CNTs; d) 500 N-Ag CNTs; e) 750 N-Ag CNTs; f) 1000 N-Ag CNTs	143
Fig. 5.14 - Example of U-T-CNTs (a) Ag 3d binding energy [eV] and (b) Ag Auger electron kinetic energy [eV]	144
Fig. 5.15 - U-T-CNTs XRD pattern	145
Fig. 5.16 - Comparison between U-T-CNTs and AT-T-CNTs XRD patterns	146
Fig. 5.17 - Comparison between U-T-CNTs and 750 N-Ag CNTs XRD patterns	147
Fig. 5.18 - Dark field TEM images of: a) U-T-CNTs; b) AT-T-CNTs; c) 250 N-Ag CNTs; d) 500 N-Ag CNTs; e) 750 N-Ag CNTs; f) 1000 N-Ag CNTs. The areas delimited by the red dotted line indicate the silver particles	148
Fig. 5.19 - TEM images of oxidized silver in: a) 250 N-Ag CNTs; b) 1000 N-Ag CNTs	149
Fig. 5.20 - Example of cracked buckypaper made of AT-T-CNTs	154
Fig. 5.21 - SEM images at different magnification of CNP made of AT-T-CNTs: a) x300; b) x5000	151
Fig. 5.22 – Schematic representation of electrical conduction in: a) graphene plate; b) graphene doped CNP. The arrows indicate the electrical conductive path with high (dark blue) or low (light blue) electrical resistance	151

Fig. 5.23 – Schematic representation of graphene doped buckypaper. The green dotted area highlights the low CNTs concentration areas	152
Fig. 5.24 – Schematic representation of copper nanoparticles (orange circles) with highlighted: a) contact area; b) gaps in between	153
Fig. 5.25 – Schematic representation of nCu doped buckypaper. The green dotted area highlights the low CNTs concentration areas	153
Fig. 5.26 – Schematic representation of electrical conduction in μ Cu doped CNP. The blue arrows indicate the electrical conductive path	154
Fig. 5.27 – Schematic representation of current conduction in silver flakes doped CNP	154
Fig. 5.28 – Schematic representation of contact between AgNWs and CNTs	155
Fig. 6.1 - Laser microscope images of cross sections for: a) PV-CNP sample (green dotted line indicates the delamination); b) PP-CNP sample (green dotted line indicates the delamination); c) RV-CNP sample; d) RP-CNP sample	161
Fig. 6.2 - SEM images of RV-CNP cross section: a) x35 with layers description (Cu/Ag = copper electrode and silver paint) ; b) x60000	162
Fig. 6.3 - SEM images of RP-CNP cross section: a) x35 with layers description; b) x30000; c) x60000	162
Fig. 6.4 - Thickness analysis for: a) RV-CNP sample; b) RP-CNP sample. The light blue vertical line indicates where thickness has been measured.	163
Fig. 6.5 - Thermal images of: a) RV-CNP sample; b) RP-CNP sample	165
Fig. 6.6 - Graphs of RV-samples characteristics registered during the heating performance test: a) temperature T; b) current I; c) resistance R. The orange lines represent the average value of the respective characteristic	167
Fig. 6.7 - Graphs of RP-samples characteristics registered during the heating performance test: a) temperature T; b) current I; c) resistance R. The orange lines represent the average value of the respective characteristic	168
Fig. 6.8 - Photos and thermal images of an RP sample during the de-icing test in the cold environment: a, c) at the beginning of the heating; b, d) after 120s heating	169
Fig. 6.9 - Graphs of temperatures registered during the de-icing test: a) RV samples; b) RP samples. 1, 2 and 3 are three samples within one testing group	171
Fig. 6.10 - DMA results for the different samples: a) Storage Modulus; b) Loss modulus; c) Tan Delta.	174
Fig. 6.11 – Three-point flexural tested samples: a) RV-ref sample; b) RP-ref sample; c) RV-CNP sample; d) RP-CNP sample	177
Fig. 6.12 - Magnified image of the crack in the three-point flexural RP-CNP sample	177
Fig. 6.13 - Laser microscope image of ILSS RV sample with crack between the two soaked CNPs. The layer configuration is described on the side	178

- Fig. 6.14 - Stress "ILSS" (MPa)/Extension "ε" curves of interlaminar shear strength test for Resin Impregnation Vacuum samples: (a) RV-CNP; (b) RV-ref. 1, 2, 3, 4 and 5 are three samples within one testing group 181
- Fig. 6.15 - Stress "ILSS" (MPa)/Extension "ε" curves of the interlaminar shear strength test for Resin Impregnation Pressure samples: (a) RP-CNP; (b) RP-ref. 1, 2, 3, 4 and 5 are three samples within one testing group 182
- Fig. 6.16 - Examples of composite samples with one layer configuration: a) EF-MWCNP; b) EL2-MWCNP 183
- Fig. 6.17 - SEM images of cross section: a, b) EL2-MWCNP (x30000, x60000); c, d) EL2-NA-CNP (x30000, x60000); e, f) EF-MWCNP (x30000, x60000) 185
- Fig. 6.18 - The electrical resistance comparison between the CNP and the respective composite sample 187
- Fig. 6.19 - Photos (left column) and thermal imaging (right column) of the de-icing test for an EF-MWCNP sample: a, d) at the beginning of the heating; b, e) during the ice melting; c, f) at the end of the ice melting 192
- Fig. 6.20 - Example of temperature versus heating time during the de-icing test for one EF-MWCNP sample and one EL2-MWCNP sample 191
- Fig. 7. 1 – a) TEM image of PECVD-grown CNTs. b) TEM image of ALD ZnO-coated CNTs. c - d) SEM images of ALD ZnO-coated CNTs [226] 196
- Fig. 7. 2 – a) 20 μm CNT/Ag composite. b) CNT/AgNW composite [63] 199

Chapter 1 Introduction

In-flight icing is a hazard to aircraft. Ice protection systems are used to protect aircraft surfaces from ice accumulation during the flight or on the ground. The existence of water drops in the atmosphere below freezing temperature is the principal cause of icing on aircraft surface [1]. The encounter of these droplets and particulates with the airframe can present several possible scenarios. One of these outcomes implies that the droplets can freeze immediately upon impact on the fuselage, splash upon the airframe, followed by freezing or erode the impact location. The ice on the aircraft surface has different names as: rime ice; glaze ice; step ice; frost. Rime ice grows as droplets rapidly freeze as soon as they strike the aircraft surface. Glaze ice is caused by water drops freezing in a location different from the impact area. Step ice is a ridge of ice along the wingspan; this type of ice can accumulate on wings beyond the protected area. A layer of frost may form on the aircraft from freezing of moist air [1].

Even the long pauses on the ground, during rain or snowfall followed by low temperatures, constitute a condition for the formation of ice, which must be removed before departure. Ground icing is characterized by the accumulation of ice while the aircraft is parked on the ground. Ground icing can be caused by the “cold-soaked wing” phenomenon. The wings are “cold-soaked” when they contain cold fuel from a flight at high altitude or from having been re-fuelled with very cold fuel. Whenever precipitation falls on a cold-soaked wing, clear icing may occur. Even in ambient temperatures above 0°C, ice or frost can form in the presence of visible moisture or high humidity, if the aircraft structure remains at 0°C or below. The temperature of the fuel affects the temperature of the wing surface above and below the tanks [2].

The icing hazards on aircraft surface often cause significant impacts, such as: alteration of the aerodynamic shape of the surfaces with consequent alteration of the aerodynamic flow (from 17% to 30% stall angle decrease, from 140% to 210% of drag increase [3]); isolation/malfunction of sensors; damage to the surfaces hit by pieces of ice detached from the wing surfaces or the leading edges of the dynamic engine intakes. An increase in profile drag, stall angle of attack and reduction of lift are the negative effects of icing on aircraft [4]. Ice accretion on aircraft surfaces can cause control and stability problems [4].

To prevent or control ice formation, several systems have been developed such as: heating element or hot air bleed ducts systems, under the wing surface; breaking up ice formations, by inflatable boots; chemical substances sprayed on the surfaces before takeoff [5]. Ice protection systems fall into two broad categories [6]: *anti-icing*, when the system prevents the ice accretion on a component surface; *de-icing*, when the system melts or helps to remove the ice that already exists on the surface of the component. The de-icing protection technologies destabilizes the ice, allowing air flows to remove it from the wings.

De-icing electro-thermal systems are frequently required in aerospace sector, to remove the ice from aircraft surface during the flight. One promising technology is conductive element integrated under the wing edge surface to directly heat the wing, preventing ice formation and accumulation. Typically an electro-thermal structure consists of a metal framework and inorganic insulator (e.g. thermosetting resin). The design challenge is to develop an icing protection system based on electro thermal heating elements that have to carry electrical current in different operating conditions. Incorporating a traditional metal foil heater technology within a composite

construction creates a weak layer, especially to inter-laminar shear. The metal foil does not have a good, durable bond to the composite structure [7]. Recent research works have focused on nanomaterials. The incorporation of nanomaterials could provide the opportunity to reinforce the composite structure and, at the same time, the capability to heat providing ice protection.

In the present work, based on weight reduction ambitions, the project aim was to fabricate self-heating nanocomposites from electrical conducting nanomaterials (e.g. nanotubes, nanowires and nanosheets, etc.), as an effective de-icing approach in aerospace. Due to the natural advances of nanomaterials, the nanocomposite electro-thermal structures are also expected to offer enhanced mechanical properties. The nanomaterials have been used to fabricate films that have been integrated into composite structures. The novelties of the project were the improvement of the film electrical conductivity, by different chemical treatments, and the mechanical tests used to analyse the mechanical behaviour of the nanocomposites. As already stated, the nanocomposite converts electrical current in heat energy; so higher the film electrical conductivity is, higher the developed heat will be. Due to static and dynamic loads during the flight conditions, it is essential to understand the mechanical characteristics of the nanocomposites. This work was focused, in accordance with the industrial partner (Meggitt Airframe Systems Divisions), on improving the electrical characteristics of the nanocomposite without compromising the mechanical properties. Characteristics and performances of the traditional heater, produced by the industrial partner, are confidential; literature values were used as comparison where necessary. Once the optimal electrical characteristics will be reach, the future work should be focused on improving the thermal properties of the nanocomposite to further increase the ice protection efficiency.

Major objectives of the project are:

1. Formation of stable dispersion consisting of conducting nanomaterials: electrical conducting nanomaterials will be treated and dispersed in appropriate solvent, to form stable dispersion. The candidate nanomaterials are carbon nanotubes (CNTs), graphene sheets and silver nanowires, which can be applied individually or combined together with different ratios.

2. Preparation of conducting network layer: conducting network layer will be prepared from the dispersion with nanomaterials. The conductive network is CNTs based and it is called carbon nanotube buckypaper (CNP). To improve the electrical conductivity of the paper, CNTs electrical characteristics will be modified by different chemical treatments, i.e. acid treatments and metal decoration.

3. Fabrication of electrical conducting nanocomposite: polymeric matrices will be applied onto the conducting network layer. Thermosetting resins were chosen as matrix candidates; those resins are the most used in aerospace environment and they are the favourite candidate in case of integration of the heating element inside the aircraft structure.

4. Microstructural characterisation and evaluation of heating performance: state of the art facilities will be used to carry out detailed material microstructural characterisation.

5. Study on the integration with industrial application: integration of the nanocomposite electro-thermal structure with industrial production system; in particular the mechanical proofs and the heating performances of the conducting

nanocomposite will be evaluated. The heating performance of the nanocomposites will be evaluated in a climatic chamber.

In this thesis, chapter 2 is dedicated to the literature review on aircraft icing issue, ice protection systems and the studies on nanomaterials integrated in new generation composites for aerospace applications.

Chapter 3 is dedicated to the description of all the used method (surface treatments, metal decoration and improvements by adding high electrical conductive particles) to improve the electrical properties of the CNTs and all the experiments of integration of the CNTs (untreated and modified) in a composite structure.

Chapter 4 is dedicated to the discussion of the results from the different surface treatments. These treatments were: acid treatments of CNTs with sulphuric and nitric acid; the application zinc oxide coatings on CNT layers. The results showed that acid treatment of CNTs with nitric acid leads to an electrical conductivity improvement of CNT papers (buckypaper, CNP). The CNT papers showed promising electrical characteristics and heating performances for possible application in self-heating composites.

In chapter 5 the results of doped buckypaper and silver decoration of CNTs, by chemical reaction, are described. The buckypaper electrical characteristics have been modified by adding high electrical conductive particles, such as graphene, micro and nanoparticles of copper (Cu) and silver (Cu). The results show that CNP modified with silver nanoparticles (silver nanowires AgNWs) obtained the highest electrical conductivity. The interaction between the carbon nanotubes and the silver nanowires caused a high electrical resistivity reduction (more than 50%) of the CNT paper.

The characteristics of the produced self-heating composites CNP based are described in chapter 6. Different configurations and production techniques have been used and the respective results have been analysed. The CNP based composites showed promising electrical characteristics, heating performances and mechanical characteristics.

Chapters 7 is dedicated to the technical discussion. The main results of each chapter have been analysed and compared to the existing works in the literature.

Chapters 8 and 9 are dedicated to conclusions and future works. The overall results indicate the CNP-based self-heating composites as promising candidates in aerospace applications as ice protection systems. More deep analysis could be done to optimize the production process and the properties of the CNP-based self-heating composites.

Chapter 2 Literature review

2.1 Aircraft icing hazards and ice protection systems

Aircraft icing is a severe problem that can compromise the aircraft performances and structural integrity. Ice formation on the leading edge of the wing can cause alteration of the aerodynamic characteristics, causing lift loss or asymmetry. The detachment of ice pieces from the wings could damage the aircraft tail or the engines in the rear. Ice formation on the engine air intake, in addition to the change in aerodynamic characteristics, causes the decrease of the useful section to the flow with consequent loss of air flow and the triggering of vibrations. Removing parts of ice in the air intake can cause damages to the rotating blades and take the turbine engine out of service. Ice can make inoperative or alter the functioning of altimeter, speed meters, thermometer, angle of attack meter and other important sensors placed on the aircraft surface [3].

Ice protection systems are basically divided depending on how they work: anti-icing and de-icing. First one avoids ice accretion on the protected surfaces. In comparison de-icing completely removes the existing ice from the surfaces [8].

Because different ice protection techniques may be applied, these strategies could be classified as: passive and active ice protection systems. Active ice protection: that uses additional power or energy supplied by external sources, such as pneumatic, chemicals or thermal energy [9].

Passive ice protection systems consist in icephobic coatings for delaying the formation of ice. Icephobic or superhydrophobic coatings (Fig. 2.1) with their anti-adherent property prevent adhesion and accumulation of ice to the surface and repulsive

features repel water from the surface. These coatings are examples of *passive anti-icing system*: they reduce the physical bonding at the interface between the ice and the solid surface [10]. The general research interest is focus on nanostructured surfaces: e.g. using nanometre-scale particles to superhydrophobicity on the solid surface [9].

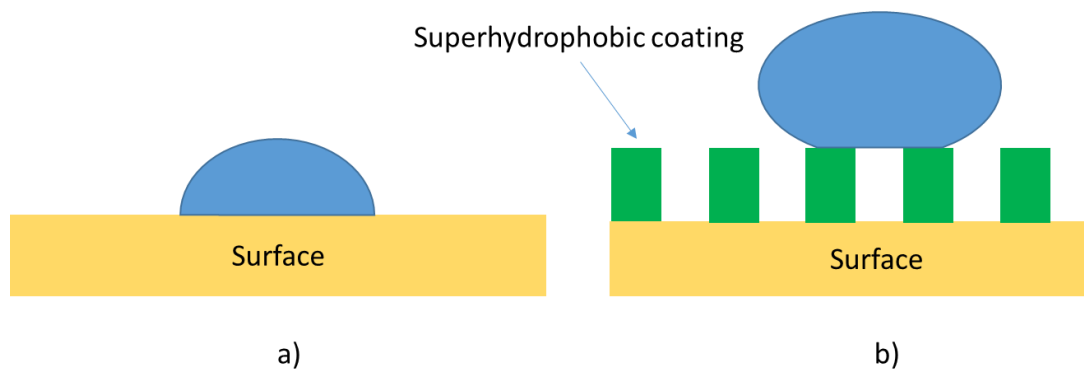
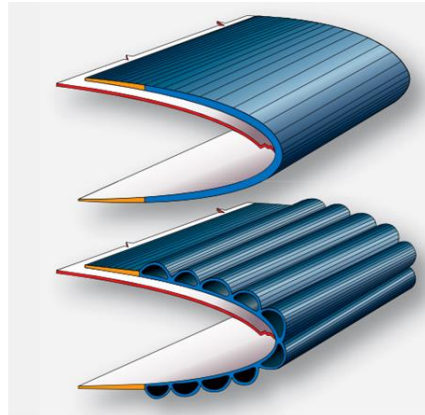


Fig. 2.1 – Schematic representation of superhydrophobic coating effect on water drop: a) water drop on an un-coated surface; b) superhydrophobic coating reduces the angle of contact of the water drop

Low cost, a protection of the complete surface, easy maintenance and no necessity of lightning protection are the advantages of these special coatings [10]. However icing prevention by coating alone is difficult to provide full ice protection, it should be combined with an active method [8].

An inflatable rubber boot (Fig. 2.2) on the leading edge of the wing turbine or wing could be defined as *passive de-icing system*. This system is designed with rubber inflatable boot glued on the leading edge. This crack the ice on the surface when it is inflated by compressed air. This helps to remove the ice through wings vibrations and wind flows. The disadvantage is that ice layers can strongly adhere to the surface and vibrations and wind flows may not be strong enough to crack it; this system compromise also the aerodynamic properties of the leading edge of the wing [5, 10].

Furthermore, during the years of service, the rubber boots will require intensive maintenance, which may not be economical.



a)



b)

Fig. 2.2 – a) Cross section of a pneumatic de-icing boot uninflated (top) and inflated (bottom); b) de-icing boot deflated (left) and inflated (right) [4]

Analogous mechanical de-icing method that exploits stresses to break the ice sheets is called Electro-Mechanical Expulsion Deicing System (EMEDS, as seen in Fig. 2.3). Current electrical pulses are applied to actuators that generate electro-magnetic fields causing them a quick change of shape. This deformation produces high frequency vibrations transmitted to the metal skin (erosion shield) of the leading edge. Vibrations help to crack and de-bond the existing ice on the surface [11]. Several advantages of this protection method are listed on Table 2.1.

Table 2.1 - Features comparison of EMEDS technology and traditional Pneumatic Boots [11]

Parameter	EMEDS	Pneumatic Boots
Surface	Metal	Elastomeric
Life time	Life of aircraft	Months, depending on service
Drag Incremental	Absent	Relevant
Deice Performance	Ice as thin as 0.12 cm & no upper limit	Greater than 0.6 cm
Power	25 amp x 28 V, DC = 0.7 kW	-

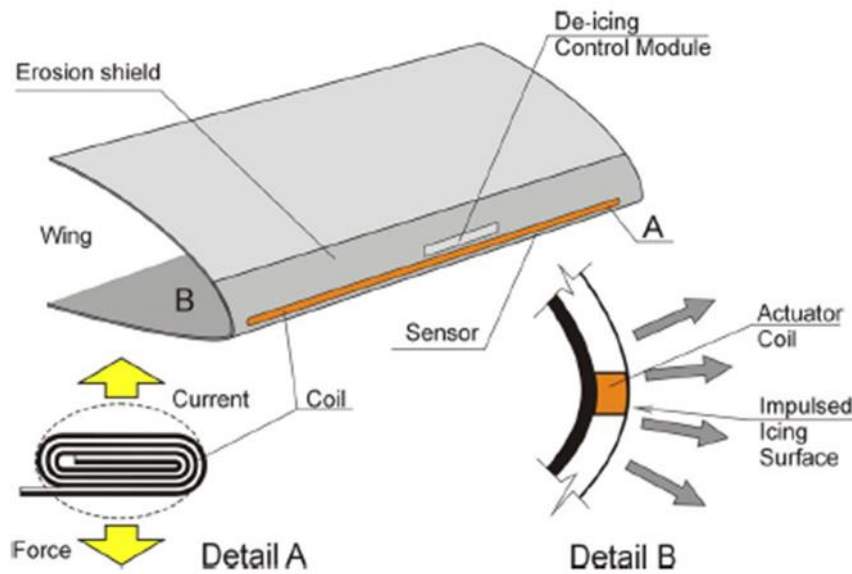


Fig. 2.3 – Electro-Mechanical Expulsion Deicing System (EMEDS) [11]

Active ice protection methods use external systems, typically thermal or chemical. Thermal systems consist in hot jet exhaust ducted through the wing leading edges other critical areas of the aircraft, or electric heaters embedded in the wings or glued to the leading edge. If the thermal system works to remove the existing ice, it can be defined as *active de-icing system*; if it works to avoid ice accretion on the surface, it can be defined as *active anti-icing system*.

The chemical substances are antifreeze or other solvents that could dissolve the ice on the surface; these fluids normally contain glycols and/or alcohols [5]. The chemical substances could be sprayed on the aircraft surfaces when it is stationary on the

ground, before the flight. Precautions must be taken to avoid fluids entry into cavities dangerous for aircraft safety. Once it takes off, the ice could be formed again.

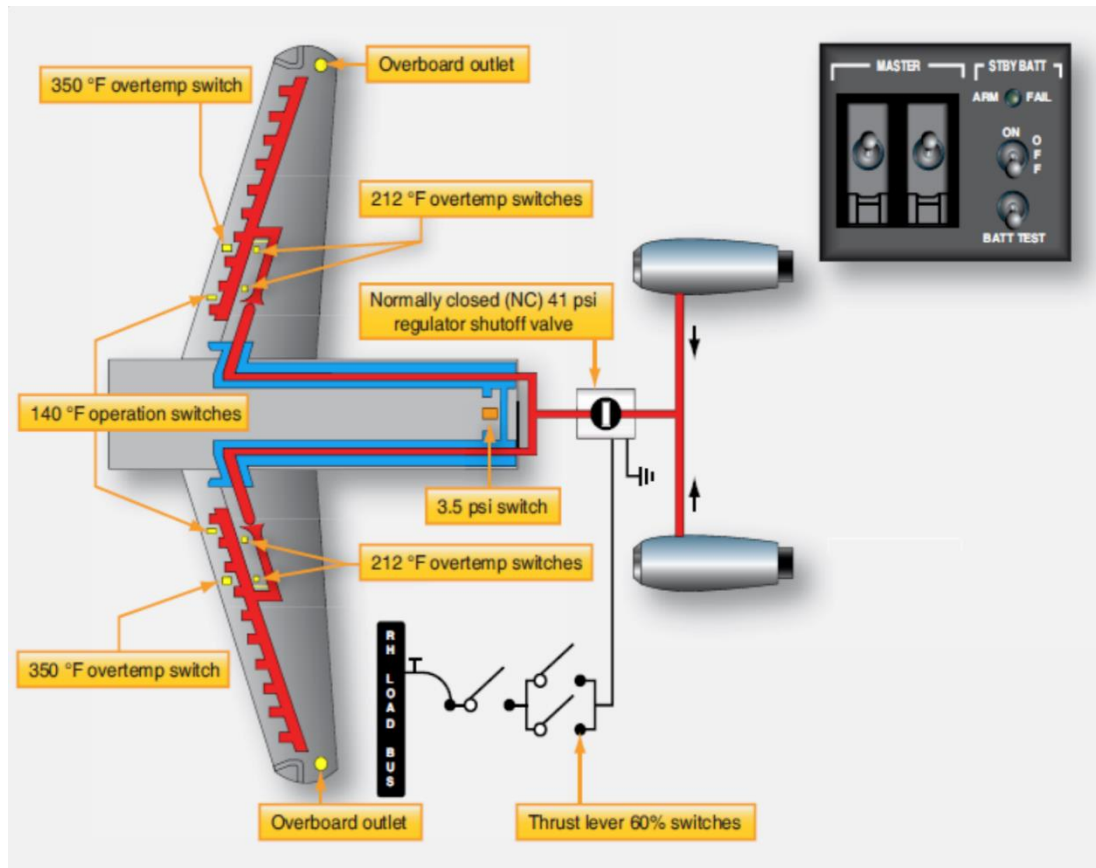


Fig. 2.4 – Hot air bleed duct systems scheme [4]

Hot air bleed systems (Fig. 2.4) usually use hot air routed along inside the wing, with the target to heat the leading edges of the aerofoil to prevent the ice formation or to remove it. The sources like the turbine compressor or engine exhaust heat exchangers could bleed large amounts of very hot air, providing icing protection heat. The hot air is directed through pipes system to each wing leading edge or other components that need to be heated [5]. The wing edge is made of two separated skin sheets (Fig. 2.5). The air directed against the leading edge is subsequently vented out of the wings through a series of vents, located in the bottom of the wingtip.

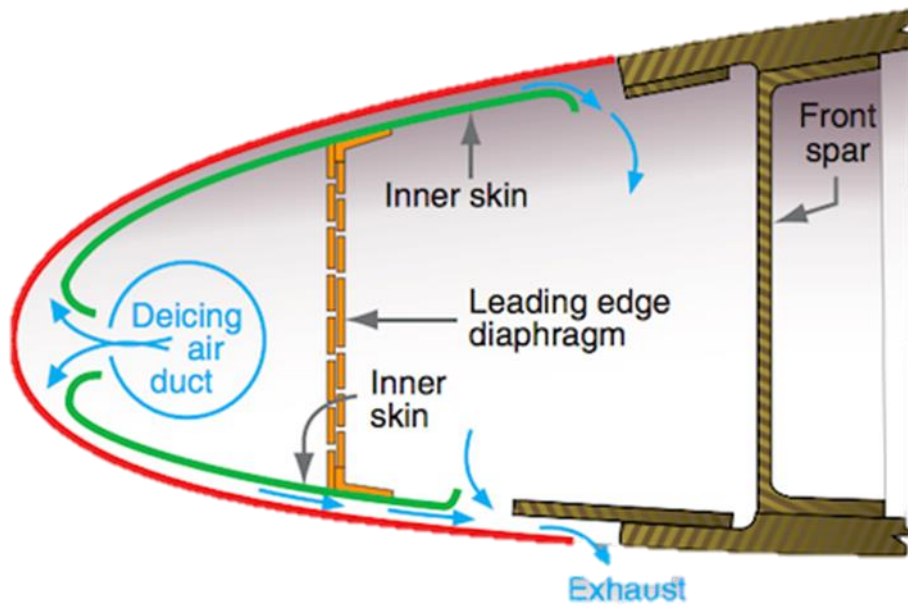


Fig. 2.5 – Heated wing leading edge [4]

The hot air protection method requires a heavy and complex piping and valve system. The most used active system consist of electro thermal heating element embedded or laminated on the wing skin [5, 11, 12]. The heating furnished by these elements melt the ice present on the surfaces. To avoid aerodynamic imbalance, these elements turn ON and OFF in paired sections.

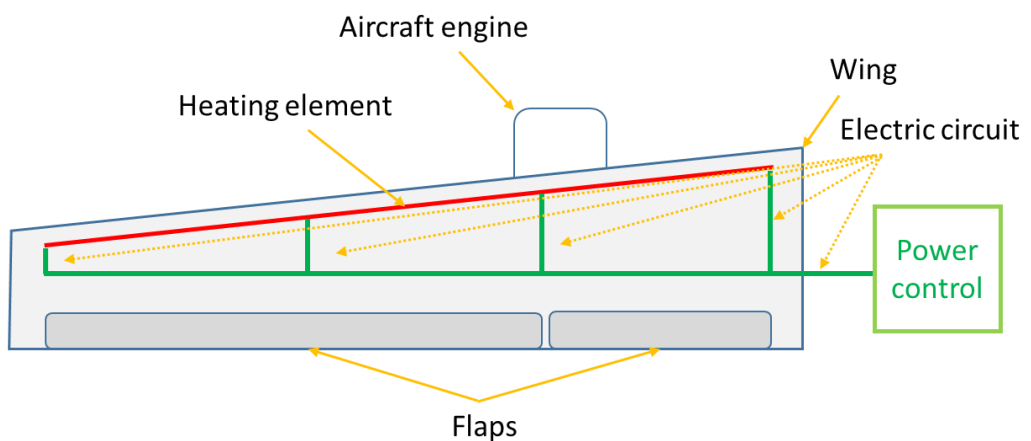


Fig. 2.6 - Electro-thermal heating system representation

Fig. 2.6 represents a scheme of how the thermal protection system is settled inside the aircraft wing. Because of the different type of heating elements (patent protected), the setup configuration (cable connection and elements disposition on the surface) varies in order to obtain the best efficiency of the whole system.

To avoid ice formation it is necessary to keep the surface dry by evaporating water drops or films on the surfaces, or just to prevent icing and maintaining it liquid form (easy to be removed by air flows). The system should work while the aircraft is on the ground or during the flight, with different levels of energy consumption.

2.2 High electrical conductive nanomaterials

A fundamental aspect of nanotechnology is the increasing ratio between surface and volume that allows new quantistic mechanical effects as the “quantum confinement” which provide a complete change of electrical properties for nano size particles of the same material [13].

One of phenomena that is characteristic of nanostructure is called ballistic conduction and it can be observed in metal nanowire, or carbon nanotubes and graphene sheets. Ballistic conduction is the transport of electrons in a low electrical resistivity medium caused by scattering. Ballistic conduction happens in materials when long distances flows of charges are not affected by scattering events.

In a solid the resistivity is caused by impurities, defects, the atoms composing the medium that scatter the electron simply oscillating around their equilibrium position. So the mean free path is defined as an average length where the electron can travel without collision that could scatter it. When the electron travels along a mean free path longer than the dimension of the medium itself, this is defined ballistic transport.

Particularly in composite environment, it has been demonstrated that these materials, incorporated into polymeric matrices, can drastically improve their electrical characteristics without compromising other relevant features, such as mechanical properties [14, 15].

2.2.1 Carbon nanotubes - CNTs

- *CNT structure and characteristics*

An ideal carbon nanotube can be described as a carbon tube made by a graphene rolled up sheet, closed at the edges by two half hemispheres. The diameter of a single wall carbon nanotube (SWCNT) ranges from 0.7 nm to 10 nm. Their high value of length and diameter ratio allow them to be considered as mono-dimensional structure. The multiwall carbon nanotube (MWCNT) are made by many concentric SWCNT and their diameter increases with the number of wall.

The electronic structure of carbon nanotubes is very similar to graphene one. Their surprising conductivity properties change with their geometry (Fig. 2.7): “Armchair” SWCNT shows a metallic behaviour; “Zig-zag” and “Chiral” SWCNT show a semiconductor behaviour.

MWCNT show similar electrical properties to SWCNT. The electronic transport takes place in the direction of length of the tube, for which they are capable of carrying high currents without overheating (ballistic conduction) [13].

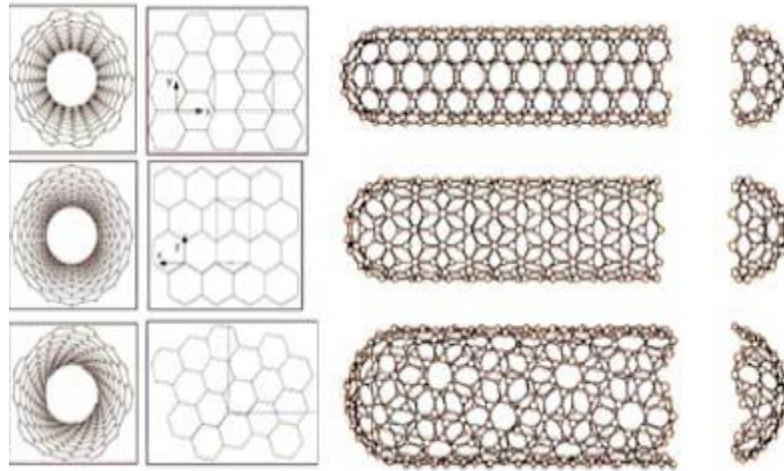


Fig. 2.7 - CNT geometric structures: armchair (top), zig-zag (middle) and chiral (bottom) [13]

Carbon nanotubes are characterized by a particular orbitals structure. Carbon nanotubes are theoretically rolled up graphene sheets, so the orbital structure of the carbon layer is altered: decreased bond length between carbon atoms, different bond angle. σ - and π -orbitals are no longer perpendicular to each other, causing a mixed state of these orbitals [16]. The π -orbitals as illustrated in Fig. 2.8b. Fig. 2.8c represents the wavefunctions of a carbon nanotube from the top view [17]: the bright areas are positive charges, while the dark areas indicate negative charges. This mixture of sp^2 and sp^3 -orbitals is defined as rehybridization [18].

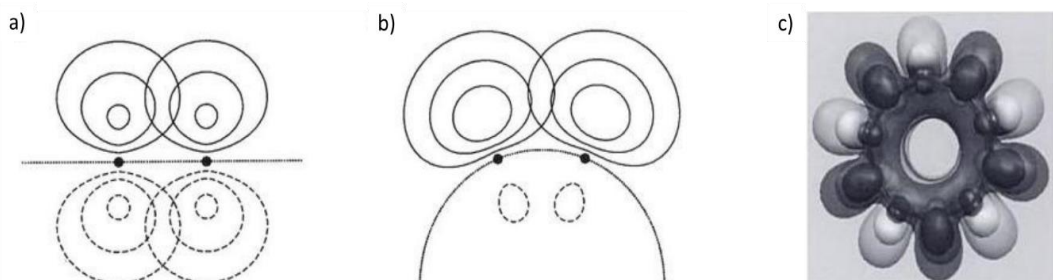


Fig. 2.8 - a) π -orbitals of graphene; b) rearrangement of π -orbitals in a nanotube; c) rehybridization of a carbon nanotube [18]

Many research works are studying different applications of carbon nanotubes, such as antiballistic vests, electro-thermal elements and transparent conductors. There are

continuous developments on CNT conducting films [19] as substitute to indium tin oxide (ITO). The ITO price is increasing due to scarcity of indium, and nowadays there is a growing demand for touch-screens and photovoltaics devices.

Nowadays it has been possible to develop SWCNT sheets with 90% transparency and 100 Ωm resistivity [20]. This surface resistivity is still substantially higher than ITO claddings. Kaempgen et al [21] have evaluated the transparency and conductivity at room temperature of different CNTs. CNT suspensions [22] were prepared with 1% sodium dodecyl sulphate in water. The sprayed suspension concentration was 1–2 mg/ml. The substrate was heated during the coating process to immediately dry the droplets on the surface (temperature of 100 °C).

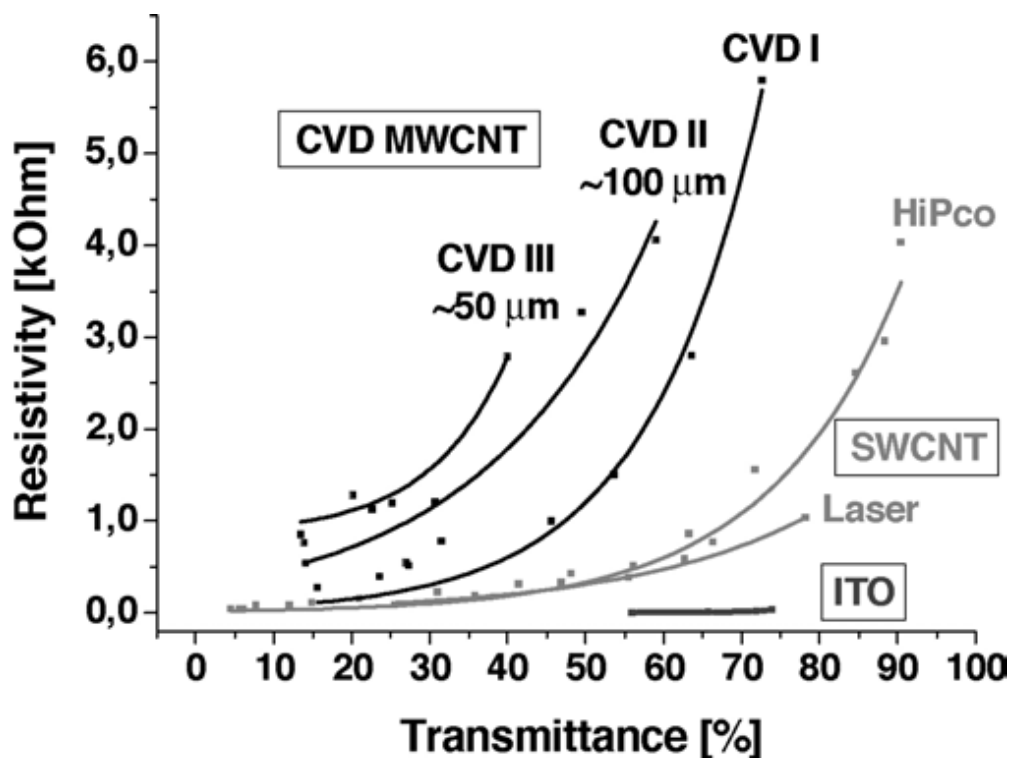


Fig. 2.9 - Transmittance vs. resistivity plot for sprayed CNT layers and ITO. Each curve represents different CNT material (black curves: MWCNT; grey curves: SWCNT; dark grey: ITO). [21]

In Fig. 2.9 the results of the experiment are illustrated. It has been clarified that [21]:

- a) Big diameter cause an increase of the absorbed light but not affect the conductivity (SWCNTs are smaller than MWCNTs). For SWCNTs, no significant differences between different synthesis methods have been observed;
- b) With the same level of transparency, longer CNTs increase the conductivity: less contacts exist between CNTs, lower is the resistance of the electrical transport [23]. This is observable for carbon nanotubes networks with tube 50 and 100 μm of average length (Fig. 2.9) [24, 25];
- c) At 90% transmittance CNTs coating with electrical sheet resistance of 1 $\text{k}\Omega/\text{sq}$, close to the ITO values.

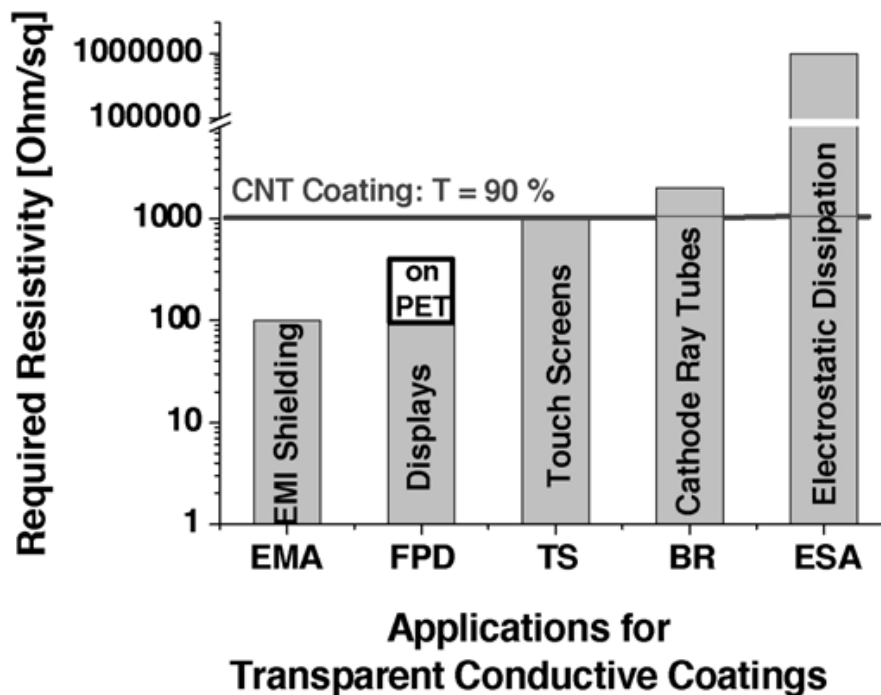


Fig. 2.10 - Required surface resistivity in typical applications for transparent conductive coatings compared to the performance of thin conductive CNT networks [24]. EMI: electromagnetic interference (10 kHz–1 MHz); FPD: flat panel display (PET: polyethylene terephthalate); TS: touch screen; EMS: electromagnetic shielding for cathode ray tubes; ESD: electrostatic dissipation [25]

The simple production processes of such carbon nanotubes coatings and their high conductivity make them interesting for several applications. In Fig. 2.10 the sheet resistance of relative CNT coatings has been evaluated for different applications.

- *Functionalisation of CNTs by oxidation*

In the last years carbon nanotubes (CNTs) have been (and still they are) investigated as strengthen agent in composite materials (polymer based matrix) thanks to their high traction resistance [26], and to improve the electrical characteristics thanks to their high value of conductivity [27-30]. Carbon nanotubes ballistic conduction lead to their high electrical conductivities [31]. Next-generation aerospace materials require increased strength, light weight and high electrical conductivities; this push an high interest in carbon nanotubes based composite materials for numerous applications [32].

Many studies have been done [26] to explain how to modify the electrical characteristics of carbon nanotubes (Fig. 2.11). Covalent attachment (e.g. by oxidation) to the CNTs structure could change their conductivity, however, it usually introduces structural defects on the nanotubes' surface. The attachment could induce charge transfer from CNT to adsorbates and subsequently invoke *p* or *n* - type doping effect. CNTs functionalisation can be achieved by chemical oxidation using acid solution, pure or mixtures.

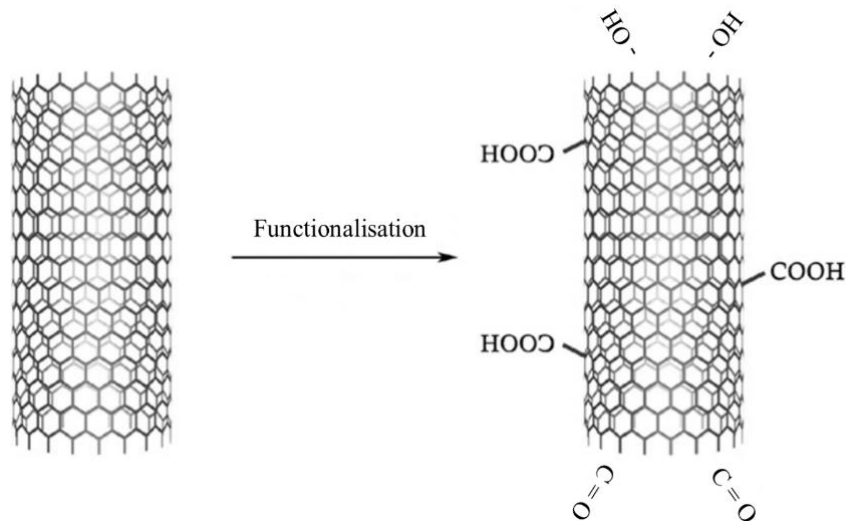


Fig. 2.11 - Functionalisation of MWCNTs by carboxylic (-COOH), carbonyl (>C=O) and hydroxyl group (-OH)[33]

Datsyuk et al. have studied the oxidation effects on multiwall carbon nanotubes structure through acid (HNO_3 , H_2SO_4 and H_2O_2) and basic (NH_4OH mixed with H_2O_2) agents [33]. Processes of chemical oxidation and purification have been carried out on MWCNTs [33] with four different treatments, as described in Fig. 2.12. With *Treatment 1* MWCNTs were stirred for 2h in HCl. After this, small quantities of powder have been treated in different oxidative solutions. In *Treatment 2* MWCNTs were magnetic stirred in HNO_3 for 48 h. In *Treatment 3* the MWCNTs were stirred in a piranha solution (mixture 70:30 of H_2SO_4 and H_2O_2) for 5 h. In *Treatment 4* the MWCNTs were poured in 1:1 mixture of NH_4OH and H_2O_2 , heated to 80°C and left for 5 h.

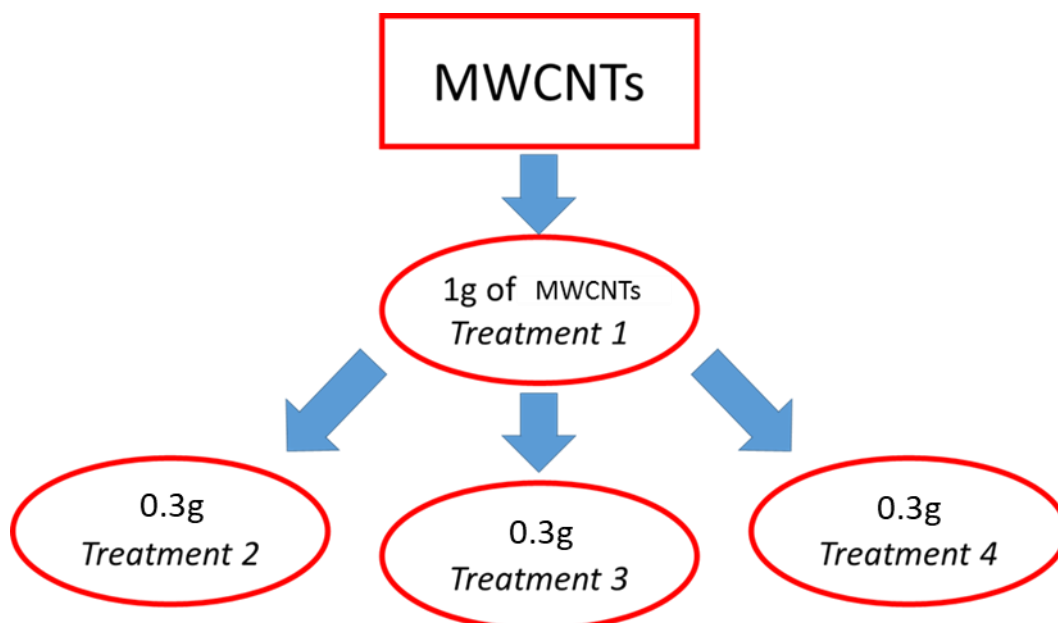


Fig. 2.12- Scheme of MWCNTs acid treatments

Electron microscopes (SEM and TEM) were used for morphological analysis on possible MWCNT changes after each treatment. As shown in Fig. 2.13a, HCl treatment did not affect the morphology of the tubes. Oxidation with strong oxidants (Fig. 2.13b, Fig. 2.13c and Fig. 2.13f) seemed to modify bundles morphology: nitric acid-treatment caused a reduction on the average length of CNTs (~700 nm) (Fig. 2.13f) [33]. Piranha solution treatment results showed a lower oxidation level than nitric acid one and no additional defects on the nanotubes surface. Using basic mixture of NH_4OH and H_2O_2 the amorphous carbon phase has been completely removed from the multiwall nanotubes specimens [33].

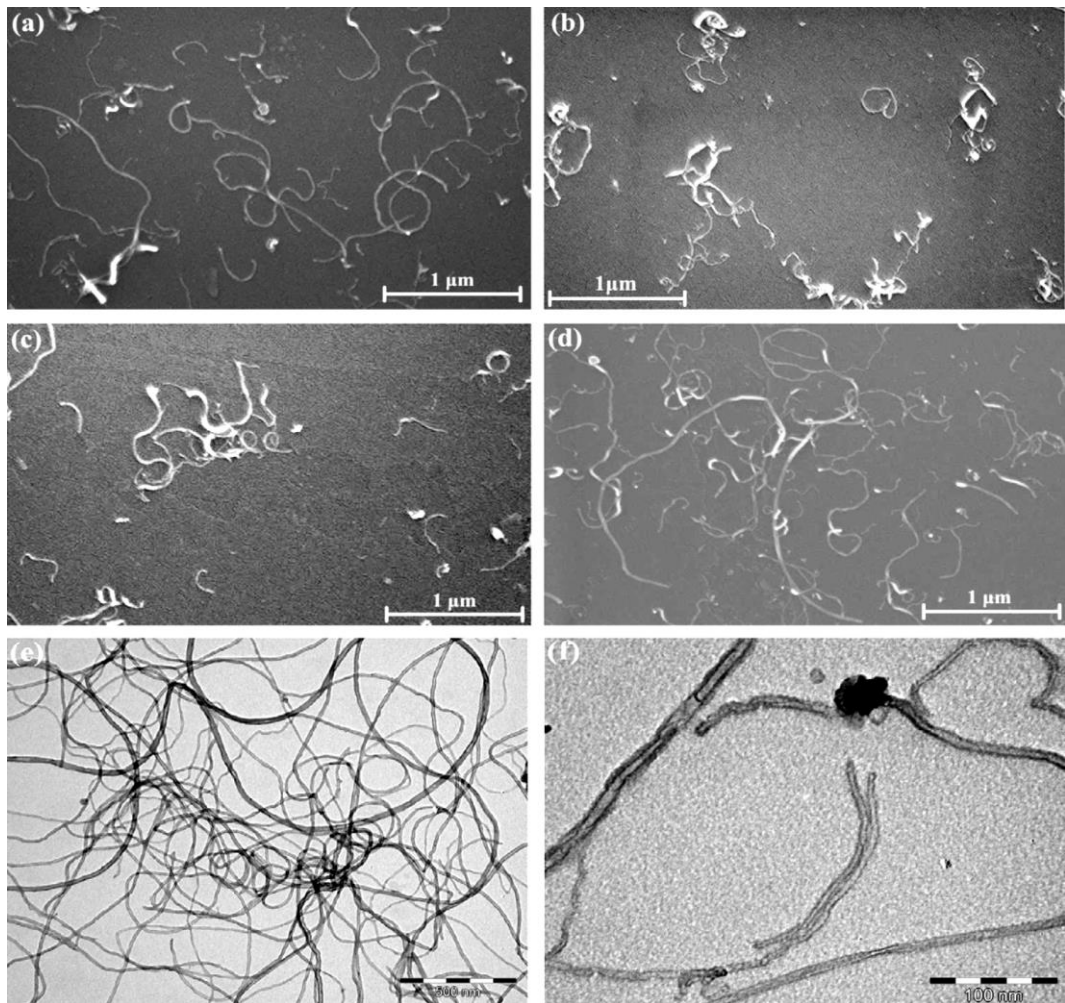


Fig. 2.13 - SEM images of the treated MWCNTs at two different magnifications: (a) after purification with HCl; (b) after nitric acid oxidation; (c) after oxidation with piranha; (d) after oxidation with ammonium hydroxide and hydrogen peroxide mixture; TEM images after modification with (e) ammonium hydroxide and hydrogen peroxide mixture and (f) after nitric acid. [33]

Acid treatment has been demonstrated to influence the conductivity of carbon nanotubes. Jiyun Kwon and Hando Kim [34] have studied the electrical conductivity of waterborne polyurethane (WBPU) modified with “pure” carbon nanotubes (CNT) and HNO₃ treated one (A-CNT). The raw carbon nanotubes have been treated to obtain CNT and then acid-treated to obtain A-CNT. To purify the raw material from impurities and make CNT, the powder has been treated with HF and HNO₃ [34]. A water based CNT dispersion was prepared with the aid of an ultrasonic bath for 60 min. Then, the dispersions were treated with nitric acid heated at boiling temperature.

As treated A-CNT were rinsed with water and acetone. Then, water based A-CNT dispersions were prepared with the previous method [34].

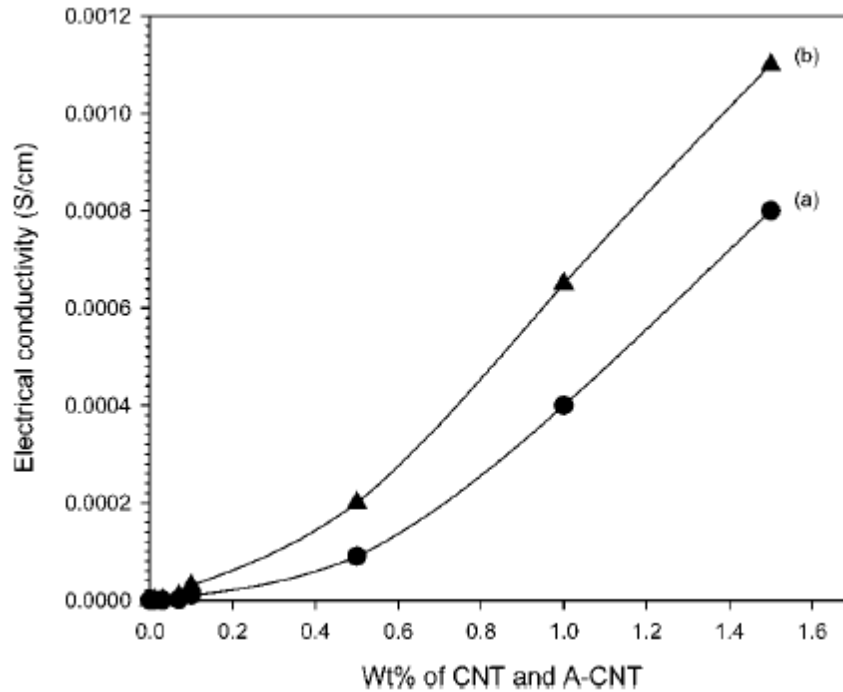


Fig. 2.14 – The graph shows the changing of the electrical conductivity in function of carbon nanotubes content. Curve (a) WBPU/CNT and curve (b) WBPU/A-CNT composite films [34]

Table 2.2 – Measured electrical conductivities of WBPU films, CNT and A-CNT sheets [35, 36].

Material	Electrical conductivities S/cm
WBPU films	2.5×10^{-12}
CNT sheets	25
A-CNT sheets	35

On Table 2.2 are listed the electrical conductivities of WBPU films, CNT and A-CNT sheets used in Kwon and Kim experiments [35]. The impurities removal and the smaller particle size should be the cause of the higher electrical conductivity of the A-CNT sheet. CNT and A-CNT improved the conductivity of the polymeric films. At equal contents, the electrical conductivities (Fig. 2.14) of the WBPU/CNT composites were lower than the WBPU/A-CNT. This could be explained by: the smaller particle

size and higher dispersibility of A-CNT; it helped to obtain also a more uniform distribution of the nano filler, giving a more homogeneous composite as a result. The acid treatment reduced the concentration of impurities in A-CNT (amorphous carbon or carbon black powders).

Recent studies analysed the doping effect of acid treatments evaluating the changing on the electrical conductivity of CNTs based film, or buckypaper. Buckypaper (CNP) is a thin porous assembly of CNTs, usually formed by filtration from their dispersion in a solvent. Buckypaper (CNP) can be obtained using the chemical vapour deposition method (CVD) [36], liquid casting, printing [37-39], droplet-drying [40], and vacuum filtration [41]. Vacuum filtration is the most common and simple method suitable for CNP production. The electrical properties of buckypaper have been studied extensively over the last few years. Zhang et al. [42] studied the effect of nitric acid treatment on MWCNT buckypaper. The result was an increase of the film electrical conductivity from $1.3 \times 10^4 \text{ S m}^{-1}$ for raw samples to $3.8 \times 10^4 \text{ S m}^{-1}$ for nitric acid treated samples. The improvement in electrical conductivity was due to the increased charge carrier concentration and its mobility [43, 44]. Another possible explanation was the improved contact conductance between tubes. The functional groups located in the contact area served as a further conductance path with lower electrical resistance [45]. Fig. 2.15 show an example of electron transfer before (Fig. 2.15a) and after (Fig. 2.15b) the acid treatment. Contact resistance was expected to be reduced thanks to functional groups and their transport path.

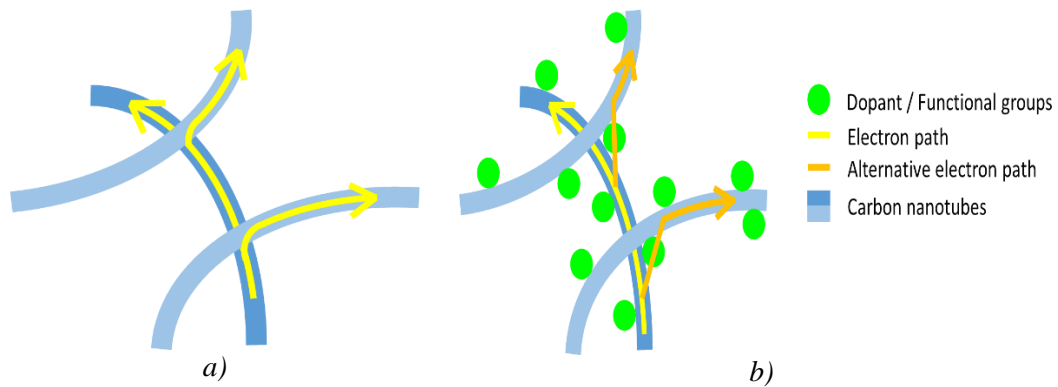


Fig. 2.15 - Schematic representation of electron transfer between nanotubes before (a) and after (b) the nitric acid treatment. The contact resistance was reduced by the low resistance path created by the functional groups

Functionalised CNTs can be used to improve the characteristics of the thermosetting resins. Gantayat et al. [46] used functionalised multiwall carbon nanotubes (f-MWCNT) to enhance the mechanical properties of an epoxy resin. The nanotubes were functionalised in two mixtures of $\text{H}_2\text{SO}_4/\text{HNO}_3$ (3:1 volume ratio) and of $\text{H}_2\text{O}_2/\text{H}_2\text{SO}_4$ (1:4 volume ratio). The f-MWCNT/epoxy mixture was then casted on a mold and cured. Functionalization of MWCNT reduce or avoid the agglomeration of the CNTs caused by the vander Waals forces between nanotubes, favoring an even distribution of the CNTs in the epoxy matrix. The tensile strength and Young modulus exhibited 27% and 14% increase, respectively, with 0,6 wt% of CNTs concentration.

Chen et al [47] demonstrated how the nitric acid treated CNTs can help either to improve the electrical and thermal properties of the epoxy resins. Chen explained the differences in nanocomposite thermal and electrical behaviors between as-received and functionalised CNTs. The difference is due to the dispersion level of the nanotubes in the matrix. As-received CNTs tend to agglomerate, causing an uneven distribution of the nanotubes in the matrix. The aggregates lead to a lower percolation threshold by increasing local contacts between neighboring CNTs. Functionalised CNTs are much easier to be dispersed in the matrix, avoiding aggregates formation. Fewer the contacts between CNTs, higher is the percolation limit. A high percolation level

indicate an increase in the amount of nanotubes that produce a continuous conductive web.

Braga et al. [48] modified the poly(trimethylene terephthalate) (PTT) using functionalised CNTs. The CNTs were functionalised with nitric acid in a heated bath for 5 h under reflux. Their study was focused on improving the electrical and the mechanical characteristics of the PTT. The addition of 1 wt% of CNT did not cause any relevant tensile strength increase, indicating a low adhesion of CNT in the polymeric matrix and a low dispersion level in the PTT matrix. Meanwhile the functionalised CNTs helped to increase the tensile strength from 29 MPa in neat PTT to 32 MPa in PTT with 1 wt% of functionalised CNTs. The mechanical improvement indicates that the functionalization improves the adhesion and dispersion of the nanotubes in the PTT matrix. The addition of 1 wt% CNT decreased the electrical resistivity of the PTT from $6.8 \times 10^{10} \Omega\text{cm}$ to $2.5 \times 10^2 \Omega\text{cm}$. The CNT conductive network decreased the electrical resistivity PTT composite. With the same amount of functionalised CNTs, the electrical resistivity decreased to $\sim 10^5 \Omega\text{cm}$. Braga explained that the lower improvement of the electrical conductivity was caused by the damages on the graphitic conductive structure of the CNT. The acids, used to functionalize the CNT surfaces, caused the damages.

Chen [47] and Braga [48] works demonstrated that if the acid treatment is too harsh, it can cause a loss in the efficiency of the nanotube on improving the electrical/thermal characteristics of the matrix. The acid treatment parameters (e.g. composition, time, temperature) should be chosen correctly, in order to obtain the best improvement of the polymer characteristics.

- *Silver decoration of CNTs*

Electrical conductivity is one of the characteristics that make carbon nanotubes more attractive in scientific research. Several works have been conducted in order to improve the electrical resistance of CNTs, despite its high value. The contact resistance between nanotubes can be possibly reduced by common techniques of deposition of high conductive metal nanoparticles (Au, Ag, Ni or Cu) on the external surface of the nanotubes. These processes are called metal decoration [49-56].

Ahmadpoor et al [57] decorated MWCNT with silver nanoparticles synthesized, on the surface of acid treated nanotubes by chemical reduction of silver nitrate (AgNO_3) and sodium hydroxide. Pristine MWCNTs were acid treated in a concentrated HNO_3 solution for 4 hours. The functionalized MWCNTs were ultrasonicated for 2 h in an aqueous solution of 0.1 M AgNO_3 while NaOH was added dropwise till the pH reaches 6. The results indicated that Ag nanoparticles were attached to the outer surface of MWCNTs.

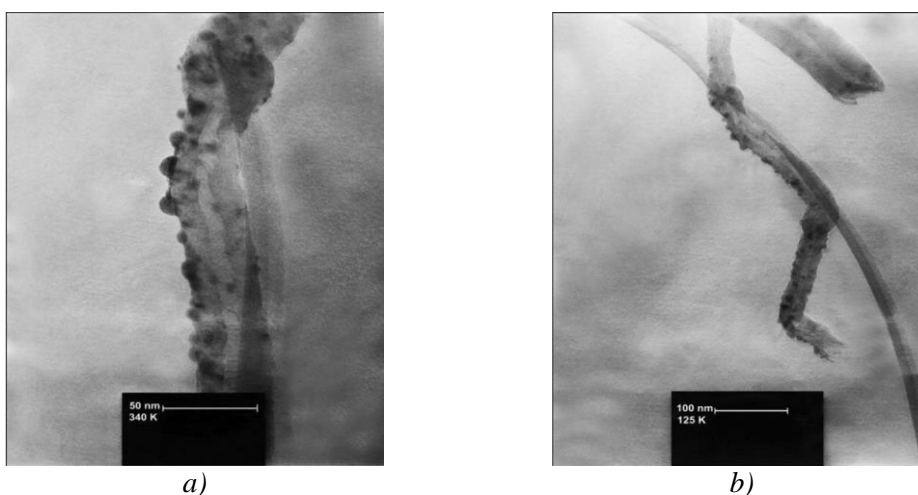


Fig. 2.16 - TEM images of MWCNTs decorated with Ag nanoparticles: a) x340000; b) x125000 [57]

Liu et al. [58] used the so-called Tollen reaction, or silver mirror reaction, to generate silver coatings on MWCNTs. MWCNTs were dispersed in 0.1% sodium dodecyl sulphate (SDS) aqueous solution under sonication. The MWCNTs suspension was

poured in a solution of 1% silver nitrate where drops of 5% ammonia were added until the brown precipitate dissolved. Subsequently 0.5 g of formaldehyde were dropped to the system while was kept stirring at 60°C for 0.5 h. Silver nanostructures (Fig. 2.17) were formed on the surface of individual CNTs and its bundles.

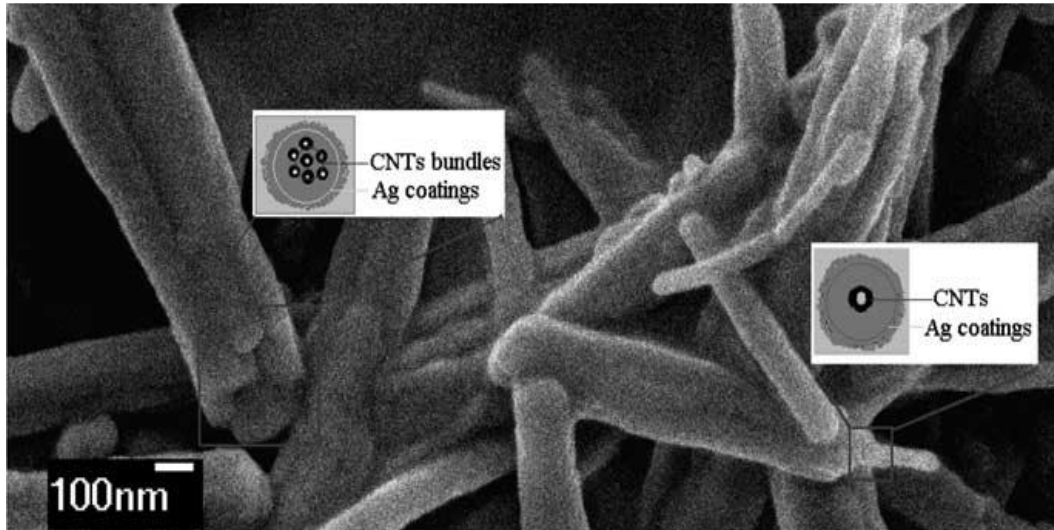


Fig. 2.17 - SEM image of the Ag-CNT products [58]

Xin et al. [59] used decorated carbon nanotubes with silver (Ag–CNTs) as fillers for polypropylene (PP) and polystyrene (PS). Compared to pristine CNT, the Ag–CNTs composites reached the highest electrical conductivity of PP and PS (up to 2.6×10^2 S/cm for Ag-CNT/PS, with 5 wt% loading). Due to the reduced Van der Waals forces between nanotubes, silver nanoparticles helped to improve the CNT dispersion in the polymeric matrix. Ag-CNTs improved tensile modulus and strength better than pristine CNTs. Electrical properties and mechanical proofs confirmed the advantage of the Ag–CNTs as effective conductive fillers.

- *Doping and jointing agents in CNT network*

Conductive coatings would help to reduce the electrical resistance in the contact area (between nanotubes), causing an increase in the electrical conductivity of the CNTs web. This coating is defined as jointing agent [60]. The most used compound is a mixture of zinc oxide (ZnO) [61]. Its effectiveness has been proved by You et al: they produced a transparent bilayer thin films with sheet resistance of 34.1 Ω/sq [61]. Guler et al. [62] investigated the electrical properties of carbon nanotubes hybrid zinc oxide (ZnO-CNTs) nanocomposites. The ZnO/CNT powder was synthesized by ball mill technique and the compacted by sintering in Ar ambient. The electrical conductivity increased from 6.55×10^{-5} S/cm (for the un-doped ZnO) to 4.01×10^{-3} S/cm (for ZnO/CNT with 1% CNT). The results highlighted how the interaction between CNT and ZnO helped to increase the electrical conductivity of the composite. Further method should be analysed in order to simplify the production process and to reduce the chemicals involved. This step would help on the scale up process for a real dimension component.

High conductive particles can be added to further improve the electrical characteristics of the conductive nanotube network. These particles can be considered as doping agents: it is an element that is introduced into a material to alter its original properties (e.g. electrical properties). Oluwalowo et al. [63] produced an Ag/CNT composite by dispersing various silver nanoparticle (AgNP), micro-particles (AgmPs) and nanowires (AgNWs) with MWCNTs. The electrical and thermal conductivity of CNT buckypaper increased by incorporating Ag particles (electrical conductivity of 1.3×10^4 S/cm and thermal conductivity of 126 W/mK for AgNW/CNT samples). The sonication process provided a uniform dispersion of the Ag/CNT suspension, resulting

in an even distribution of the Ag particles/AgNW into the buckypaper. The Ag formed a network of conductive (with low electrical resistance) paths between the nanotubes, resulting in an improved electrical conductivity of the CNT network [63, 64]. Patole et al. [65] produced polyvinyl alcohol (PVA) incorporated CNT-graphene hybrid buckypaper (HBP [66]) composites with enhanced electrical conductivity. The nanotubes and the graphene were dispersed in a water based PVA solution. The resulting composite was obtained using wet filtration-zipping method [67]. The resulting composite showed an electrical conductivity of 82 S/cm, which is five orders higher than the neat PVA films (10^{-5} S/cm). Byrne et al. [68] developed a Cu doped buckypaper by substrate-enhanced electroless deposition. The electrical conductivity increased with the quantity of copper deposited onto the buckypaper. The electrical conductivity increased up to 3.5 times that of the pristine buckypaper [68]. An alternative method to produce Cu doped buckypaper would consist on mixing copper particles with CNTs, as Oluwalowo and Patole did in their work. This method would reduce the chemicals involved in the process.

- *CNT for ice protection systems*

Aircraft icing develops because of the existence of frozen water droplets in the atmosphere that collide with aircraft during the flight [4]. The reduction of angle of attack and the increased profile drag, caused by ice accretion, can lead to control and stability problems [6].

From engineering point of view [69], the high conductivity of CNTs can be exploited to make de-icing system based on heating element. The main problem with conventional heating element, used for de-icing application, is their not durable bond between the metal sheet and the protective layer. This weak bond between metal and

matrices is the fundamental cause of non-uniform heating [69, 70] and a possible critical point for the mechanical performances.

The conventional de-icers composite-metal bonding is less uniform and stronger than a comp-comp (comp = composite) bonding in a composite electro-thermal heater. CNT sheet/matrix bonding would produce a more homogeneous heating without need of high voltages, thanks to the high electrical conductivity of CNT sheets [69].

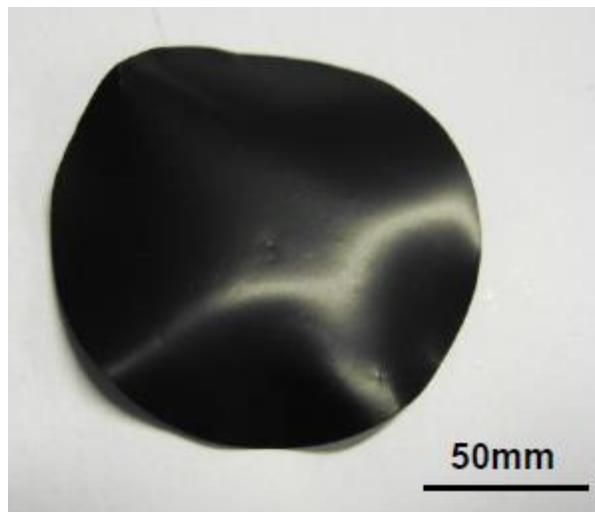


Fig. 2.18 - Silver decorated MWNTs sheet [69]

For de-icing applications Zhao et al. [69] studied a hybrid laminate (Fig. 2.18) consisting of Ag decorated multiwall carbon nanotubes sheets, prepared by vacuum assistant resin transfer method. As seen in Fig. 2.19, higher is the heating current higher is maximum temperature reached by the composite sheets. A consistent conductivity (430 S/m), the fast rising temperatures and cooling rate are very promising characteristics for icing protection applications, in this case for working in de-icing mode.

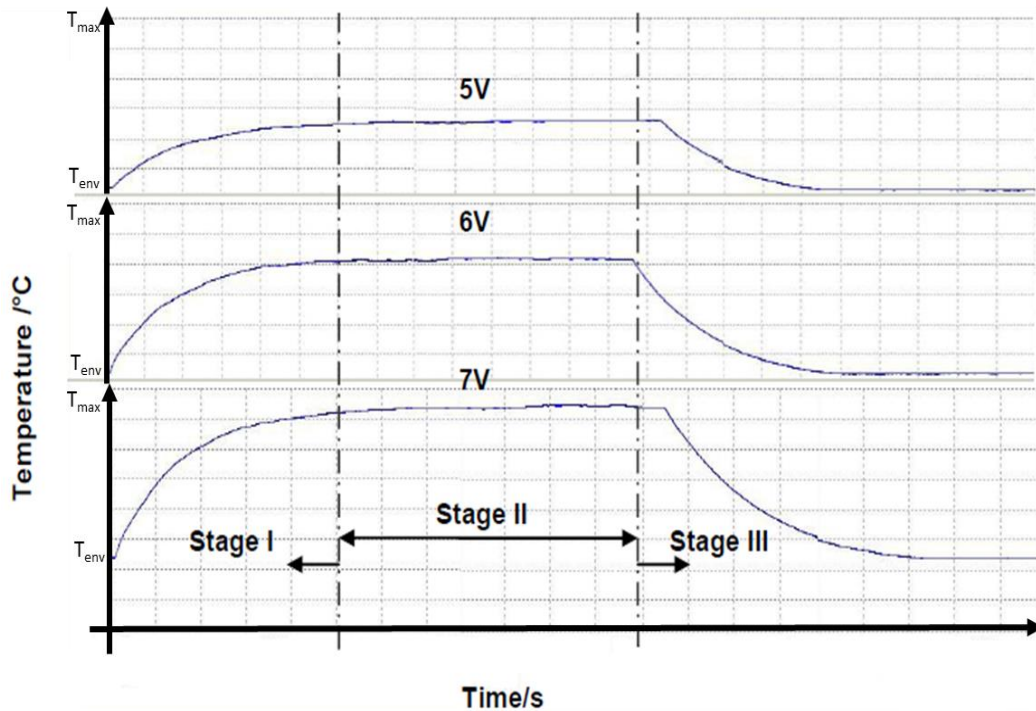


Fig. 2.19 - Thermal cycles from environment temperature (T_{env}) and maximum temperature (T_{max}) reachable with 5, 6, 7V of input voltages: stage I, ramping up, stage II: stable-state and stage III: cooling down [69]

Another similar example for the same application is described in a study of Chu et al. [71] where an electro thermal heating glass fibre/epoxy composite carbon nanotube buckypaper (CNP) based, has been employed. The fabrication process of the CNP composite is represented in Fig. 2.20. The heating composite exhibited incredible electric heating properties at environment temperatures from -22°C to 15°C , and a 14 m/s wind speed and de-icing times in the range of 4 to ~ 7 minutes. Moreover, thanks to the CNP composite excellent characteristics and performances (conductivity of 64.9 S/cm, heating and resistance stability) it could be used as thermal source for icing protection application. De-icing or anti-icing it depends on how much power it could be used for the system.

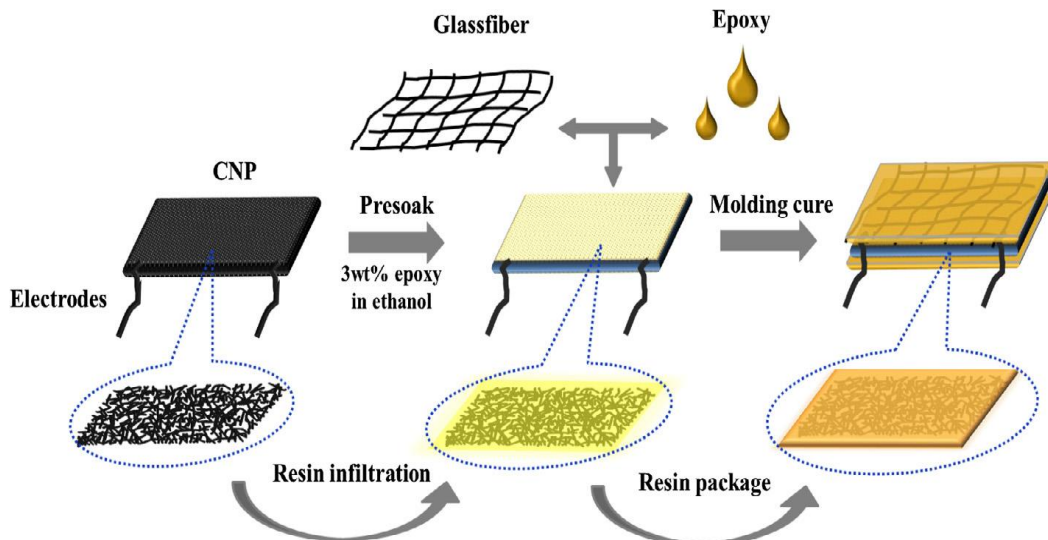


Fig. 2.20 - The fabricating process of CNP/glass fiber/epoxy composite. Magnified areas are the schematic drawing of the CNP at different stages [71]

Recently Yao et al [72] developed a horizontally oriented CNT film produced by chemical vapour deposition and embedded in glass fibre (GF) fabric (Fig. 2.21). During the de-icing test the CNT/GF composite removed accreted ice within 15 s under a constant voltage of 16 V.

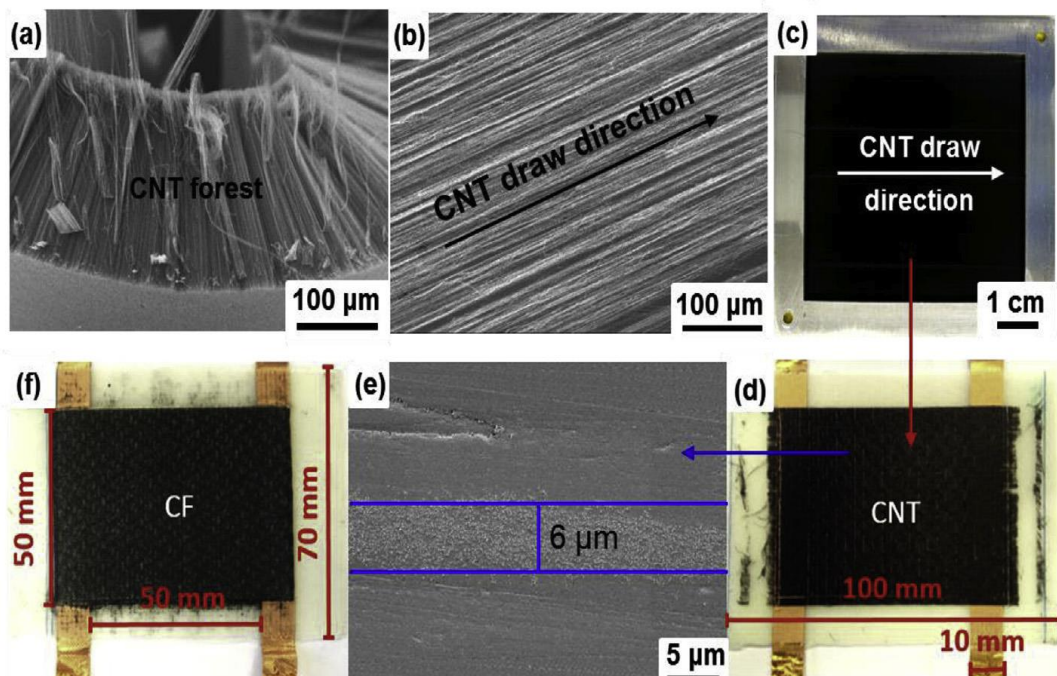


Fig. 2.21 - (a) Scanning electron microscopy (SEM) image of drawable CNT forests (b,c) CNT webs (d) GF/CNT/GF epoxy composite (e) Cross-section SEM of the sample with 10 layers of CNT web (f) GF/CF/GF epoxy composite [72]

A similar system was developed by Buschhorn et al. [73]. Their ice protection system used the heat developed by aligned CNT arrays to create highly efficient de-icing and anti-icing of aerosurfaces. The ice wind tunnel test demonstrated the efficiency of the system under a range of operating regimes (-20.6°C at 55.9 m/s). The peak power used in the experiments was around 8 kW/m^2 . Power density of 1 kW/m^2 was sufficient for anti-icing purposes, in the less harsh conditions.

Moreover, Zhao et al. [74] developed a multi-layered ice protection coating by a combination of a multiwall carbon nanotubes (MWCNTs) heating element and a super-hydrophobic layer (Fig. 2.22). The heating element was a mixture of acrylic resin and MWCNTs. Compared to traditional heating elements, the super-hydrophobic electric heating element showed up to 58% heating power saving. However, the overall electrical resistance of the CNTs based structure still needs to be reduced. Moreover the mechanical characteristics of these self-heating composites have not been studied. Further works should be done to analyse electrical characteristics, heating performances and mechanical characteristics at the same time.

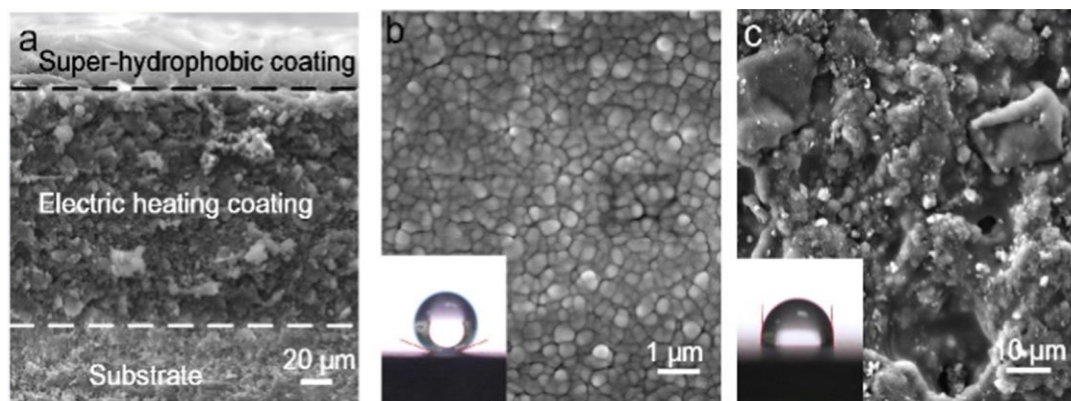


Fig. 2.22 - SEM images of super-hydrophobic coating combined with electric heating coating (a), super-hydrophobic coating surface (b) and electric heating coating surface (c) and the insets are the contact angles of $10\text{ }\mu\text{l}$ of water droplets on the surfaces [73]

2.2.2 Silver nanowires

The research into metal nanowire based conductive coating is in constant evolution; its interest is fuelled by their unique properties and because they exceed their existing rivals in a broad range of applications. Metals owe their high conductivity to their high free-electron densities [60]. Silver nanowires (AgNWs) is one of the most conductive metal nanowires, thanks to its highest electrical conductivity (6.3×10^7 S/cm) [75]. The synthesis of AgNWs is relatively easy, compared to other metals [75] and cheaper than ITO [76].

- *Silver nanowires structure and characteristics*

The atoms of the wires have the face - cubic centred (fcc) lattice structure of silver. Grav et al. [77] describe the wires to consist of a prism with a pentagonal section. As it is represented in Fig. 2.23, his solid consist on five prisms with triangular section constructed from the silver face centred cubic structure. Their possible explanation is a *fivefold symmetry* round the wire axis [77].

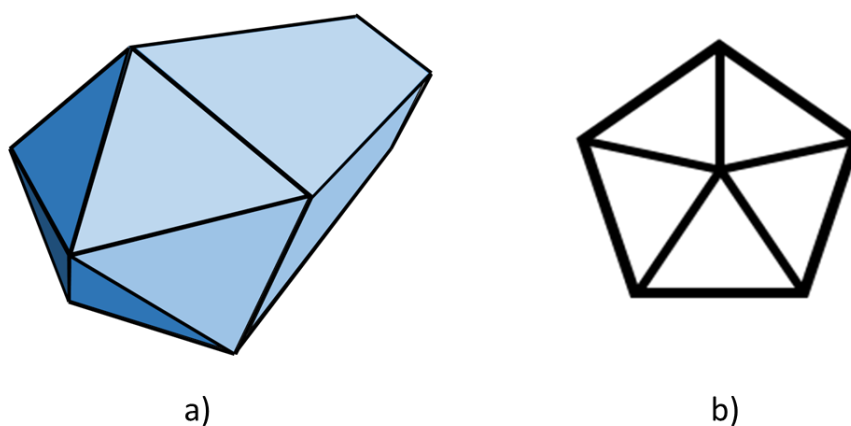


Fig. 2.23 - Silver nanowire structure representation: a) three dimensional and b) cross section

Unlike Ohm mechanism of incoherent scattering electrons conduction, in the nano-sized wires, electrical conductivity is mainly due to surface boundary and coherent modes of the electron wavefunctions [77]. Diffuse surface scattering becomes the more prevalent conduction electron effect when dimensions of the material reach values smaller than the free path of in the bulk [78]. Electron mean free paths have been estimated about the double wire diameter [79].

- ***Silver nanowires based coating production***

Flexible and wearable electrodes have been applied in a wide range of electronic devices as skin [80], sensors [81], flexible displays [82], organic solar cells [83] and heaters [84]. Several nanomaterials have been used to achieve highly thermal and electrical performance for these devices [85, 86]. Silver nanowires based devices exhibited promising electrical characteristics and mechanical performances for these applications. Many different techniques can be used to produce the silver nanowires conductive film: drop casting [87], vacuum filtration, electrophoretic deposition, transfer printing [88] and air spraying [89] from nanowires suspension.

This last technique offers a cheap and simple solution, it doesn't request high temperatures, therefore is suitable for scale-up [90]. Substrate temperature is an important/critical parameter: high temperature allow fast evaporation of the droplets avoiding amalgamation into larger droplets [90, 91].

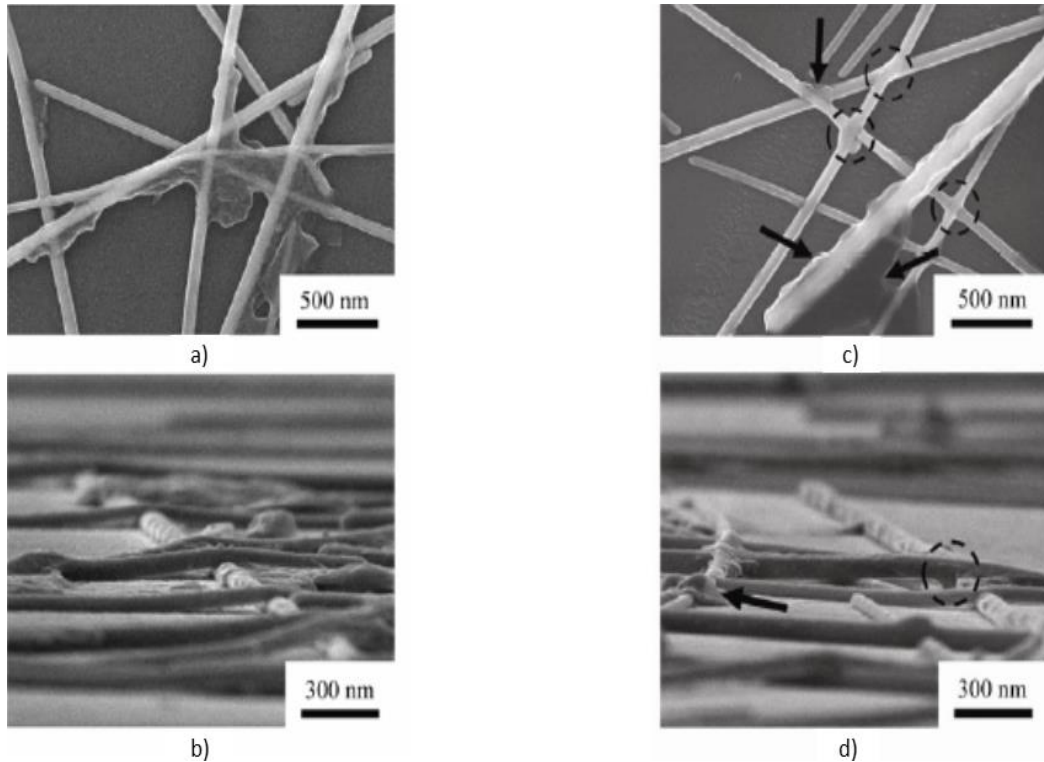


Fig. 2.24 - a) & b) SEM images of air dried AgNW; c) & d) SEM images of AgNW heat treated at 200°C: melting and fusion of AgNWs (inside circles) and reduction of solvent residues help to decrease the electrodes sheet resistance [89]

Scardaci et al [90] produced by spray deposition highly conductive, large area silver nanowires films. It has been demonstrated that controlling the droplet size help to control network uniformity leading to improved film performance. Performances such as films with transmittance $\sim 90\%$ for sheet resistance $\sim 50 \Omega / \text{sq}$, next to be a strong candidate for ITO replacement.

A problem with nanowires is that the solution, derived from suspension, could remain in the substrate, preventing contact between wires and causing high electrical resistance [92]. Another issue is the junction to junction resistance (Fig. 2.24). Nirmalraj et al. suggests that this is the principal source of resistance [93, 94]. To solve this problem, ultra-thin and ultra-long nanowires production is studied to reduce the number of wires connections and the overall coating resistance. Other solution as

thermal or electrical annealing [95] and encapsulation have been demonstrated to reduce the nanowire web resistance [60].

Many electrical devices such as organic solar cells [87, 88, 90, 96], solid-state dye-sensitized solar cells [91], OLEDs [92], polymer light emitting diodes [97], and touch screens [98] have been produced with AgNWs onto flexible substrates by low cost and scalable manufacturing proces. Flexibility and durability of AgNWs coating, their easy and inexpensive process and their high conductivity make them a must in modern industry.

- *Silver nanowires for electrical conductive coatings*

Young Kim et al studied a manufacturing process for transparent, flexible and conductive AgNW electrodes by a solution based synthetic method and utilized exfoliated clay platelets to change the solution and the coating properties. This method produced an uniform nanowire networks efficiently interconnected. Furthermore, this AgNW network has been utilised as transparent sheet heater. This study can lead to new type of defrosters or flexible outdoor panel displays [99-101].

The AgNWs were dispersed in water with a dispersing agent and synthetic nano clay platelets. The incorporation of clay platelets has favoured the uniform dispersal of the AgNWs. This supplement caused the negative side effect of increasing the solution viscosity, but it helped to obtain a more uniform AgNW coating.

In this study, a wire-wound rod method was used to deposit AgNW suspension onto a poly (ethylene terephthalate) (PET). An AgNWs films with resistance $91.3 \Omega \text{ sq}^{-1}$ has been made with 2/1 AgNW/clay weight ratio [99].

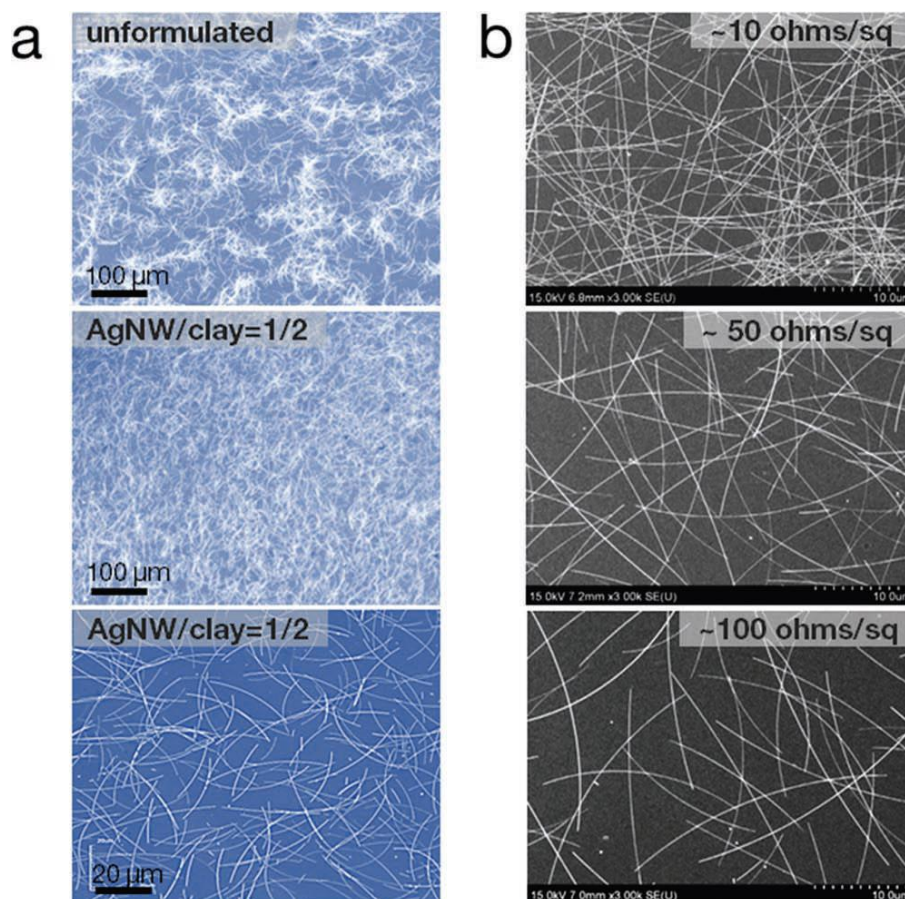


Fig. 2.25 - a) Top-view laser scanning microscopy (LSM) images of AgNW films derived from unformulated AgNW ink and formulated AgNW ink with clay platelets (middle). b) Top-view SEM images of AgNW-coated films with different densities, in which the AgNWs are shown to be a continuous network [98]

The addition of clay yielded a change in the AgNW sheet resistance. The clay coating caused a small increase in the silver nanowires film resistance, because of the contiguously interlinked film of electrically charged platelets that it formed [99]. Without clay platelets the AgNWs tended to agglomerate, causing a non-homogeneous nanowires distribution (Fig. 2.25) [99]. Uniformly dispersed nanoplatelets and the high ink viscosity reduced the self-aggregation problem.

As defrosting experiment, the AgNW film has been applied to a glass substrate and frozen for 30 min. Within 60 s and 12 V applied to the electro thermal heater composite, the ice completely disappear from the surface [99].

AgNWs are combined with various nanomaterials to improve their mechanical and chemical stabilities [102]. Zhang et al. [103] studied an approach for synthesizing random AgNW networks simultaneously covered with graphene oxide (GO) microsheets to construct GO/AgNW hybrid film. This architecture can provide: a high electronic conductivity of the film (interactions between AgNWs and GO microsheets); optical transmittance, based on controllable thickness of overall film; protective effect of the GO over-coating layer, that avoid/reduce the oxidation in air of metal wires.

The hybrid films were fabricated through vacuum-filtrating, controlled transferring and subsequent thermal reduction. The hybrid films exhibit good transparency and electrical conductivity, good oxidation resistance and thermal stability, and good heating performances. It is mainly due to the correct combination of the electrical networks of AgNWs and the protection effect of GO over-coating layer.

As defrosting features, the hybrid film (Fig. 2.26) samples showed promising performances: placed into a fridge with a temperature of -4°C for 30 min, the ice completely disappear from the surface within 40 s, operating at 10 V [103].



Fig. 2.26 - Defrosting test results of GO/AgNW hybrid film heater: optical photo before (a) and after (b) frost formation, and (c) after the defrosting test operated at 10 V [102]

To improve chemical and thermal stability of AgNWs film, Wang et al. [104] studied a combination of tri-layer rGO/AgNWs/GO (GO: graphene oxide; rGO: reduced graphene oxide) composite film. The film was fabricated by spray and pressure transfer process. The Van der Waals and π - π interactions between the rGO and the GO layers helped to improve the electrical characteristics of the AgNWs film. Moreover the tri-layer film exhibited good mechanical characteristics (up to 1500 cycles bending without failing), thermal (Fig. 2.27) and chemical performances (the film resisted in 0.9% NaCl solution for 1000 s), indicating the tri-layer composite as a promising candidate for flexible electronics and heaters.

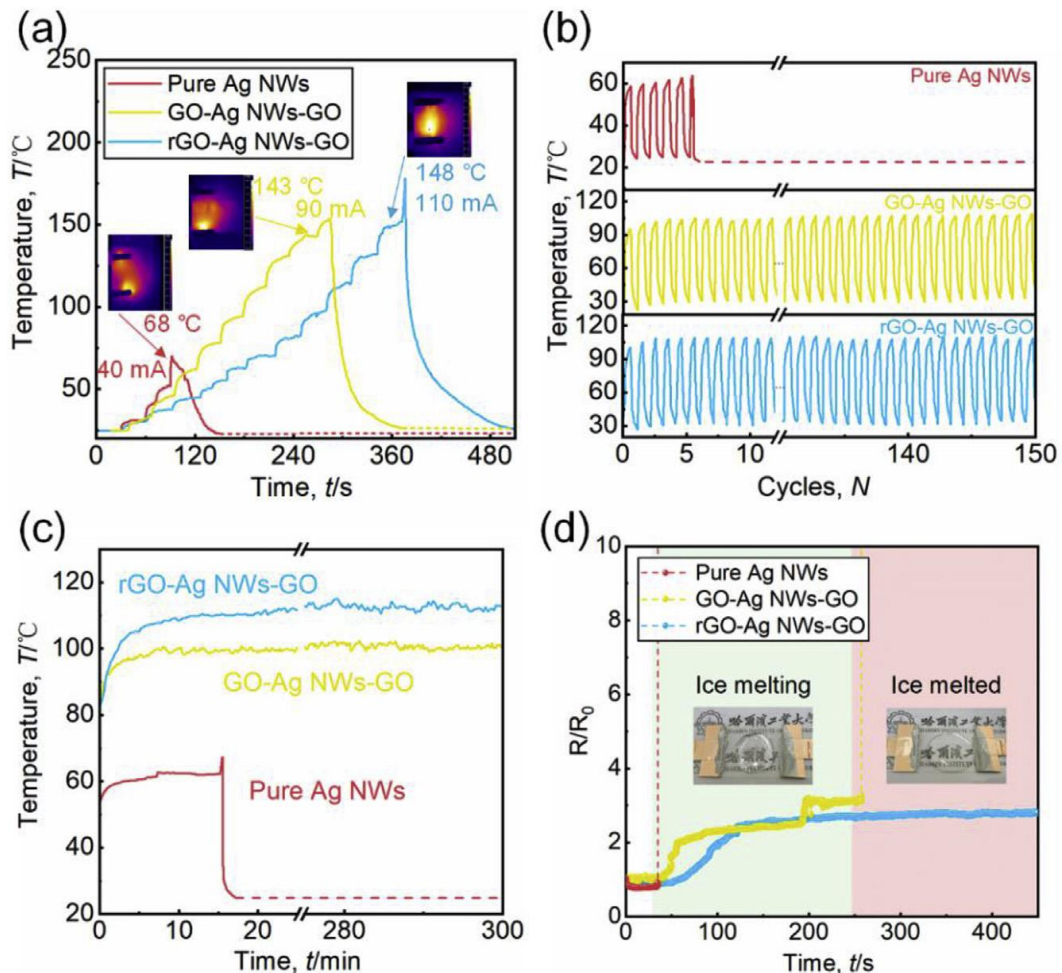


Fig. 2.27 - (a) Ultimate thermal performance of heaters based on pure AgNWs, GO/AgNWs/GO, and rGO/AgNWs/GO, respectively. (b) Heating and cooling tests of heaters under current on/off interval of 60 s, and (c) long-time working stability of them. (d) Defrosting performance and working stability of different heaters. Inset images in (a) are infrared images of heaters working at the highest temperature [103]

Cai et al. [105] combined silver nanowires with the single-wall carbon nanotubes to make transparent heating films (THFs) for use as windshield-glass heater. First the AgNWs and then SWCNTs were sprayed on Polyethylene terephthalate (PET) substrate. The film transmittance, its sheet resistance and its heating performances (Fig. 2.28) indicated that the AgNWs/SWCNTs combination is suitable for windshield-glass heater purposes.

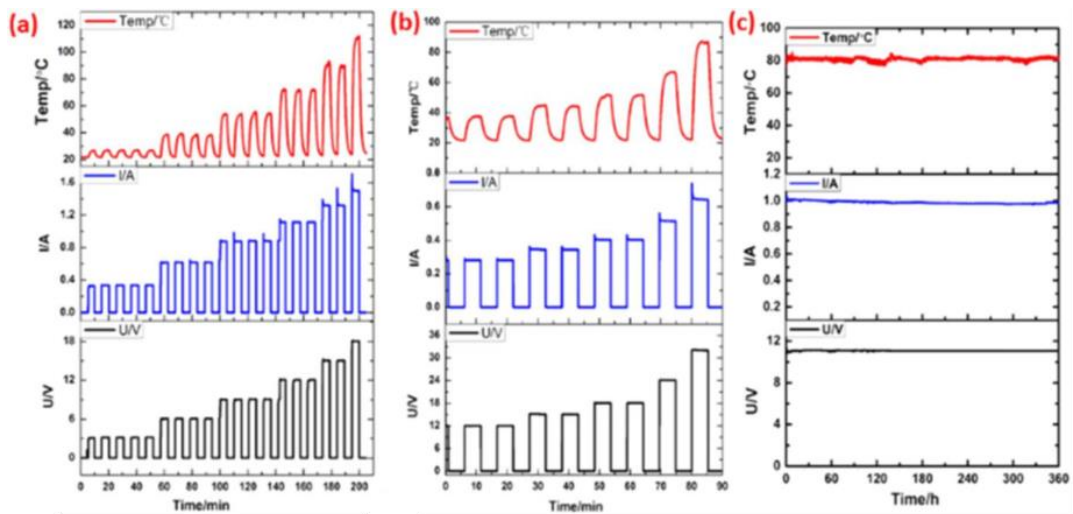


Fig. 2.28 - Thermal performance of 10 cm × 10 cm SWCNT/AgNW THFs with a sheet resistance of (a) 9 Ohm/sq, (b) 30 Ohm/sq on PET, (c) thermal stability at 80 °C for 360 h [104]

The results presented here in AgNW-based conductive film heaters can significantly promote the rapid development and applications of high-performance, such as cheap and transparent coatings for large-scale film heaters.

2.2.3 Graphene

- Graphene structure and characteristics

Single layer (atomic thickness of 0.345 nm) of graphite is named graphene; a carbon compound with hexagonal lattice of carbon atoms with sp^2 hybridisation (Fig. 2.29).

These properties give graphene extraordinary performances in terms of mechanical strength and electro/thermal conductivity [15, 106-108].

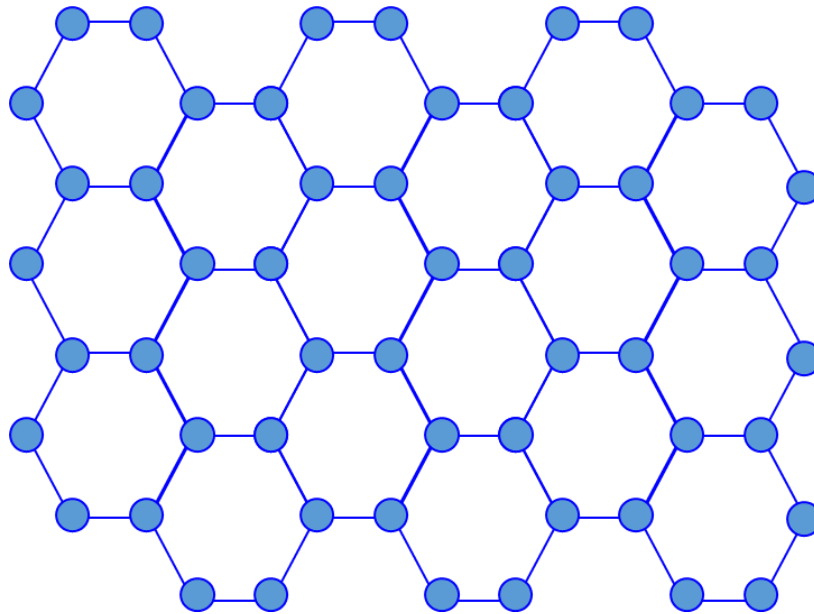


Fig. 2.29 - Graphene structure: single layer of graphite

Graphene owes its high electrical conductivity to its zero-overlap semimetal behaviour. It depends on the 4 outer shell electrons: three are used for the chemical bonding with other carbon atoms on the plane, the fourth (π or pi-electrons) is available in orbitals located above and below the graphene sheet for electronic or thermal conduction. Carbon to carbon bonds in graphene are enhanced by the overlap of these orbitals (π or pi). With this configuration, graphene sheets could reach resistivity of $\sim 1 \times 10^{-8} \Omega\text{m}$ and current density of over 10^8 A/cm^2 [106].

- ***Graphene based ice protection systems***

The metal based electro thermal systems used today are structurally intricate and heavy systems. Electrically conductive paints (highly conductive metal filled resins [109]) are another possible solution. Because of the high density of metal conductive

fillers, this solution does not avoid the problem of the weight and it may be subject to corrosion.

Kim Lynge Sørensen et al. [109] studied for UAV an alternative (Fig. 2.30) made by a flexible electro-thermal conducting graphite sheet covered by an outer electro-thermal conductive layer [109]. The coating is low-viscosity liquid based on graphene and carbon black nano-powders [109, 110].



Fig. 2.30 - Wing with electro-thermal protection system [108]

Rapid heat increase with low voltages (12/24 V) are made possible by the electrical conductivity of the coating ($R < 1\Omega$). Different tests have been carried out with various coating configurations, with temperatures ranging from $+25^{\circ}\text{C}$ to -25°C . It has been proved that an entire length coating is capable of fast increase the temperature of aerofoil surface temperature (working as de-icing protection system) and to maintain it constant (working as anti-icing protection system) if necessary.

Rice University [111] has developed another new graphene-based electrothermal coating (Fig. 2.31). The researchers coated with an epoxy resin and graphene nanoribbons (GNR, "unzipped" carbon nanotubes) composite a rotor blade. It has been noticed that in an epoxy/graphene composite with 5% of the ribbons, enough electrothermal heat was produced to melt a layer of ice on the surface.

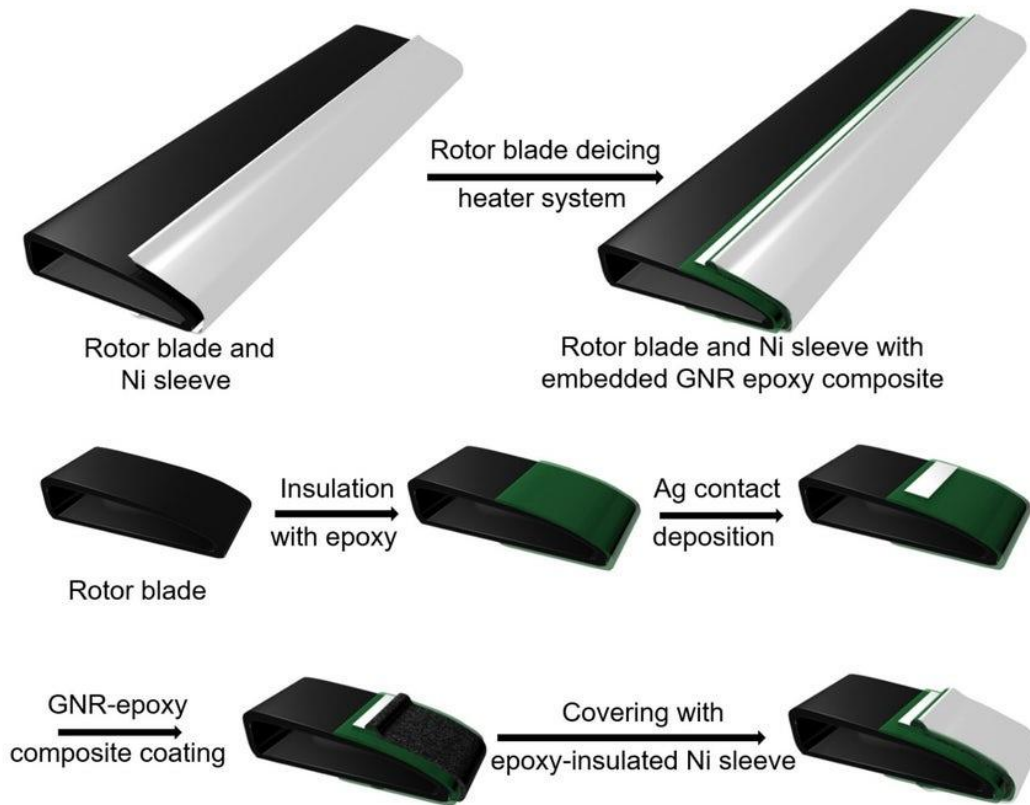


Fig. 2.31 - Schematic of the coating of a rotor blade segment with the graphene nanoribbons-epoxy composite [110]

By applying an electrical current, the composite reached a temperature of 93° C and it could melt away a 10 mm thick layer of ice from the rotor blade in a -20° C environment [111].

Recently Redondo et al. [112] developed an epoxy coating doped with graphene nanoplatelets (GNP, up to 12 wt%) for ice protection applications. The graphene powder was mixed with the epoxy resin in a three-roll mill by the application of shear forces that helped to disperse the nanoplatelets [113-117]. Glass fibre substrates were coated with the graphene/epoxy composite (thickness ~194 µm). Low temperatures tests, between -10°C and -30°C, confirmed that the coating could work as an anti-icing and a de-icing system. Although the applied voltage were relative high (700 V - 800 V) and the power consumption was low (1 ~ 3 W).

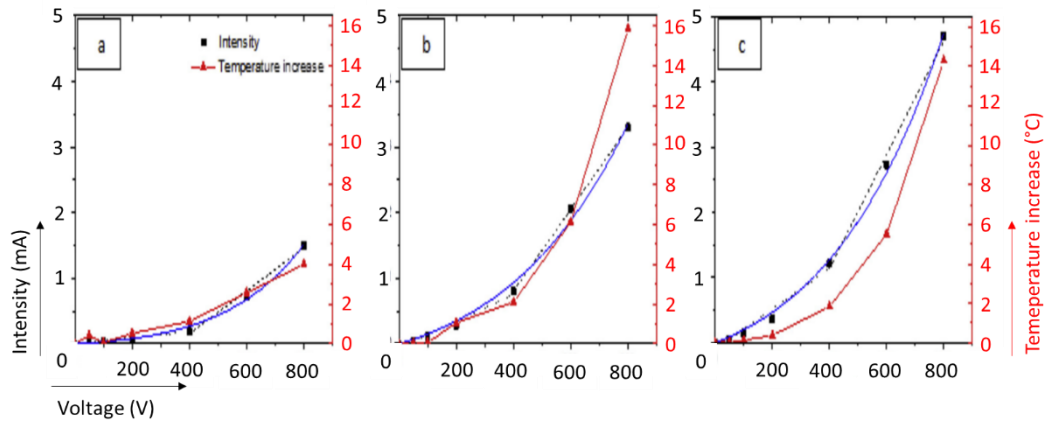


Fig. 2.32 - Electrical current intensity (black square symbol) and increase of temperature (red triangle symbol) as a function of the electrical voltage applied for coatings doped with (a) 8, (b) 10, and (c) 12 wt%. Experimental data fitting with equation (blue solid line) and with Ohm's law at low and high voltage (black dotted lines) [111]

Better results were obtained by Karim et al. [118], whom reported a route to synthesize graphene based ink using microfluidic exfoliation technique. In order to demonstrate a potential de-icing application of the graphene-based ink, glass rovings were coated using a dip-dry-cure technique and then used to manufacture a glass–epoxy composite using a vacuum resin infusion process. Heating performances of the composite were analysed at different voltages (Fig. 2.33). The de-icing capability of the graphene-based composites was demonstrated by dipping it into an ice bucket. The temperature of the bucket increased from -0.1°C to 27.3°C within 5 min.

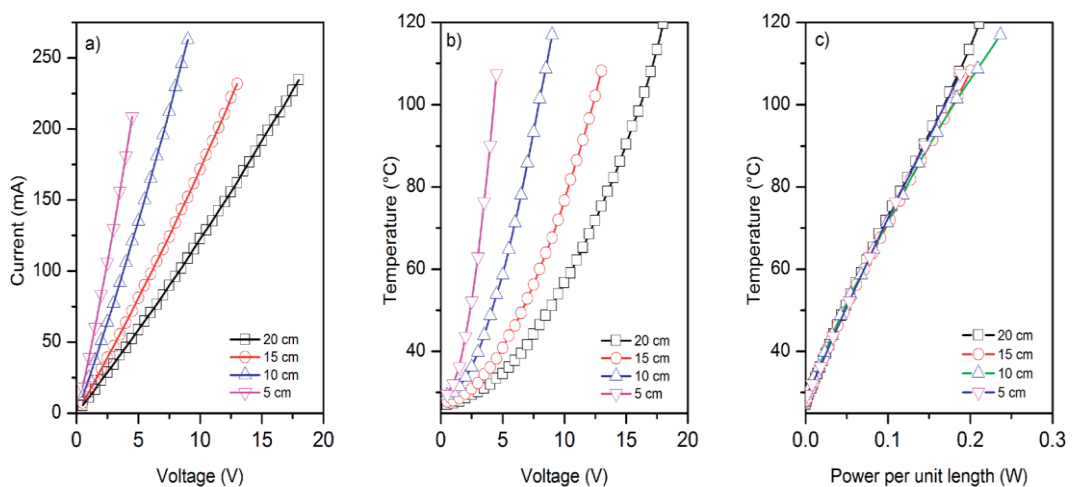


Fig. 2.33 - The change of (a) current and (b) temperature of graphene-based glass rovings at various voltages; (c) the power consumption per unit length of graphene-based glass rovings shows linear relationship with the increase of temperature [117]

2.3 Electro-thermal properties improvements of nanocomposites

As described before, most electro-thermal de-icing systems use a conductive metal heater element. They are not always the best suited to the harsh and extreme aerospace environment; the metal foil heating may not be uniform and the heater could failure the heating efficiency due to localized damage. Moreover heating elements are typically placed between two composite foils (defined also as protecting layer) and metal foil does not have a durable bond to the matrix.

Carbon fibre reinforced plastics employment has been increased in many aerospace applications, like aircraft frame and body, thanks to their good corrosion resistance, high strength-to-weight ratio and excellent fatigue properties. Due to the poor feature of their matrices, composite laminates have poor properties in the thickness direction [119]. Carbon fiber reinforced plastics have relatively low electrical conductivity ($\sim 10^3$ S/m in-plane and ~ 1 S/m through-thickness) and thermal conductivity (~ 10 W/m K in-plane and ~ 1 W/m K through-thickness) [119]. Next research steps are definitely to improve the through-thickness thermo-electrical characteristics avoiding the reduction of the laminated composite mechanical properties. A possible solution may involve exploiting synergistic interactions of different nano-dimension fillers. A comp-comp bonding in a composite based heating element is stronger and more uniform than the one in traditional metallic icing protection systems [69]. Nano fillers/matrix bonding would result in a homogeneous heating. Thermal ice protection can be achieved without need of high voltages, thanks to fillers high electrical conductivity. Many studies focus on how to disperse these nano fillers as much homogeneous as possible, in order to obtain an increase in the thermal conductivity and avoiding a deterioration of mechanical properties. The target of these works is to

find a way to integrate icing protection system into components (e.g. aircraft wings and wind turbines) without influencing their performances. Yamamoto et al. [120] enhanced the electro-thermal conductivity of fiber-polymer composites by using CNTs (thermal conductivity 2000 - 6000 W/m K) as bridges between different alumina fiber layers. A CNT-fiber-polymer composite was fabricated by directly growing CNT on fibers in a woven fabric and then infiltrated with the thermosetting resin (e.g. epoxy resin). The radially aligned CNTs formed an inter/intra-laminar conductive network that helped to enhance the thermal (~1.7 times higher) and the electrical conductivity (improved by ~7 orders of magnitude). Carbon fibers would be the perfect candidate for further enhancement of the thermal conductivity, by CNTs bridges between fibers, due to their higher thermal conductivity [120].

Yang and co-workers reported a thermal conductivity increase (23%) with 0.5 vol% graphene nano-platelets in epoxy [121]. Low thermal conductivity improvement seemed to be due to agglomeration of nanoplatelets inside the matrix causing increased thermal contact resistance (low heat transfer). Zaman and co-workers studied how to improve the electrical characteristics of epoxy composites by modified graphene platelets (thermal conductivity ~ 4000 W/m K) integration [122]. As negative side effect, the composite tensile strength has decreased [123, 124]. Everson Kandare et al. [119] studied the different geometries nano-fillers integration (silver nanoparticles, nanowires and graphene sheets) to create three dimensional networks to enhance heat transfer and electron transport across the matrix (carbon fibre/epoxy laminates). The through-thickness thermal and electrical conductivity increased, by 40% and 55-75% relatively, with the simultaneously addition of graphene and silver nanowires (thermal conductivity ~ 330 W/m K) [119]. The features increase suggests synergistic

interactions between nano-fillers. All these studies are a further step after the introduction of the composite electro-thermal layer inside the wings structure.

2.4 Materials for electro thermal ice protection systems

A number of different systems are currently used to protect aircraft against icing. Two common systems are hot air jets from the aircraft engine routed to the leading edges, while another use rubber boots on the leading edges which can be inflated to force ice off. Electrical thermal systems, to keep wings free from ice and heated, currently require a substantial amount of power, so they can be implemented in aircraft big enough to support their energy consumption. An example is the heating mat, made by GKN Aerospace, implemented in Boeing 787 [125].

The electro-thermal layer could be made of a pre-impregnated woven fabric in which the conductive material creates the electric circuit. GKN Aerospace [125] has developed a metal heater mat, copper based, with relevant performances as active de-icing and anti-icing system. Most electro-thermal systems use conductive metal heater element to converts, by Joule effect, electrical energy into heat energy. The materials traditionally used are not always the best suited to the harsh and extreme aerospace environment [126]. As negative aspects, metal based heater are not very harsh environment resistant (low corrosion resistance) and easy to failure efficiency because of local damage.

In the most common case of copper heating elements, long narrow strips of very thin foil are laid down in a pattern so as to attempt to create a region of heating [127]. Typically a heating element is composed by at least two insulating layer (upper and

lower epoxy fibre glass sheets) and a structural one for the leading edge skin made of metal (e.g. aluminium).

One possible technique to form the heating element is the photographic etching process [127]. This chemical milling process uses photoresist and etchants to fabricate metals circuits that could be applied between the two insulating layers. In comparison to the total surface, the area covered by the strip is small; as result in the surface there are gradients of temperatures and different heat flows. Metal shield that cover the heater outer surface allows the heat to more easily spread and provide erosion protection for the heating element [126].

GKN Aerospace (Redditch, U.K.) has developed a composites-based solution for commercial use on the wing leading edge of civil aircraft (e.g. Boeing 787). It uses a metal alloy sprayed on a glass fiber fabric to produce an electrical circuit that heats the wing leading edge. Fundamentally, GKN made what it calls a heater mat [125] (Fig. 2.34). A dry woven glass fiber fabric is placed between metal sprayed circuit and the carbon fiber stack as insulative layer and to prevent galvanic corrosion. The heater mat is a cured and airfoil section shaped.

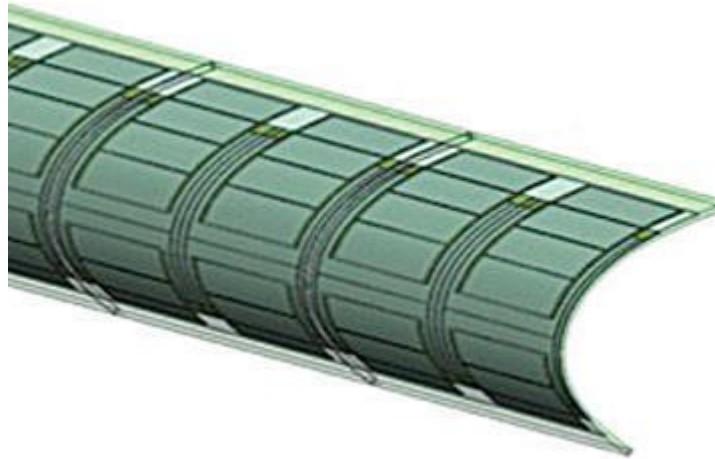


Fig. 2.34 - GKN leading edge heating element for the Boeing 787 [124]

In a Boeing 787, when the heater uses [125] between 45 to 75 kW, the mat is able to work as de-icing system, so to remove the existing ice from the surface. When the heater works between 150 to 200 kW, the mat is able to work as anti-icing system, so to avoid the ice formation.

The copper foil heater could reduce or failure the heating efficiency due to localized damage. Any break at any location of the wide heater area would result in total failure. Currently manufactured aerospace heaters have to face this problem very frequently, especially when used on propellers. Stones or sand and other small particles are continually being drawn into the aircraft surface, damaging it and its heaters.

The ideal material for electro-thermal composite should have the following characteristics:

- *Damage resistant*: the localized damage should not cause the total failure of the heater.
- *Corrosion resistant*: the harsh aerospace environment should not compromise the heater electrical characteristics.

- *Enhancement of the composite mechanical characteristics:* the filler addition should help to improve the mechanical properties of the composite.
- *High electrical conductivity:* as already stated, the electro-thermal system converts electrical current in heat energy.
- *Simple production process.*
- *Low cost.*

As it has been described, numerous ice protection systems have been developed. Recent studies have focused on the production processes of nanomaterials based heating elements. Some of them still need deep investigation and testing. Thanks to the high quantities produced by the developed processes, some nanomaterials have become very cheap (<100 £/kg). Their high electro-thermal conductivity could help to improve the heating efficiency, avoiding high consumption energy levels and efficiency loss due to local damaging of the heater [13]. Due to the complex mechanical loads condition (static and dynamic) during the flight, a deep and complete knowledge of the mechanical properties of the nanocomposites should be acquired before their commercial use. The most promising nanostructured materials are: Graphene; Carbon Nanotubes (CNTs: Single or Multiwall, respectively SWCNTs and MWCNTs); Silver nanowires (AgNW).



Fig. 2.35 – De-icing test with the ice protection system carbon nanotube based developed by Fraunhofer Institute for Structural Durability and System [127]

Next generation ice protection system carbon nanotube based has been developed [128] for aircraft wings by Fraunhofer Institute for Structural Durability and System (Fig. 2.35). The heating element (which composition is a corporate secret) was embedded between composite sheets of the wing. The tested wings were divided in three leading edge segments: two were equipped with different heating system configurations, and the last segment was heating system free, for reference purposes. In the first model, in order to obtain a uniform surface temperature different voltages were applied. The other model was compound by different size (resistance) heating zones to enable operation at the same voltage and to obtain a homogeneous surface temperature. The results in the wind tunnel showed a promising performance, both in the de-icing and anti-icing mode.

The nanocomposite based ice protection systems would solve the problem by using less power than traditional systems. CNTs electrical characteristics could be improved by surface treatments or metal decoration. The proper combination of these treatments will be studied to obtain the self-heating composites with the best characteristics and performances. The knowledge of the mechanical properties of self-heating composites is critical. More research work should be carried out to better understand the behaviour of the self-heating composites nanomodified during flight conditions. Due to static and dynamic loads suffered by the composite parts during the flight conditions, it is essential to have better understanding on the mechanical behaviours of the CNP-based electro-thermal composite structures. Further advantages of a nanomaterial based electrical system will be weight reduction of the system itself, because it will allow the wings leading edge to be full composite structure rather than metallic. The research and development of CNT based self-heating composites will be a step forward for lighter and more efficient aircraft [129].

Chapter 3 Methodologies

CNTs have been chosen as candidates for the experiments. The effects of different treatments on MWCNTs have been analysed.

Acid treatments on CNTs were performed to study if they can improve the electrical conductivity of the MWCNTs. Covalent attachment of functional groups to the CNT structure could change their electrical conductivity. The functional groups could serve as a conductive path with low electrical resistance. The effect of sulphuric acid treatment, nitric acid treatment and their combination have been analysed. High temperature / short time experiments have been executed to select the best acid treatment. Results were analysed on CNTs coatings applied on glass substrates by spray technique. The resulting best acid has been used for low temperature / long time treatment. This last class of acid treated nanotubes has been used for carbon nanotube buckypaper production. The resulting buckypapers characteristics were analysed.

A further enhancement of the CNT web electrical characteristics was analysed applying zinc oxide coatings. Zinc oxide was applied with different methods as jointing agent to reduce the electrical resistance of the MWCNT web. The experiments have been executed on untreated CNT coatings applied on glass substrates by spray technique. Further analysis have been carried out to check the effects of ZnO on buckypaper.

Moreover, the effects of CNT decoration with high electrical conductive metal particles were studied. As the functional groups for acid treated CNTs, the metal particles could create a low electrical resistance conductive path in the CNT web. Silver decoration techniques have been used to increase the electrical conductivity of the MWCNT web. The effect of the silver decoration methods have been compared

and analysed. The MWCNTs treated with the best silver decoration method have been used for CNP production.

The characteristics of the treated buckypapers (made with treated MWCNTs) have been compared to the untreated buckypaper (made with untreated MWCNTs). The buckypapers with the best electrical characteristics have been used in the production of the self-heating nanocomposite. Self-heating nanocomposite made with untreated buckypaper have been produced as reference. Different production configurations have been used. Electrical and heating performances of the produced composites have been evaluated. In research works, just the electrical and heating performances have been studied. One of the objective of this work is to increase the knowledge on self-heating composites and their mechanical characteristics. Mechanical proofs as three-point flexural strength, interlaminar shear strength and dinamyc mechanical analysis have been evaluated to indicate the most appropriate method for self-heating nanocomposite production. A scheme with the overall steps is shown in Fig. 3.1. The details of each process and characterization experiment will be discussed in their dedicated section.

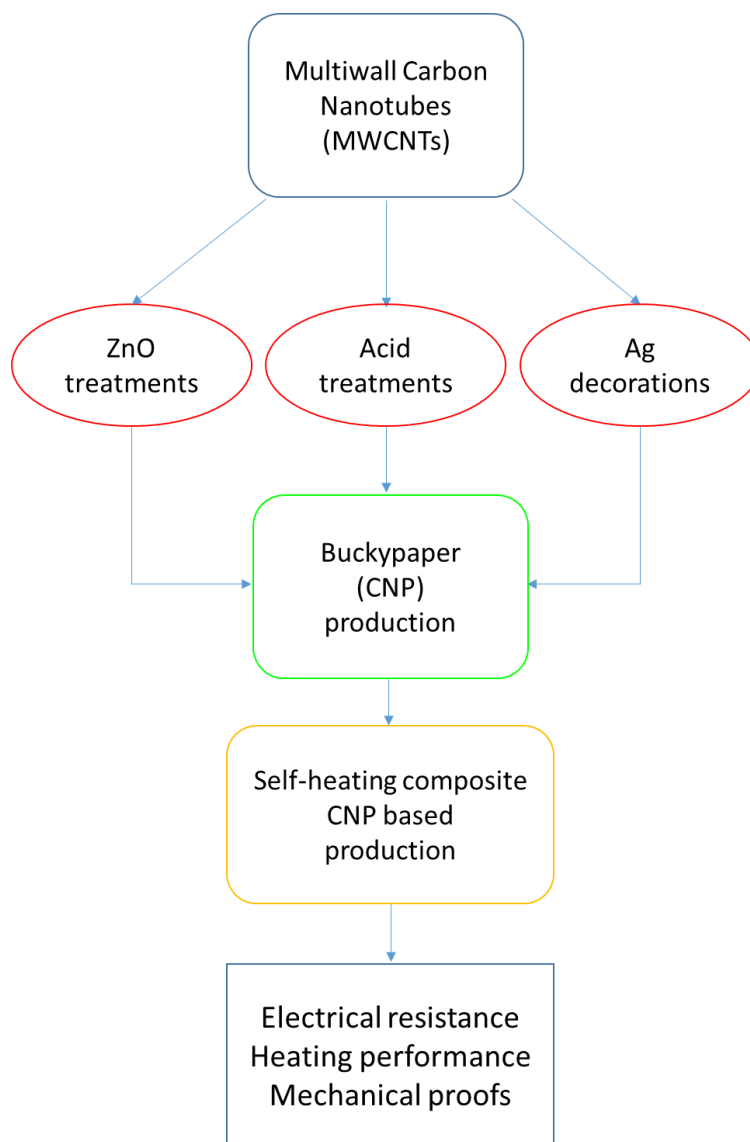


Fig. 3.1 - Flow chart of overall steps

As further work, several doping agents have been used to improve the electrical characteristics of the carbon nanotube buckypaper. The doping agents that have been used were: silver nanowires (AgNWs), silver flakes (Ag), graphene powder (GPH), copper micro-powder (μCu) and copper nano-powder (nCu). The electrical characteristics of each different product have been analysed to determine the best doping agent.

3.1 Raw materials and chemicals

The first batch of multiwall carbon nanotubes (Outer Diameter \times Length: 6-9 nm \times 2.5-20 μ m) were purchased by Merck KGaA, Darmstadt, Germany. The second batch of multiwall nanotubes (Outer Diameter \times Length: 5-15 nm \times 10-30 μ m) were purchased from Carbon Nanotubes Plus, Madisonville, USA.

All the chemicals listed below were supplied by Merck:

- Sulphuric acid (H_2SO_4 , 100 wt%, 15 - 16 M);
- Nitric acid (HNO_3 , 85 wt%, 15 - 16 M);
- Acetone ($\text{C}_3\text{H}_6\text{O}$);
- Sodium dodecyl sulphate ($\text{NaC}_{12}\text{H}_{25}\text{SO}_4$);
- Isopropyl alcohol ($\text{C}_3\text{H}_8\text{O}$);
- 2-Methoxyethanol ($\text{C}_3\text{H}_8\text{O}_2$);
- Ethanolamine ($\text{C}_2\text{H}_7\text{NO}$);
- Zinc acetate dehydrate ($\text{ZnC}_4\text{H}_6\text{O}_4$);
- Diethyl Zinc ($(\text{C}_2\text{H}_5)_2\text{Zn}$);
- Sodium hydroxide pellets (NaOH);
- Ammonia (NH_3);
- 4-Octylphenol polyethoxylate or Triton X-100 ($\text{C}_{14}\text{H}_{22}\text{O}(\text{C}_2\text{H}_4\text{O})_n$).

Silver nitrate (AgNO_3) was bought from Gute abcr Chemie, Karlsruhe Germany.

Formaldehyde (CH_2O , 36 wt%) was bought from VWR International S.A.S (Briare, France).

Thermosetting resins characteristics are described below:

- Araldite MY750 supplied by Huntsman (Switzerland) and hardener HX300G/NC was supplied by Robnor Resins (United Kingdom) which were mixed at a weight ratio of 100 to 31.
- EL2 laminating resin and its hardener AT30 SLOW purchased from EasyComposite.co.uk.
- The hybrid silicone-epoxide resin known as Silikopon EF was provided by Evonik Industries AG (Essen, Germany).

The pre-pregs used in this work were: DM435 and CEL100-1 glass fibres pre-preg. The glass fabric pre-pregs used in this work were, DMS435 and CEL100-1-G105-4ES-45%RW-1270mm. The DM435 pre-preg was supplied by Meggitt Airframe Systems Division, Shepshed, UK. The matrix of the DMS435 pre-preg fabric was made of resin MY750 mixed with hardener HX300G/NC and silica nanopowder. The nominal resin content by weight was 50%; the volume fraction of the glass fiber and the silica powder are confidential value of the industrial partner. The CEL100-1 pre-preg was supplied by SHD Composites, Sleafrod, UK. The CEL100-1 is a cyanate ester pre-preg with a 4-harness glass fabric and nominal resin weight content of 45%. The glass fibre fabric used in the one layer configuration experiments was purchased from EasyComposite.co.uk (GF, thickness 0.185 mm).

The characteristics of the doping agents are described below:

- Copper micropowder (μCu) was supplied by Inoxia Ltd., UK. The average particles size was 0.1% > 63 μm , 96.1% < 45 μm .

- Copper nanopowder (nCu) was supplied by Suzhou Canfuo Nanotechnology Ltd, China. The average particles size was 10 - 30 nm and purity of > 99.9%.
- Carbon nanotubes doped with 52 wt% graphene nanopowder was purchased by Nanografi Co. Ltd., Germany. The graphene nanopowder (GPH, 99% purity) had an average diameter of 1 - 12 μm and a thickness of 5 nm. The nanotubes (> 97% purity) had an average outer diameter >50 nm and length of 15 - 25 μm .
- Silver flakes suspension (58% solid content) was supplied by Agar Scientific Ltd., UK.
- Silver nanowires suspension (AgNWs, 0.5 wt%) was supplied by Merck KGaA, Germany. The nanowires had an average of 120 - 150 nm and length of 20 - 50 μm .

3.2 Fabrication of CNT network

The preparation methods of the carbon nanotubes samples are described in the following sections.

3.2.1 Fabrication of CNT network by spray technique

Treated powder was used to prepare a suspension of CNTs with weight percentage of 0.01%. To improve the stability of the suspension, a surfactant was added. Sodium dodecyl sulphate (SDS) was adopted (SDS weight percentage ~2% of carbon nanotubes weight). The suspension was ultrasonicated for 30 min at 50% of 500 W (20 kHz Cole-Parmer 500 Watt Ultrasonic Homogenizer). The characteristics of spray solutions used are listed in Table 3.1. Isopropanol alcohol was added to facilitate/accelerate/increase evaporation rate during spray coating.

Table 3.1 - Suspension volumes utilised for spray technique

Suspension Volume (ml)	Added Isopropanol (ml)	Total Volume (ml)
10.0	20.0	30.0
12.5	17.5	30.0
15.0	15.0	30.0
17.5	12.5	30.0
90.0	10.0	100.0

For comparison purpose, untreated CNT coatings were made adopting the same volumes listed in Table 3.1.

The samples with 30 ml volume were sprayed by manual compressed air gun at 0.3 bar of pressure while the substrate was heated to 200°C. High-pressure pump (model WIZ) and spray gun (CAB-2P air brush kit in Fig. 3.2) were supplied by Clarke Air. Before start, all the instruments were cleaned with distilled water and acetone to avoid contamination from previous experiments. After cleaning, the CNT solution was dropped in a specific spray gun container. Once the spray gun was attached to the pump, the coating procedure started. At the end of the process, the coated samples were left in an oven to dry at 60°C. Parameters as distance, angle and gun movement rate were maintained as much constant as possible to ensure an equal coating process for each sample. The dimension of sprayed area was a square of 75 mm x 75 mm made of sand blasted glass plate. All this area was divided in 9 little square of 25 mm x 25 mm each.



Fig. 3.2 - Spray gun supplied by Clark Air

The 90.0 ml suspensions were sprayed by an automated spray system. This was composed by (Fig. 3.3):

- Rotating hot plate;
- Fluid pump (REGLO Digital, ISMATEC® tubing pumps);
- High-pressure air pump;
- Automated arm connected to liquid and air intake;
- Adjustable spray nozzle: the screw on the top of it can control the air flow coming from the air supply system.

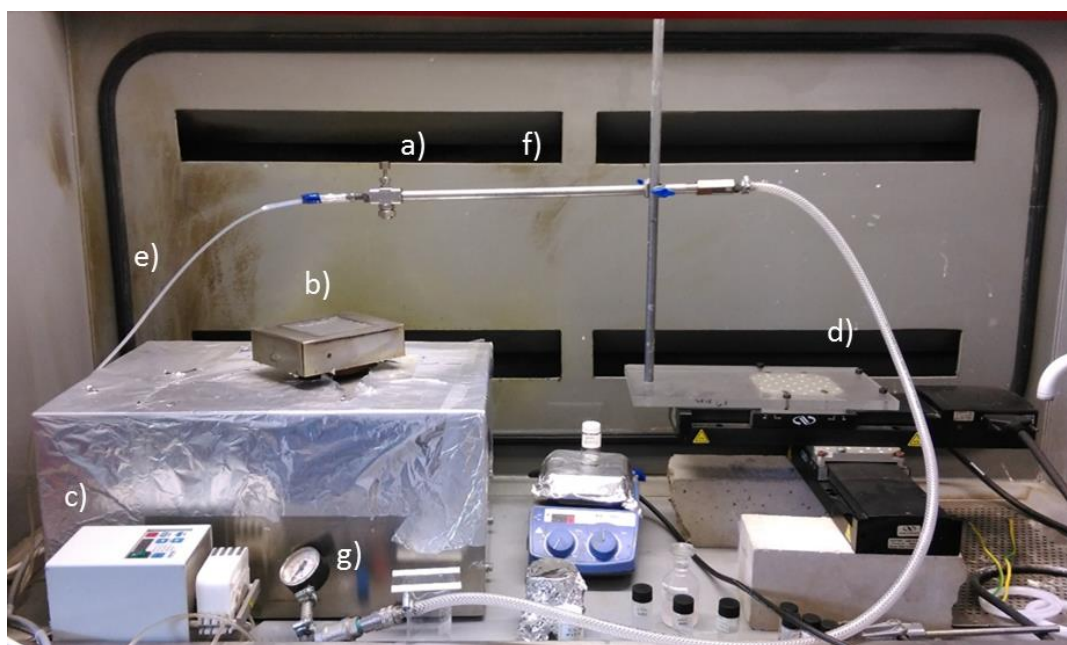


Fig. 3.3 – Automated spray system: a) adjustable spray nozzle; b) rotating hot plate; c) fluid pump; d) automated arm. This last is connected to (e) liquid intake and f) air intake tubes. (e) is connected to the fluid pump (c); (f) is connected to (g) air supply

Parameter of the spray process are listed as follows:

- Rotating hot plate speed: 14 rpm;
- Nozzle distance from hot plate: 150 mm;

- Substrate surface temperature: 200°C;
- Air pump pressure: 0.3 bar;
- Fluid pump flow rate: 10 ml/min.

A software (ESP-Util 4.2), installed in an external computer, controlled the automated arm. It was set to cover the samples area uniformly (Fig. 3.4).

All the parameters were chosen, after several optimization tests, to allow samples to be coated as much homogeneous as possible. The samples were prepared in safety conditions, under fume cupboard in a well-ventilated area.

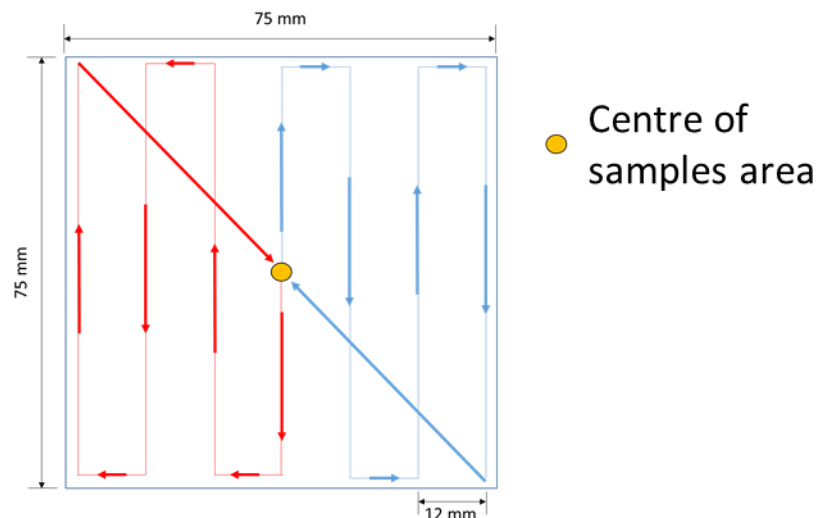


Fig. 3.4 - Automated spray gun pattern to cover the samples area

3.2.2 Buckypaper production

Carbon nanotubes buckypaper (CNP) is a macroscopic aggregate of carbon nanotubes (CNTs). To produce CNTs buckypaper, a water-based suspension of multiwall carbon nanotubes (treated, untreated or containing doping agents) and surfactant (0.1 wt% Triton X-100) was ultrasonicated for 30 min (50% of 500 W, 20 kHz) and then filtered by a PTFE membrane (Omnipore Membrane Filter PTFE, 1 µm pores). The CNP was detached from the membrane after drying at 35°C overnight. The obtained samples

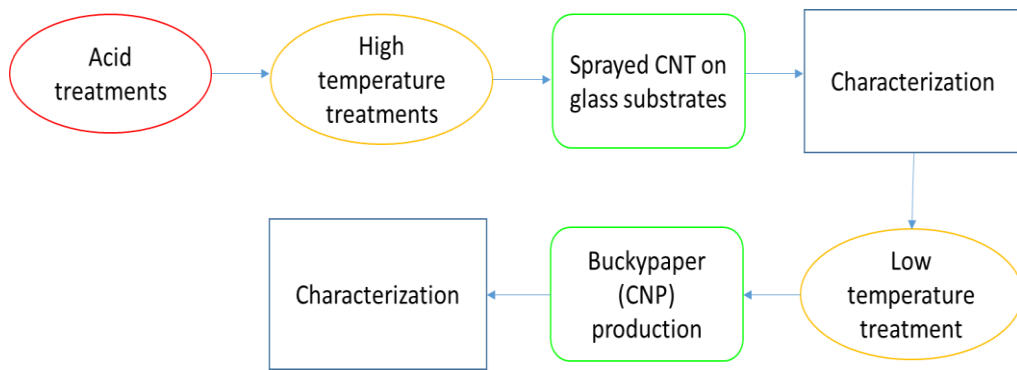
(Fig. 3.5) were 55 mm x 55 mm squares. The thickness of the buckypaper was measured in 9 different points of the surface of the sample by a digital feeler gauge. The CNPs were named accordingly to the nanotubes treatment.



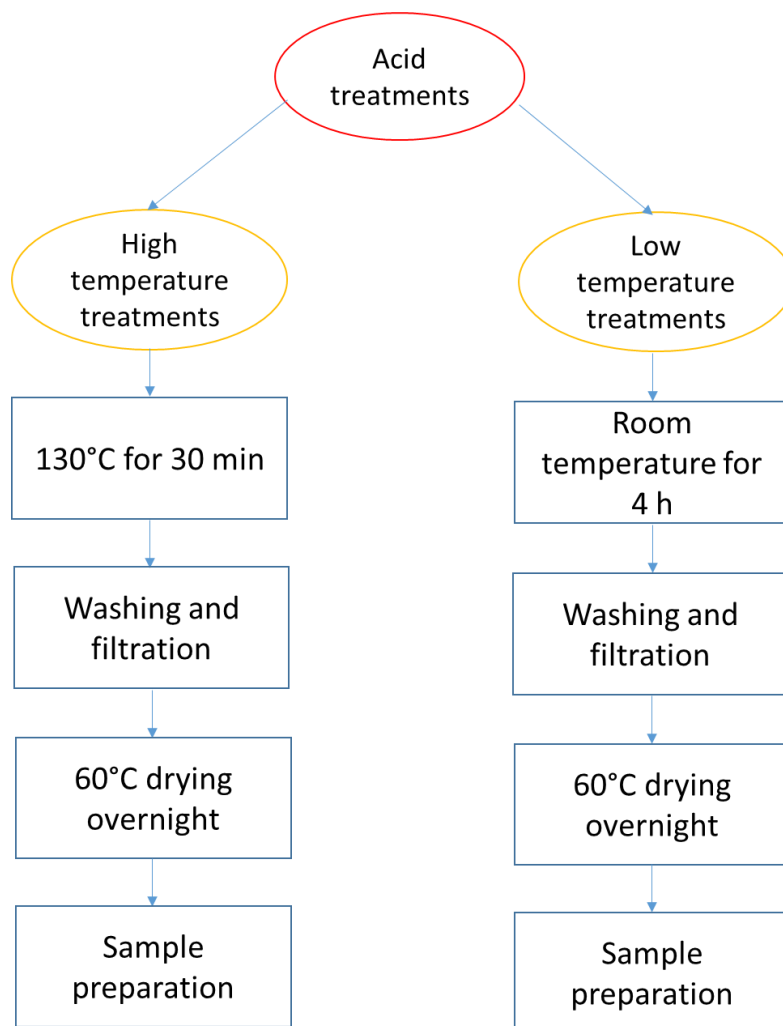
Fig. 3.5 - Example of carbon nanotube buckypaper (CNP)

3.3 Acid treatments of CNTs

To verify if the conductivity of carbon nanotubes can be modified, the effect of oxidation by acid treatment were studied. A scheme with the overall steps is shown in Fig. 3.6.



a)



b)

Fig. 3.6 - Flow chart of the overall steps for acid treatments experiments: a) acid treatments procedure: for the left branch the first batch of nanotubes have been used, for the right branch the second batch of nanotubes have been used; b) acid treatments experiments description.

As described in Fig. 3.6 the first batch of raw MWCNTs powder was acid treated with different solutions at high temperature (130°C) for a short time (30 min). These conditions were adapted from existing report [34]. The harsh treatment conditions will indicate the less damaging treatment for the nanotube structure. The best candidate will be used in the second phase of the acid treatment experiments. Fig. 3.6b indicates that the second phase involved the second batch of MWCNTs and the acid treatment was executed at low temperature (room temperature) but long time (more than 1 h). These conditions were adapted from existing report [57].

In the first part of the acid treatment experiments an amount of 200 mg of powder was added in a flux system with 10 ml of acid, heated at 130°C and then kept for 30 min. At the end of the treatment, the powder was washed through the use of distilled water and a vacuum filtration system with an inorganic membrane (Fig. 3.7) and then dried at 60°C overnight. Table 3.2 describes the different solutions utilized and the respective samples' name. The sprayed CNT coatings have been used to test the effect of the high temperature acid treatments. The samples have been prepared following the procedure described in section 3.2.1.

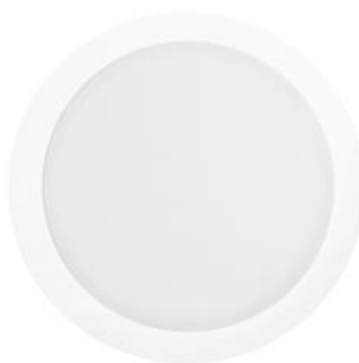


Fig. 3.7 - Whatman[®] Anodisc inorganic filter membrane used in the vacuum filtration system: diam. 47 mm, pore size 0.02 μm ; high purity alumina matrix manufactured electrochemically

Table 3.2 - Acid treatment parameter: volume utilised and relative ratio of nitric and sulphuric acid

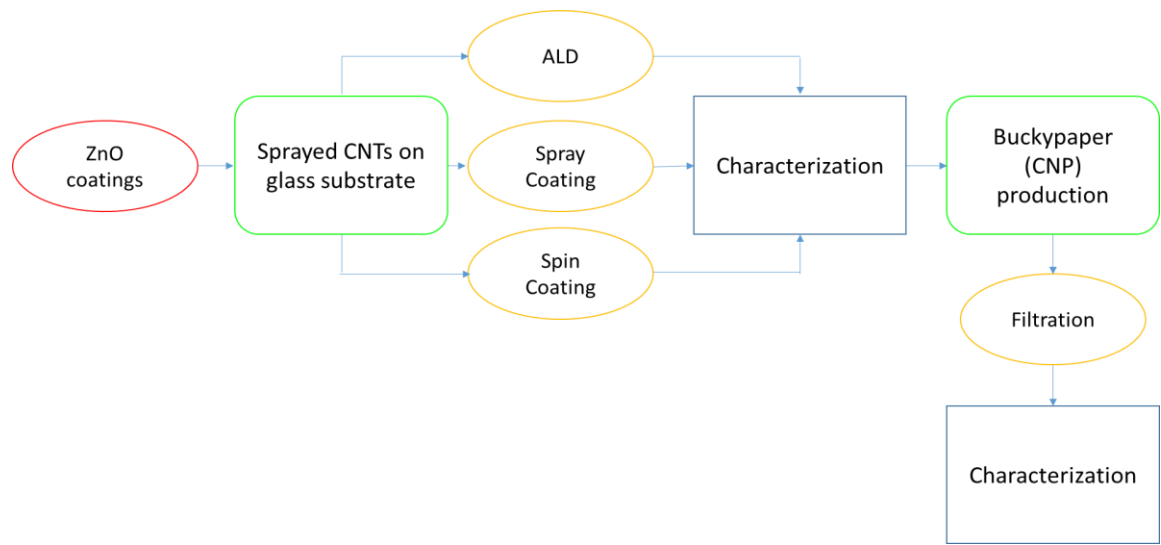
Sample name	Acid	Vol%	Acid Volume
HT-SA	Sulphuric	100	10 ml
HT-SA25-NA75	Sulphuric / Nitric	25 / 75	
HT-SA40-NA60	Sulphuric / Nitric	40 / 60	
HT-SA60-NA40	Sulphuric / Nitric	60 / 40	
HT-SA75-NA25	Sulphuric / Nitric	75 / 25	
HT-NA	Nitric	100	

The characterization experiments will determine the best acid treatment that will be used in the second phase. 100 mg of MWCNTs (second batch) were dispersed in 50 ml of the best acid. The suspension was ultrasonicated in a bath for 2 h and then stirred for 2 h. At the end of the treatment, the suspension was filtered, washed with distilled water until pH reached 7 and dried at 60°C overnight. The acid treated powder was used to prepare CNP samples (section 3.2.2). The acid treated powder and the respective buckypaper were characterized following the procedure described in Fig. 3.6b.

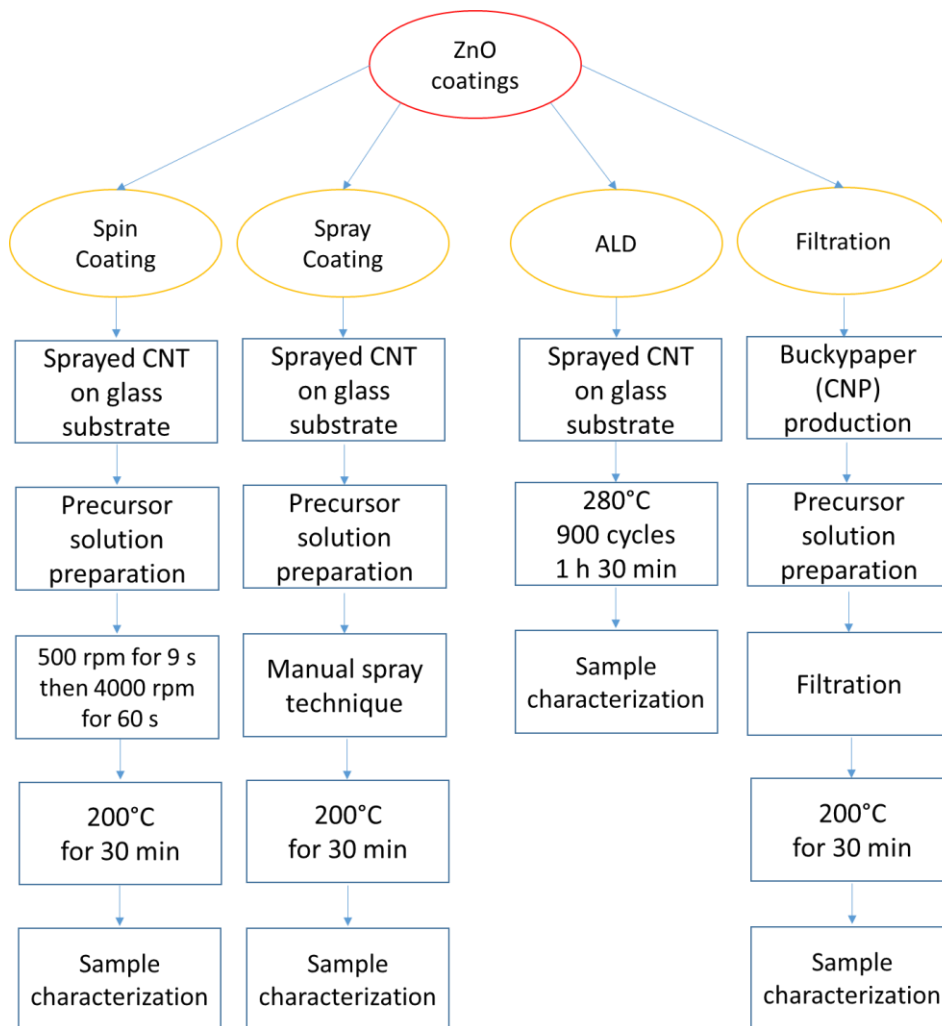
3.4 Enhancements of CNT and CNP electrical characteristics using zinc oxide coatings

The ZnO experiments have been executed as described in Fig. 3.8. The resulting zinc oxide helped to bond each other the carbon nanotubes and it reduced the relative junction electrical resistance. To verify the efficiency of ZnO as jointing agent, ZnO coatings were applied on sprayed CNTs on glass substrate (section 3.2.1). The first batch of MWCNTs were used for the coatings. For comparison purpose, uncoated CNT sheets were left. As described in Fig. 3.8b, ZnO coatings were applied and

characterized even on CNP samples. CNPs treated with ZnO were made with second batch MWCNTs.



a)



b)

Fig. 3.8 - a) Flow chart of the overall steps for ZnO coatings experiments; b) flow chart of the overall steps for ZnO coatings preparation

The experiments described in Fig. 3.8a are:

- Spray coating;
- Spin coating;
- Atomic layer deposition (ALD).

These three techniques were applied only on untreated CNTs coatings with 90 ml suspension volume (automated sprayed).

3.4.1 Spray technique for ZnO coatings

For the spray technique chemicals listed in Table 3.3 have been used. Quantities and preparation from Choi et al works [130] were adopted to deposit ZnO.

Table 3.3 - Chemicals used for Zinc oxide coating

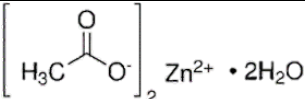
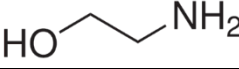
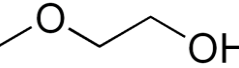
Chemical Name	Linear Formula	2D structure
Zinc Acetate Dihydrate	$Zn(CH_3COO)_2 \cdot 2H_2O$	
Ethanolamine	$NH_2CH_2CH_2OH$	
2-Methoxyethanol	$C_3H_8O_2$	

Table 3.4 - Quantities of chemicals used

Chemical	Quantity
Zinc Acetate Dihydrate	1.427 g
Ethanolamine	0.197 ml
2-Methoxyethanol	25.000 ml

The quantities are described in Table 3.4 and the procedure was the following: zinc acetate dehydrate was added to 2-methoxyethanol and mixed until completely dissolved. Ethanolamine was then added to the solution and everything was heated at 60°C and mixed in a magnetic stirrer for 30 min.

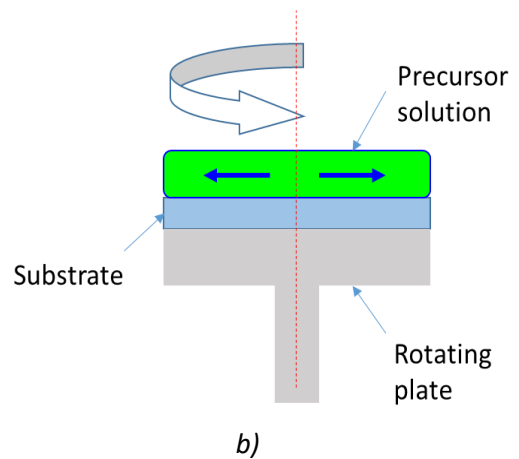
The whole ZnO precursor solution was sprayed. Same parameters and procedure of manual spray technique (section 3.2.1) were used. The resulting coated samples were annealed at 200°C for 30 min to complete the ZnO precursor reaction and to remove any solvent left. Samples of ZnO spray coated only were prepared for a morphological analysis comparison with coated CNTs.

3.4.2 Spin coating

Spin coating is used to coat substrates by centrifugal force. A small amount of liquid coating precursor is applied on the centre of the substrate. In order to spread the liquid by centrifugal force, the substrate is then rotated at high speed. The machine used is called a spin coater. For spin coating technique the same solution of Table 3.4 was used. A volume of 100 µl was applied with a pipet: it was enough to cover completely the surface of the sample. This (25 mm x 25 mm CNTs coated square) was fixed to the spin coater machine (Fig. 3.9) with a double sided sticky tape. The settings for the spin coater were:

- Initial spin speed of 500 rpm for 9 s;
- Then 4000 rpm for 60 s.

The resulting coated samples were annealed at 200°C for 30 min to complete the ZnO precursor reaction and to remove any solvent left. Samples of ZnO spin coated only were prepared for a morphological analysis with coated CNTs.



a)

Fig. 3.9 – a) Chemat KW-4A spin coater; b) scheme of spin coating process

3.4.3 Atomic layer deposition

Atomic layer deposition has been chosen as the third zinc oxide coating technique. This technique is a thin film deposition process: the surface of the samples is exposed to alternate precursors (red and blue circles in Fig. 3.10) of the coating material. They are delivered in the reaction chamber as a series of sequential pulses. The first precursor (blue circles) reacted with the surface within all the reactive sites were consumed and any excess is removed from the chamber. The second precursor (red circles) was added and reacted with the first precursor layer. The second precursor excess was then cleared and this process was repeated until the cycles ended. Modifying the number of cycles is possible to grow a desired material thickness.

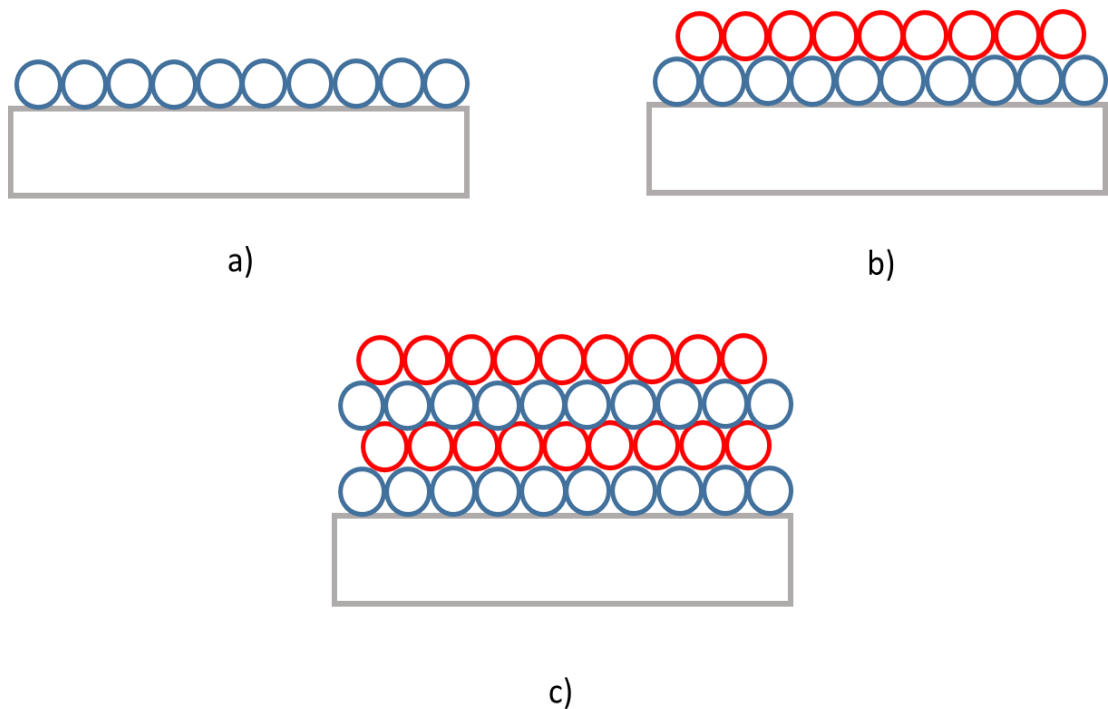


Fig. 3.10 - Schematic process of atomic layer deposition: a) first precursor layer (blue circle); b) second precursor layer (red circle); c) repetition of the two previous steps until desired thickness

The parameters of the deposition process were:

- Chamber temperature: 280°C;
- Pulse duration 0.5 s;
- Time between pulses: 5 s;
- Number of cycles: 900;

Duration of the process: 1h 30 min.

The system is furnished by CambridgeNanotech (Fig. 3.11). Diethyl Zinc ($(C_2H_5)_2Zn$) was used as zinc oxide precursor (Merck). Samples of ZnO ALD coated only were prepared for a morphological analysis.

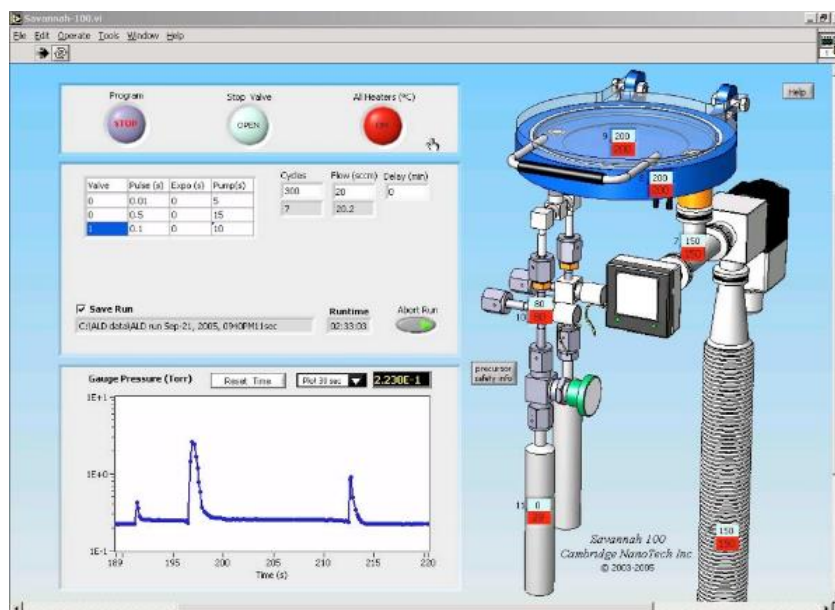


Fig. 3.11 - Example of ALD software from CambridgeNanotech.

3.4.4 ZnO coatings by filtration

To coat the buckypaper with ZnO, the solution described in Table 3.5 was poured in the filtration system while the CNP was still attached to the membrane. When all the solution was filtered, the soaked CNP were annealed at 200°C for 30 min to complete the ZnO precursor reaction and to remove any solvent left.

Table 3.5 - Quantities of chemicals used

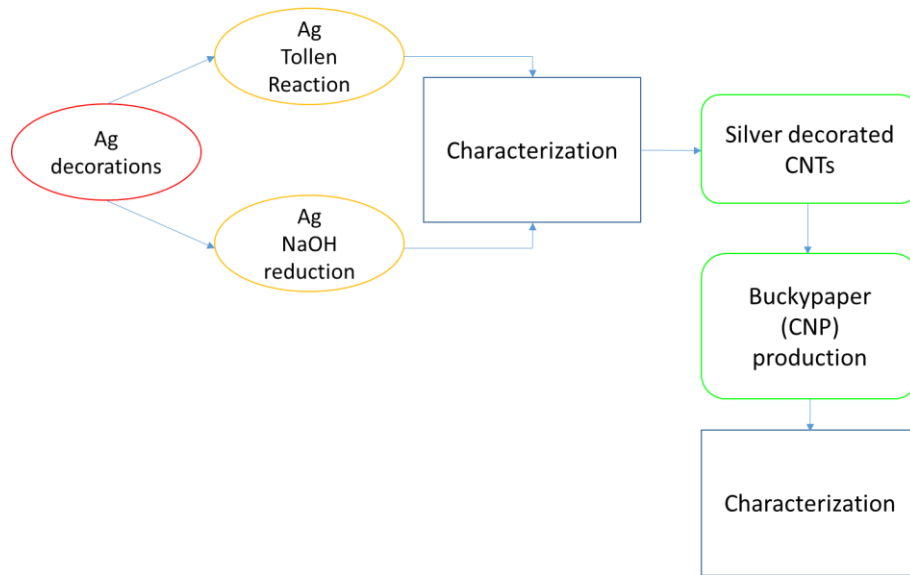
Chemical	Quantity
Zinc Acetate Dihydrate	0.014 g
Ethanolamine	0.197 ml
2-Methoxyethanol	25.000 ml

The thickness of the resulting buckypaper was measured in 9 different points of the surface of the sample by a digital feeler gauge.

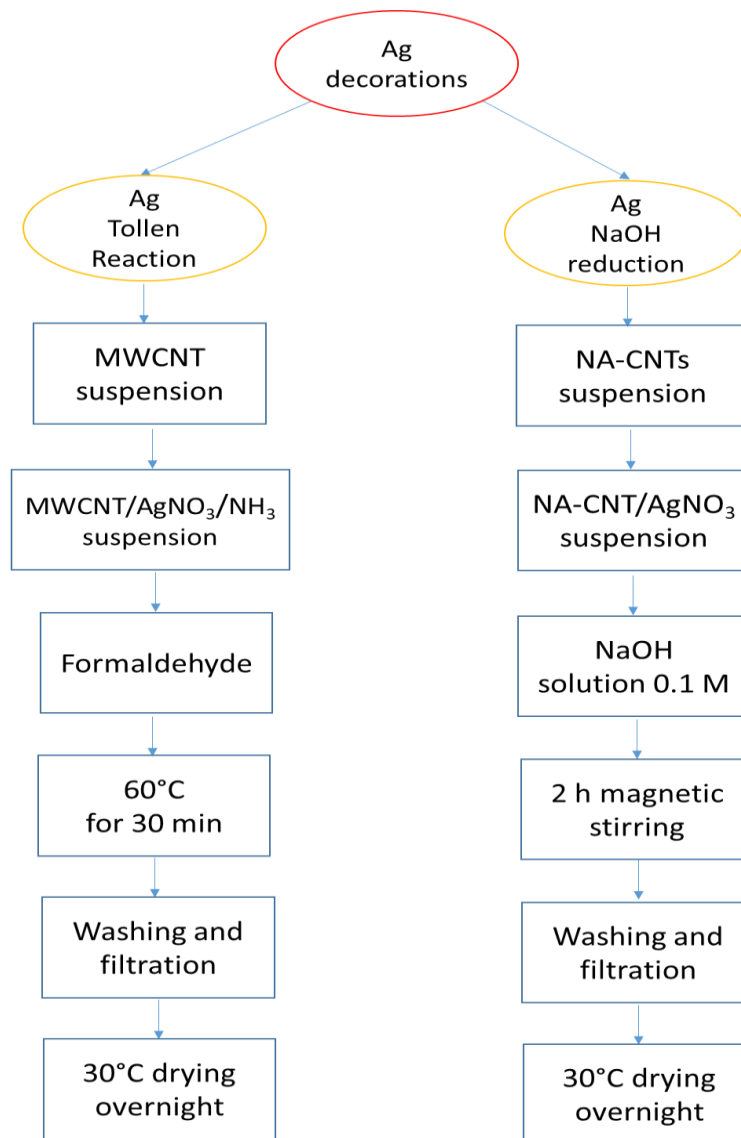
3.5 Enhancements by electrical conductive particles

3.5.1 Silver decoration

As described in Fig. 3.12a, two silver decoration approaches were performed in order to reduce the electrical resistance of the carbon nanotubes. The characterization aim was to identify the most effective treatment approach. The best silver decorated CNT powder has been used to produce CNP samples. The first silver decoration method was based on a wet chemistry reaction [57]. Sodium hydroxide (NaOH) has been used as reducing agent of silver salt. The second silver decoration method is based on Tollen reaction [58]. It is a common technique used to produce silver coatings.



a)



b)

Fig. 3.12 - a) Flow chart of the overall steps for silver decoration experiments; b) flow chart of the overall steps for silver decoration procedures

The first method was divided in two steps: functionalization by acid treatment (HNO_3) and silver decoration. In the first step, pristine carbon nanotubes (100 mg) were poured in 50 ml nitric acid. The suspension was ultrasonicated in a bath for 2 h and then stirred for 2 h. At the end of the treatment, the suspension was filtered and washed with distilled water until pH reached ~ 7 . The acid treated MWCNTs were dried at 60°C overnight. The product was named NA-CNTs as Nitric Acid-treated CNTs. Subsequently 50 mg functionalized multiwall nanotubes were suspended in 20 ml of distilled water by an ultrasonic probe (30 min at 40% of 500 watts, 20 kHz). Then AgNO_3 aqueous solution (20 ml, 0.1 M) was added into the NA-CNTs suspension and mixed by a magnetic stirrer. Sodium hydroxide was added into the suspension and kept under magnetic stirring for 2 hours. To study the relationship between reducing agent and silver produced, different amounts of NaOH solution (0.1 M) were used. The treated CNTs were named according to the used NaOH volume: 250 N-Ag CNTs for 250 μl , 500 N-Ag CNTs for 500 μl , 750 N-Ag CNTs for 750 μl and 1000 N-Ag CNTs for 1000 μl respectively. The decorated nanotubes were collected by filtering the suspension and washing it several times with distilled water. Finally, the filtered powder was dried at 30°C overnight.

Silver deposition to generate reflective mirrors was made by a traditional chemical reaction known as Tollens reaction, or silver mirror reaction. In this operation, aqueous ammonia (5 wt%) was added dropwise to 50 ml of 1% AgNO_3 solution to induce the formation of silver oxide (brown precipitate). Further addition of ammonia (average total volume of ammonia solution was ~ 16 ml) helped to dissolve the oxide and give a clear solution of diamminesilver complex ($[\text{Ag}(\text{NH}_3)_2]^+$). Pristine multiwall carbon nanotubes (100 mg) were ultrasonicated (30 min at 40% of 500 watts, 20 kHz) in 25 ml de-ionized water with 0.1 wt% sodium dodecyl sulphate (SDS). The MWCNT

suspension was dropped into the diamminesilver complex solution under magnetic stirring. Afterwards 250 ml of formaldehyde were added to the suspension and kept in 60°C bath for half an hour. The product was centrifuged (5000 rpm for 15 min), washed in a filtration system with distilled water and then dried at 30°C overnight. Same steps were also followed using NA-CNTs, besides untreated carbon nanotubes. In this method, the silver decorated MWCNTs were named as U-T-CNTs for untreated carbon nanotubes and AT-T-CNTs for acid treated carbon nanotubes (NA-CNTs).

The samples were characterized as described in Fig. 3.12a and the best silver decorated technique were used to produce CNPs made of silver decorated nanotubes (Fig. 3.12b).

3.5.2 Doping agents

Highly conductive particles (doping agents) have been added in the carbon nanotubes suspension to improve the electrical characteristics of the buckypaper. These doping agents were: silver nanowires (AgNWs), silver flakes (Ag), graphene powder (GPH), copper micro-powder (μCu) and copper nano-powder (nCu). The second batch of MWCNTs was used for these experiments. The procedures to produce these doped buckypapers are described below.

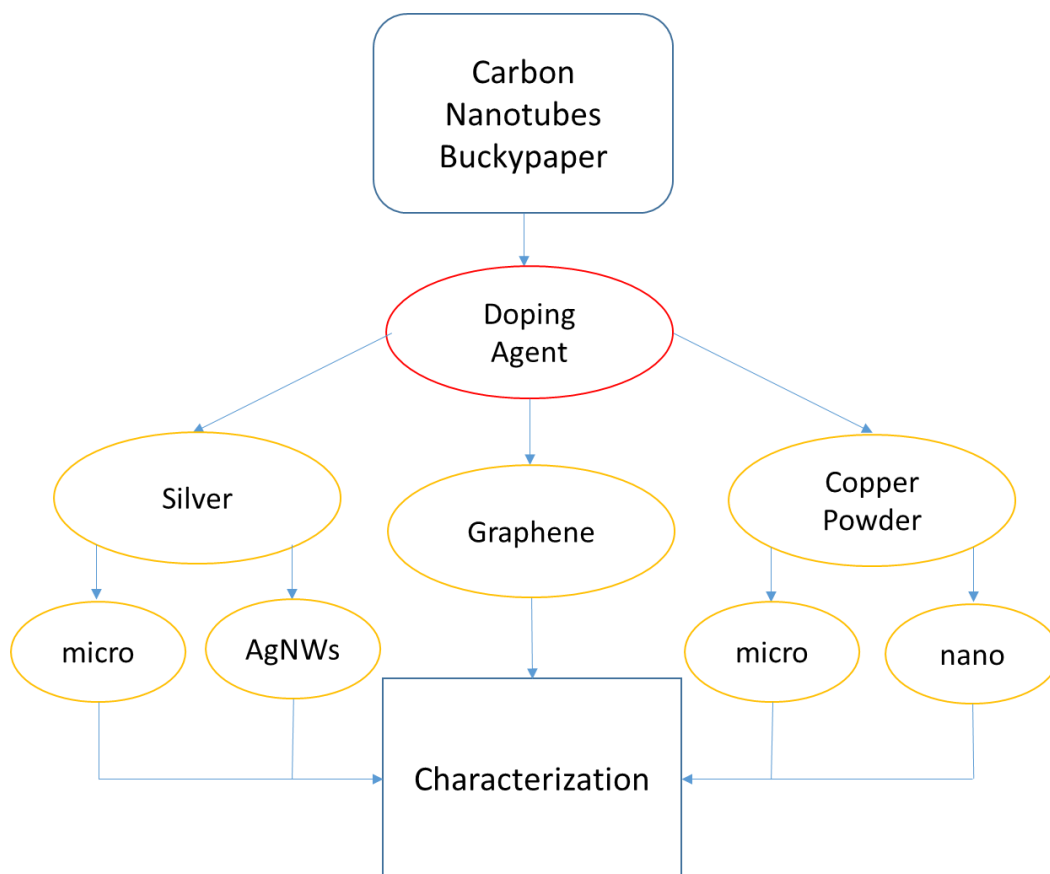


Fig. 3.13 - Flow chart of the overall steps for doping agents experiments. The second batch of nanotubes have been used.

For micro-size silver particles, 1 g of silver flakes suspension (0.58 g silver content) have been stirred with 1 ml of Triton X-100 for 15 min. The product was then diluted in distilled water (0.03 wt%) and sonicated for 30 min. Different amounts of this first silver suspension were mixed with a water based suspension of MWCNTs, as described in Table 3.6. To help the dispersion of the different phases, Triton X-100 was added as surfactant. The final surfactant concentration in the suspension was ~ 0.3 wt%. The doped buckypaper were prepared following the procedure described in section 3.2.2. The CNP samples were named based on the silver suspension quantity: 150Ag-CNP, for 150 ml of Ag suspension used in 300 ml of MWCNTs suspension; 50Ag-CNP, for 50ml of Ag suspension used in 300 ml of MWCNTs suspension.

Table 3.6 - Samples name and characteristics for silver flakes doped CNP

Sample name	Total volume (ml)	Suspension 1 Volume (ml)	Ag content (g)	MWCNT content (g)
150Ag-CNP	300	150	0.3	0.1
50Ag-CNP	300	50	0.1	0.1

For silver nanowires as doping agents, different amounts of silver nanowires suspension have been dropped in multiwall carbon nanotubes suspension (100 mg MWCNTs in 300 ml of distilled water), stirred for 90 min and sonicated for 30 min. To help the dispersion of the different phases, Triton X-100 was added as surfactant. The final surfactant concentration in the suspension was ~ 0.3 wt%. The doped buckypaper were prepared following the procedure described in section 3.2.2. The silver nanowires suspension volumes (Table 3.7) used were 20 ml and 2 ml. The CNP samples were named 20AgNWs-CNP and 2AgNWs-CNP, respectively.

Table 3.7 - Samples name and characteristics for silver nanowires doped CNP

Sample name	Total volume (ml)	AgNWs suspension (ml)	AgNWs content (g)	MWCNT content (g)
20AgNWs-CNP	300	20	0.1	0.1
2AgNWs-CNP	300	1	0.01	0.1

For copper micro-powder, different amounts of powder have been poured in multiwall carbon nanotubes suspension (100 mg MWCNTs in 300 ml of distilled water), stirred for 90 min and sonicated for 30 min. To help the dispersion of the different phases, Triton X-100 was added as surfactant. The final surfactant concentration in the suspension was ~0.3 wt%. The doped buckypaper were prepared following the procedure described in section 3.2.2. The copper micropowder quantities (Table 3.8) used were 0.3 mg and 0.09 mg. The CNP samples were named 3 μ Cu-CNP and 9 μ Cu-CNP, respectively.

Table 3.8 - Samples name and characteristics for CNP doped with copper micro-powder

Sample name	Total volume (ml)	Cu content (g)	MWCNT content (g)
3 μ Cu-CNP	300	0.3	0.1
9 μ Cu-CNP	300	0.09	0.1

For copper nano-powder, different amounts of copper nanopowder have been poured in multiwall carbon nanotubes suspension (100 mg MWCNTs in 300 ml of distilled water), stirred for 90 min and sonicated for 30 min. To help the dispersion of the different phases, Triton X-100 was added as surfactant. The final surfactant concentration in the suspension was ~ 0.3 wt%. The doped buckypaper were prepared following the procedure described in section 3.2.2. The copper nanopowder quantities (Table 3.9) used were 0.3 mg and 0.09 mg. The CNP samples were named 3nCu-CNP and 9nCu-CNP, respectively.

Table 3.9 - Samples name and characteristics for CNP doped with copper nano-powder

Sample name	Total volume (ml)	Cu content (g)	MWCNT content (g)
3nCu-CNP	300	0.3	0.1
9nCu-CNP	300	0.09	0.1

To obtain different graphene doping level, Nanografi powder has been mixed with Nanotubes Plus powder. The final nanopowder amount, between graphene doped CNTs and MWCNT from Nanotubes Plus, was 100 mg. This amount was then poured in 300ml of water, stirred for 90 min and sonicated for 30 min. To help the dispersion of the different phases, Triton X-100 was added as surfactant. The final surfactant concentration in the suspension was ~ 0.3 wt%. The doped buckypaper were prepared following the procedure described in section 3.2.2. The CNP samples were named based on the graphene quantity (Table 3.10): 50GPH-CNP, for 50 mg of graphene; 10GPH-CNP, for 10 mg of graphene.

Table 3.10 - Samples name and characteristics for CNP doped with graphene powder

Sample name	Total volume (ml)	GPH content (g)	MWCNT content (g)
50GPH-CNP	300	0.05	0.1
10GPH-CNP	300	0.01	0.1

All the doped buckypaper have been characterized as described in Fig. 3.13. The characterization experiments indicated the best doping agent.

3.6 Self-heating composite preparation

In this work, the CNT (second batch MWCNTs) film based self-heating nanocomposites have been produced by different processing methods and with different thermosetting resins. The respective electrical and mechanical properties were investigated to indicate which method was the most appropriate to produce self-heating nanocomposites. Fig. 3.14 shows that the processes were divided in two main branches: one layer and two layers configuration. EF and EL2 indicate Silikopon EF resin and EL2 laminating resin, respectively, that were used in the one layer configuration experiments. For the resin impregnation method, RV and RP indicate the two different treatments that were used for the samples production. The same goes for PV and PP in the pre-preg method.

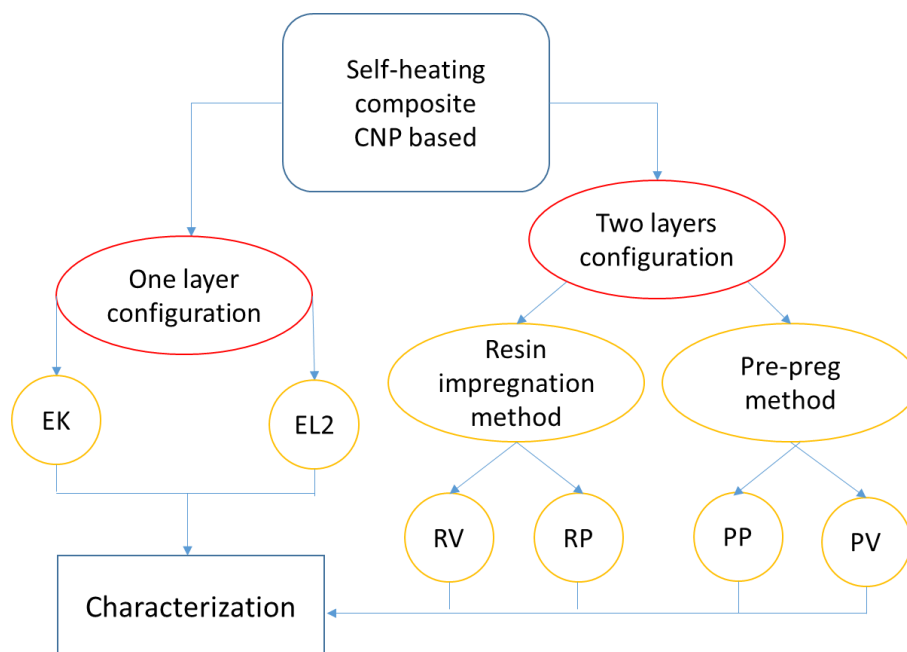


Fig. 3.14 - Flow chart of the overall steps for self-heating nanocomposite production and characterization.

3.6.1 One layer configuration

In this procedure, EL2 and the Silikopon EF resins were used. The composite samples were prepared by laminating one layer of buckypaper between two glass fibres (GF) fabric layers (60 mm x 60 mm square). The GF/CNP structure was soaked in 1.5 g of thermosetting resin (EL2 or Silikopon EF). The electrodes were copper stripes of 5 mm x 140 mm x 0.2 mm. Silver paint (Quick drying silver paint from Agar Scientific) was manually applied on the surfaces in contact with the CNPs. The electrodes were placed between the first GF layer and the CNP. The mold was made of two aluminium plates covered with PTFE and fixed with clamps. A schematic representation of the mold and the lay-up configuration are represented in Fig. 3.15. The composites have been heat-treated in an oven with different curing cycles.

The EL2 laminating resin was mixed with AT30 SLOW hardener, with a weight ratio of 100 to 30 respectively, at 200 rpm for 30 min. The soaked GF/CNP was placed in

the mold and cured in the oven at 65 °C for 12 hours, with temperature increase rate of 1 °C/min.

The silicone-epoxide hybrid resin was prepared by mixing 6 g Silikopon EF with 1.5 g curing agent. The solution was stirred for 5 hours at 200 rpm. The soaked GF/CNP was placed in the mold and cured at 110 °C for 16 hours, with increase rate of 1 °C/min.

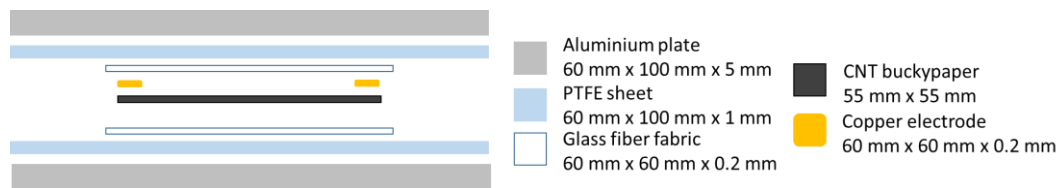


Fig. 3.15 - Schematic diagram of the mold layer structure

3.6.2 Two layers configuration

- Resin impregnation method

CNP samples were soaked in 2 g of epoxy/acetone (100/30 weight ratio) solution for 30 min. Soaked samples (SCNP) were kept under vacuum for 30 min, to allow solvent evaporation and to degas the resin. The buckypapers were soaked in the epoxy resin and then laminated with pre-preg glass fibres fabric consisting of the same epoxy resin; the lay-up configuration was arranged according to the test to be carried out. The epoxy resin used in this method was araldite MY750. The pre-preg glass fibres fabric was the DM435. The curing cycles for this method are described as below.

RV treatment: heating rate 2 °C/min and curing at 150 °C for 1 hour under vacuum.

The samples from this process were named as resin impregnation vacuum samples (RV-CNP).

RP treatment: heating rate 2°C/min and curing at 150°C for 1 hour under 0.4 MPa pressure. The samples from this process were called resin impregnation pressure samples (RP-CNP).

- ***Pre-preg method***

The buckypapers were laminated between pre-preg glass fibres fabric of CEL 100-1. The lay-up configuration was arranged according to the test to be carried out. The curing cycles for this method are described below.

PV treatment: heating rate 0.5°C/min and curing at 90°C for 6 hours under vacuum. The samples from this process were named as pre-preg vacuum samples (PV-CNP).

PP treatment: heating rate 0.5°C/min and curing at 90°C for 6 hours under 0.6 MPa pressure. The samples from this process were called pre-preg pressure samples (PP-CNP).

- ***Lay-up configuration***

For electrical resistance, heating performance and ice protection tests, the samples (Fig. 3.16c) were 60 mm x 60 mm squares. The heating area corresponded to the CNP surface area. Its lay-up included 3 pre-preg fabric layers / CNP (or SCNP) / copper electrode / CNP (or SCNP) / 3 pre-preg fabric layers. The electrodes were copper stripes of 5 mm x 14 mm x 0.2 mm. Silver paint (Quick drying silver paint from Agar Scientific) was manually applied in contact with the CNP (or SCNP) which was used to help with electrical resistance reduction at the interface between CNP (or SCNP) and copper electrodes.

For mechanical tests, samples (Fig. 3.16b) were machined from a 100 mm x 200 mm rectangle, containing 8 pre-preg fabric layers / 2 CNP (or SCNP) / 8 pre-preg fabric layers.

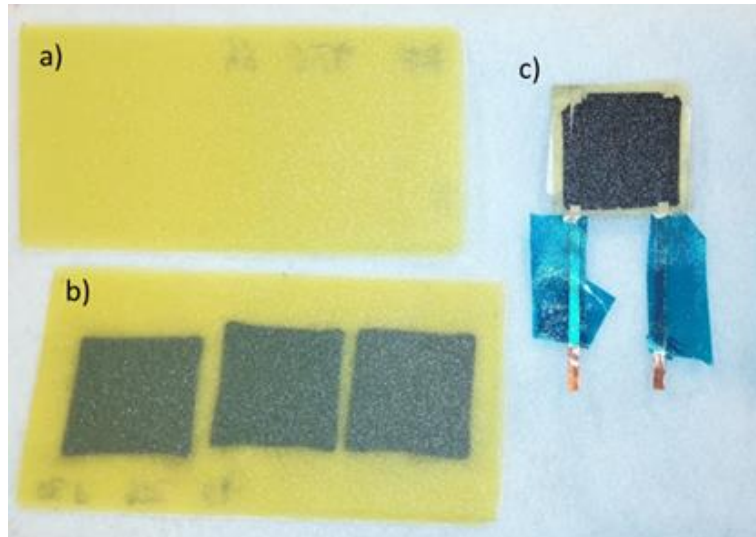


Fig. 3.16 - Composite samples of two layers configuration class: a) reference material for mechanical tests; b) CNP-composite for mechanical tests; c) CNP-composite for electrical resistance, ice protection and heating performance tests

3.7 Microstructure and characterization

3.7.1 Scanning Electron Microscope

High definition Scanning Electron Microscope (JSM - 7100F field emission scanning electron microscope), for morphological characterization. The scanning electron microscope (SEM, Fig. 3.17) used a focused beam of high-energy electrons to generate signals from electron-sample interactions (secondary electrons). Those signals would reveal information about the sample external morphology, chemical composition, crystalline structure and orientation. These signals were then translated into a 2-dimensional image that displays spatial variations in these properties.

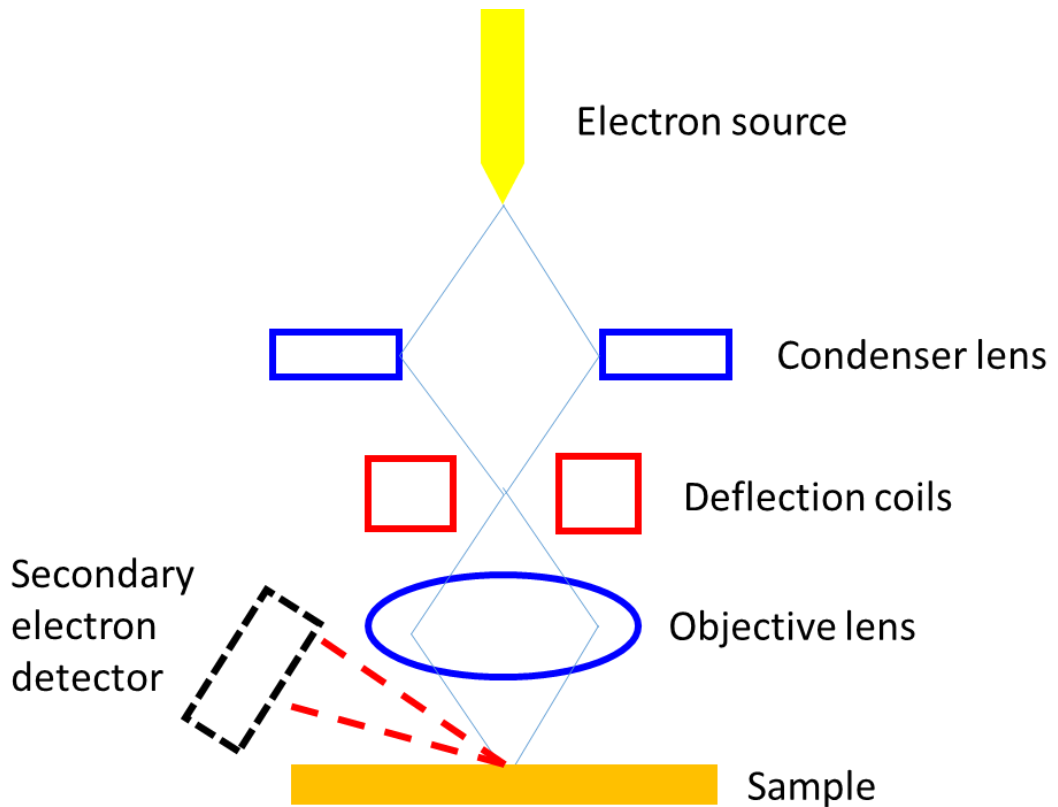


Fig. 3.17 - SEM schematic representation

Samples analysed did not require any particular procedure to be prepared. The material must be conductive to be analysed in SEM. CNTs coatings and buckypapers (treated and untreated) were stucked on the microscope samples holder using carbon tape. Composite cross section samples were coated with Pt layer (few nanometers) by physical vapour deposition.

3.7.2 Transmission Electron Microscope

Transmission electron microscopy (TEM) is a microscopy technique in which a beam of electrons is transmitted through a specimen to form an image. The specimen is most often a thin section or a suspension on a grid. The image is formed from the interaction of the electrons with the sample as the beam is transmitted through the specimen.

The characterization experiments were carried out by a Jeol 2100F FEG-TEM with field emission electron gun (FEG) providing electron source at 200 kV, equipped with a GATAN Orius SC1000 camera for conventional TEM and JEOL STEM detector for high angle angular dark field (HAADF). Samples were prepared by dripping few drops of the MWCNTs suspension on a 300 mesh lacey carbon-coated copper grids.

3.7.3 X-Ray Diffraction

X-Ray Diffraction (XRD) is used for phase identification of a crystalline material. The X-rays beam interacts with the sample by scattering those X-rays. In materials with regular structure, the scattered X-rays undergo constructive and destructive interference (diffraction). The diffracted X-rays are detected and analysed by the software of the machine.

The X-Ray Diffraction was carried out by Bruker D8 Advance diffractometer with Cu k-alpha x-rays (wavelength 0.15406 nm) at 40kV and 35mA. DIFFRAC-PLUS Measurement and DIFFRAC-PLUS Evaluation software packages were used to analyse the results. To detect silver the analysis was focused on 2θ angles between 33° and 47° with steps of 0.02° . Each powder sample was manually grinded and transferred onto a silicon sample holder for diffraction.

3.7.4 X-ray Photoelectron Spectroscopy

X-ray photoelectron spectroscopy (XPS) is a quantitative spectroscopic technique used to analyse the samples composition. XPS spectra are obtained by irradiating a material with a beam of X-rays while simultaneously measuring the kinetic energy and number of electrons that escape from the analysed sample. XPS on acid treated carbon nanotubes and zinc oxide coatings were carried out by the photoelectron spectrometer JPS-9010 MC (JEOL Ltd., Tokyo, Japan) with an X-ray source of

monochromatic MgK α (output 10 kV, 10 mA). The measurements were conducted in the vacuum chamber at around 2×10^{-7} Pa. In order to neutralize the surface charge during data acquisition, a low-energy electron flood gun was used to deliver the electrons to the sample surface. The other XPS analysis were carried out by a Kratos Liquid Phase Photoelectron Spectrometer (LiPPS) in ultra-high vacuum (5×10^{-9} mbar) environment with monochromated Al K α X-ray source (1486.6eV) operated at 10 mA emission current and 12 kV anode potential (120 W). A charge neutralizer filament was used to prevent surface charging. Hybrid-slot mode was used to measure a sample area of approximately 0.5 mm². Three areas per sample were analysed. A wide scan at low resolution (1400 -5 eV binding energy range, pass energy 80 eV, step 0.5 eV, sweep time 20 minutes) was used to estimate the total atomic % of the detected elements. High-resolution spectra at pass energy 20 eV with step of 0.1 eV, sweep times of 5, 10 or 20 minutes each were also acquired for photoelectron peaks from the detected elements which were used to study the chemical composition. The high-resolution spectra were charge corrected to the C 1s peak set to 285 eV. CasaXps software was used for quantification and spectral modelling.

The Auger parameter was used as the fundamental value to understand if the deposited material was metal or not. Using silver (Ag) as example, the Auger parameter is the sum of Ag 3d electron binding energy and Ag Auger electron kinetic energy. The Auger parameter value depends on the material state, metallic or oxide [131-139].

3.7.5 Raman spectroscopy

Raman spectroscopy is the most used method to analyse the structure and the electronic/phonon properties of carbon nanotubes. It is a spectroscopic technique typically used to determine vibrational or rotational modes of atoms. It is a

spectroscopic technique based on inelastic scattering of monochromatic light, usually from a laser source. Photons of the laser light are absorbed by the sample and then reemitted. Frequency of the reemitted photons is different from the original monochromatic frequency, which is called the Raman effect. This shift provides information about vibrational and rotational transitions.

Raman spectra were collected at room temperature by means of a triple monochromator (T-64000, Jobin-Ivon/Horiba Group, Kyoto, Japan) equipped with a charge-coupled device (CCD) detector. The obtained spectra were normalized and analyzed by commercially available software (LabSpec, Horiba/Jobin-Yvon, Kyoto, Japan). The excitation source used a 532 nm Nd:YVO₄ diode pumped solid-state laser (SOC JUNO, Showa Optronics Co. Ltd., Tokyo, Japan) operating with a nominal power of 200 mW. The lateral resolution of the Raman microprobe was in the order of 1 μm .

3.7.6 Laser scanning microscope

3D laser scanning microscope (Keyence VK-X150K) has been used to obtain digital images of composite cross section and to evaluate the surface roughness of the CNP. The VK-X150K is equipped with laser confocal technology that obtains images with a large depth of field that are in focus across the entire screen.

In the laser confocal optics, a pinhole in front of the position where the reflected light from the sample forms an image (photoreceptor) ensures that no light other than that which passes through the focal point of the objective lens reaches the photoreceptor. Use of this type of optics as a sensor allows for the maximum possible amount of light to reach the photoreceptor and allows changes in the focal point to be measured and used as height information.

3.8 Tests and properties

3.8.1 Electrical resistance

- *Electrical sheet resistance of CNT coatings*

The electrical sheet resistance of CNT coatings (section 3.2.1) has been measured by a 4-point probe (Jandel HM21 4-point probe, Fig. 3.18): several readings were taken for the same sample to record an average value. The system was set at 100 μA and give an electrical sheet resistance value in Ω/sq .



Fig. 3.18 - Jandel HM21 system (a) and head of 4-point probe (b)

The 4-point probes method is an electrical-impedance measuring technique that use two separate pairs of sensing (voltage and current carrying as represented in Fig. 3.19a) to make more accurate measurements than the simpler and more usual two-terminal sensing. Four-point probes are also used to measure electrical sheet resistance of thin coating.

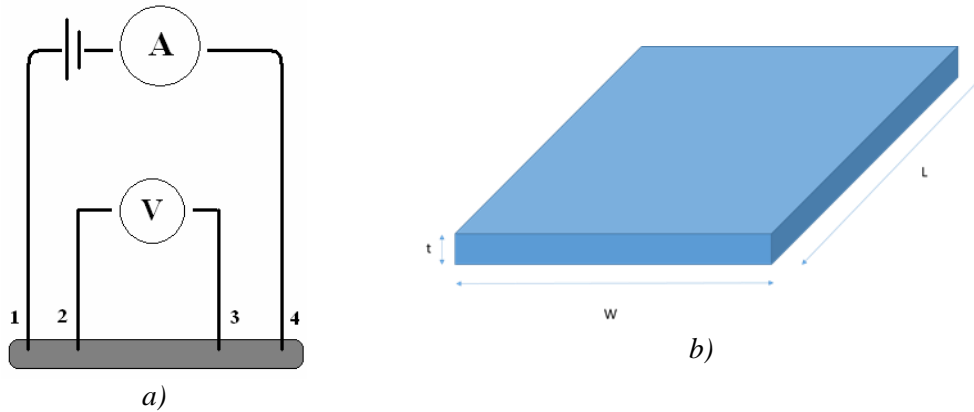


Fig. 3.19 – a) Four point resistance measurement scheme. A: current applied. V: voltage control. 1, 2, 3 and 4: probes. b) Geometry of the ideal film

The four point probe contains four thin tungsten probes to contact the sample under test. Current is made to flow between the outer probes, and voltage V (or sheet resistance R_s) is measured between the two inner probes.

The resistance can be defined as:

$$R = \rho \times \frac{L}{W \times t} \quad \text{Equation (3.1)}$$

$$R = \frac{\rho}{t} \times \frac{L}{W} = R_s \times \frac{L}{W} \quad \text{Equation (3.2)}$$

$$R_s = \frac{\rho}{t} \quad \text{Equation (3.3)}$$

where ρ (Ωm) is the resistivity, W the width (m), t the thickness (m) and L (m) the length and R_s is the sheet resistance of the film (Fig. 3.19b). The term (L/W) can be defined as the number of squares of side W that can be superimposed on the length L. The term "squares" is a pure number, dimensionless. The electrical sheet resistance has the unit of "ohms per square" since the sheet resistance produces the resistance of a resistor (with $L/W = 1$) when multiplied by the number of squares. The sheet resistance standard unit of measure is the Ω/sq . In this study the values should not be

higher than 200 k Ω /sq, otherwise they are too high to provide meaningful comparison for electrical conductivity analysis

- ***Electrical resistance of buckypaper***

Fig. 3.20 shows a device assembled in this work and it was used for electrical resistance and heating performance test of CNP. The device was composed of: two aluminium sheets (60 mm x 60 mm x 2 mm), two Polyether Ether Ketone (PEEK) films (70mm x 70 mm x 100 μ m) placed between the aluminium sheets, CNP layer and two T-shape copper electrodes attached on the CNP layer. The CNP films were laminated between the two PEEK sheets. Clamps were used to fix the devices and to keep the buckypaper in contact with the electrodes.

The CNP (treated and untreated) samples were connected to a power supply that provided a constant electrical potential difference to measure the electrical resistance. The electrical current was recorded and the resistance of the sample was calculated by Ohm's law.

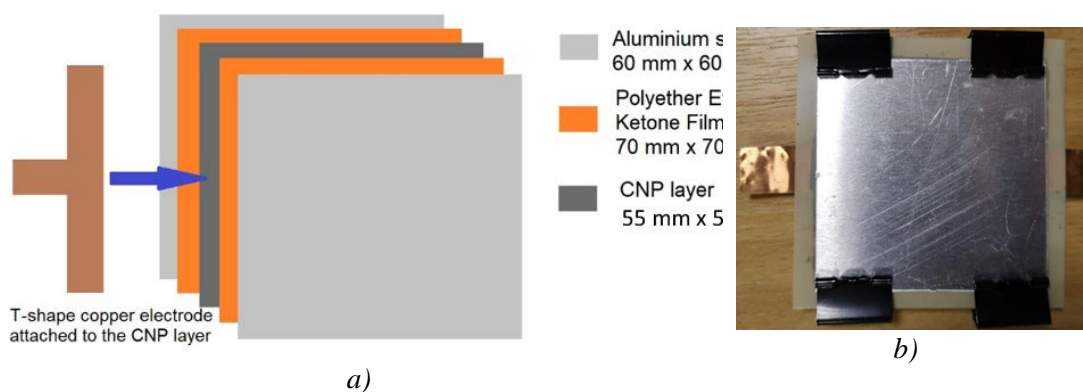


Fig. 3.20 - Device for electrical resistance and heating performance tests: a) schematic diagram of layer structure; b) photo of the assembled device

- *Electrical resistance of composite samples*

The electrical resistance of the composite samples was evaluated by connecting the samples to an ohmmeter. The value appeared on the instrument screen.

3.8.2 Heating performance

The sample was connected to a power supply that provided a constant electrical potential difference (V [V]) of 5 V, in order to analyse the heating performance. The current (I [A]) value appeared on the power supply screen. The electrical resistance (R [Ω]) of the sample was calculated by Ohm's law. A thermal imaging camera (FLIR E4) was used to measure the sample temperature during the test. The camera was operating in Multi-Spectral Dynamic Imaging mode. FLIR camera takes two images at once, one with the built-in digital camera and one with the thermal camera. Built-in software extracts visible light details from the digital image and embosses them over thermal images in real time. The highest surface temperature and the electric current were registered every 15 s since the application of the voltage. The power (P [W]) generated by the samples was calculated by the following equation:

$$P = R \times I^2 \quad \text{Equation (3.6)}$$

3.8.3 Ice melting test

The sample was placed in a cold environment (Fig. 3.21a) at -35°C where 100 ml of water were nebulized by the nebulizer machine (Omron Ultra Air NE-U17) at 3 ml/min. A 2 mm thickness of rime ice was formed on the top surface of the sample. The sample was connected to a power supply (Fig. 3.21b) and a constant potential electrical difference of 5 V was applied until the ice disappeared from the surface. The highest surface temperature and the electric current were regularly registered every

15 s since the start of the heating. A thermal imaging camera (FLIR E4) was used to measure the sample temperature during the test. The camera was operating in Multi-Spectral Dynamic Imaging mode.

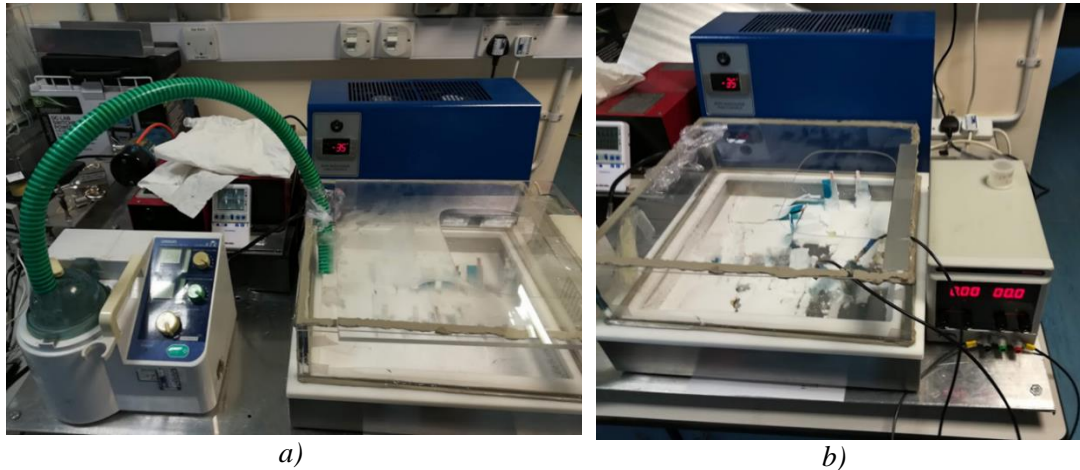


Fig. 3.21 - a) composite samples in the cold chamber (on the right) connected to the water nebulizer; b) composite sample connected to the power supply

3.8.4 Mechanical tests

The mechanical characteristics of the two layers configuration samples have been analysed. The analysis were carried out to highlight the effect of the CNP on the composite structure. The tests were performed in the laboratory of the industrial partner (Meggit); the tests parameters were chosen accordingly to the company standards. Three mechanical tests had been performed: Dynamic Mechanical Analysis (DMA), three-point flexure test and Interlaminar Shear Strength (ILSS). Samples dimensions and configuration were prepared according to the test, as represented in Fig. 3.29. For flexural strength test, the CNP layers did not cover all the sample length. However, the CNP layers were placed in the middle of sample, where the flexural stress is maximum. The samples were named accordingly to their production process: RV-CNP referred to CNP composites produced with RV treatment; RP-CNP was assigned to CNP composites produced with RP treatment. Reference samples were

produced with lay-up of just pre-preg fabrics and they were named RV-ref for RV treatment and RP-ref for RP treatment, respectively.

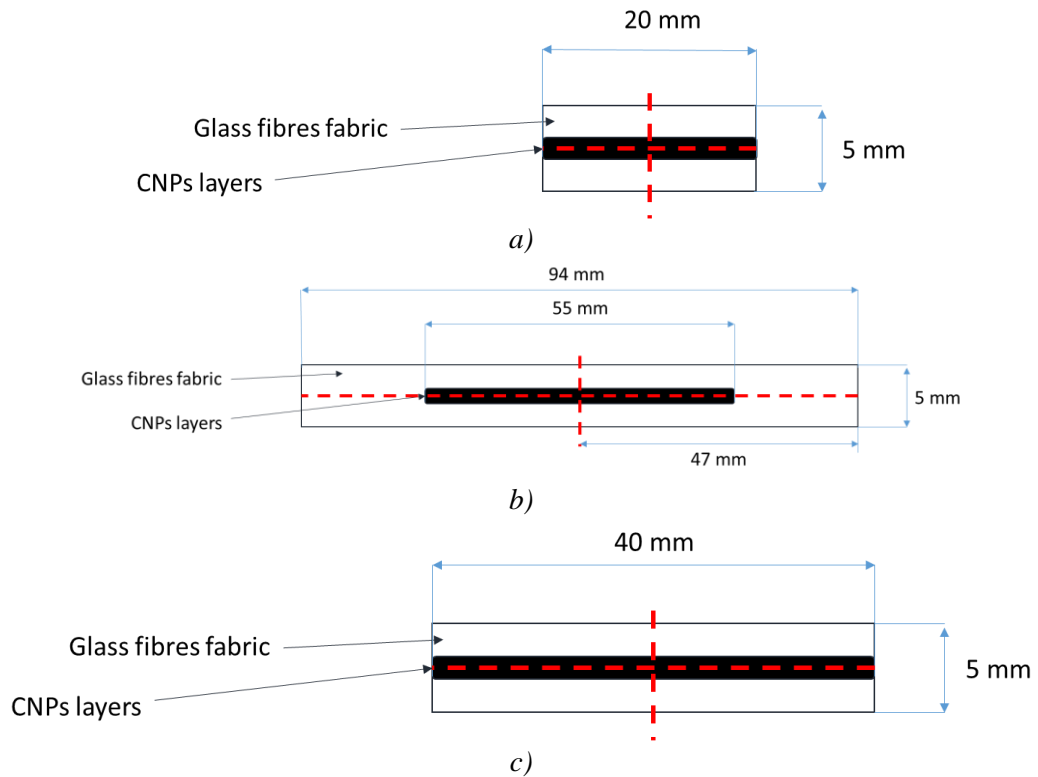


Fig. 3.22 - Schematic representation of: a) DMA test sample; b) three point flexure test sample; c) ILSS test sample

- **Dynamic Mechanical Analysis**

In the Dynamic Mechanical Analysis (DMA) a sinusoidal stress (**torsional stress**) was applied and the strain in the material was measured. Due to the viscoelastic properties of the composite samples, the stress and the strain will be out-of-phase. The phase shift δ can be measured. This test allowed to determine the complex modulus of the composite material: Storage modulus (E' [GPa]) and Loss modulus (E'' [GPa]). The Storage modulus (E') is a measure of elastic response of a material, it measures the stored energy. Loss modulus (E'') is a measure of viscous response of a material, it measures the energy dissipated as heat. $\tan \delta$ (E''/E') is the ratio of Loss to Storage

modulus; it gives a measure of which is the prevailing response. The modulus can be calculated by the following equations:

$$\sigma = \sigma_0 \sin (t\omega + \delta) \quad \text{Equation (3.7)}$$

$$\varepsilon = \varepsilon_0 \sin (t\omega) \quad \text{Equation (3.8)}$$

$$E' = (\sigma_0/\varepsilon_0) \cos \delta \quad \text{Equation (3.9)}$$

$$E'' = (\sigma_0/\varepsilon_0) \sin \delta \quad \text{Equation (3.10)}$$

$$\text{Tan } \delta = E'' / E' \quad \text{Equation (3.11)}$$

Where σ (MPa) is the stress, σ_0 (MPa) is the stress amplitude, ε is the strain, ε_0 is the strain amplitude, t (s) is the time, ω (s^{-1}) is the frequency.

TA Instruments Q800 DMA module (Fig. 3.23) was used. The method of testing was in accordance with LP138 Meggitt's operation procedure:

- Temperature range: 20°C to 400°C;
- Heating rate: 3.0 \pm 0.1°C/minute;
- Frequency: 1Hz;
- Amplitude: 15 μ m.
- Sample dimension: 40 mm x 7 mm x 5 mm (Fig. 3.22a)

Temperature range and the other parameters are used for testing their existing commercial product. For better comparison, the same values have been used.

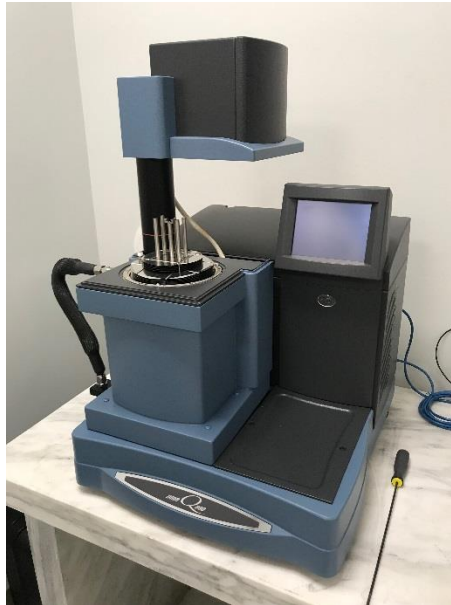


Fig. 3.23 - TA Instruments Q800 DMA

- *Three-point flexural test*

The Tinius Olsen H50K machine was used for this test. According to ASTM D790, three-point flexure test was used to measure flexural strength and modulus. The sample was placed over two support points (80 mm span) and then a force was applied to the top of the material through one point of contact. The support span-to-depth ratio of 16:1 was used to determine the length of the sample and the specimen width did not exceed one fourth of the support span for thickness greater than 3.2 mm. The specimen shall be long enough to allow for overhanging on each end of at least 10 % of the support span. The size of the samples was: 94 mm x 10 mm x 5 mm (Fig. 3.29b).

- *Interlaminar Shear Strength*

The Interlaminar Shear Strength (ILSS) was measured by three-point flexure test. It indicates the maximum shear stress existing between layers of a laminated material. The length/thickness ratio of the tested samples was small enough to create a shear stress along the middle plan of the thickness. As represented in Fig. 3.22c, the sample

dimension were 20 mm x 10 mm x 5 mm. The load range was up to 3 kN and the displacement range was up to 1.5 mm. (CRAIG 100 method [140]). The same flexural test machine was used for the ILSS test (Tinius Olsen H50K).

Chapter 4 Chemical oxidation of CNTs and electrical conductivity improvements by ZnO coatings

The results from chemical oxidation by acid treatments and ZnO surface coatings of CNTs have been analysed in this chapter. Acid treatments on CNTs were conducted in order to study whether they can improve their electrical conductivity of MWCNTs. Experiments were divided into two branches: high temperature with short time treatments and low temperature with long time treatment. Sulphuric acid, nitric acid and their combination have been analysed in the first testing branch. High temperature / short time experiments have been executed to select the best acid treatment. All the sulphuric containing treatments caused undesirable changes on the carbon nanotubes structure and electrical conductivity. Nitric acid was chosen as candidate for the second testing branch treatment and the respective acid treated nanotubes have been used for carbon nanotube buckypaper preparation. The buckypaper made with nitric acid treated nanotubes were named NA-CNP. CNPs made from untreated nanotubes were used as reference. NA-CNP showed improved electrical conductivity and promising heating performance.

For further improvement, zinc oxide was applied, using different methods, as jointing agent to reduce the electrical resistance of the MWCNTs web. ZnO was applied by spray technique, spin coating and atomic layer deposition (ALD). Sprayed and spin coated samples did not show any improvement of the electrical properties. Results from ALD showed high electrical resistance reduction for the coated samples. The experiments confirmed the jointing function of the ZnO. Further analysis have been carried out to study the effect of ZnO on buckypaper.

4.1 Acid treatments effects on nanotubes

4.1.1 Characteristics of high temperature acid treated CNTs

Fig. 4.1 shows the comparison between the first (1°MWCNT, Merck, blue line) and the second (2°MWCNT, Nanotube Plus, green line) batch of MWCNTs. To compare the structures of the nanotubes, Raman spectroscopy has been used and the data have been normalised in order to compare the samples spectra. Both samples showed similar result from the Raman spectroscopy. The main features in the Raman spectrum (Fig. 4.1b) are: D band, D' band and G band. The D band, at 1350 cm^{-1} [141-148], is caused by disordered structure or discontinuity/defect in the carbon nanotube network. The presence of disorder in sp²-hybridized carbon systems results in resonance Raman spectra [149]. The G band at 1580 cm^{-1} [150-156] is induced by the crystalline graphitic structure. The distributed impurities, or defects in the nanotube structure, can cause the G-peak split into two peaks, G-peak (1583 cm^{-1}) and D'-peak (1610 cm^{-1}). The split is due to the interaction between the vibrational modes of the impurities and the carbon atoms of the nanotubes structure [149].

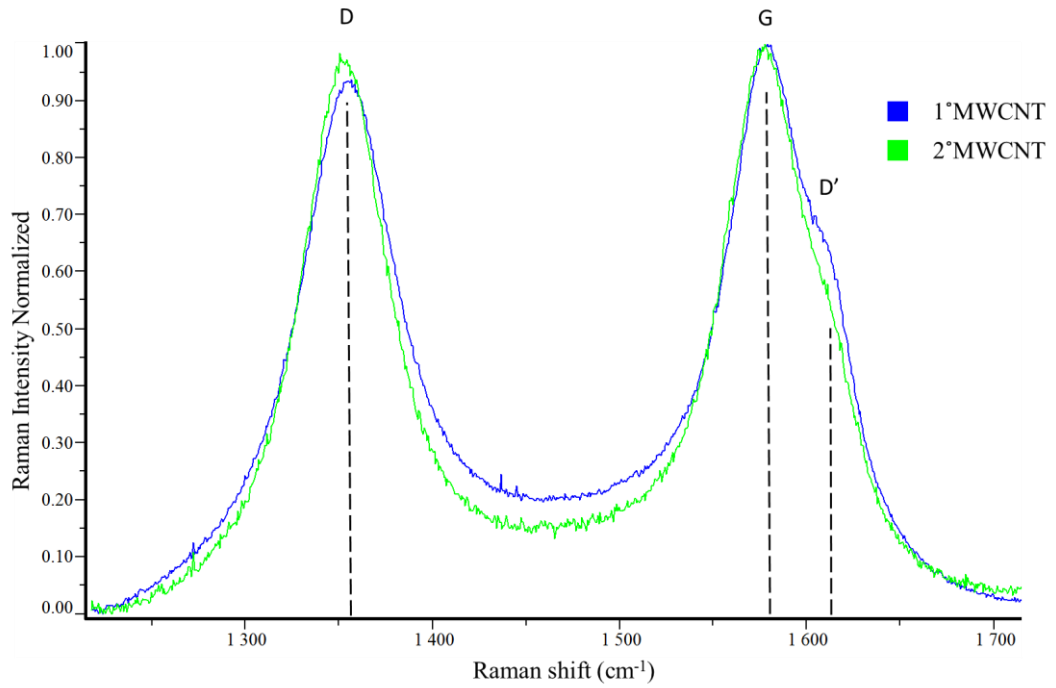
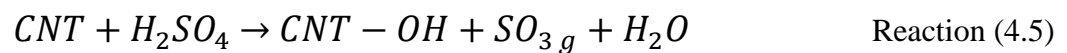
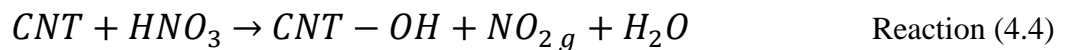
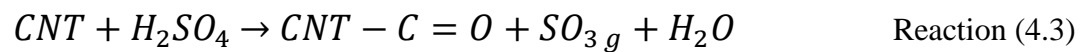
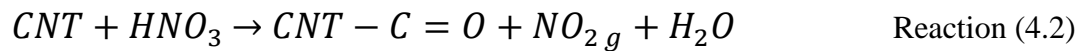
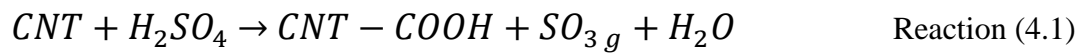
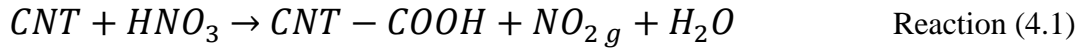


Fig. 4.1 - Raman spectra comparison of MWCNTs of first (blue line) and second (green line) batch

Regarding acid treatment, some theoretical reactions mechanisms are described as below:



Gas formation was observed especially during nitric acid (pure and mixed) treatments: NO_2 is a reddish brown gas. The acid treatments attacked the nanotubes, modifying the tube structure. The damages of the nanotubes, caused by the high temperature acid treatments, were detected by the TEM. Fig. 4.2 shows TEM images of untreated MWCNTs (1°MWCNT, Fig. 4.2a), sulphuric acid treated nanotubes (HT-SA, Fig. 4.2b) and nitric acid treated nanotubes (HT-NA, Fig. 4.2c). The red-dotted circles highlight the damages caused by the acid treatments. The open head of the tube indicates one place where the acids attacked the structure. The changes in the nanotubes structure, caused by acid treatments, cannot be quantified and compared in detail from the pictures.

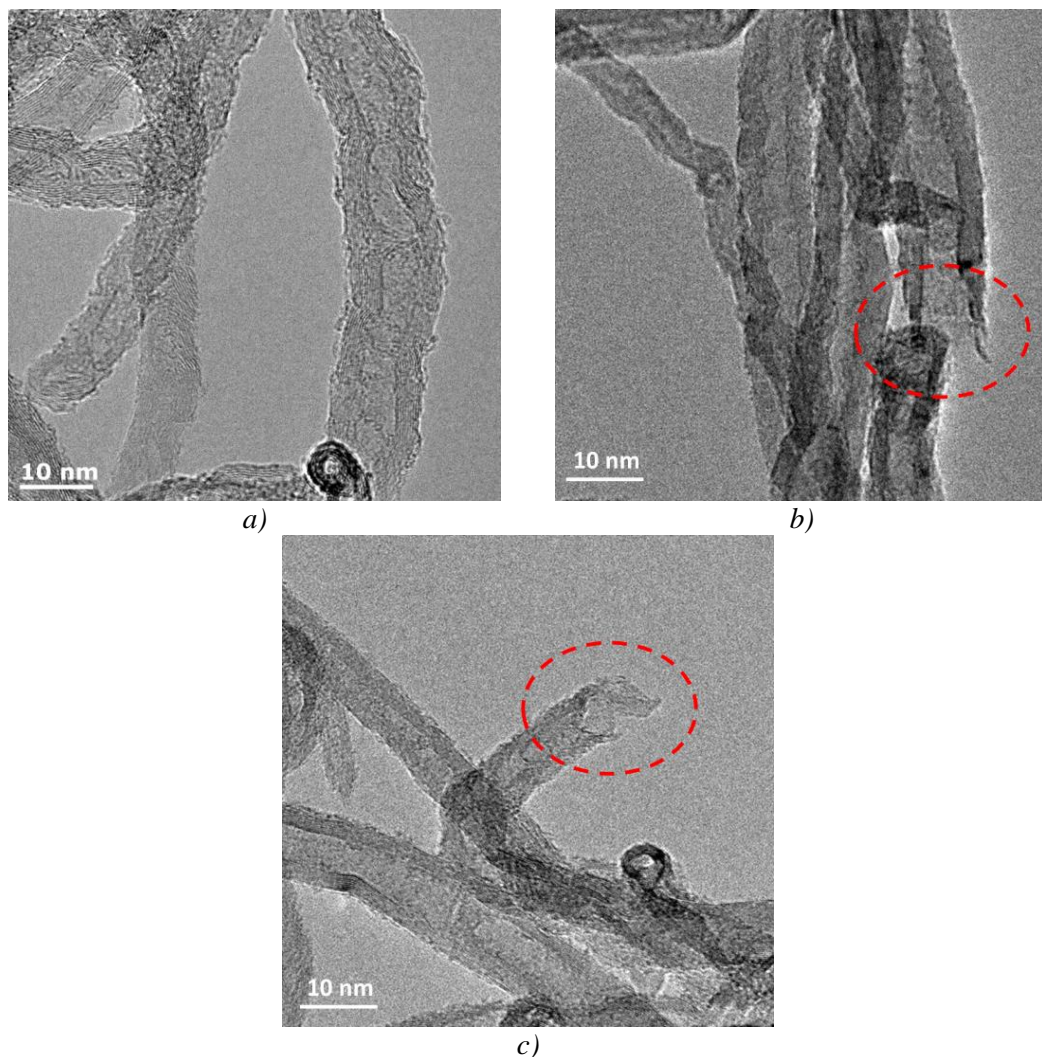


Fig. 4.2 - TEM images of : a) 1°MWCNT; b) HT-SA c) HT-NA

To functionalise the CNT surface (C=O, C-OH, -COOH groups), the pristine nanotubes have been treated at high temperature with concentrated nitric acid (HNO₃), sulphuric acid (H₂SO₄) and their mixed solutions. The changes on the carbon nanotubes surface, caused by the different acid treatments, have been analysed from the XPS results of C1s orbital.

XPS results on C1s orbitals (Table 4.1) can indicate the level of carbon sp³ or carbon sp² on the surface of the nanotubes. Carbon nanotubes are a rolled up graphene sheet with altered structure of carbon orbitals. On the nanotube surface there is a mixed state of σ (sp³) and π (sp²) orbitals induced by the curvature called rehybridization [17]. The rehybridization level depends on how many bonds, between C=C (284.2 eV) and C-C (284.9 eV), there are on the carbon nanotubes surfaces [157]. A comparison between untreated and acid treated samples indicates the changes on the nanotubes surfaces caused by the treatments. As described in Table 4.1 the untreated samples have concentrations around 10 at% for C-C and 68 at% for C=C. The reduced C=C and increased C-C concentration values are caused by the increase of the functional groups.

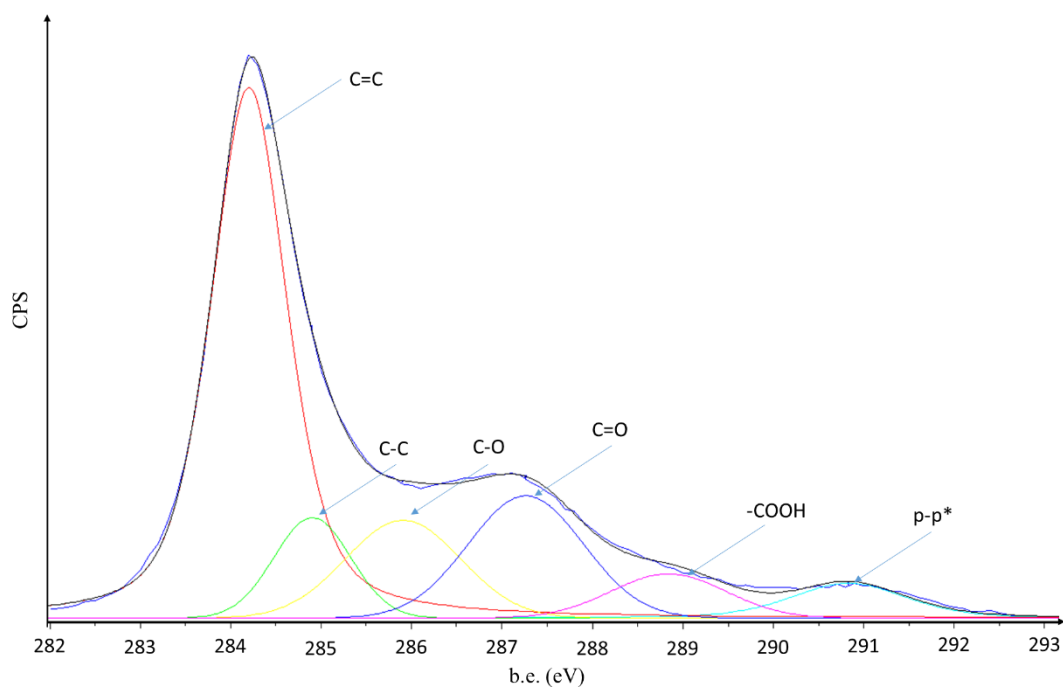


Fig. 4.3 - Example of deconvolution C1s orbital scan component (XPS C1s orbital scan of HT-NA)

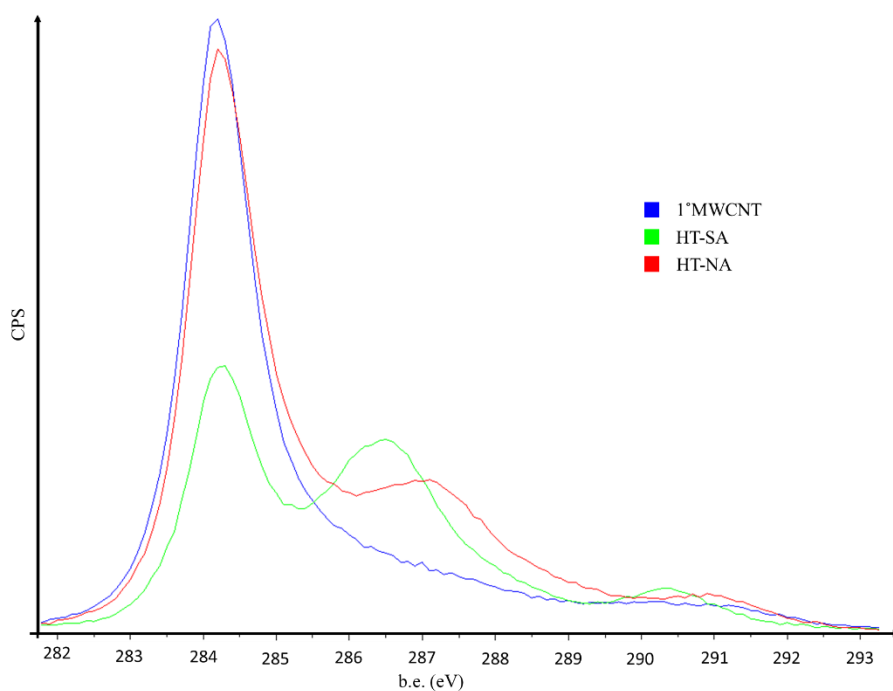
The deconvolution of the C 1s peak (Fig. 4.3) helped to quantify the concentrations (at%) of C=C or C-C bonds and the amount of oxygen containing groups (C-O, C=O and -COOH) in the samples (Table 4.1). Untreated MWCNTs (1^oMWCNT row in Table 4.1) have been used as reference. The acid treatment creates defect sites on the graphitic network. The defect can be described as one carbon atom, from CNT lattice, replaced by functional groups such as carboxylic acid (-COOH) and hydroxyl (-OH) on the CNT surface. The peaks (Fig. 4.4) due to carbons attached to different oxygen-containing groups are shown at 286.0 eV (C-O), 287.1 eV (C=O) and 288.8 eV (-COOH) [157-161]. Any signal with eV > 289 was classified as p-p* transition [158, 162, 163].

Acid treatments caused an increase of the functional groups, as described in Table 4.1. HT-SA has the highest oxidising effect. HT-SA has the highest C=O concentration (19 at%). HT-SA75-NA75 obtained the second highest oxidation effect. Among the

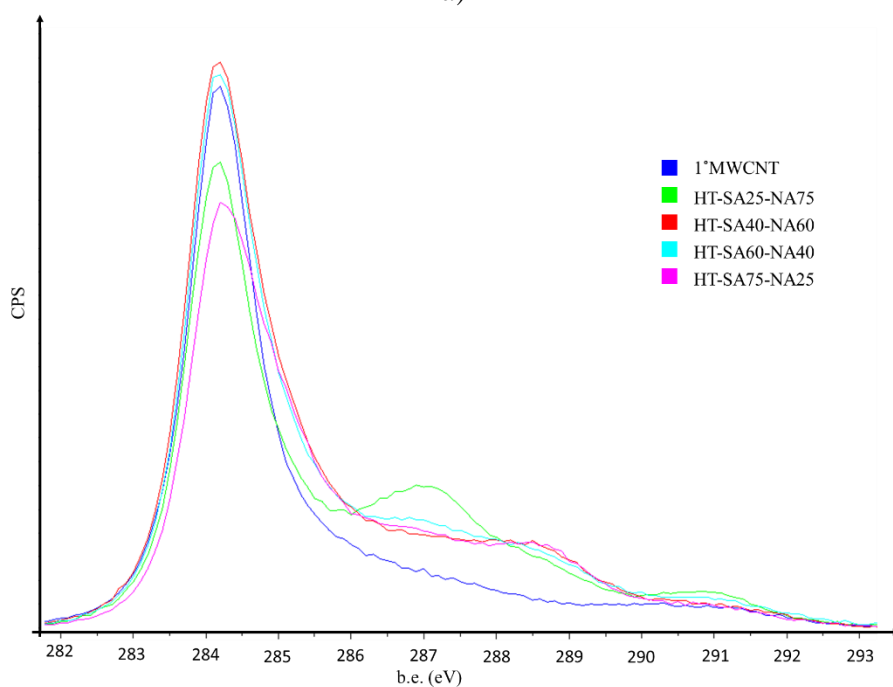
mixed acid treatments, HT-SA25-NA75 has the highest concentration of C-O (12 at%) and -COOH (7 at%). The mixed acid solutions have a lower oxidation effect compared to the pure one, except for HT-SA25-NA75 sample. The boiling point of the nitric acid is 83°C. The addition of sulphuric acid should have increased the nitric acid solution reactivity. It looks like the volume ratio between sulphuric and nitric acids 1:3 (S:N) is the most reactive ratio.

Table 4.1 - Quantitative results for C1s scan

Samples	C 1s					
	C=C (at%)	C-C (at%)	C-O (at%)	C=O (at%)	-COOH (at%)	p-p* (at%)
1°MWCNT	65.1	9.4	7.0	4.0	2.7	2.6
HT-NA	49.4	9.4	9.1	11.4	4.1	3.3
HT-SA	30.4	10.4	12.1	19.0	6.4	5.2
HT-SA75-NA25	38.6	20.9	7.7	6.1	2.6	1.0
HT-SA60-NA40	40.5	23.1	7.5	5.9	3.6	2.7
HT-SA40-NA60	46.0	17.3	6.5	6.4	3.0	1.9
HT-SA25-NA75	42.6	14.3	11.8	5.8	6.6	3.8



a)

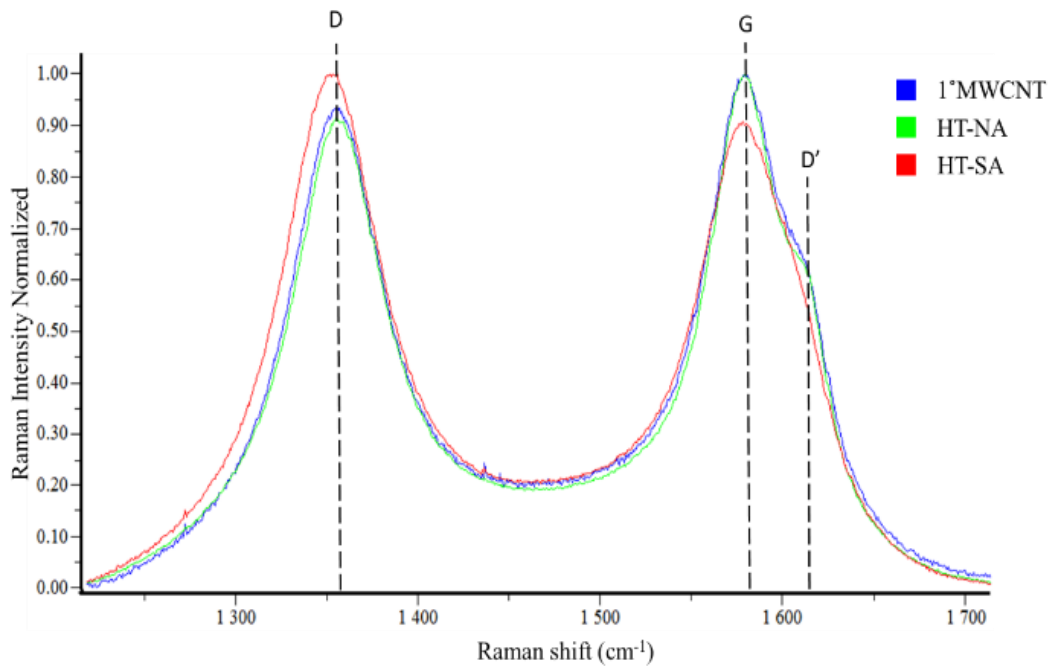


b)

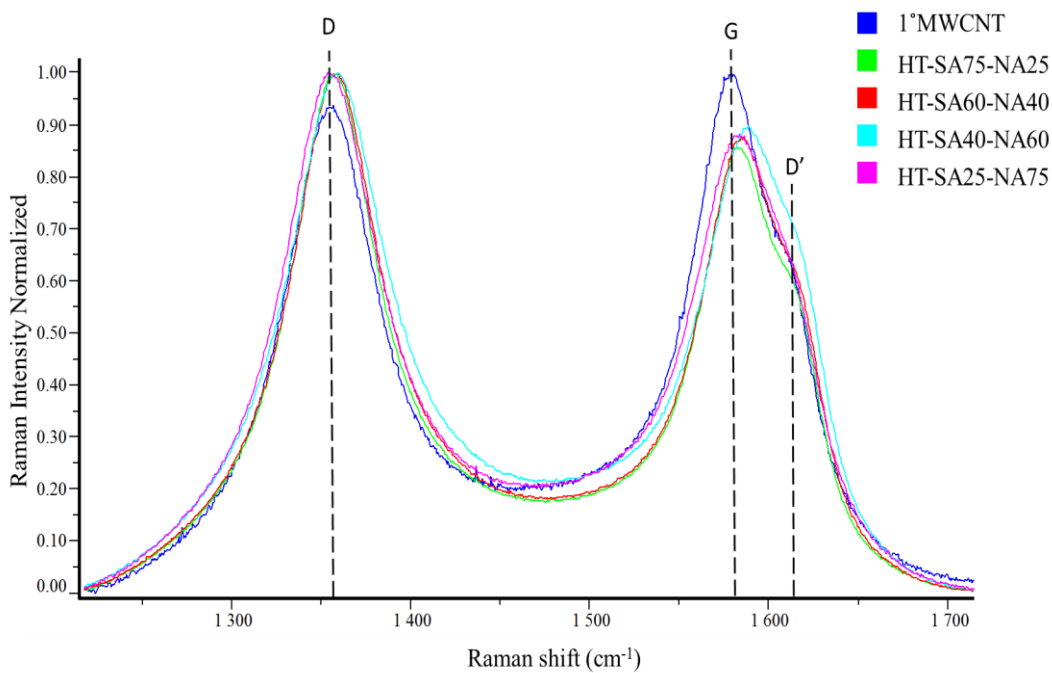
Fig. 4.4 - XPS C1s orbital scans of high temperature treated samples: a) pure acid solutions treated MWCNTs; b) mixed acid solution treated MWCNTs

Fig. 4.5 shows the normalized Raman spectra of the HT samples. The main features in the Raman spectrum are: the D and D' bands at 1350 cm^{-1} and 1610 cm^{-1} , and the G at 1580 cm^{-1} . Despite the oxidation effect, the nitric acid treatment did not change

the structure: the intensity ratio between G and D peaks are the same between MWCNT and HT-NA. This result indicates that the amounts of amorphous and crystalline carbon remain almost unchanged. HT-SA, HT-SA25-NA75, HT-SA40-NA60, HT-SA60-NA40 and HT-SA75-NA25 exhibit an altered crystalline graphitic structure. Due to the increased amount of amorphous carbon and defects in the nanotube structure, the ratio between the intensity of G and D bands change visibly and the width of the D band of HT acid treated samples is bigger than the 1°MWCNT one. Moreover the crystalline structure of the nanotubes has been slightly modified. This is visible in the G peak in mixed acid treated samples: the peak is slightly up-shifted from the original value of the 1°MWCNT.



a)



b)

Fig. 4.5 - Normalized Raman spectra of high temperature treated samples: a) pure acid solutions treated MWCNTs; b) mixed acid solution treated MWCNTs

Electrical sheet resistance values of CNTs coatings on glass substrate (Fig. 4.6) are listed in Table 4.2 and Table 4.3. Results indicated that sheet resistance of mixed acid treated coatings (Table 4.2) is higher than that of the untreated coatings. The value “>200” indicates that the electrical sheet resistance value was higher than 200 k Ω /sq; this results highlighted that the acid treatments did not improve the electrical characteristics of the coatings. These values were out of the selection criteria.

Table 4.2 - Electrical sheet resistance values for HT mixed acid treated coatings compared to the untreated

Sample	Volume of suspension	Sheet electrical resistance
	(ml)	(k Ω /sq)
1°MWCNT	10.0	102.7
	12.5	45.6
	15.0	22
	17.5	13.8
HT-SA25-NA75	10.0	>200
	12.5	>200
	15.0	>200
	17.5	>200
HT-SA40-NA60	10.0	>200
	12.5	>200
	15.0	>200
	17.5	>200
HT-SA60-NA40	10.0	>200
	12.5	>200
	15.0	>200
	17.5	>200
HT-SA75-NA25	10.0	>200
	12.5	>200
	15.0	>200
	17.5	>200

The mixed acid treatments caused a deterioration of the electrical sheet resistance of the CNTs coatings. Electrical sheet resistance of HT-SA and HT-NA coatings with 90 ml suspension are described in Table 4.3. Both acid treated samples have electrical

sheet resistance values similar to the untreated sample ($\sim 1.5 \text{ k}\Omega/\text{sq}$). Neither of the treatments caused any change to the electrical characteristics of the CNT coatings.

Table 4.3 - Electrical sheet resistance values and their relative standard deviation of 90 ml suspension coatings: pure, nitric and sulphuric acid treated

Sample	Electrical sheet resistance ($\text{k}\Omega/\text{sq}$)	St. deviation ($\text{k}\Omega/\text{sq}$)
1°MWCNT	1.45	0.17
HT-NA	1.46	0.13
HT-SA	1.49	0.15

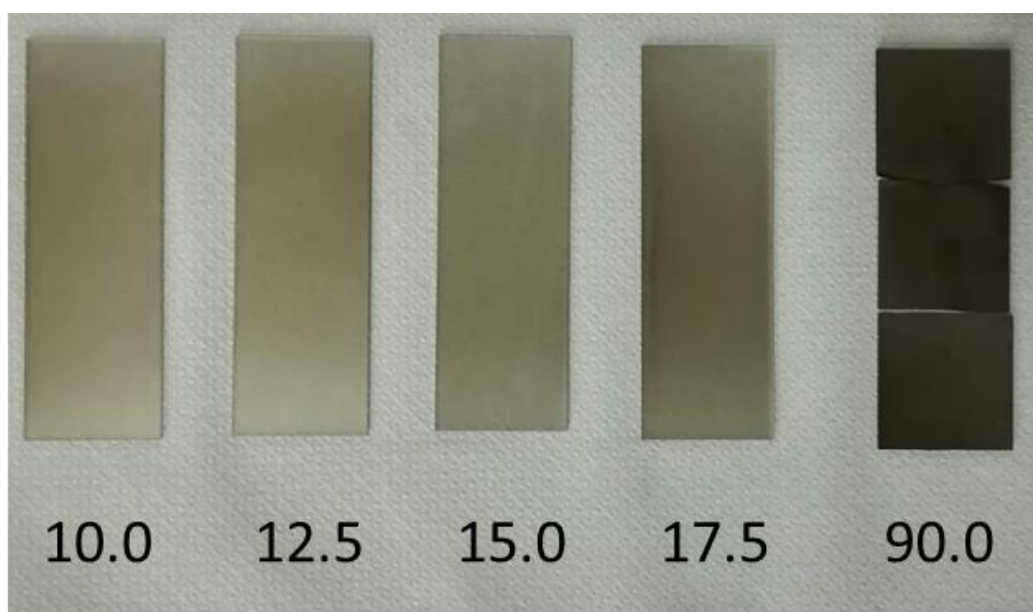


Fig. 4.6 - Pictures of CNTs coatings on glass substrates. The respective volumes (ml) of used suspensions are labelled in the picture

4.1.2 Characteristics of low temperature acid treated CNTs

The overall results indicated that acid treatments with sulphuric acid containing solutions altered the nanotubes structure and their electrical properties. Nitric acid has been chosen as candidate for the long time / low temperature treatment. The treated nanotubes (second batch) were named NA-CNT. The oxidizing effect is clearly different from the HT treatment. The functional groups concentrations for NA-CNT

sample are listed in Table 4.4. In HT-NA, the concentration of C=O, -COOH and C-O groups is higher than in NA-CNT.

Table 4.4 - Quantitative results for C1s scan

Samples	C 1s					
	C=C	C-C	C-O	C=O	-COOH	p-p*
2°MWCNT	51.6	34.7	3.8	2.7	1.8	3.5
NA-CNT	57.5	19.7	8.6	3.2	1.9	1.9
HT-NA	49.4	9.4	9.1	11.4	4.1	3.3

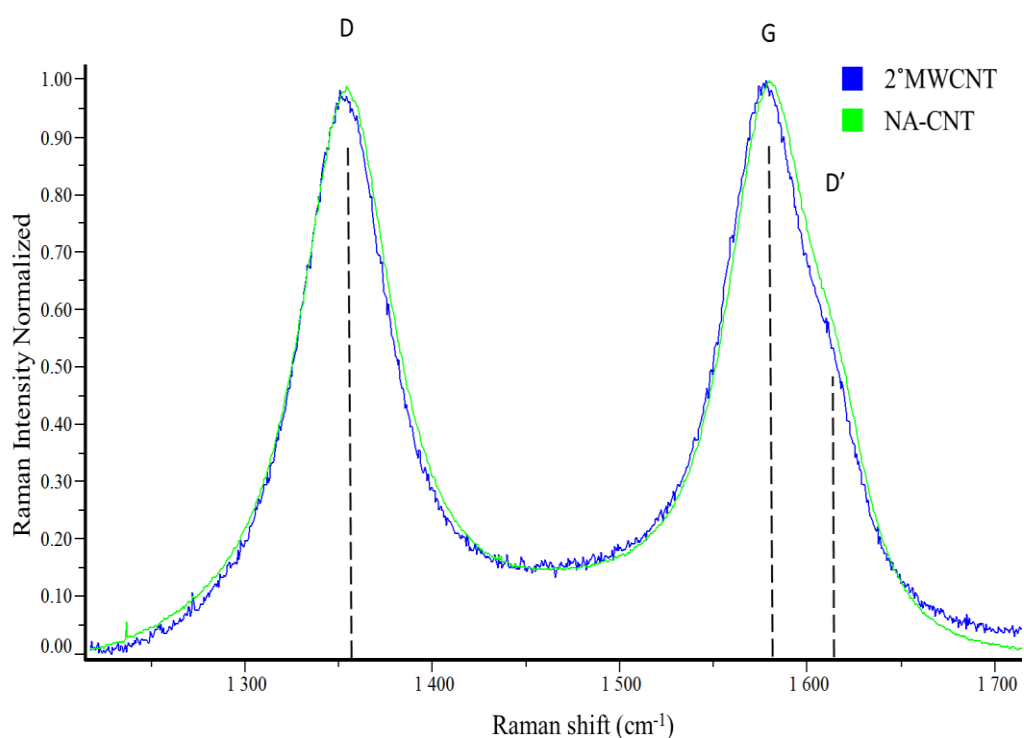


Fig. 4.7 - Normalized Raman spectra for 2°MWCNT (blue line) and NA-CNT (green line)

Raman spectra (Fig. 4.7) showed the two similar spectra of 2°MWCNT and NA-CNT. The intensity ratio between G and D peaks are the same between MWCNT and NA-CNT. This result indicates that the amounts of amorphous and crystalline carbon remained almost unchanged. Fig. 4.8 shows TEM images of untreated (2°MWCNT, blue line) and nitric acid treated (NA-CNT, green line) samples. On the external surface of the nanotubes treated by nitric acid (Fig. 4.8b), the amorphous carbon content is lower than in the untreated one (Fig. 4.8a). The strong oxidant treatment

could have reduced the amorphous carbon. Raman spectra (Fig. 4.7) indicated that the relative ratio between amorphous/disordered and crystalline carbon quantities did not change: the loss of the amorphous carbon was compensated by the defects generation. For the nitric acid-treated CNTs, obvious structural changes occurred as observed in Fig. 4.8 where the graphene layers of CNT present different misalignment spots. The red circles highlight the area in which the acid may have attacked the nanotubes and the functional groups are likely to attach onto the external wall.

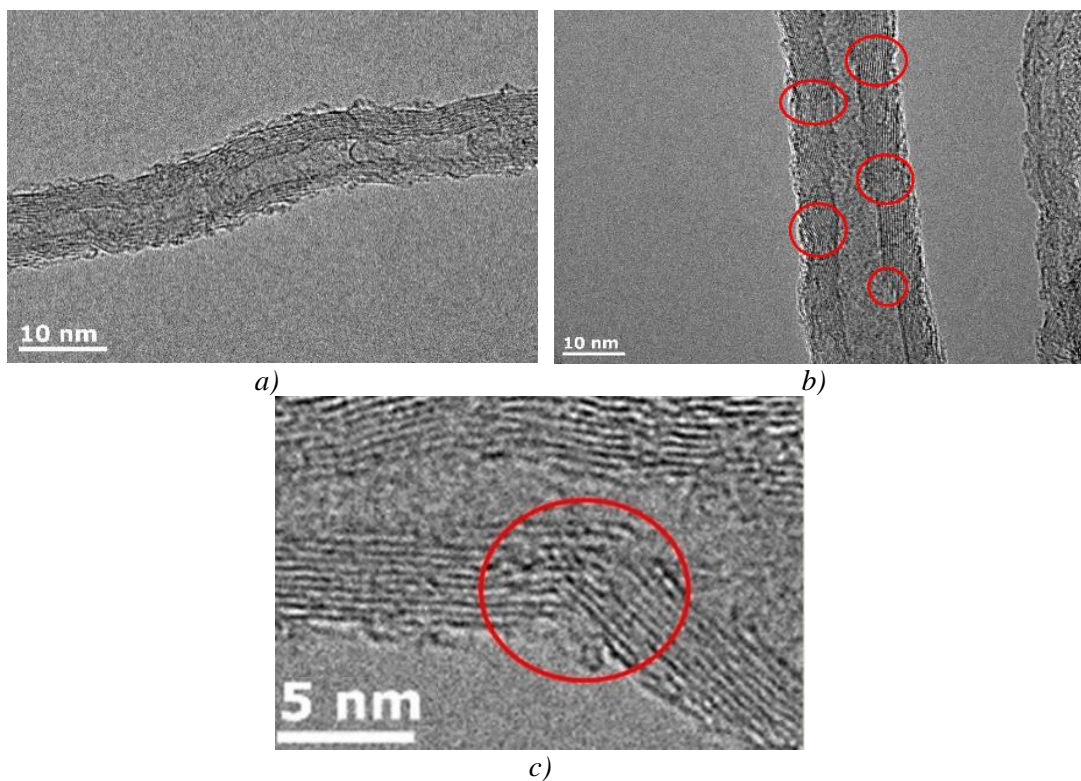


Fig. 4.8 - TEM images of: a) untreated multiwall carbon nanotubes; b) formed defects (red circles) on MWCNTs walls after nitric acid treatment; c) magnified image of one acid attacked position

NA-CNT were used for the CNT buckypaper fabrication: NA-CNP were made using nitric acid-treated CNTs; while MWCNP referred to buckypaper fabricated using untreated CNTs. In Table 4.5 the buckypapers characteristics like surface area, thickness and thickness standard deviation are listed. Δ Thickness is the thickness change ratio compared with MWCNP references.

Table 4.5 - Carbon nanotube buckypapers characteristics

Samples	Surface area (m²)	Thickness (mm)	Thickness St.dev. (mm)	ΔThickness (%)
MWCNP	3 x 10 ⁻³	0.120	0.010	0.0
NA-CNP	3 x 10 ⁻³	0.081	0.012	-32.2

SEM images of the two types of buckypaper are shown in Fig. 4.9. On MWCNP (Fig. 4.9a and Fig. 4.9b) surface, nanotube aggregates are distributed randomly on the surface, with the size around half to one micron. On NA-CNP (Fig. 4.9c and Fig. 4.9d), the amount of aggregates seems to be significantly reduced, due to the effect of the MWCNTs oxidation [33, 141, 164], which makes the NA-CNP surface much flatter than MWCNP. Nitric acid is a strong oxidizing agent, therefore some amorphous carbon would be removed [164]. As amorphous carbon in MWCNT has much less contribution to electrical conductivity, the reduction of amorphous carbon allows a more compact (around 32% less thickness) configuration of NA-CNP, without sacrificing conductivity.

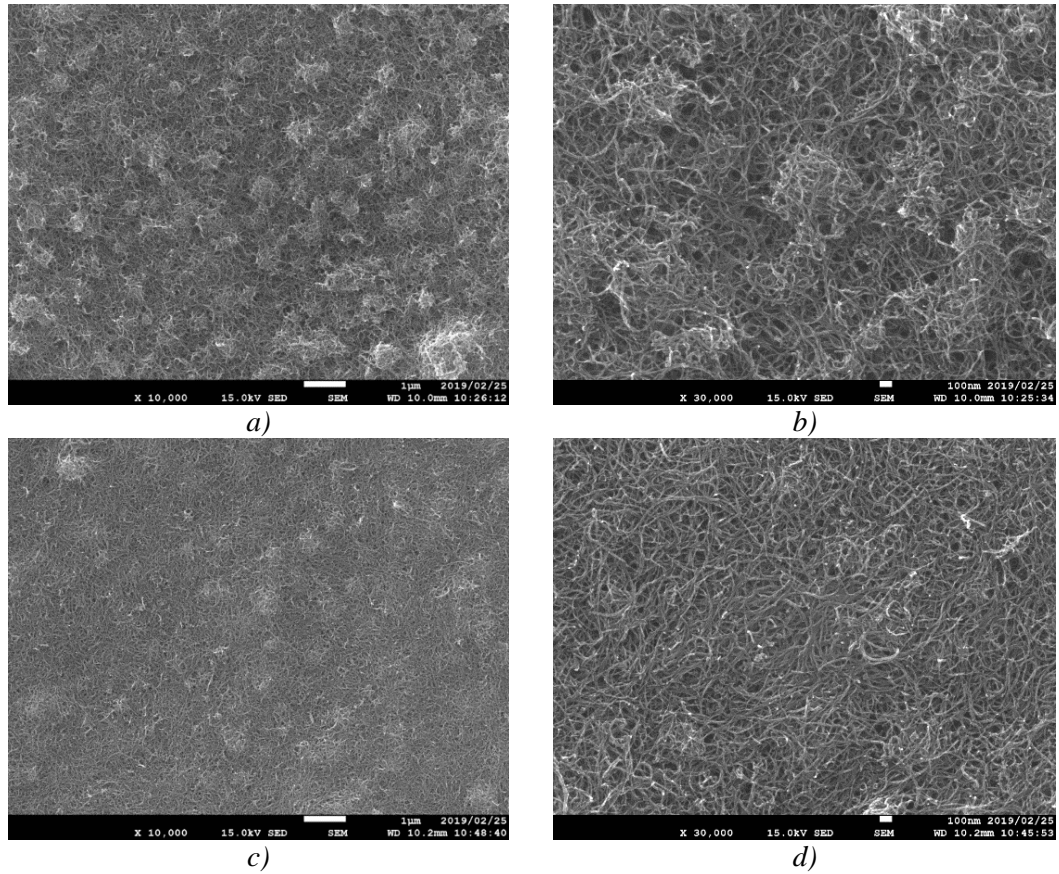


Fig. 4.9 - SEM images of: a) $\times 10000$ MWCNP; b) $\times 30000$ MWCNP; c) $\times 10000$ NA-CNP; d) $\times 30000$ NA-CNP

The electrical properties of buckypaper are listed in Table 4.6, including electrical resistance and its standard deviation, electrical resistivity ρ and electrical conductivity σ . $\Delta\rho$ and $\Delta\sigma$ are the change rate of electrical resistivity and electrical conductivity, respectively, compared with MWCNP reference. The NA-CNPs have the lowest electrical resistivity and, as a consequence, the highest electrical conductivity (about 35% increase).

Table 4.6 - Electrical properties of carbon nanotubes buckypaper

Samples	Resistance (Ω)	Resistance St.dev. (Ω)	ρ ($10^{-3}\Omega\text{ m}$)	$\Delta\rho$ (%)	σ (S/m)	$\Delta\sigma$ (%)
MWCNP	5.5	0.5	0.661	0.0	1513.2	0.0
NA-CNP	6.0	0.8	0.489	-26.0	2045.3	35.2

4.1.3 Ice protection evaluation of acid treated CNP

A double layer configuration has been tested, in which two CNP films were laminated in the testing device and connected to the power supply. Untreated (2-MWCNP) and nitric acid-treated (2-NA-CNP) buckypaper has been compared and the results are listed in Table 4.7.

Table 4.7 - Electrical properties for two-layered carbon nanotubes buckypapers

Samples	Resistance (Ω)	Resistance St.dev. (Ω)	ρ ($10^{-3} \Omega \text{ m}$)	$\Delta\rho$ (%)	σ (S/m)	$\Delta\sigma$ (%)
2-MWCNP	2.4	0.6	0.574	0.0	1741.7	0.0
2-NA-CNP	2.3	0.7	0.374	-34.9	2675.0	53.6

Doubling the thickness clearly improved the electrical characteristics of CNP: 35% reduction in electrical resistivity and 54% increase in electrical conductivity. Although the untreated and nitric acid-treated double layers samples show close electrical resistances, a much thinner two-layer structure is formed when using the acid-treated nanotubes. Therefore the nitric acid-treated CNTs are more effective in the construction of the thin-layer electrical conducting nanostructure network.



Fig. 4.10 - Ice formed on the sample surface in a cold environment (-20°C)

The double-layered buckypaper configuration was chosen for the electro-thermal de-icing test. Untreated (2-MWCNP) and nitric acid-treated (2-NA-CNP) buckypapers were tested. The samples were covered in rime ice at -20°C (Fig. 4.10), an electrical

potential was applied to start the heating. This test condition was to simulate an ice protection system working in de-icing configuration.

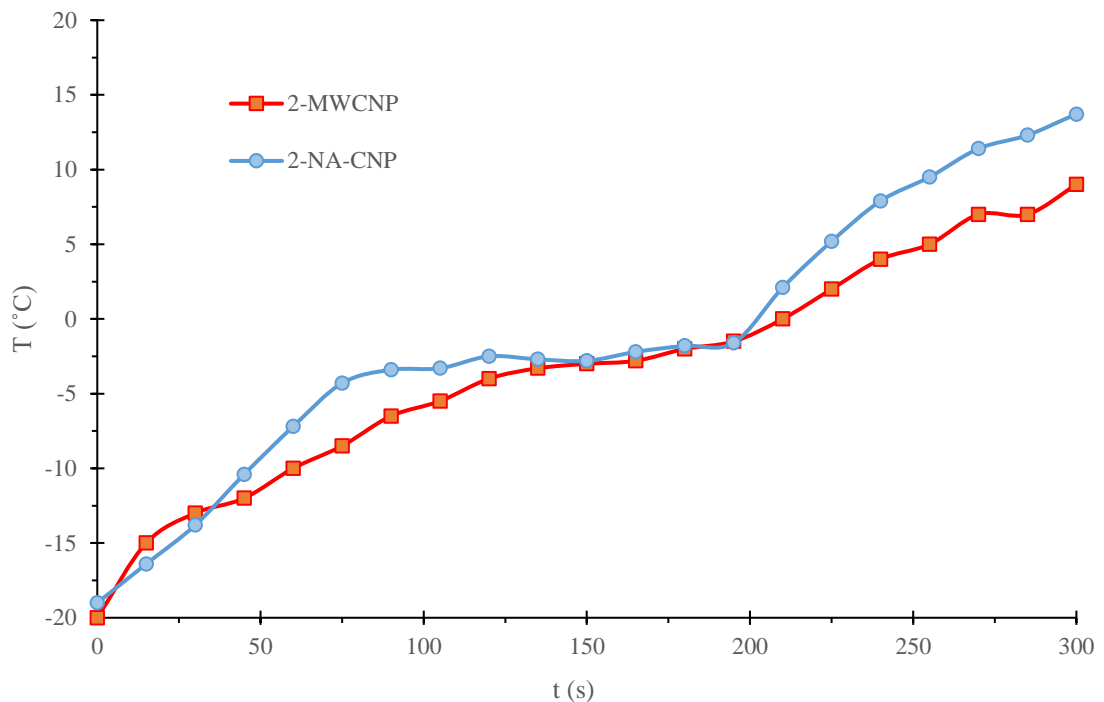


Fig. 4.11 - Example of temperature versus heating time during the de-icing test for one 2-MWCNP sample and one 2-NA-CNP sample

Fig. 4.11 shows an example of the increase of surface temperature T of two samples (2-MWCNP and 2-NA-CNP) during the de-icing test. 2-MWCNP and 2-NA-CNP samples showed similar behaviour during the de-icing test. Fig. 4.12 shows the images of the de-icing test and where the sample temperature was measured. Fig. 4.12b shows that the ice starts melting at the borders of the device, where the clamps were placed. The clamps improved heat transfer between the CNPs and the metal plate. During ice melting, the measured temperature was slightly below 0°C (around $-1^{\circ}\text{C} \sim -2^{\circ}\text{C}$). The results indicated an average ice melting time of 100 s for both devices (2-MWCNP and 2-NA-CNP). The ice melting time is characterized by a plateau of temperature values; this plateau is visible in Fig. 4.11 from 100 s to 200 s. The camera was measuring temperature in the centre of the sample where, during ice melting, there

was an ice/water mixed phase. For this reason the measured temperature was not exactly 0°C, as thermodynamically expected. The ice melting started when melting spots appeared on the metal plate, as in Fig. 4.12b and Fig. 4.12e. The ice was completely melted when the temperature rose over 0°C.

The power consumptions during the de-icing test are listed in Table 4.8. The surface of the samples is approximately 0.003 m². For both samples, the ice was completely removed after 200s. At the end of the experiments, power density values were around 3 kW/m², which were within the range of the reported power density of electro-thermal heating for ice protection systems using single-wall CNP composite [71]. The data have been compared to a traditional heater configuration (copper based heating element), studied by Zhao et al. [74]; the traditional system need a power density of 7 kW/m² to reach a similar ice protection performance. The power density of the CNP based heater is around 62% lower than the power density of the traditional heater. This highlight the potential application of the CNP as ice protection system.

Table 4.8 - Power densities of the ice protection test

Samples	Power density (kW/m²)	St.dev. (kW/m²)
2-MWCNP	2.5	0.4
2-NA-CNP	2.7	0.5
Traditional [74]	7.0	-

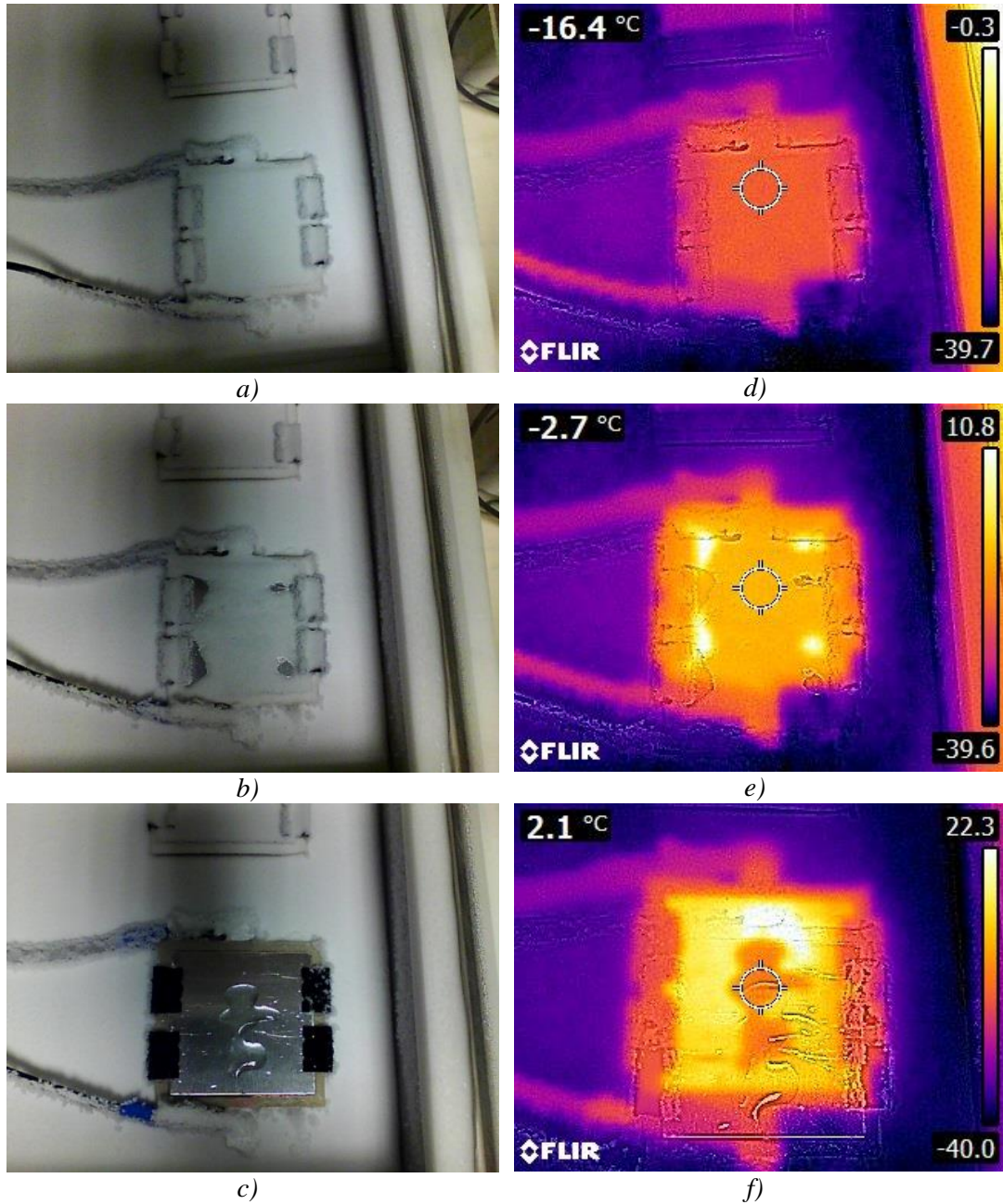


Fig. 4.12 - Photos (left column) and thermal images (right column) of the de-icing test: a, d) at the beginning of the test; b, e) during ice melting; c, f) at the end of ice melting

4.2 Electrical resistance reduction with ZnO coatings

4.2.1 Electrical characteristics and morphological analysis

Electrical sheet resistance of ZnO coated CNTs are listed in Table 4.9. The ZnO coatings have been applied on CNT coatings sprayed on glass substrates (90 ml suspension, automatic spray system). Untreated (1°MWCNT) CNT coatings were used as reference. The ZnO should work as jointing agent to reduce the electrical resistance contact between the nanotubes. The results indicate that ALD was the most effective method. The electrical sheet resistance reduction is more than 50% for the untreated samples (1°MWCNT). Spin coating method did not show any improvement in the electrical conductivity of the CNT coating. The electrical resistance of spray coated ZnO samples was higher than the reference sample values. The results can be explained by the morphological analysis of the ZnO coatings.

Table 4.9 - Electrical sheet resistance values and their relative standard deviation of 90 ml suspension coated with ZnO

Sample	ZnO coatings	Electrical sheet resistance (kΩ/sq)	St. deviation (kΩ/sq)
1°MWCNT	CNT	1.45	0.17
	Spin	1.7	0.16
	Spray	>2k	/
	ALD	0.56	0.20

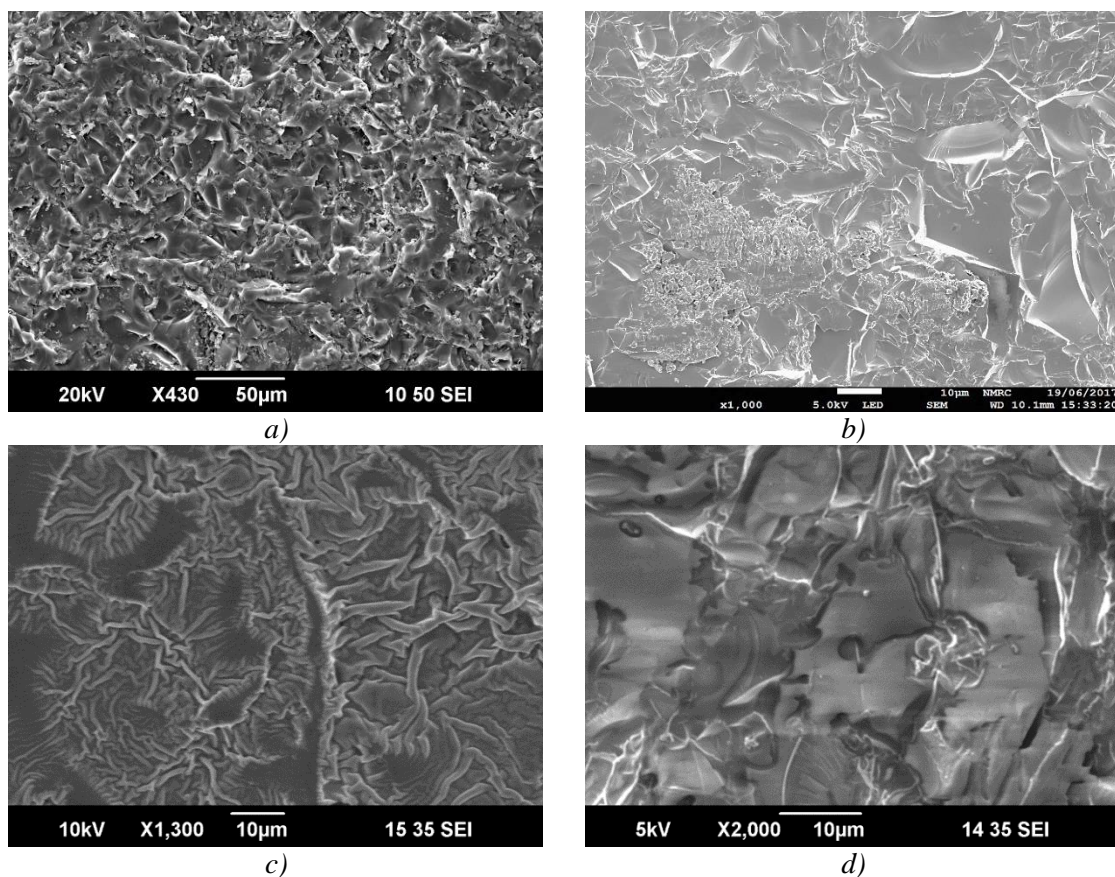


Fig. 4.13 - SEM images of a) sand blasted glass; b) ZnO ALD coating c) ZnO spray coating; d) ZnO spin coating.

The morphology of sand blasted glass substrate (Fig. 4.13a) and ZnO coatings are illustrated in Fig. 4.13. The sand blasted glass was coated with a metal coating (few nanometers of Pt by PVD), in order to make the sample electrically conductive and detectable by the electron microscope. As it can be seen for zinc oxide, different techniques produce different morphologies. The spray coating has a branched structure (Fig. 4.13c), while spin (Fig. 4.13d) and ALD (Fig. 4.13b) coatings cover most of the irregular surface. The XPS analysis on ZnO coated CNTs confirmed that in each method ZnO was deposited. The ZnO concentrations of each method are listed in Table 4.10. The CNP/ZnO raw refer to the experiments with buckypaper coated with ZnO.

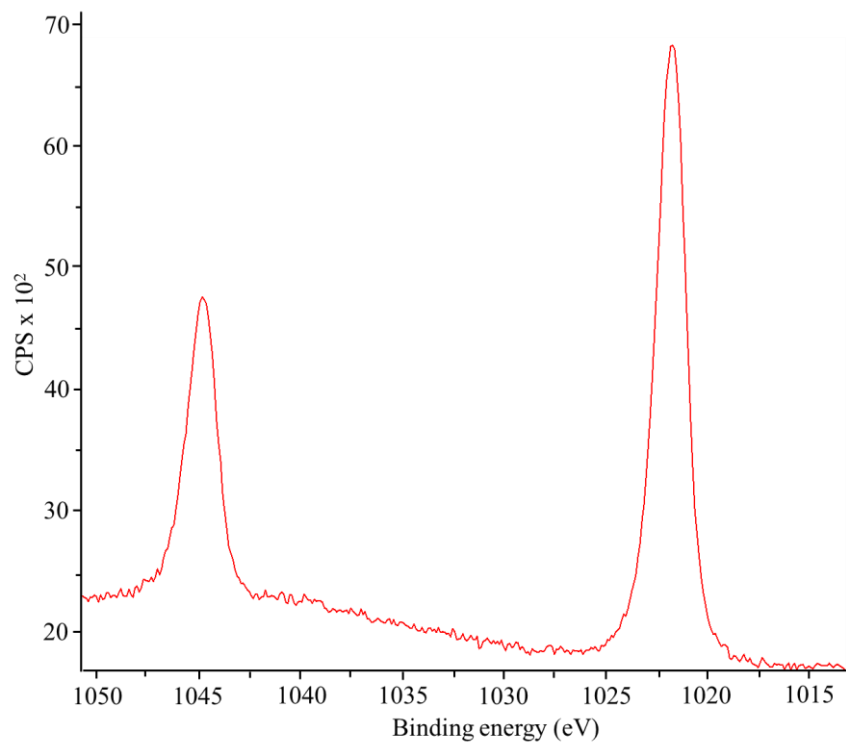
Table 4.10 - Quantitative results from XPS scans of ZnO coatings

ZnO coating	Zn (at%)
Spin	3.6
Spray	23.2
ALD	28.9
CNP/ZnO	0.6

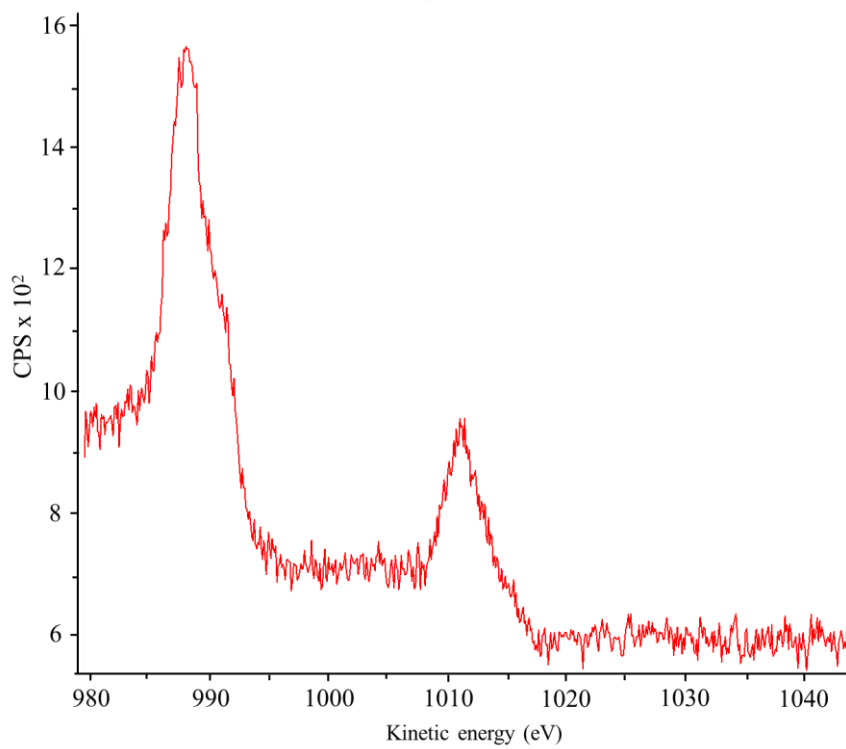
The Zn signal analysis confirmed the presence of the oxide phase. The Zn 2p orbital and Zn Auger peaks are shown in (Fig. 4.14). The Auger parameter was used to confirm the oxide status of Zn coating. In Zn 2p orbital scan (Fig. 4.14a) the 1021.6 eV peak is consistent with metallic or oxide Zn states, which overlap in binding energy. To assign this correctly, the Auger parameter should be calculated. The Zn Auger parameter (2010.4 eV, Table 4.11) has been obtained by adding the binding energy of the Zn 2p orbital (1021.6 eV, Fig. 4.14a) and the kinetic energy of the Zn Auger peak (988.8 eV, Fig. 4.14b). The parameter value is consistent with the ZnO. Further evidence is the FWHM (Full Width at Half Maximum) of the Zn 2p peak (1021.6 eV) which is 1.8 eV [165, 166]. This value is consistent with published values and broader than the metallic peak (~1 eV FWHM) [167]. This interpretation applies to all the samples.

Table 4.11 - Zn signals and Auger parameter from XPS scan

Signal	Type of energy	Energy (eV)
Zn 2p electron	Binding	1021.6
Zn Auger electron	Kinetic	988.8
Zn Auger parameter	Binding + kinetic	2010.4



a)



b)

Fig. 4.14 - XPS result for CNT spin coated with ZnO: a) Zn 2p orbital scan; b) Zn Auger peaks

Fig. 4.15 shows SEM images of CNTs coatings to be compared to the ZnO coated CNTs. SEM images of Untreated CNTs ZnO covered with spin coating technique are shown in Fig. 4.16a and Fig. 4.16b. It is noticed that all the nanotubes are covered by ZnO layer. A hypothesis is that spin coating is not as homogenous (through thickness direction) as the ALD. This could be the cause of the ineffective reduction of the electrical sheet resistance of spin coated CNTs (Table 4.9). Due to technical limits, spin coating is used just for small surfaces. The proper composition of ZnO precursor solution and/or spin coatings parameters should be studied to obtain a more homogeneous ZnO coating. The homogeneous distribution of the ZnO should lead to better improvements of the electrical conductivity.

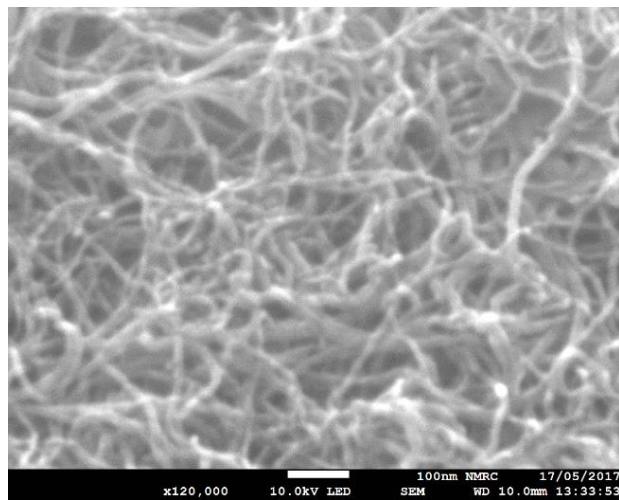


Fig. 4.15 - SEM images of carbon nanotubes: 1st-MWCNT

SEM images of Untreated CNTs ZnO covered with spray coating technique are shown in Fig. 4.16c and Fig. 4.16d. It can be noticed that the superficial morphology of the sample is the same as the pure ZnO sample pictured in Fig. 4.13. It could be hypothesized that the oxide layer completely covered the nanotubes coating. Because of the relatively high ZnO resistance, the CNTs web conductivity decreased (Table 4.9). Further studies should be performed to find the proper ZnO precursor composition and/or parameters for the spray technique. The coating should be able to

cover the nanotubes following the CNT coating web morphology. The improved morphology should help to improve the electrical characteristics of the CNTs coatings.

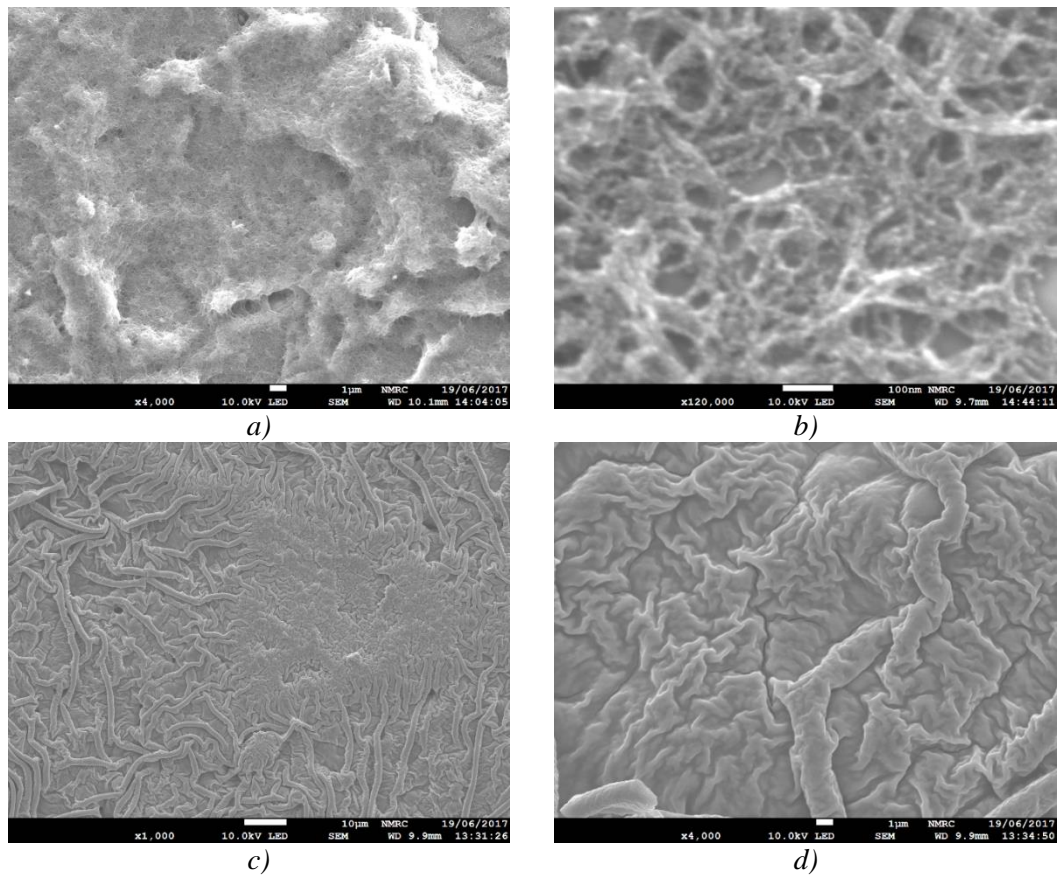


Fig. 4.16 - SEM images of Untreated CNTs sprayed using 90 ml suspension: a) ZnO spin coated, x4000; b) ZnO spin coated, x120000; c) ZnO sprayed coating, x1000; d) ZnO sprayed coating, x4000

SEM images of Untreated CNTs ZnO coated with ALD technique are shown in Fig. 4.17. It is observed that zinc oxide completely cover the surface of the sample, following the morphology of the nanotubes coating. The high vacuum condition and the small amount of precursors injected in the reacting chamber allowed the formation of the coating around the carbon nanotubes. Each nanotube and their junction areas were covered by zinc oxide. This is a fundamental step to understand the electrical sheet resistance results (Table 4.9). The homogeneous morphology of the ZnO coating caused the highest reduction in electrical sheet resistance.

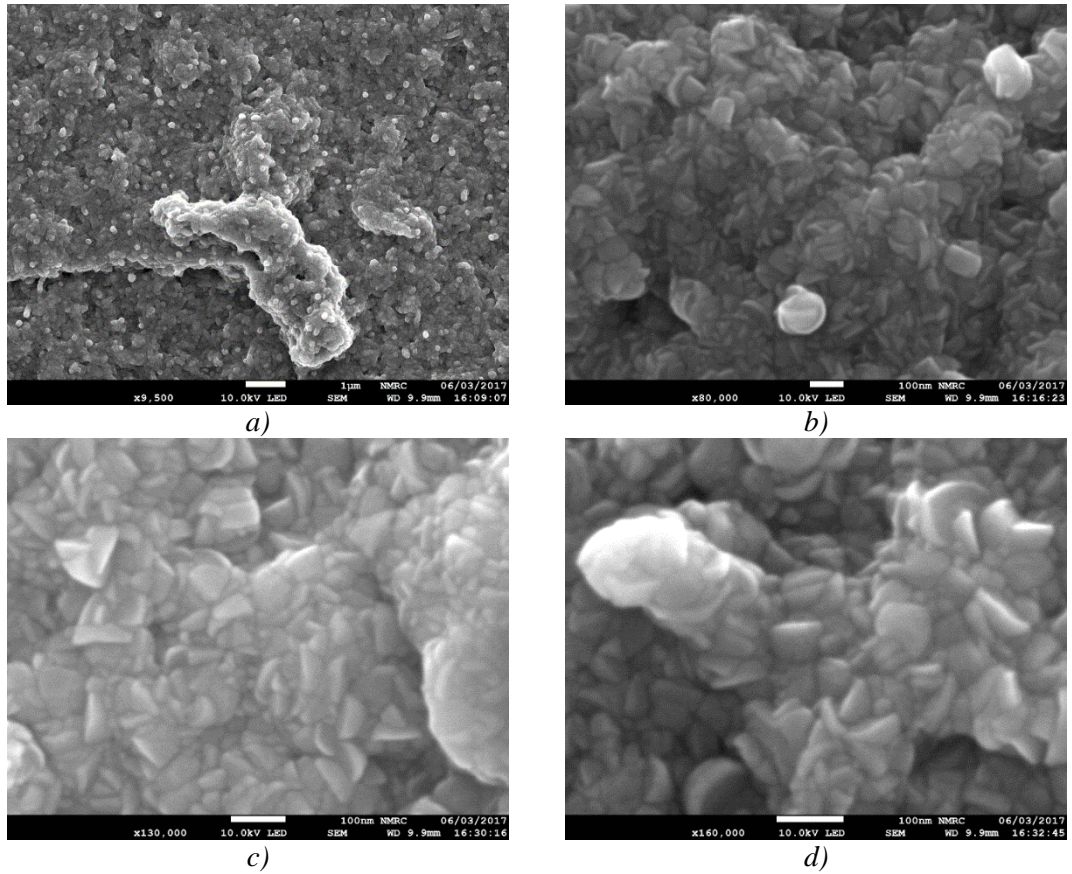


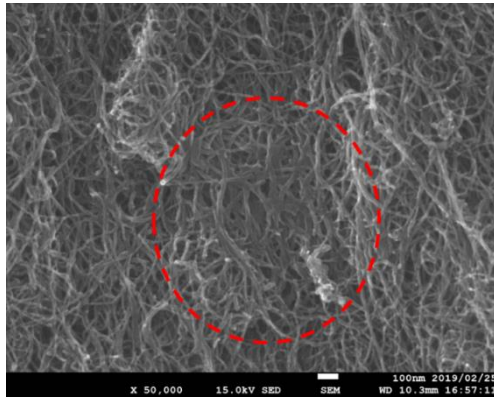
Fig. 4.17 - SEM images of Untreated CNT, ZnO coated with ALD technique, sprayed using 90 ml suspension: a) x9500; b) x80000; c) x130000; d) x160000

4.2.2 Results for ZnO coated CNP

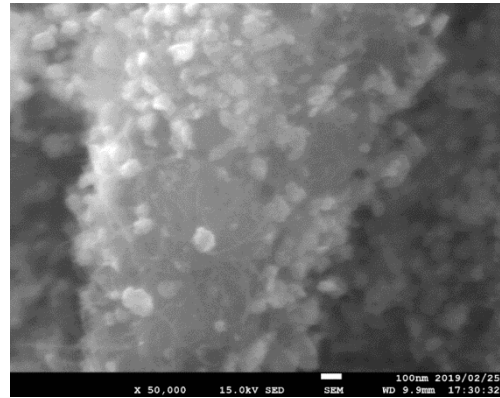
The electrical sheet resistance results of ALD samples confirmed that ZnO can work as jointing agent. Further experiments have been carried out and MWCNT buckypapers have been coated with ZnO following the procedure in section 3.4.4.



a)



b)



c)

Fig. 4.18 - Example of cracked CNP coated with ZnO (a) and SEM images of ZnO coated CNP: b) the red dotted circle highlights an area in which ZnO coated the nanotubes; c) CNT bundle coated by ZnO

Fig. 4.18a shows an example of ZnO coated CNP. The ZnO coating caused the embrittlement of the CNP. The coated CNP broke during the electrical resistance measurements. The ZnO coating is not evenly distributed on the CNP surface. The ZnO coating showed different morphologies. The oxide could have covered the single nanotube and the junction point with another nanotube, as illustrated in Fig. 4.18b. Otherwise the oxide could have covered the whole CNT bundles, as illustrated in Fig. 4.18c.

The irregular distribution of the ZnO coated spots could have caused the weakening of the CNP. The uneven distribution of the ZnO coating could be the reason of the

CNP breaking (Fig. 4.19). Despite the electrical sheet resistance reduction for ALD coatings, the results indicated the ineffectiveness of the ZnO in reducing the electrical resistance of the buckypaper. Further work could be done to investigate the best process to use ZnO as jointing agent in CNP. The proper precursor solution should penetrate through the CNP, coating the single CNTs and their junction areas. The obtained coating should lead to a CNP with improved electrical characteristics, without compromising its structural integrity.

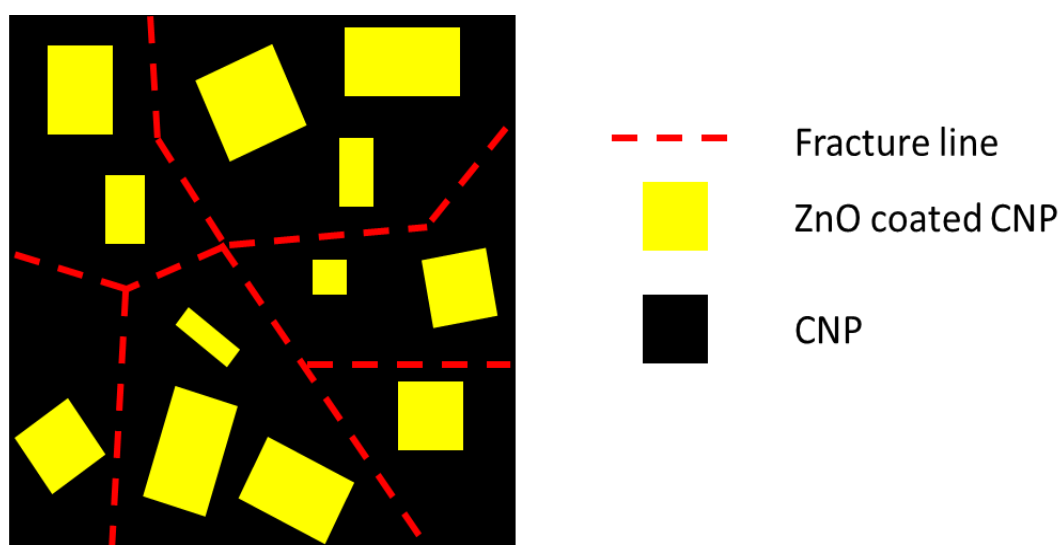


Fig. 4.19 - Schematic representation of uneven ZnO coated CNP

4.3 Summary

To modify the carbon nanotube conductivity, MWCNTs have been acid treated at high temperature with different acid solutions. The treatments containing sulphuric acid caused structure changes of the MWCNTs and ruined the electrical conductivity of the CNT web. The nitric acid treatment at high temperature did not cause obvious deterioration of CNTs characteristics. The nitric acid was selected for room temperature treatments of the carbon nanotubes. The nitric acid treated nanotubes (NA-CNT) were used for buckypaper (CNP) production. The resulting buckypaper (NA-CNP) was around 32% thinner of a CNP layer made with untreated nanotubes

(MWCNP). The electrical resistance of a single MWCNP was approximately 6Ω . Due to NA-CNP reduced thickness, the electrical conductivity of the buckypaper has been improved. During the ice melting test, the NA-CNP reached power density values around 3 kW/m^2 . The ice melting test demonstrated a good potential of NA-CNP as a self-heating element that could be integrated into a composite structure.

ZnO was used as jointing agent to further reduce the electrical resistance of the CNT layer. The ALD method caused the highest reduction in electrical sheet resistance reduction of the CNTs layer. The electrical sheet resistance of sprayed CNTs was around $1.45 \text{ k}\Omega/\text{sq}$, whereas the electrical sheet resistance of ALD coated CNTs was approximately $0.45 \text{ k}\Omega/\text{sq}$. The oxide covered completely the junction area between the nanotubes, causing the electrical sheet resistance reduction (more than 60%).

Chapter 5 Effects of metal decoration and doping agents on CNT network

A further method to improve the electrical conductivity of the carbon nanotubes is by mixing them with high electrical conductive particles. These particles were defined as doping agents. The particles were classified as pre-formed, if they were supplied by industry, and chemically formed, if they were prepared in the laboratory. Several pre-formed doping agents have been used to improve the electrical conductivity of the carbon nanotube buckypaper. The doping agents used were: silver nanowires (AgNWs), silver flakes (Ag), graphene powder (GPH), copper micro-powder (μCu) and copper nano-powder (nCu). The electrical characteristics of the different products have been analysed to determine the best doping agent.

For comparison purposes, silver was chosen as the candidate for the chemically formed particles. Two silver decoration techniques have been used to increase the electrical conductivity of the MWCNTs. The first method used sodium hydroxide (NaOH) as reducing agent, whereas the second was based on Tollen reaction. Silver nanoparticles were synthesized by chemical reduction of Ag cations on the MWCNTs structure (external surface or inner walls). The effect of the silver decorations have been compared and analysed. Microscope images confirmed that silver nanoparticles have been deposited on MWNTs by both silver decoration approaches. The Tollen samples showed an inhomogeneous distribution of silver particles aggregated on the nanotubes, causing the formation of CNTs bundles. For the NaOH based method, the TEM images show that some particles are distributed on the external surface of the nanotubes and others are located in the inner walls of the tube. The Tollen samples

were used for CNP production and the resulting buckypaper cracked. Chemically formed silver particles did not behave as the pre-formed ones.

5.1 Doping using pre-formed nano/micro particles

5.1.1 Graphene and copper as doping agents

The electrical properties of doped buckypaper are listed in Table 5.1, including electrical resistance and its standard deviation, electrical resistivity ρ and electrical conductivity σ . $\Delta\rho$ and $\Delta\sigma$ are the change rate of electrical resistivity and electrical conductivity, respectively, compared with MWCNP reference. MWCNP is the buckypaper made just with untreated multiwall nanotubes.

Table 5.1 - Electrical characteristics of buckypaper doped with graphene and copper (micro and nano) powders

Samples	Resistance (Ω)	Resistance St.dev. (Ω)	ρ ($10^{-3}\Omega\text{ m}$)	$\Delta\rho$ (%)	σ (S/m)	$\Delta\sigma$ (%)
MWCNP	5.5	0.5	0.661	0	1513.2	0
50GPH-CNP	cracked	/	/	/	/	/
10GPH-CNP	7.0	0.1	1.128	70.7	886.2	-41.4
3nCu-CNP	cracked	/	/	/	/	/
9nCu-CNP	9.9	1.9	1.605	142.8	623.1	-58.8
3 μ Cu-CNP	9.4	0.9	1.490	125.4	671.3	-55.6
9 μ Cu-CNP	6.6	1.0	0.848	28.3	1179.1	-22.1

The conductivity of the doped buckypaper were lower than the MWCNP (up to 59%). Graphene and copper (nano and micro) powders were not effective as doping agents. They increased the CNP electrical resistance. 50GPH-CNP (Fig. 5.1a) and 3nCu-CNP (Fig. 5.1b) cracked during the peeling-off process. For both cases, the doping process produced CNPs with low crack resistance. The results can be explained by the morphological analysis of the doped CNP.

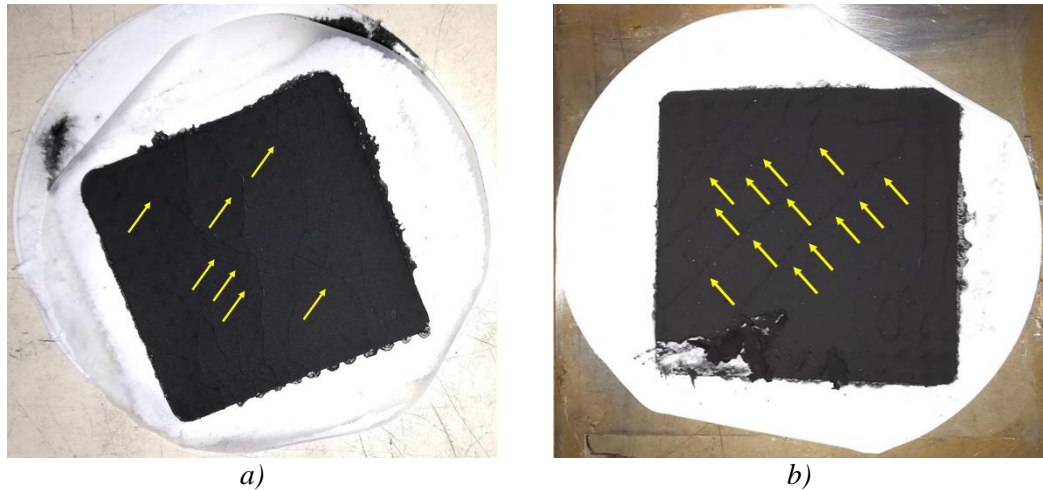


Fig. 5.1 - Pictures of cracked buckypaper doped with: a) graphene (50GPH-CNP); b) copper nano-powder (3nCu-CNP). The yellow arrows highlights the crack on the surface

Fig. 5.2a and Fig. 5.2b show SEM images of 10GPH-CNP. Graphene plates ($\sim 1\mu\text{m}$) are not clearly visible on the CNP surface. The yellow arrows indicate the possible areas where the nanotubes envelope the graphene plates. As it can be noticed from the irregular shape and distribution of the areas, the graphene plates are randomly oriented in the CNP. The nanotubes cover the graphene plates, as illustrated in Fig. 5.2c, causing the irregular morphology of the surface. The conductive path in the 10GPH-CNP is increased by the random orientation of the graphene particles. Furthermore, gaps may be created in the CNP by the random orientation of the graphene plates. The random orientation can cause an interruption in the conductive path and, at the same time, it weakens the CNP. For the 50GPH-CNP samples, a high concentration of the GPH/CNT agglomerates (randomly oriented) is the cause of the weak CNP structure (Fig. 5.1a). Future works could be focused on obtaining a more GPH oriented/aligned configuration to improve the CNP electrical properties, without compromising its integrity.

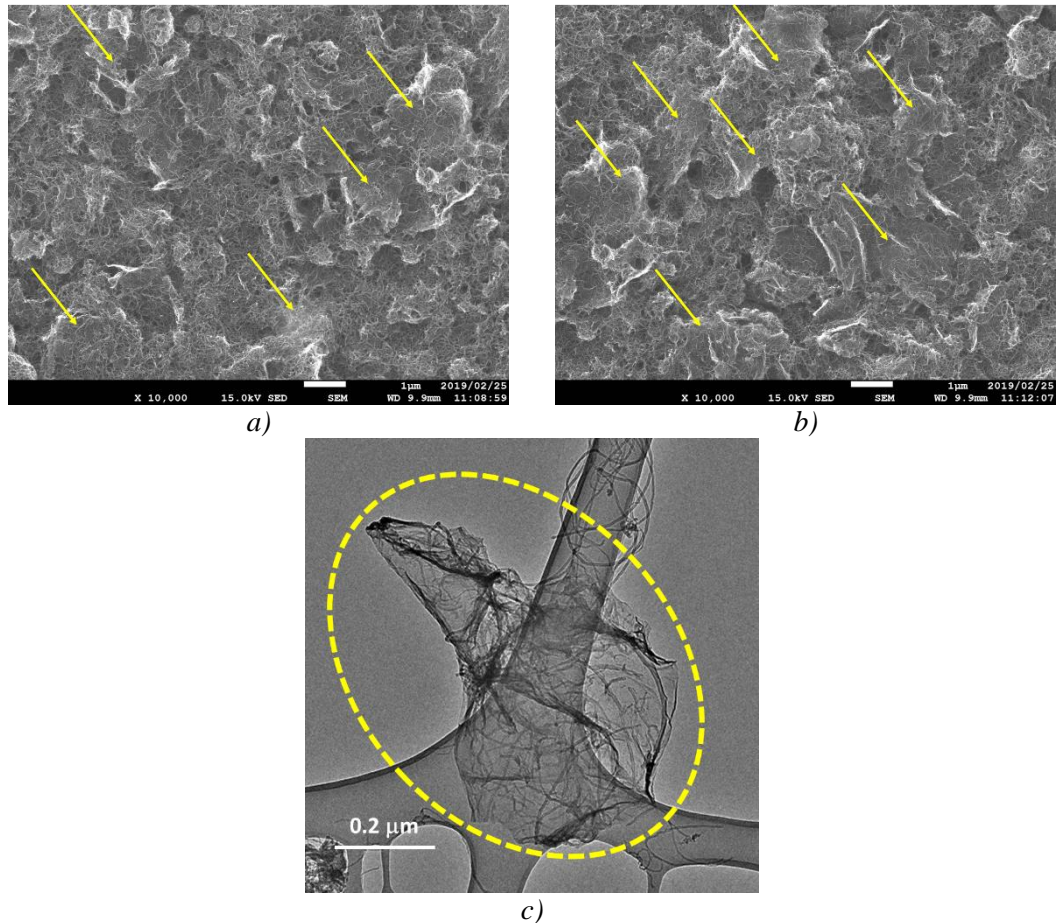


Fig. 5.2 - a, b) SEM images of 10GPH-CNP (x10000). The yellow arrows highlight the possible area of the graphene plates. c) TEM image of graphene plate covered with MWCNTs (highlighted by the yellow dotted circle)

Fig. 5.3 shows SEM images of 9nCu-CNP. The white spots are the Cu nanoparticles which tend to agglomerate together. These Cu agglomerates are surrounded by big amounts of nanotubes and embedded in the CNP surface. The Cu agglomerates reduced the CNT contact causing local increases of the electrical resistance. This agglomerated structures decreased the electrical conductivity of the doped CNP (around 59% less). Furthermore, gaps may be created in the CNP from the Cu/CNT agglomerates. The agglomerate causes an interruption in the conductive path and, at the same time, it weakens the CNP. For the 3nCu-CNP samples, a high concentration of the Cu/CNT agglomerates is the cause of the weak CNP structure (Fig. 5.1b). Further research works could be conducted to obtain a more homogeneous distribution

of the Cu nanoparticles to improve the CNP electrical properties, without compromising its integrity.

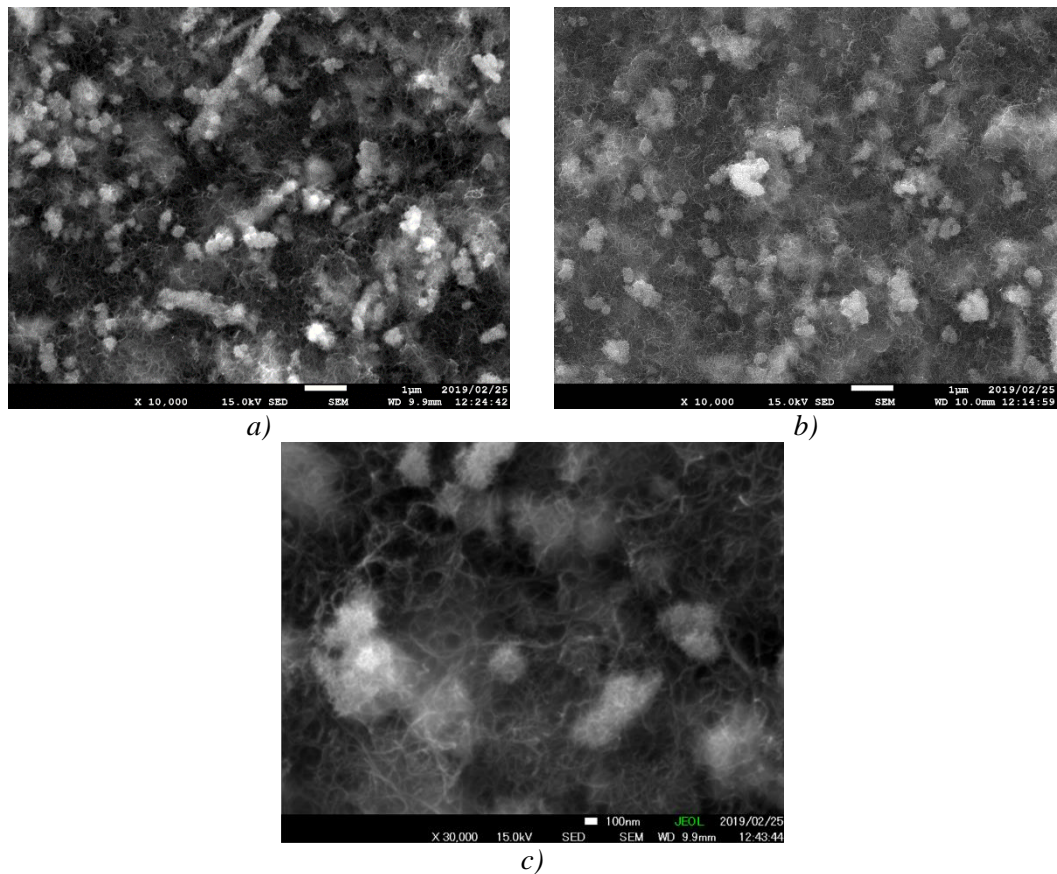


Fig. 5.3 - SEM images of 9nCu-CNP: a, b) x10000; c) x30000

Fig. 5.4 shows SEM images of 9µCu-CNP. The yellow arrows and the yellow dotted circles indicate the copper microparticles. The nanotubes cover the copper microparticles, causing the irregular shape of the surface. To verify any physical changing during the doped CNP fabrication, a small quantity of copper micropowder has been analysed on XPS. Fig 5.5a shows the XPS results for the µCu powder. The Cu main peaks are Cu 2p_{3/2} at ~933 eV and Cu 2p_{1/2} at ~952eV [168]. The shape of the peaks is broad and not sharp, indicating a possible oxidation state of the powder. Moreover a signal around 945 eV, between the two main peaks, appears; research works defined it as a further proof of oxidized copper presence [168, 169]. The

interaction area between the CNTs and the oxidized Cu micropowder caused a local increase of the electrical resistance. The CNP electrical resistance was increased by these high electrical resistance areas. Further research could be carried out to produce a copper doped CNP avoiding the oxidation problem of the copper micropowder.

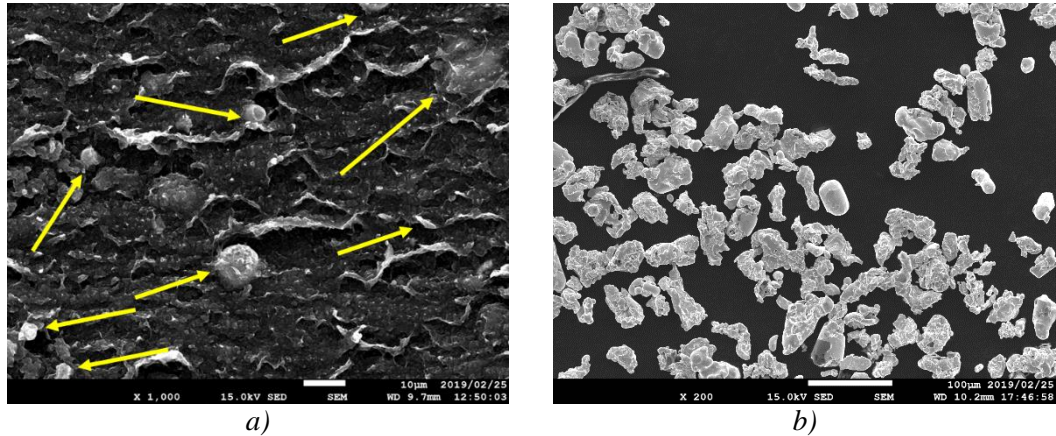


Fig. 5.4 - a) SEM images of $9\mu\text{Cu-CNP}$ (x1000); b) copper micropowder (x250). The yellow arrows and the yellow dotted circles indicate the copper microparticles

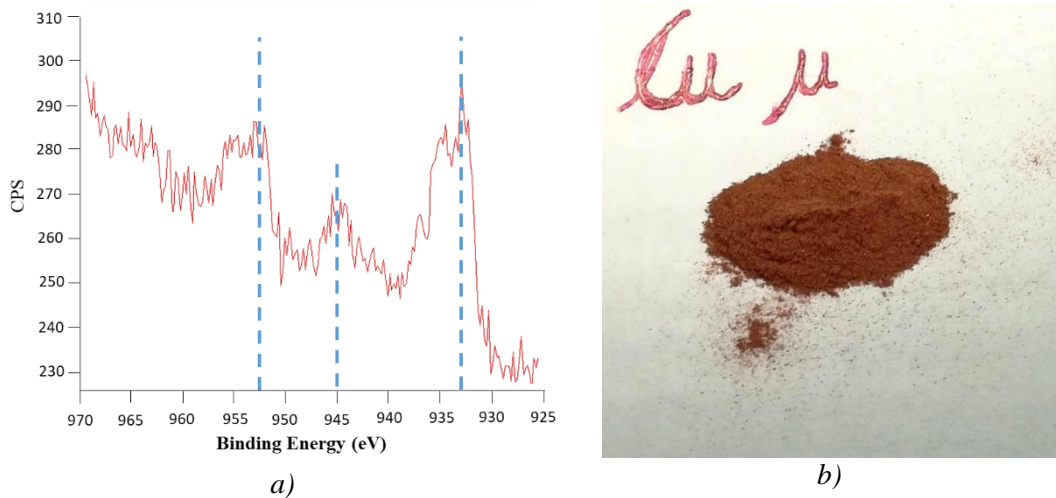


Fig. 5.5 – a) XPS results for μCu powder; b) photo of copper micropowder

5.1.2 Silver particles as doping agents

The different doped CNP electrical resistances are listed in Table 5.2, including thickness and electrical conductivity σ . ΔR , ΔTh , and $\Delta\sigma$ are the change rate of electrical resistance, thickness and electrical conductivity respectively, compared with MWCNP reference. Silver doped buckypapers showed electrical conductivity improvements. Silver nanowires were able to increase the CNP electrical conductivity up to 60%.

Table 5.2 - Electrical characteristics of buckypaper doped with silver flakes and nanowires

Samples	Resistance (Ω)	Resistance St. Dev (Ω)	ΔR (%)	Thickness (mm)	ΔTh (%)	σ (S/m)	$\Delta\sigma$ (%)
MWCNP	5.5	0.5	0.0	0.120	0.0	1513.2	0.0
150Ag-CNP	2.8	0.2	-49.1	0.204	69.8	1750.7	15.7
50Ag-CNP	4.4	0.5	-20.0	0.189	57.3	1202.5	-20.5
20AgNWs-CNP	3.0	0.4	-45.5	0.138	14.9	2415.5	59.6
2AgNWs-CNP	5.3	0.3	-3.6	0.126	4.9	1497.5	-1.0



Fig. 5.6 - Picture of 150Ag-CNP (50 mm x 50 mm)

150Ag-CNP has the lowest electrical resistance (2.8 Ω). Despite the thickness increase (up to 70%), caused by the silver flakes (diameter $>1\mu\text{m}$), there is a 16% increase in electrical conductivity. The Fig. 5.6 shows the silver particles (grey dots) distributed on the doped CNP surface. The cross section image in Fig. 5.7a shows that the particles

are evenly distributed through the whole thickness of the buckypaper. The silver doped-CNPs have been placed in a SEM sample holder in order to have the cross section perpendicular to the electron beam.

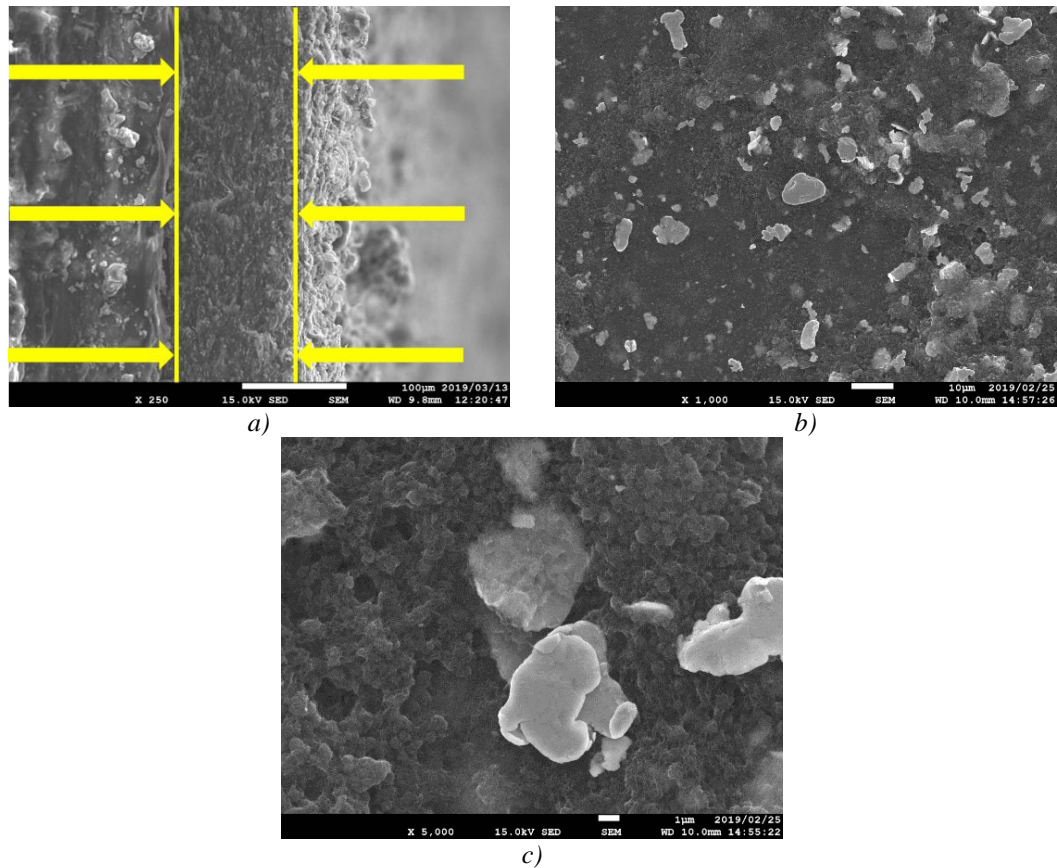


Fig. 5.7 - SEM images of: a) 150Ag-CNP cross section (x250); b, c) 150Ag-CNP surface (x1000, x5000)

Nanowires doped CNP 20AgNWs-CNP show electrical resistance value close to 150Ag-CNP, despite the low silver amount (0.1 g for 20AgNWs-CNP, instead of 0.3 g). Even the nanowires are evenly distributed through the thickness of the doped buckypaper (Fig. 5.8). The stirring and the sonication allowed a homogeneous distribution of the Ag particles in the suspension before the filtration, avoiding accumulation of particles on the surface of the CNP [63]. Better interactions between AgNWs and MWCNTs are the reason of the low amount of silver required to reduce the electrical resistance. 20AgNWs-CNP and 50Ag-CNP have the same amount of silver (with different particles dimensions), however the improvements of electrical

characteristics with AgNWs are better than using Ag flakes. Moreover, nanowires allow a more compact configuration than silver flakes doped CNP; the average thickness of 20AgNWs-CNP samples is lower than 150Ag-CNP samples. The more compact configuration caused an increase of the electrical conductivity up to 60%. The amount of nanowires in 2AgNWs-CNP (0.01 g) is not enough to obtain any relevant improvement. The difference in the nanowires distribution, through the thickness of the doped buckypaper, can be noticed by comparing the cross sections of 20AgNWs-CNP and 2AgNWs-CNP. The content of AgNWs in Fig. 5.8c is obviously lower than it in Fig. 5.8a.

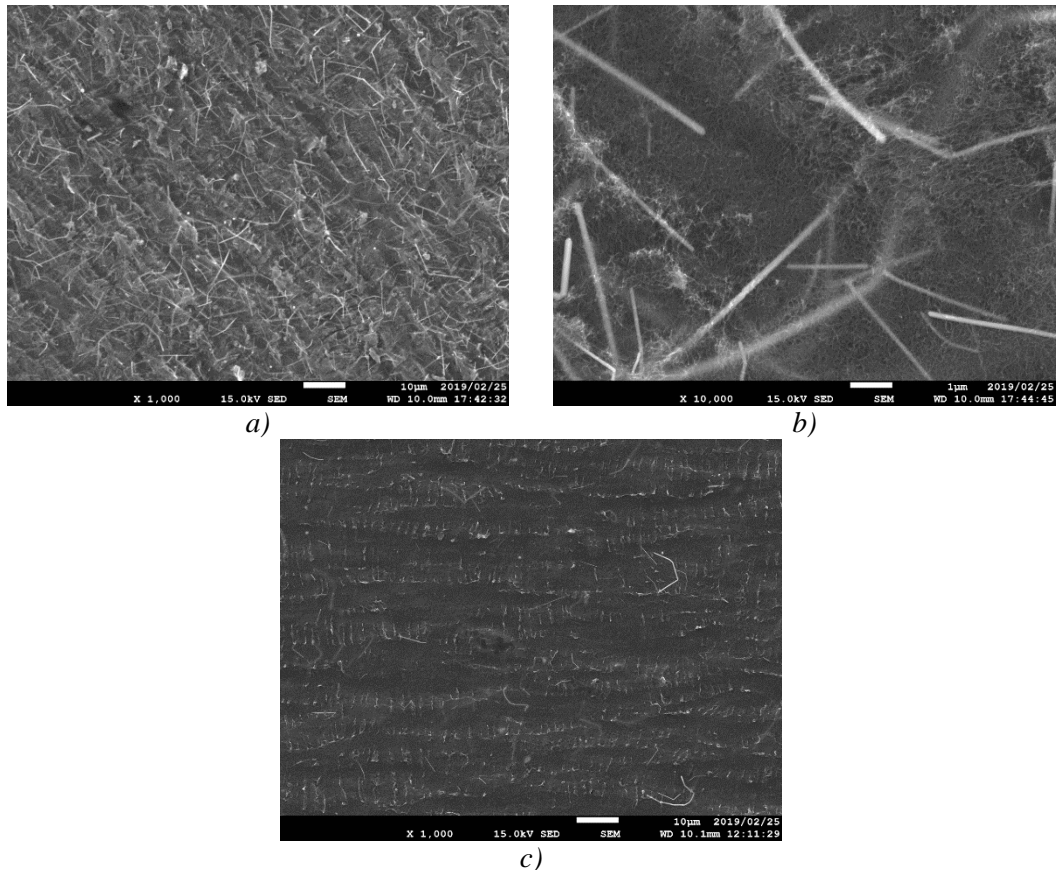


Fig. 5.8 - SEM images (x1000, x10000) of: a, b) 20AgNWs-CNP cross section; c) 2AgNWs-CNP cross section

Superficial roughness of the improved buckypapers has been analysed by 3D laser scanning microscope. MWCNP, NA-CNP, 150Ag-CNP and 20AgNWs-CNP have been analysed. The surface roughness results are listed in Table 5.3.

As already verified from SEM images, surface roughness of NA-CNP is lower than MWCNP one. This confirms the reduced amount of nanotubes aggregates in the NA-CNP, which allows a more compact configuration (reduced paper thickness).

The silver flakes distributed on the CNP surface caused a high superficial roughness. The high deviation standard value indicates an irregular surface for silver flakes doped CNP. About 20AgNWs-CNP, its superficial roughness value is close to that of MWCNP. This could mean that most of the silver nanowires are embedded in the CNP surface.

Table 5.3 – Surface roughness values and their standard deviation

Sample	Superficial roughness (µm)	St. deviation (µm)
MWCNP	0.98	0.18
NA-CNP	0.57	0.05
150Ag-CNP	2.96	0.86
20AgNWs-CNP	0.92	0.10

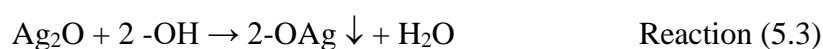
Silver flakes doping result was a CNP with increased electrical conductivity (16% increase). The micron size flakes, covered by MWCNTs, interact with the carbon nanotubes, reducing the electrical resistance of the CNT/Ag web. CNT/Ag agglomerates are distributed through the CNP thickness forming a continuous conductive path, unlike graphene plates, with improved electrical conductivity. The continuous path makes the CNP crack resistant, avoiding its rupture during the peeling-off procedure. The minimum amount of silver nanowires (0.1 g) to improve the CNP electrical resistance (around 46% increase) is lower than the silver flakes

amount (0.3g). Silver nanowires interaction with carbon nanotubes is better than silver flakes. Silver nanowires should be an ideal candidate as doping agent. A combination of acid treated multiwall nanotubes and silver flakes could lead to a cheap buckypaper with optimal electrical characteristics for the integration in electro-thermal composite structure and for ice protection purposes.

5.2 Effect of silver decoration

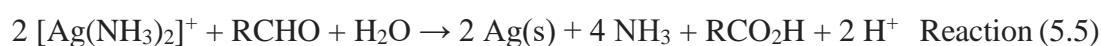
The silver decoration methods are based on two redox reactions that involve different compounds.

Wee et al. [170] explained a mechanism for the sodium hydroxide based method. The carboxyl and hydroxyl groups ($-\text{COOH}$ and $-\text{OH}$), produced by acid treatment on the CNTs surface, act as the nucleation sites. To explain the mechanism, the possible reactions [57, 171] are described below:



Carboxyl and hydroxyl groups together with hydroxyl ions (OH^-) act as the reducing agents in the reduction of Ag^+ to Ag. Silver nitrate interacts with carboxyl and hydroxyl groups, forming $-\text{COOAg}$ or $-\text{COAg}$ groups [172-177]. These groups would act as nucleation sites.

The Tollen method is based on the following reactions:



Aqueous ammonia induces the formation of solid silver oxide (brown precipitate) in the silver nitrate solution. Additional ammonia helps to dissolve the oxide and give a clear solution of diamminesilver complex ($[\text{Ag}(\text{NH}_3)_2]^+$). This Ag-complex oxidizes the aldehyde to a carboxylate ion and is reduced to silver and aqueous ammonia [178-187].

5.2.1 Comparison between magnetic stirring and ultrasound for NaOH method

From XPS data (next section), low concentration of silver was observed for sodium hydroxide based silver decoration. 500 N-Ag and 750 N-Ag CNTs composition sample were prepared using 1h ultrasound (40% of 500 watts, 20 kHz) instead of 2h magnetic stirring. Afterwards X-ray Photoelectron Spectroscopy was carried out to check the differences between the two processes. New samples were called 500 N-US-Ag CNTs and 750 N-US-Ag CNTs respectively. The XPS results show that there are no differences between the silver atomic concentration of 500 N-Ag CNTs (0.14 at%) and 500 N-US-Ag CNTs (0.13 at%). On the contrary a drastic difference is noticed between 750 N-Ag CNTs (0.72 at%) and 750 N-US-Ag CNTs (0.07 at%).

Fig. 5.9 shows the difference between Ag 3d/5 orbital scans of the stirred sample 500 N-Ag CNTs (a) and ultrasonicated 500 N-US-Ag CNTs (b). The latter one shows narrow Ag 3d peaks, suggesting that the silver is in metallic form. The Auger electron signal is not high enough to evaluate the silver form.

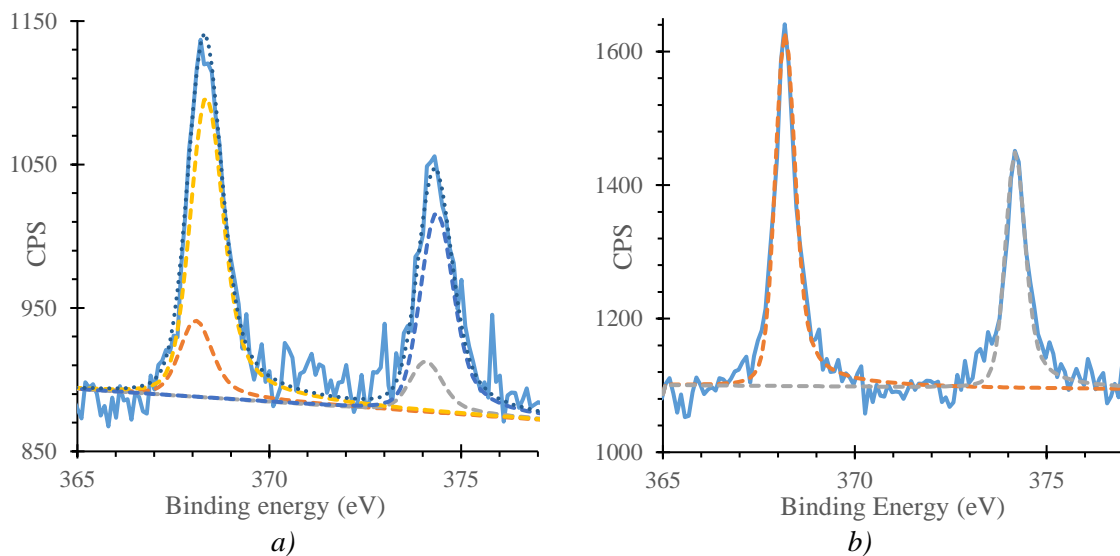


Fig. 5.9 - Comparison between Ag 3d/5 orbital scans of: (a) 500 N-Ag CNTs and (b) 500 N-US-Ag CNTs

Fig. 5.10 shows the difference between Ag 3d/5 orbital scans of stirred sample 750 N-Ag CNTs (a) and ultrasonicated one 750 N-US-Ag CNTs (b). Broader Ag 3d peaks suggest oxidation of the silver in both samples. In 750 N-US-Ag CNTs the atomic concentration of silver (either metallic or oxide) is lower than the stirred sample. Ultrasound, hydroxyl ions concentration and silver ions in the suspension could have promoted the formation of AgOH that prevents the growth of metallic silver [170].

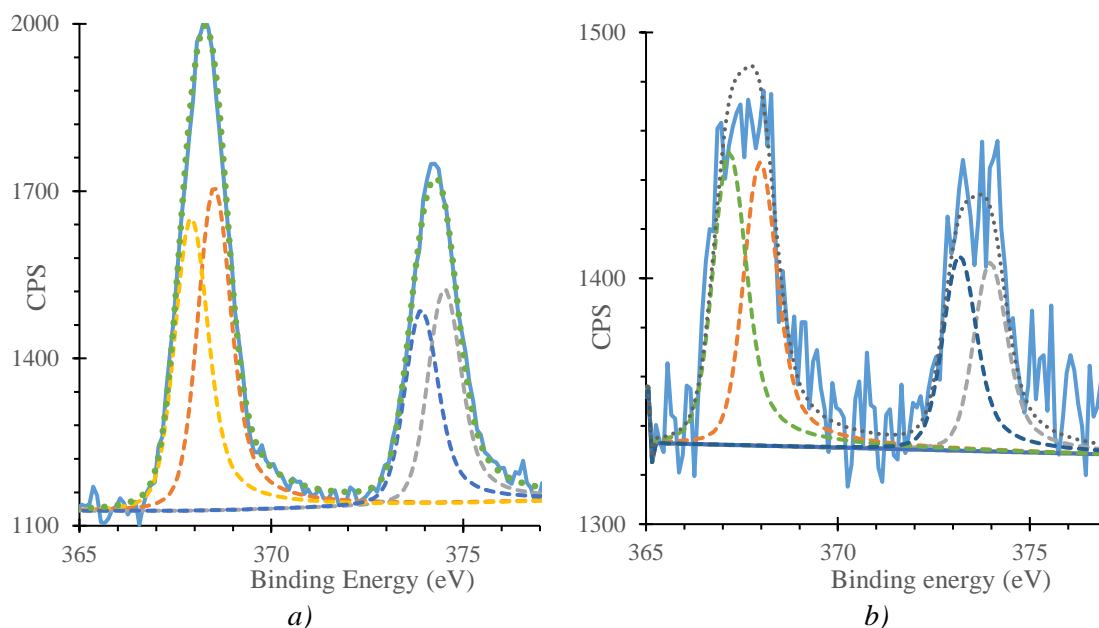


Fig. 5.10 - Comparison between Ag 3d/ 5 orbital scans of: (a) 750 N-Ag CNTs and (b) 750 N-US-Ag CNTs

5.2.2 Silver quantification

XPS was used to quantify the silver produced in each treatment. The results (Table 5.4) are expressed in atomic percentage (at%). Three areas per sample have been analysed in XPS, acquiring a wide scan (Fig. 5.11) at low resolution and high resolution scans for Ag 3d, O 1s, C 1s orbitals and the Ag MNN Auger transitions.

Table 5.4 - XPS results: Ag, C and O atomic percentages of each sample

Sample	Ag at%	C at%	O at%
U-T-CNTs	2.78	95.06	2.15
AT-T-CNTs	5.89	91.22	2.89
250 N-Ag CNTs	0.10	96.14	3.75
500 N-Ag CNTs	0.14	97.00	2.87
750 N-Ag CNTs	0.72	96.29	2.99
1000 N-Ag CNTs	0.44	96.91	2.65

From Table 5.4, there is less Ag in the NaOH treated samples than in the Tollen samples. CNTs treated with 750 μ l NaOH seem to have the highest average value of Ag atomic percentage (at%) of its class. AT-T-CNTs sample has the highest silver

atomic concentration value (5.89 at%), almost double to that of U-T-CNTs sample. This could be explained by reaction (7). The functional groups on the nanotubes surface act as nucleation sites, causing an increase in silver deposition.

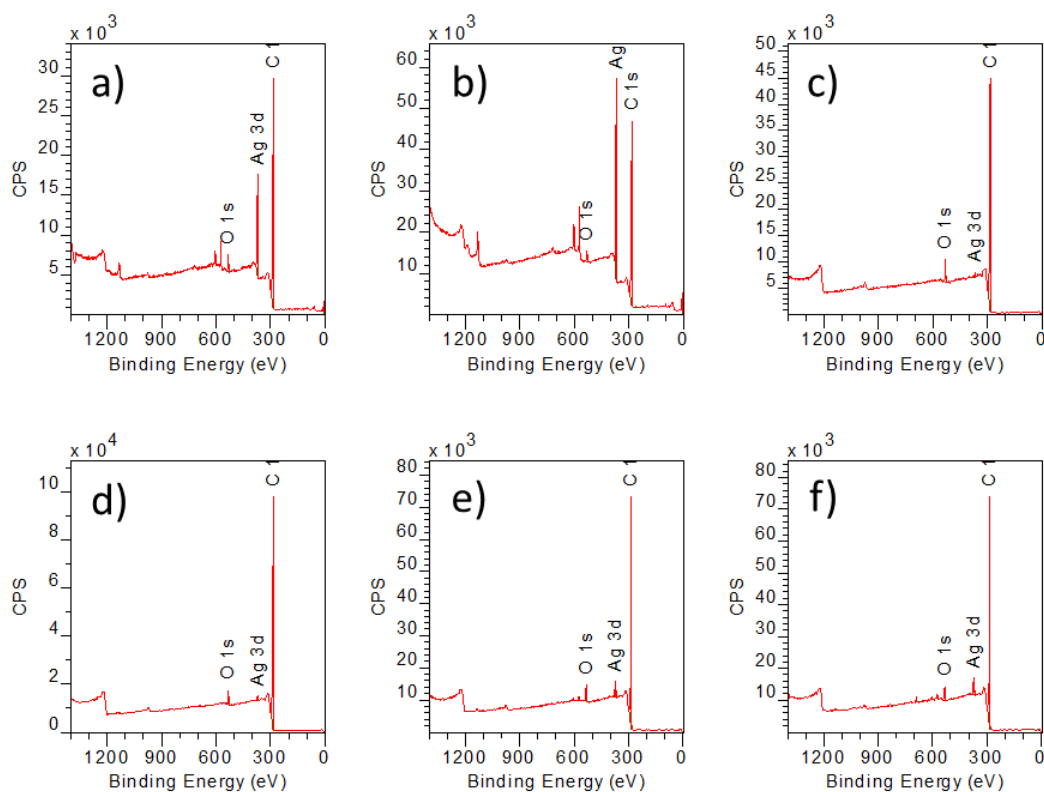


Fig. 5.11 - XPS wide scans of: a) U-T-CNTs; b) AT-T-CNTs; c) 250 N-Ag CNTs; d) 500 N-Ag CNTs; e) 750 N-Ag CNTs; f) 1000 N-Ag CNTs

All samples have a large proportion of carbon (90-97 at%) and there were no major changes to this peak across the samples.

There were trace amounts of oxygen on all samples ranging from 2-4 at%. The peaks (Fig. 5.12) were complex and had at least three components, i.e. three chemical states. The oxygen in CNT is often attributed to OH groups, which is probably consistent with at least one of the O 1s peaks. Oxygen could be derived from atmosphere [188], functional groups attached to the CNTs (e.g. -COOH, -OH) and metal oxide.

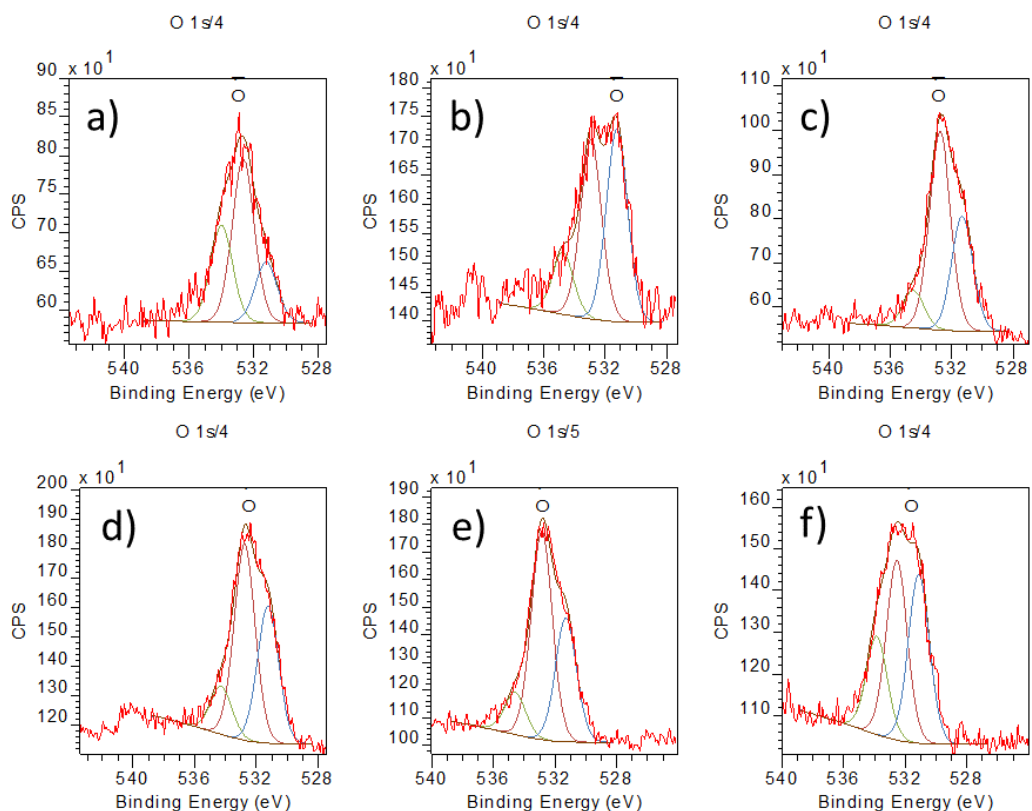


Fig. 5.12 - XPS O 1s/4 orbital scans of: a) U-T-CNTs; b) AT-T-CNTs; c) 250 N-Ag CNTs; d) 500 N-Ag CNTs; e) 750 N-Ag CNTs; f) 1000 N-Ag CNTs

Ag 3d is a doublet, it has an unusual behaviour in XPS as the binding energy does not increase with oxidation state [133]. The peak width, shape and position of the Auger peaks in Fig. 5.13 indicate the reduced oxidation states in some cases. Tollen U and AT samples have high Ag 3d peaks, which are narrow and asymmetrical, suggesting that the silver is in metallic form.

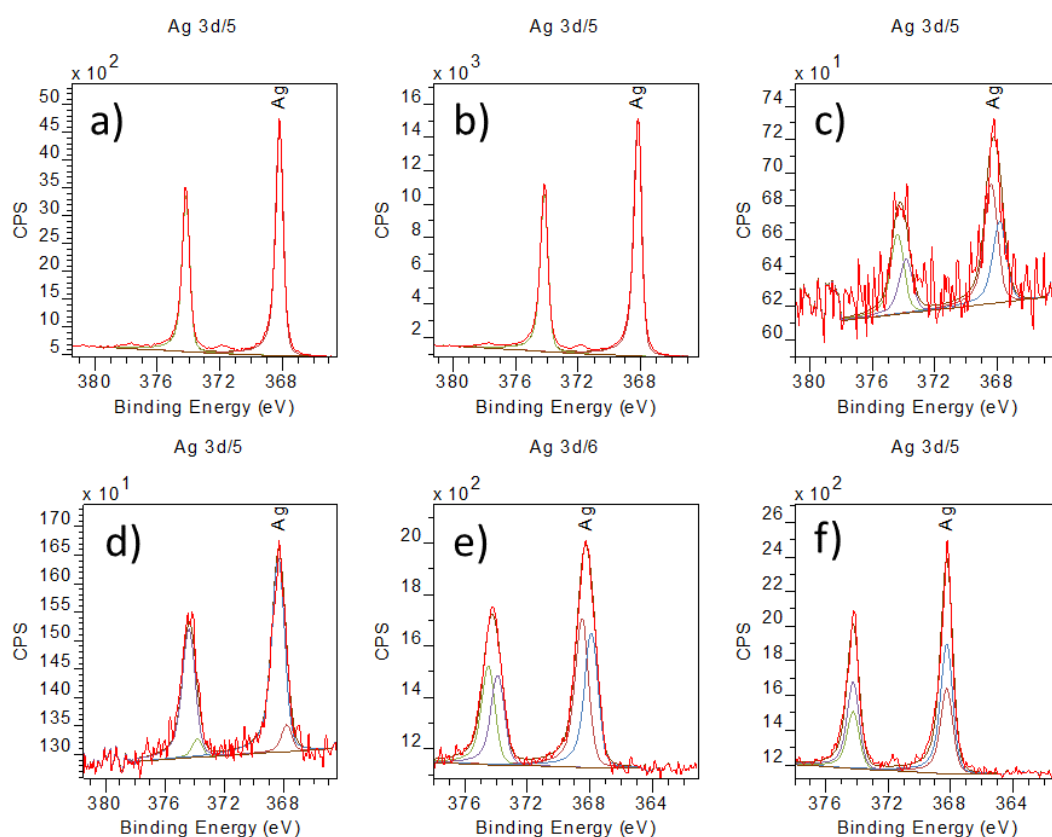


Fig. 5.13 - XPS Ag 3d/5 orbital scans of: a) U-T-CNTs; b) AT-T-CNTs; c) 250 N-Ag CNTs; d) 500 N-Ag CNTs; e) 750 N-Ag CNTs; f) 1000 N-Ag CNTs

For the signal interpretation, the Auger kinetic energy, used later for the Auger parameter evaluation, has been extracted as shown in Fig. 5.14. The concerned peak for both samples is the one labelled by a blue dashed rectangle. The Auger electrons are emitted with kinetic energies dependent only on the electronic state of the element. The Auger parameter was obtained by adding the binding energy of the Ag 3d electrons (368 eV) to the kinetic energy of the Ag Auger electron (358 eV). The Auger parameters (~ 726 eV) listed in Table 5.5, compared with the values in the literature, confirm silver metallic form [133].

Table 5.5 - Ag 3d electron binding energy, Ag Auger electron kinetic energy and Auger parameter of respective U-T-CNTs and AT-T-CNTs samples

Sample	Ag 3d electron Binding energy (eV)	Ag Auger electron Kinetic energy (eV)	Auger Parameter (eV)
U-T-CNTs	368.1	357.9	726.0
AT-T-CNTs	368.1	358.0	726.1

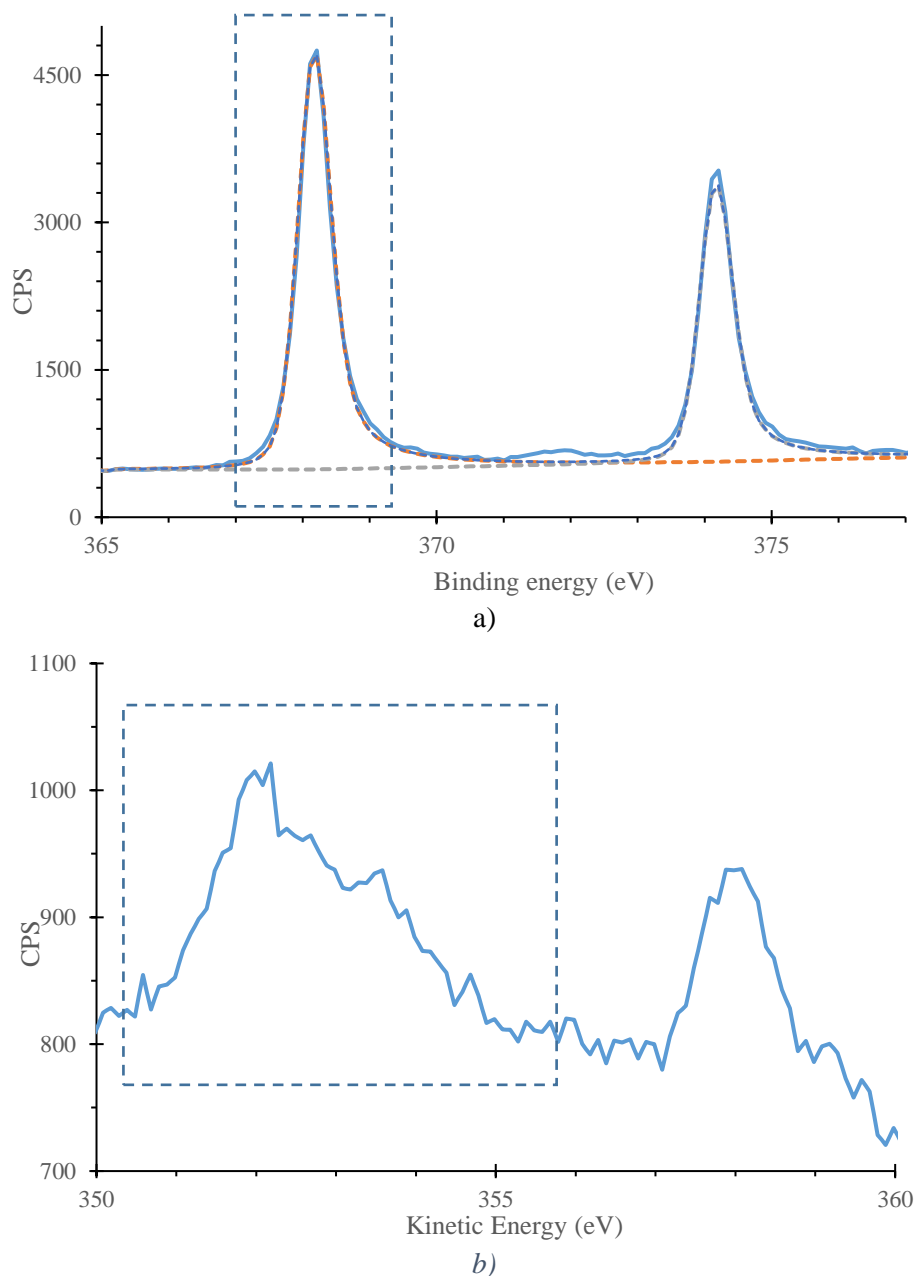


Fig. 5.14 - Example of U-T-CNTs (a) Ag 3d binding energy [eV] and (b) Ag Auger electron kinetic energy [eV]

The NaOH treated samples have much broader Ag 3d peaks suggesting the possible oxidation of the silver. The peak position does not change significantly, indicating Ag₂O or AgO. The Auger peaks for the NaOH treated samples are too small to make any diagnosis between the two chemical states.

5.2.3 Phase analysis and distribution

Further confirmation of metallic silver presence was given by XRD. To detect it the analysis was focused on angles between 33° and 47° with steps of 0.02° . The typical FCC (Face Centred Cubic: $a, b, c = 4.08620$ and $\alpha, \beta, \gamma = 90^\circ$) silver peaks are expected at 38.4° and 44.5° [189]. Both peaks were detected in all the silver decorated samples. An example of one sample XRD pattern is illustrated in Fig. 5.15.

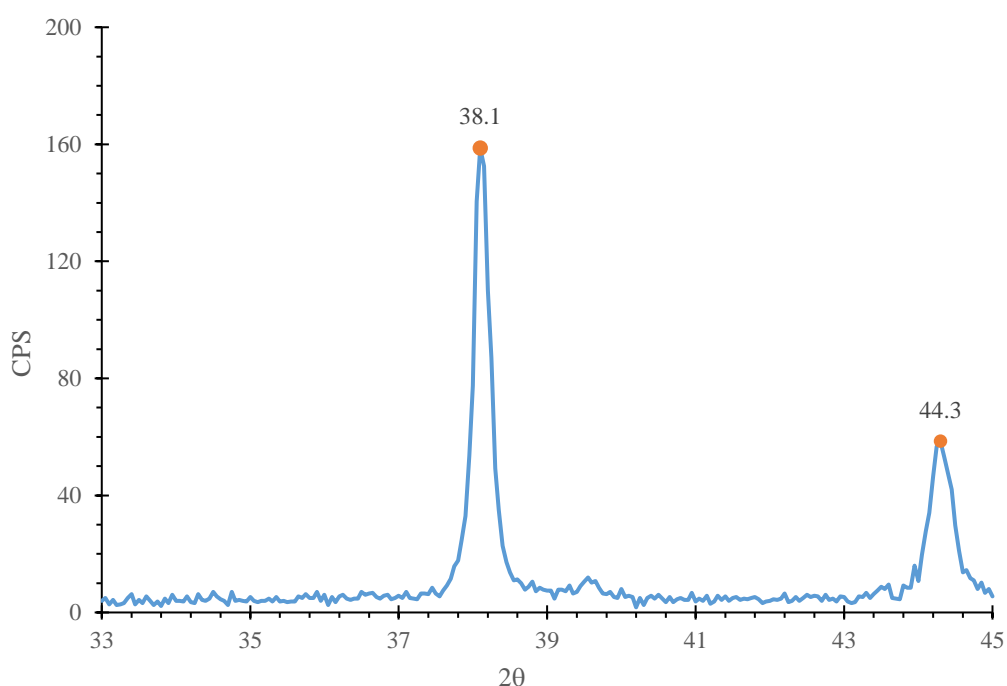


Fig. 5.15 - U-T-CNTs XRD pattern

Fig. 5.16 shows a comparison between two Tollen samples. The acid treated sample has lower intensity at 38.1° , but a small signal at $\sim 36^\circ$ is detected. From DIFFRAC-PLUS database, that signal is assigned to hexagonal silver ($a, b = 2.88620$; $c = 10.0$; $\alpha, \beta = 90^\circ$; $\gamma = 120^\circ$). The different surface conditions of the nanotubes, due to the presence of functional groups, could have caused a different orientation of silver crystals deposited on the surface.

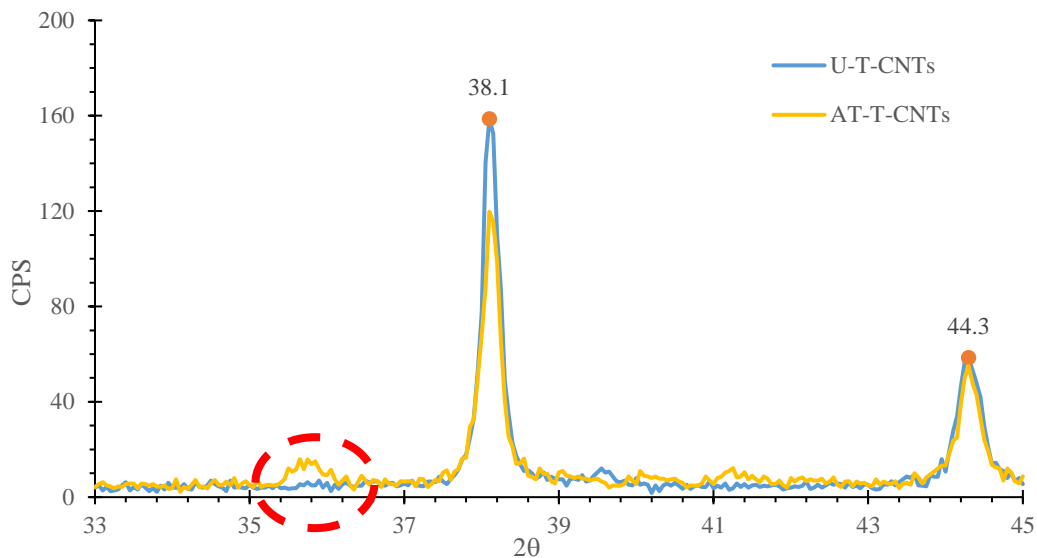


Fig. 5.16 - Comparison between U-T-CNTs and AT-T-CNTs XRD patterns

Fig. 5.17 shows a comparison between U-T-CNTs and 750 N-Ag CNTs. Some major differences between the two patterns can be observed. Tollen samples signal is wider than NaOH samples signal. Tollen reaction developed larger crystals than NaOH method, as confirmed by TEM images. The intensity of the signal is even related to the Ag amount. Tollen samples signal is more intense than NaOH samples signal. XPS analysis confirmed that Tollen reaction produced more Ag than the NaOH method.

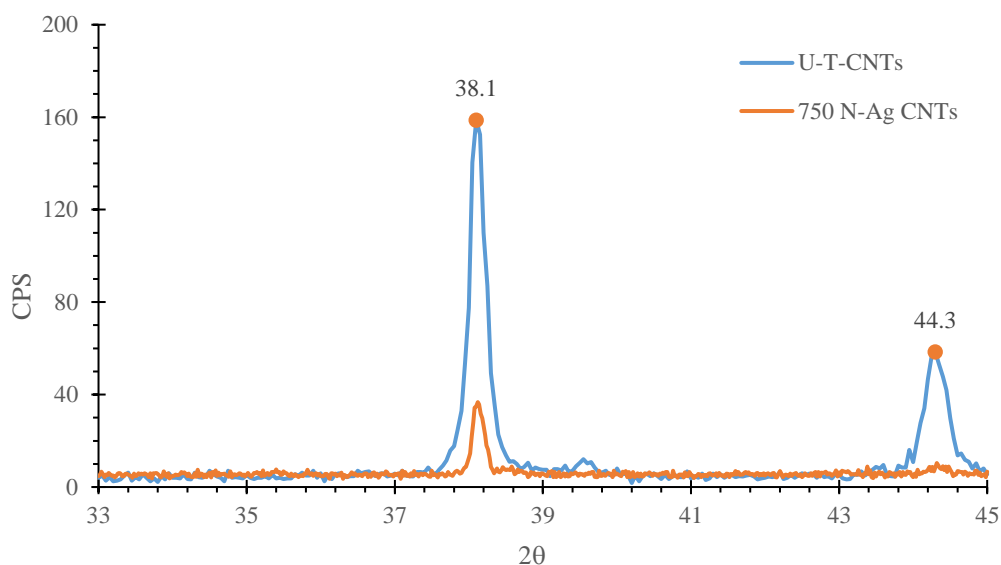


Fig. 5.17 - Comparison between U-T-CNTs and 750 N-Ag CNTs XRD patterns

TEM images show how the silver is distributed on the MWCNTs surfaces. In dark field images, silver particles appear brighter than carbon walls, because the silver atomic weight is higher than carbon atomic weight. As it can be noticed, U-T-CNTs samples images (Fig. 5.18a) show silver particles agglomerate (>100 nm diameters) non-uniformly on the carbon nanotubes surfaces. The agglomerates are too large to be used as “bridge” between each CNTs. These spots could tangle the nanotubes web and increase the electrical resistance of the coating. In AT-T-CNTs (Fig. 5.18b) the agglomerates look smaller than in U-T-CNTs. Small dots in the AT-T-CNTs image (Fig. 5.18b) could be due to silver nucleated in functional groups sites. The sodium hydroxide treated samples show more desirable decoration. The N-Ag samples images (from Fig. 5.18c to Fig. 5.18f) show that most of the silver is deposited in the inner structure/wall of the tube. The silver particles look oriented along the tube inner wall shape. The deposition on the inner walls is caused by the phenomenon defined as “confinement effect” [190-192]. The curvature of CNT walls causes an electric potential difference between the concave inner and the convex outer surface. Because

of this electric potential difference, the inner walls can be used as reaction chambers for the absorbed silver ions.

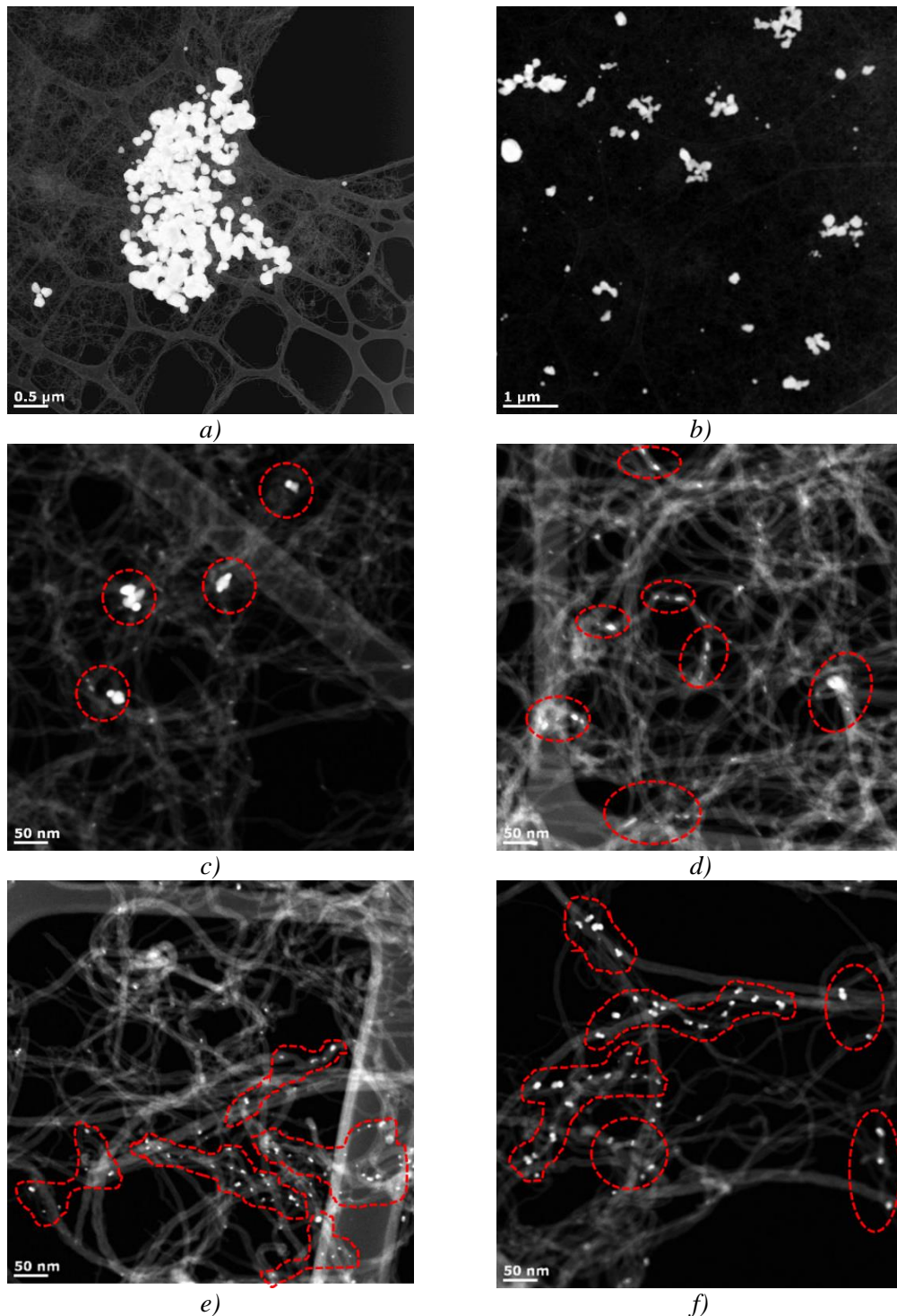


Fig. 5.18 - Dark field TEM images of: a) U-T-CNTs; b) AT-T-CNTs; c) 250 N-Ag CNTs; d) 500 N-Ag CNTs; e) 750 N-Ag CNTs; f) 1000 N-Ag CNTs. The areas delimited by the red dotted line indicate the silver particles

Increasing the amount of NaOH, silver seems to be more homogeneously distributed. Nevertheless, crystals distribution is not enough to form an effective low resistance pathway. Conventional TEM images for NaOH samples (Fig. 5.19) clearly show the presence of a second phase (oxide, light grey colour pointed out by the arrows) attached to the silver metal particle. This explains the broad XPS peaks. Probably the reaction solution was not stirred enough, causing the reaction of the Ag^+ ions with some unreacted OH^- . The Ag^+/OH^- reaction caused the silver oxide/hydroxide formation. The presence of silver oxide could reduce the metal decoration effect (to improve the electrical conductivity) insulating the MWCNTs and increasing the electrical resistance of the network. The sodium hydroxide treated CNTs shows better deposition, however, the amount of produced silver was very low (< 1 at%) and the presence of silver oxide could reduce the effectiveness of the decoration. Therefore, the electrical characteristics of the sodium hydroxide treated CNTs have not been tested. Further work should be conducted to improve the Ag amount produced by NaOH method and to avoid its oxidation.

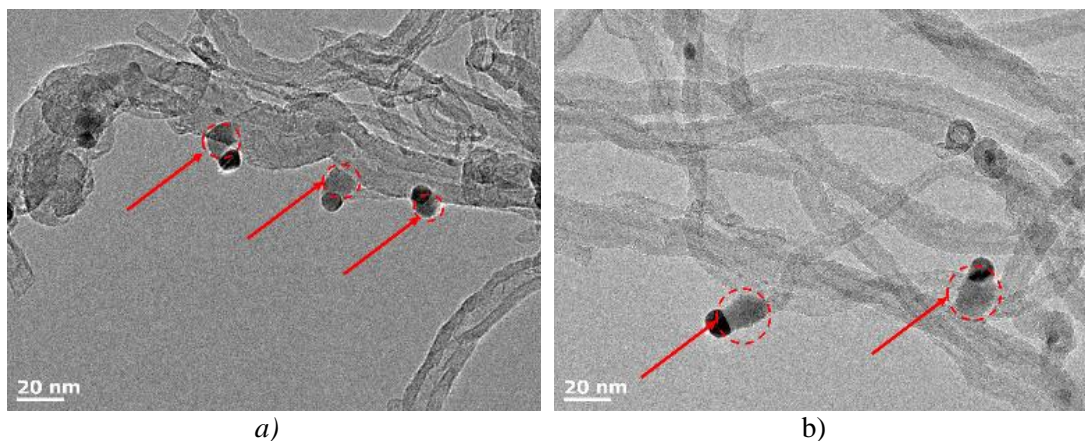


Fig. 5.19 - TEM images of oxidized silver in: a) 250 N-Ag CNTs; b) 1000 N-Ag CNTs

5.2.4 Electrical resistance

The AT-T-CNTs have been chosen as candidate for CNP production, because of their high silver content (XPS results). The resulting film cracked during the peeling off operation. Fig. 5.20 shows an example of cracked buckypaper made of AT-T-CNTs. The silver agglomerates tangled the nanotubes and they weakened the CNT film, causing the buckypaper failure.



Fig. 5.20 - Example of cracked buckypaper made of AT-T-CNTs

The CNP rupture can be explained by observing the SEM images in Fig. 5.21. There are many Ag/MWCNTs irregular agglomerates on the CNP surface. As in the graphene doped CNP, gaps are created by the Ag particles agglomerates in the CNP structure. These gaps interrupt the conductive path of the CNP. The high concentration of the Ag/CNT agglomerates is the cause of the CNP weakening and its low crack resistance. Future works could be focused on improving the Ag particles dispersion to improve the CNP electrical properties and avoiding its rupture.

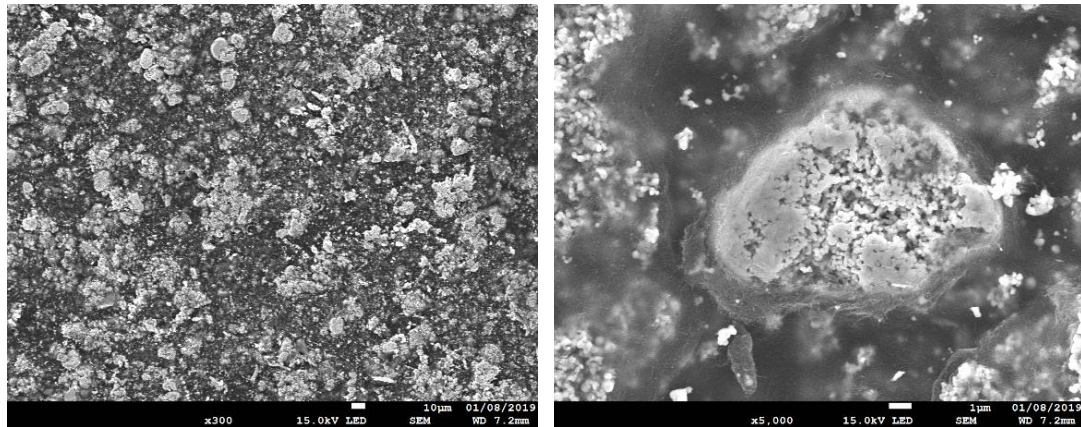


Fig. 5.21 - SEM images at different magnification of CNP made of AT-T-CNTs: a) x300; b) x5000

5.3 Electrical conduction and fracture mechanisms in doped CNP

In Fig 5.22 is illustrated a possible reason why the graphene doped CNP did not show any electrical conductivity improvements. Graphene plates have very low electrical resistance along the surface, as represented in Fig 5.22a. Generally, the resistivity of a material is caused by defects or impurities that scatter the electron while it is moving inside the material.

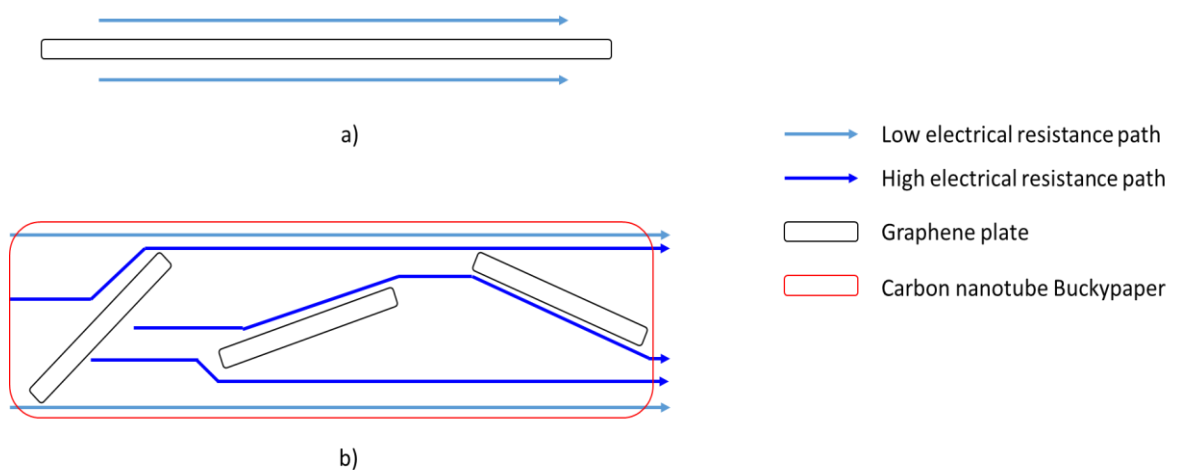


Fig. 5.22 – Schematic representation of electrical conduction in: a) graphene plate; b) graphene doped CNP. The arrows indicate the electrical conductive path with high (dark blue) or low (light blue) electrical resistance

The high electrical conductivity of the graphene plates and carbon nanotubes is due to the ballistic transport/conduction: the transport of electrons in a medium having very low electrical resistivity. In the graphene doped CNP, the random orientation of the GPH plates caused an increase in the electrical resistance of the conductive path. Every time the electron reach the graphene plate, it follows the path with the lowest electrical resistance. To “pass through” the graphene plate would be a high electrical resistance option. A more aligned configuration of the graphene plates would help to improve the electrical conductivity of the CNP doped with graphene. The alignment should follow the desired direction of the current flow. Moreover, Fig. 5.23 illustrates a possible reason of the GPH doped CNP’s crack. The green dotted lines represent low CNTs concentration areas. The areas are located between the graphene plates. In the overlap areas between the graphene plates the CNTs concentration was probably lower than in the other areas. A possible reduction of the CNTs concentration should have created weak points in the CNP structure. A high concentration of randomly oriented graphene plates caused a high number of these low CNTs concentration areas and, as consequence, a low crack resistance.

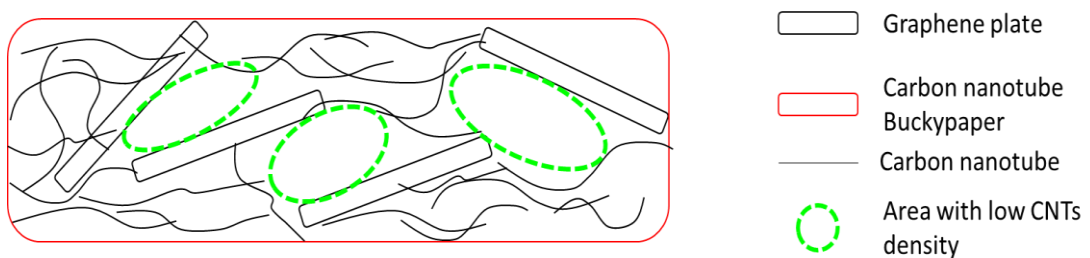


Fig. 5.23 – Schematic representation of graphene doped buckypaper. The green dotted area highlights the low CNTs concentration areas

A schematic representation of Cu nanoparticles agglomerate is shown in Fig 5.24. The blue dotted circles represent the nanoparticles contact area. The lower the contact area is, the higher the electrical resistance becomes in the contact area. The gaps (green

dotted circle) between the Cu nanoparticles further reduce the contact areas, increasing the electrical resistance of the copper agglomerate. For these reasons, the agglomerate become a high electrical resistance spot. The agglomerates were distributed in the CNP structure.

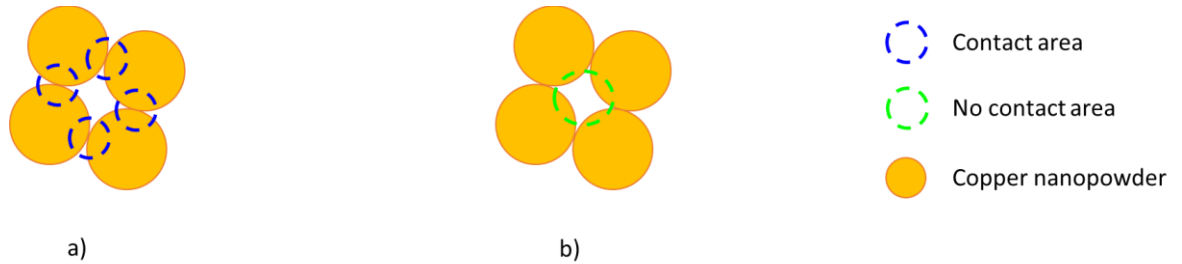


Fig. 5.24 – Schematic representation of copper nanoparticles (orange circles) with highlighted: a) contact area; b) gaps in between

The distribution of these high electrical resistance spots should explain the low electrical conductivity results for the nCu doped CNP. To improve the nCu doped CNP electrical characteristics the Cu nanoparticles should be evenly distributed in CNTs network, avoiding the agglomerates formation. A further problem caused by the nCu agglomerates is illustrated in Fig. 5.25. As for the graphene doped CNP, in the nCu doped CNP the Cu agglomerates probably caused the formation of low CNTs concentration areas. Reducing the number of Cu agglomerates would improve the CNP electrical characteristics without compromising its crack resistance.

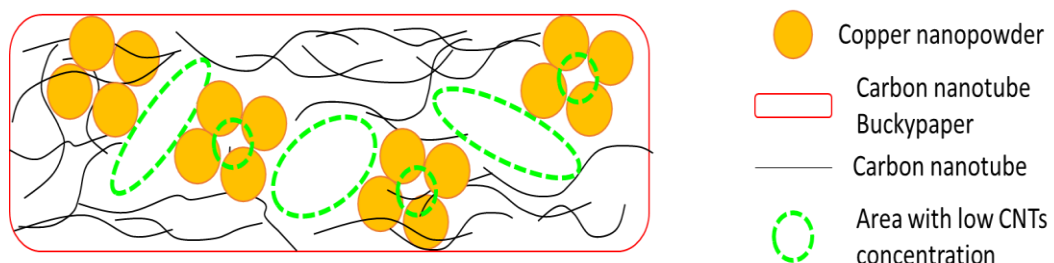


Fig. 5.25 – Schematic representation of nCu doped buckypaper. The green dotted area highlights the low CNTs concentration areas

Fig. 5.26 shows a schematic representation of how the copper microparticles decreased the electrical conductivity of the CNP. As demonstrated by the XPS results, copper micropowder was oxidized. For purely illustrative purpose, it is assumed that the oxidation was only superficial as illustrated in Fig. 5.26. In the μCu doped CNP, the copper particles (orange ellipsis) were covered by the copper oxide (dark red lines). The low electrical conductivity of the oxide did not allow the electrons to pass through the metallic copper particle. The oxide layer acted as a barrier for the electron path. These obstacles represent an increase in the electrical resistance of the CNP. The copper oxide ruined the conductive paths of the doped CNP.

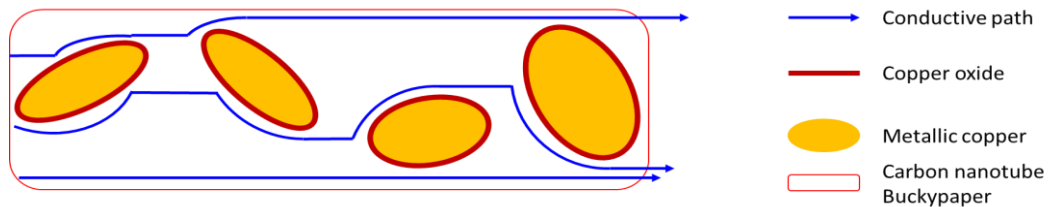


Fig. 5.26 – Schematic representation of electrical conduction in μCu doped CNP. The blue arrows indicate the electrical conductive path

Fig. 5.27 shows the schematic representation of current conduction in Ag flakes doped CNP. Silver electrical conductivity ($\sim 6 \times 10^7 \text{ S/m}$) is higher than the CNTs one (up to 10^7 S/m) [141]. Unlike the oxidized copper particles, the silver flakes did not represent a barrier for the electron path. Their presence helped to reduce the electrical resistance of the doped CNP, because of their high electrical conductivity. The interaction between the CNTs and the silver flakes created a high electrical conductive path, reducing the CNP electrical resistance.

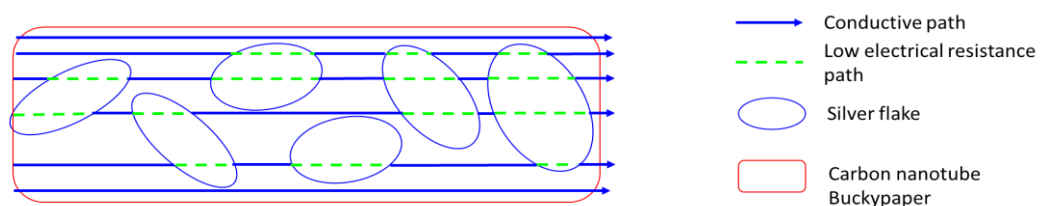


Fig. 5.27 – Schematic representation of current conduction in silver flakes doped CNP

As for the silver flakes, AgNWs behaved similarly. The large contact surface between CNTs and AgNWs allowed a better interaction and a reduction of the contact electrical resistance. The contact electrical resistance (R) is inversely proportional to the contact surface (S): $R \propto 1/S$ [193]. The larger the contact area, the lower the contact electrical resistance becomes in the contact area. Because of the reduced contact electrical resistance, the interaction between AgNWs and CNTs (Fig. 5.28) created a highly electrical conductive path, which reduced the CNP electrical resistance. 0.3 g of silver flakes reduced the CNP electrical resistance from 6 Ω to 3 Ω . The low electrical resistance interaction between AgNWs/CNTs reduced the amount of silver necessary (0.1 g) to obtain the same result. The amount of AgNWs indicates that the interface between AgNWs and CNTs has a lower electrical resistance than the interface between Ag flakes and CNTs. The lower the electrical resistance at the interface is, the lower the amount of needed Ag particles becomes.

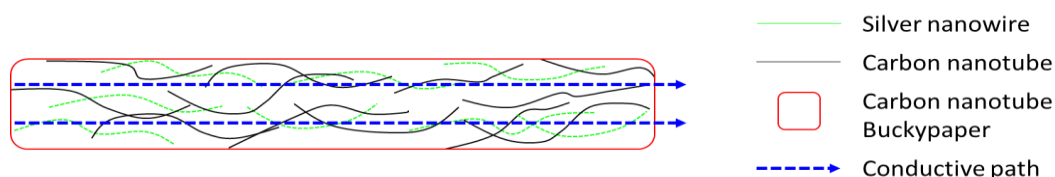


Fig. 5.28 – Schematic representation of contact between AgNWs and CNTs

5.4 Summary

Two silver decoration analysis confirmed that silver nanoparticles have been deposited on MWCNTs by both approaches. The silver particles in Tollen samples had inhomogeneous distribution and they formed agglomerates with CNTs bundles. The Ag particles generated by NaOH reaction were visible on the external surface of the nanotubes and in the inner walls of the tube. The formed silver particles in NaOH based samples had an even distribution, but the Ag amount was low and not just in

metallic phase. The U-T-CNTs had the highest electrical resistance, probably caused by the formation of Ag/CNT agglomerates with high electrical resistance. The more compact configuration of NA-T-CNTs samples caused an increase of the electrical conductivity. Buckypapers were produced with NA-T-CNTs. The high concentration of the Ag/CNT agglomerates was the cause of the CNP weakening and its rupture.

Different doping agents were used to improve the electrical characteristics of the CNP. The doping agents experiments showed different results. In GPH doped CNP, the conductive path was altered by the random orientation of the GPH/CNT agglomerates, causing no electrical conductivity improvements. The high concentration of the GPH/CNT agglomerates was the cause of the CNP weakening and its low crack resistance. For μ -Cu doped CNP, the oxidized powder increased the CNP electrical resistivity (around 125% more). The CNP electrical conductivity was decreased by these high electrical resistance particles. In n-Cu doped CNP, CNT/Cu agglomerates reduced the electrical conductivity of the CNP (around 59% less). The high concentration of these agglomerates caused the 3nCu-CNP weakening and rupture.

The silver-based particles (silver flakes and silver nanowires) were more effective as doping agents. The Ag flakes interacted with the carbon nanotubes, reducing the CNP electrical resistance. Silver flakes doped CNP had higher electrical conductivity than the MWCNP (around 16% more). The electrical resistances of 150Ag-CNP and 20AgNWs-CNP were around 3 Ω . The silver nanowires amount was 0.1 g in 20AgNWs-CNP, while in 150Ag-CNP the silver particles amount was 0.3 g. Compared to 150Ag-CNP, 20AgNWs-CNP obtained a similar electrical resistance value, but with a lower amount of silver particles. The better interaction between AgNWs and CNTs caused a reduction in the necessary amount of silver particles to reduce the electrical resistance.

Chapter 6 Analysis of self-heating composites characteristics

Electro-thermal de-icing constructions are frequently required in the aerospace sector, to prevent ice accumulation and to remove the ice from aircraft surfaces during the flight. Typically an electro-thermal structure consists of a metallic element/circuit, which is normally complicated patterned and heavy, and an inorganic insulator (thermosetting resin) [6, 11]. Incorporating a traditional metal foil heater technology within a composite construction may lead to a weak layer, especially for inter-laminar shear loads [7]. There has been some recent progress on the fabrication of self-heating composites based on carbon nanotubes for electro-thermal de-icing applications [69, 71, 72, 194]. A thin layer of carbon nanotube buckypaper could be placed between glass fibre fabrics, then be infiltrated with a thermosetting resin and underwent curing treatments. The formed composites exhibited excellent electrical heating performance and stability. However, the simultaneous influence of the conducting CNT buckypaper on the mechanical properties of the composites has yet to be studied. Due to static and dynamic loads suffered by the composite parts during the flight, it is essential to have better understanding of the mechanical behaviours of CNP-based electro-thermal composite structures.

In this work, carbon nanotube buckypapers embedded in fibre reinforced polymer composites have been fabricated by two processing routes and the related electro-thermal and mechanical properties were investigated. CNP layers were laid up together with pre-preg fabrics. The characteristics of the treated buckypapers (made with treated MWCNTs) have been compared to the untreated buckypaper (made with untreated MWCNTs). The buckypapers with the best electrical characteristics have been used in the production of the self-heating nanocomposite. Among all the treated buckypaper, silver doped CNP and NA-CNP showed improved electrical

characteristics. NA-CNP has been chosen as candidate for the composite experiments. MWCNP based self-heating composite were used as reference. All the CNP were made of the second batch MWCNTs. For the fabrication of an integrated composite structure using self-heating CNT buckypaper, two different methods were used, involving different thermosetting resins (Resin impregnation Method and Pre-preg Method). Morphology and electrical characteristics have been evaluated to indicate the most appropriate method for self-heating nanocomposite production. CNP-composite heating performance has been evaluated by de-icing test in a cold environment. In the literature, the mechanical properties of the ice protection system based on nanocomposite materials have not been studied yet. In this work three-point flexural strength, interlaminar shear strength (ILSS) and dynamic mechanical analysis (DMA) have been executed to analyse the properties of the produced samples and to further increase the knowledge on self-heating nanocomposites. The overall results indicated the samples produced by resin impregnation method are promising candidates as self-heating composites for ice protection system applications.

In the recent research works the super-hydrophobic surfaces [195-199] have been studied as anti-icing coatings. Zheng et al. [199] fabricated micro-nanostructured super-hydrophobic surface capable of delaying the icing time and temperature. Super-hydrophobic coatings have the ability to delay ice nucleation, reduce ice adhesion, repel water droplets [200] and reduce the energy consumption in traditional electric heating anti-icing systems [201]. The super-hydrophobic coatings alone are not capable of achieving complete anti-icing effects in severe icing conditions. It is promising to combine them with an electro-thermal anti-icing method to melt ice, thus promoting the effect of anti-icing and improving the energy efficiency of the self-heating composite. Further experiments have been carried out with a new generation

resin known as Silikopon EF (Evonik Industries AG). The hybrid silicone-epoxide resin displays promising anti-icing properties. In the ice adhesion test, the EF resin showed 39.6 kPa of ice adhesion strength (measured by centrifuge method [202]) that is more than 10 times lower than the ice adhesion strength of an aluminium surface. The use of resins with anti-icing properties would help to further improve the ice protection performances of the self-heating composites. CNP based composites have been produced using the Silikopone EF resin. Reference samples have been produced using a standard commercial product (EL2 laminating resin). The morphology, the electrical characteristics and the heating performances of the composites samples have been analysed. Results indicated the composites with icephobic resin as promising candidates for ice protection applications.

6.1 CNP based self-heating composites

6.1.1 Electrical resistance

The electrical resistances of CNP composites are listed in Table 6.1, together with other characteristics like standard deviation (St. Dev.), thickness, electrical resistivity ρ and electrical conductivity σ . The electrical resistivities are calculated from the composite thickness. Samples were named according to the process and the CNP used (e.g. RV-CNP: RV method, 2 CNP buckypapers). The difference in thickness between the resin impregnation samples (RV and RP) and the pre-preg samples (PV and PP) are due to the different glass fibre fabric used.

Table 6.1 - Electrical resistance values for the composite samples

Sample	Resistance (Ω)	St. Dev. (Ω)	Thickness (mm)	ρ ($10^{-3} \Omega \text{ m}$)	σ (S/m)
MWCNP	5.5	0.5	0.12	0.7	1513.2
NA-CNP	6.0	0.8	0.08	0.5	2045.3
RV-CNP	3.8	0.6	2.8	10.6	94.0
RP-CNP	3.7	0.2	2.6	9.6	104.0
PV-CNP	1.8	0.3	1.0	1.8	555.6
PP-CNP	1.7	0.2	1.0	1.7	588.2
PP-NA-CNP	2.3	0.3	0.9	2.1	483.1

Pre-preg samples (PP and PV) have almost ~50% lower electrical resistance than resin impregnation ones. These values are even lower than the electrical resistance of two CNPs layers. At the interface between CNP/electrode and CNT/CNT, the resin would affect the electrical resistance except in pre-preg method. This could be due to the low amount of resin involved in the process, coming from the pre-preg fabric. The buckypaper used in pre-preg method were not previously soaked in any thermosetting resin. Samples with the lowest electrical resistance were obtained with PP method. NA-CNP buckypapers were used to prepare the class of samples called PP-NA-CNP.

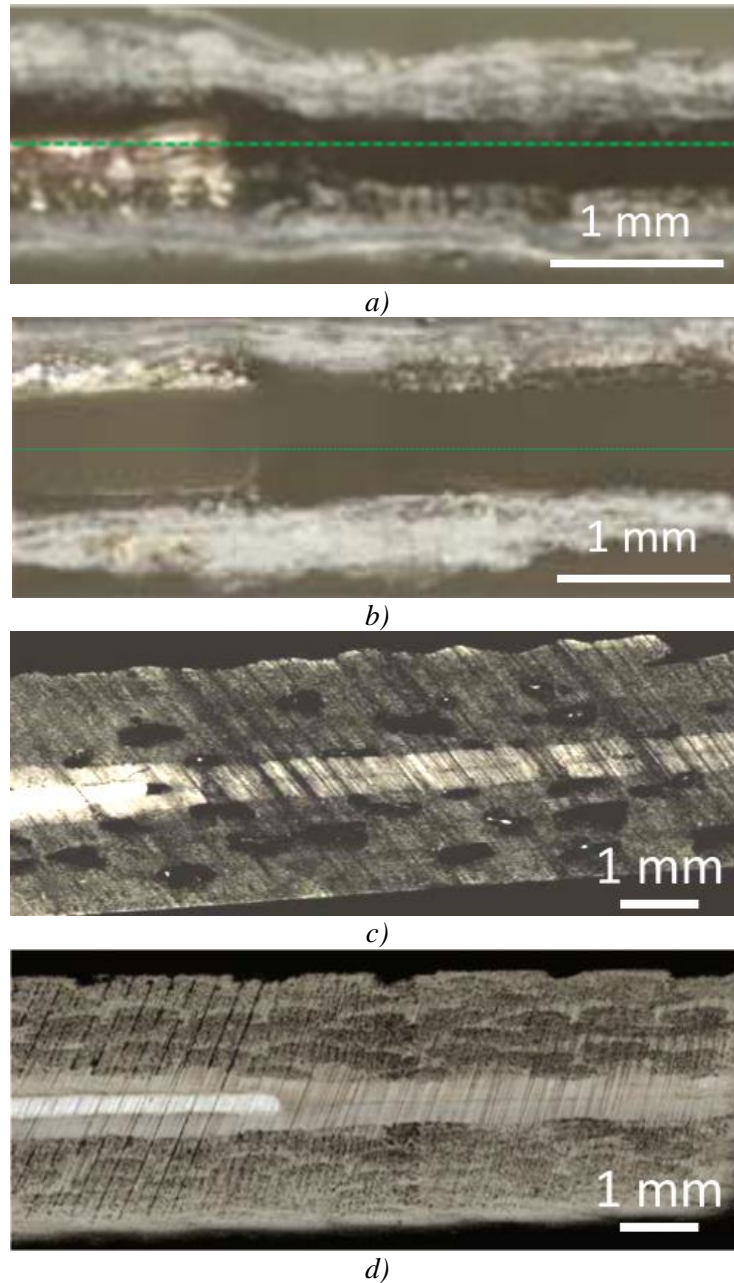


Fig. 6.1 - Laser microscope images of cross sections for: a) PV-CNP sample (green dotted line indicates the delamination); b) PP-CNP sample (green dotted line indicates the delamination); c) RV-CNP sample; d) RP-CNP sample

During machining procedure for morphological analysis and mechanical tests, delamination occurred for samples fabricated by pre-preg method. For PV (Fig. 6.1a) and PP (Fig. 6.1b) samples, delamination occurred along the interface between the CNPs. This phenomenon was likely to happen when the resin did not infiltrate the layers and formed proper bonding. The amount of resin coming from the pre-preg fabric was not enough to completely impregnate the CNT sheets and to affect/increase

their electrical resistance. The lower electrical resistance values of PP and PV samples could be due to the silver paint applied on the electrodes surfaces. The silver paint helped to increase the electrical conductivity at the interface between the CNP and the electrodes.

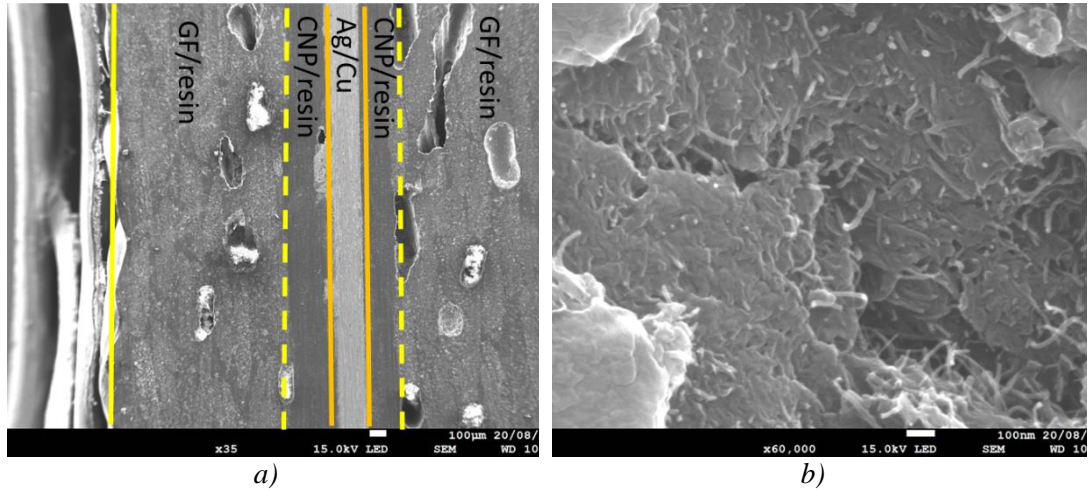


Fig. 6.2 - SEM images of RV-CNP cross section: a) x35 with layers description (Cu/Ag = copper electrode and silver paint) ; b) x60000

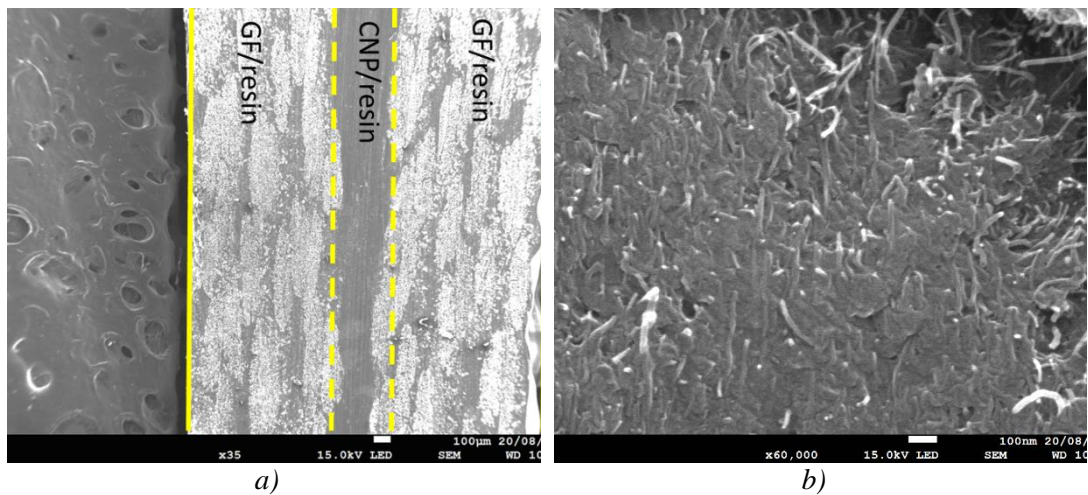


Fig. 6.3 - SEM images of RP-CNP cross section: a) x35 with layers description; b) x30000; c) x60000

The low standard deviations have proved that the pressure helped to obtain a more repeatable result in the resin impregnation method. The electrical resistances of RP and RV samples are higher than that of the pure double CNP layers. This is probably

due to the resin electrical insulating characteristics: the involved resin reduced the direct contacts of CNTs. MWCNTs are randomly distributed on the surface forming the conductive network (Fig. 6.2 and Fig. 6.3). The electrical conduction in the composite samples is attributed to the combination of MWCNTs and their junctions. The electrical resistance along a carbon nanotube is much lower than the junction electrical resistance, so that the CNP network can be illustrated by a series of resistors consisting of compactly connected nanotubes [69, 71, 203, 204]. The contacts between the CNTs create the pathways for the electrical current to flow through. Electrical resistance of 2-MWCNP has a low variation compared with the CNP/resin, due to the fact that the thermosetting resin around the CNT bundles is electrically insulating. This means that the conductive path in the MWCNT network is not significantly affected by the insulating resin. Compared to the one layer composite samples (section 6.2), for the two layers composite samples the ruining effect of the insulating resin is lower. The use of acetone can explain the difference. The dilution of the resin with acetone reduced the resin viscosity. The resin with low viscosity has been able to produce small CNT bundles, thus reducing the electrical resistance increase.

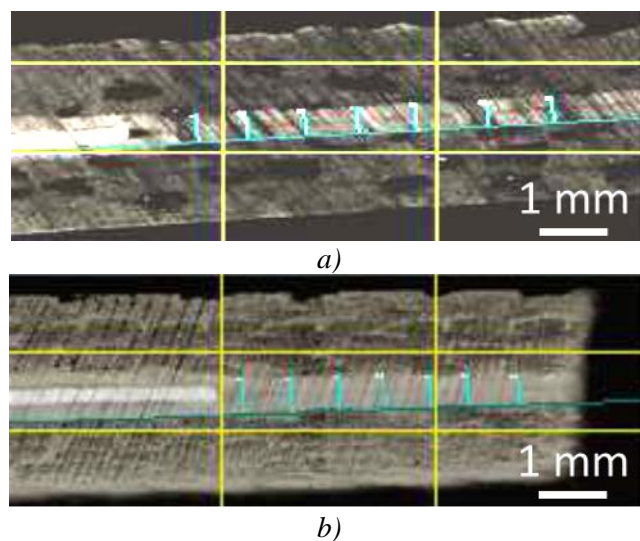


Fig. 6.4 - Thickness analysis for: a) RV-CNP sample; b) RP-CNP sample. The light blue vertical line indicates where thickness has been measured.

The real conductive section is thinner than the whole composite. Because of the resin's insulating characteristics, the conductive area is limited to the CNPs area. In order to calculate a more accurate electrical resistivity, the RV and RP composites cross section has been analysed. Thickness analysis of RV-CNP and RP-CNP samples are shown in Fig. 6.4. Thickness values are listed in Table 6.2. RV-CNP/resin and RP-CNP/resin are referred to the two soaked buckypapers layers used in resin impregnation methods. MWCNP and 2-MWCNP (2 layer of MWCNP) has been used as reference. In both RV and RP method, the CNP/resin thickness is higher than the 2-MWCNP thickness. The resin impregnation causes the thickness increase and thus the electrical resistance/resistivity increase.

Table 6.2 - Electrical characteristics of CNP: soaked in resin and not

Sample	Thickness (mm)	Thickness St.dev. (mm)	Resistance (Ω)	Resistance St.dev. (Ω)	ρ ($10^{-3} \Omega \text{ m}$)	σ (S/m)
RV-CNP/resin	0.40	0.03	3.8	0.6	1.6	625.1
RP-CNP/resin	0.41	0.01	3.7	0.2	1.5	662.4
MWCNP	0.120	0.010	5.5	0.5	0.7	1513.2
2-MWCNP	0.240	0.015	2.4	0.6	0.6	1741.7

In existing reports, CNTs had been mixed with polymer resins to produce electrical conducting nanocomposites, but the resulting structures often exhibited relatively low electrical conductivity (less than 1 S/m) [205-214], as the impregnation of polymer matrices decreased the continuity of the CNT conducting network for the current flow [204, 215-217]. The CNP based composites in this study have demonstrated higher electrical conductivity thanks to the better integration of the formed CNT conducting network, in which the negative impact from the polymeric resin would be minimized.

6.1.2 Heating performance

In Fig. 6.5 two thermal images show the heat distribution on the composite samples surface. The heat developed by electro-thermal effect is proportional to the electrical power (Eq. 6, section 3.8.2) generated by the samples. If a constant voltage is applied, self-heating composites with different electrical resistances generate different amounts of heat. Both images show an even heat distribution on the sample surface, between the two electrodes. It means that the current flow is constant over the entire surface.

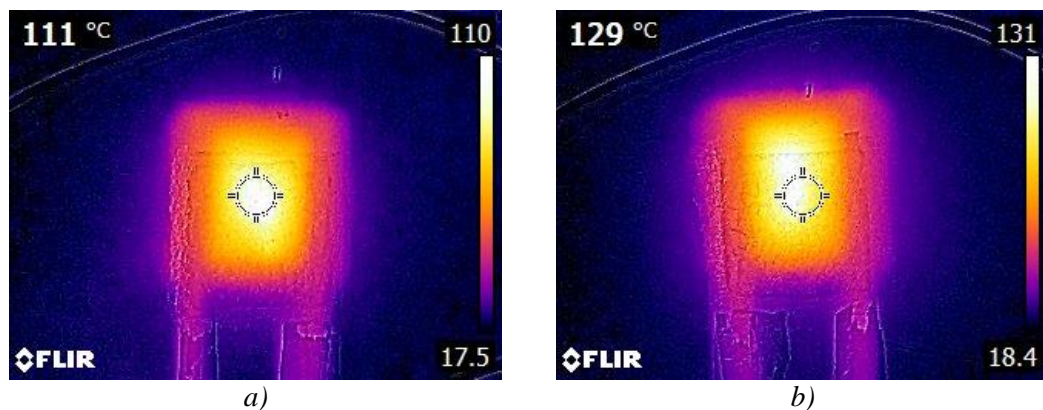


Fig. 6.5 - Thermal images of: a) RV-CNP sample; b) RP-CNP sample

The curves in Fig. 6.6 and Fig. 6.7 show the changes of temperature T , current I and resistance R of the different samples during the heat performance test. The measured temperature is proportional to the heat developed by the samples. At constant voltage (5 V), samples with different electrical resistances reach different temperatures. Samples with low electrical resistance (high current) will reach temperatures higher than samples with high electrical resistance (low current). It can be noticed that RP samples have much constant values of RV samples. It is likely that the pressure during the curing process helped to stabilise the electrical resistance value. All the RV and RP samples curves can be divided in three parts. There is a linear temperature increase (first), followed by a decreasing of temperature rising speed (second) until the temperature reaches a stable value (third). Current (I) and electrical resistance (R) did

not change during the test. The variation from the initial value is minimal. The samples kept a constant value for the entire duration of the experiment. This indicates that the electrical resistance of the samples is not affected by the operating temperature of the self-heating composite. The constancy of these characteristics is fundamental during the service time of the system in the aircraft. The power consumption of composite samples during the heating tests are listed in Table 6.3 and Table 6.4. Power density values were around 2 kW/m² and the reached temperatures were higher than 100°C. For de-icing systems, lower temperatures as well as lower power densities could be used to avoid possible thermal damages of the composite structure. The sample with the lowest electrical resistance reached the highest power density value (2.4 kW/m² for RV class and 2.2 kW/m² for RP class) and the highest temperature (133°C for RV class and 132°C for RP class).

Table 6.3 - Heating performance and testing characteristics of RV-samples

Sample	Current (A)	Resistance (Ω)	Power (W)	Power density (kW/m²)	T_{MAX} (°C)
1	1.0	4.9	5.2	1.7	111
2	1.3	3.9	6.4	2.1	120
3	1.4	3.5	7.1	2.4	133

Table 6.4 - Heating performance and testing characteristics of RP-samples

Sample	Current (A)	Resistance (Ω)	Power (W)	Power density (kW/m²)	T_{MAX} (°C)
1	1.2	4.0	6.2	2.1	118
2	1.3	3.7	6.7	2.2	132
3	1.3	3.8	6.7	2.2	130

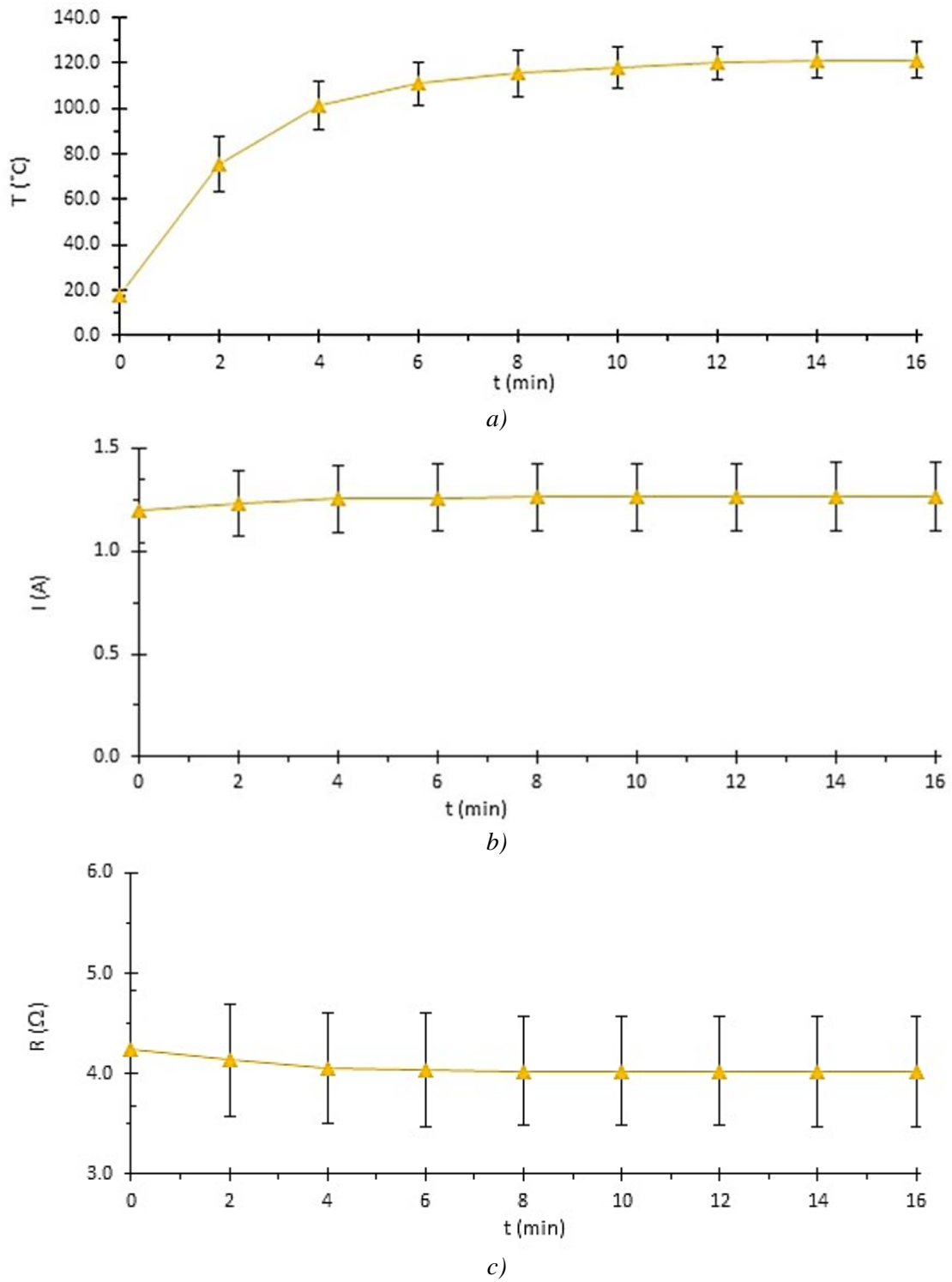


Fig. 6.6 - Graphs of RV-samples characteristics registered during the heating performance test: a) temperature T ; b) current I ; c) resistance R . The orange lines represent the average value of the respective characteristic

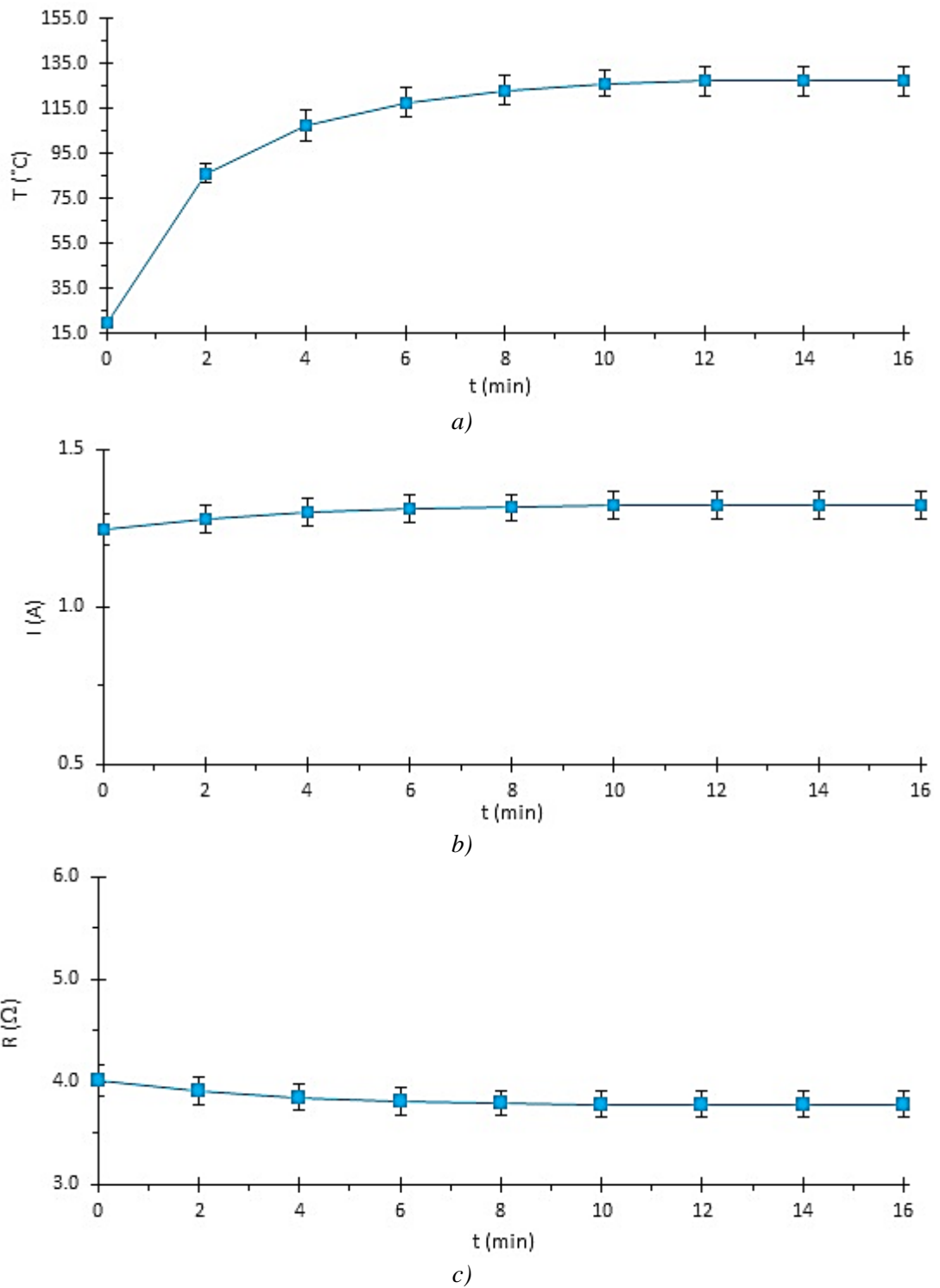


Fig. 6.7 - Graphs of RP-samples characteristics registered during the heating performance test: a) temperature T ; b) current I ; c) resistance R . The orange lines represent the average value of the respective characteristic

6.1.3 Ice melting test

Fig. 6.8 shows the sample covered by rime ice in a cold environment at -20°C (Fig. 6.8a and Fig. 6.8c) and the sample after 120s heating generated by electrical current (Fig. 6.8b and Fig. 6.8d). Due to the Joule effect, the temperature rises where the electrical current flows, as heat distribution indicates in Fig. 6.8d. This test condition is to simulate the ice protection system working in de-icing configuration. When the ice between the electrodes is completely removed, as in Fig. 6.8b, the test is finished.

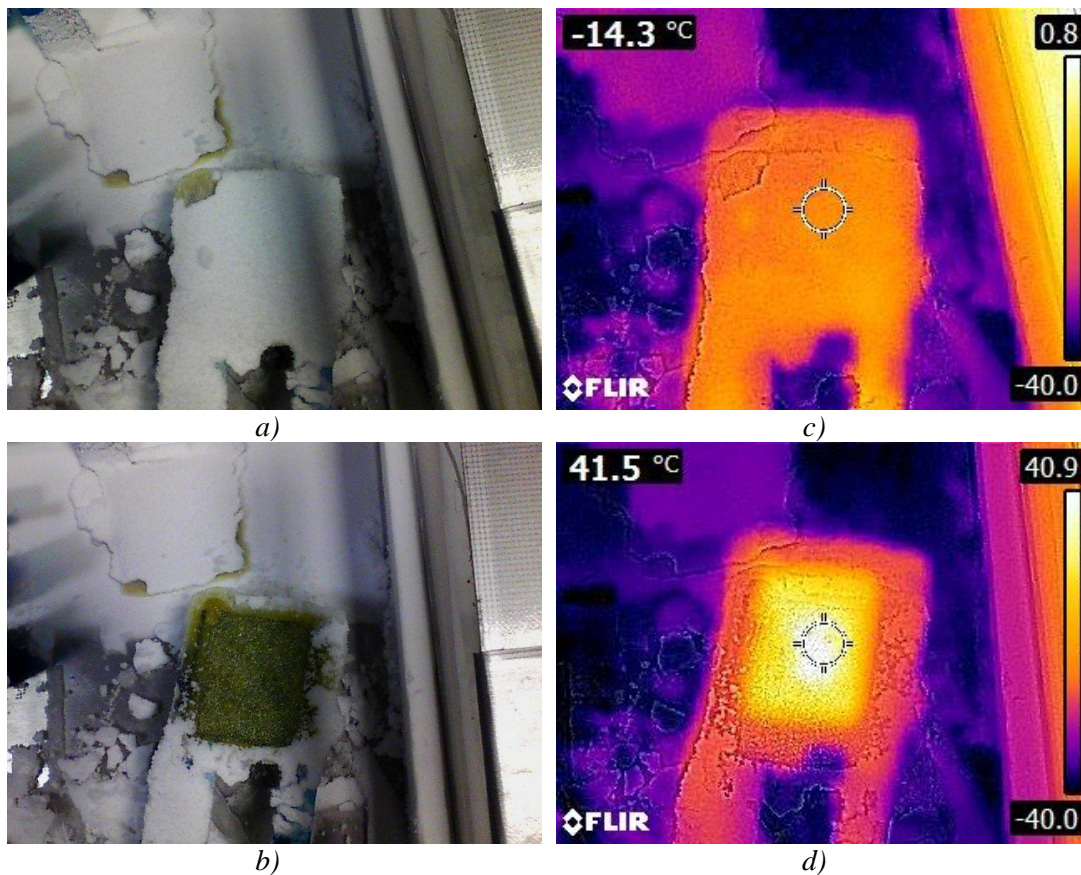


Fig. 6.8 - Photos and thermal images of an RP sample during the de-icing test in the cold environment: a, c) at the beginning of the heating; b, d) after 120s heating

The electrical power is directly proportional to the heat developed by samples (Eq. 6, section 3.8.2). A 5 V voltage has been applied to the samples. Low electrical resistance composites will generate more heat than high electrical resistance composites. Less generated heat causes longer ice melting time. Fig. 6.9 shows the behaviour of

temperature T of the different samples during the de-icing test. The temperature plateau, due to ice melting, is not clearly visible for all the samples. During ice melting, the measured temperature was slightly below 0°C (around $-1^{\circ}\text{C} \sim -2^{\circ}\text{C}$). The camera was measuring the temperature of the ice/water mixed phase on the surface of the sample. For this reason, the measured temperature was not exactly 0°C , as thermodynamically expected. It is considered as ice melting time the moment, after the beginning of the test, in which the sample average temperature rose over 0°C . Ice melting time range of RV samples was between 30s and 60s while RP samples ice melting time range was between 30s and 40s. When the ice was melted, the temperature of the RV and RP samples rose at $\sim 0.8^{\circ}\text{C/s}$.

It can be noticed that RP samples range values of temperature, electrical current and electrical resistance are narrower than RV samples ones, as already demonstrated by the heating performance test. Samples with different electrical resistances generate different amounts of heat. As verified during the heating performance, RV samples have a wider electrical resistance range than RP samples.

The power consumptions and power densities of de-icing are listed in Table 6.5. In all the samples, the ice was removed after 120s. At the end of the experiment, temperature was still rising. Lower voltages could be used, causing the increase of ice melting time, but working temperature would be lower to avoid any possible thermal damage of the composite structure. Power density values around 2kW/m^2 were within the range of reported values in literature [69, 71, 72]. The power density of the CNP based heater $\sim 70\%$ lower than the power density of the traditional heater (copper foil based, Zhao et al. [74]). A low power density indicates a low power consumption of the ice protection system. The CNP composite heater shows an impressive energy saving

result. This result highlights the potential application of the CNP based heater as ice protection system.

Table 6.5 - De-icing tests characteristics for RV and RP samples

Sample	Power (W)	Power St.dev. (W)	Power density (kW/m ²)	Pow.Den. St.dev. (kW/m ²)
RV-CNP	6.0	0.7	1.99	0.25
RP-CNP	6.5	0.4	2.14	0.14
Traditional [74]	-	-	7.0	-

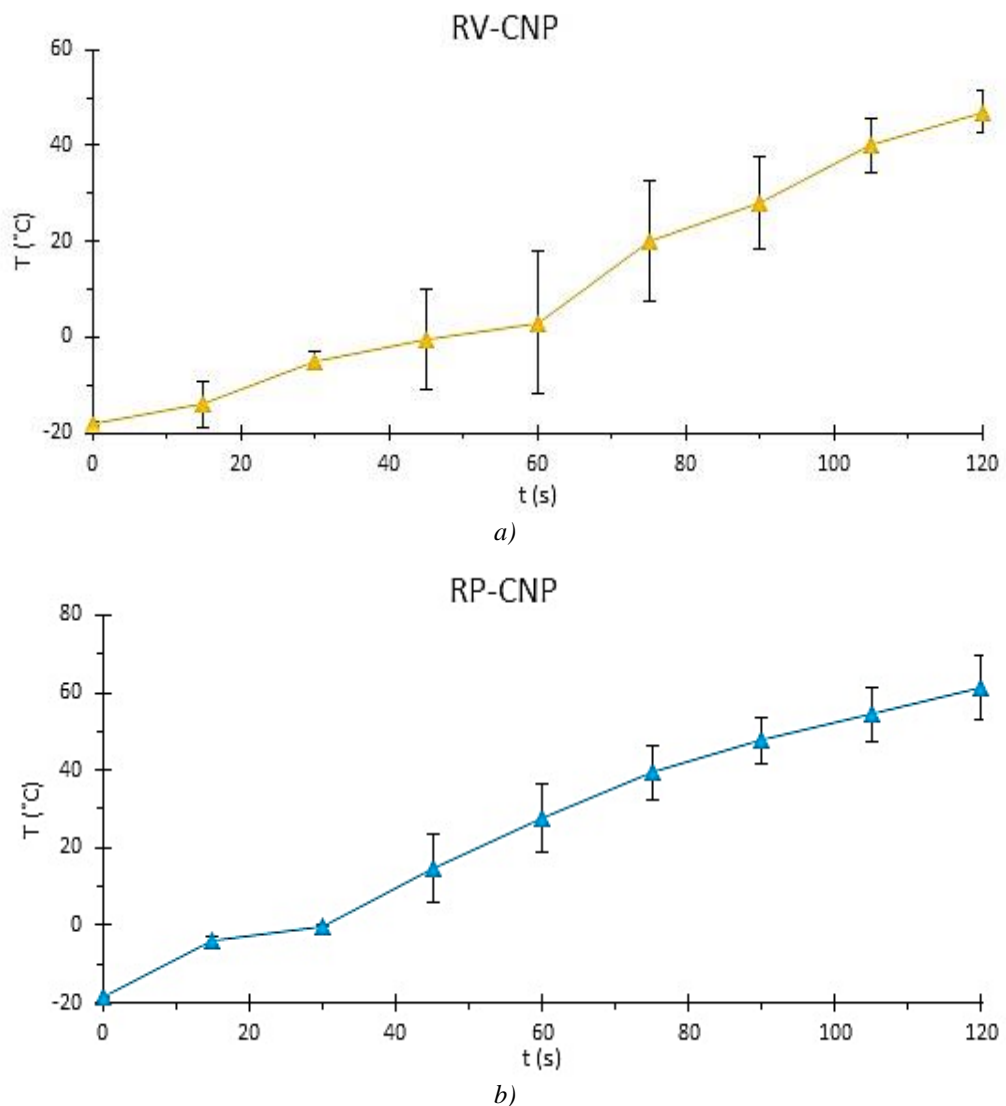


Fig. 6.9 - Graphs of temperatures registered during the de-icing test: a) RV samples; b) RP samples.

6.1.4 Mechanical test

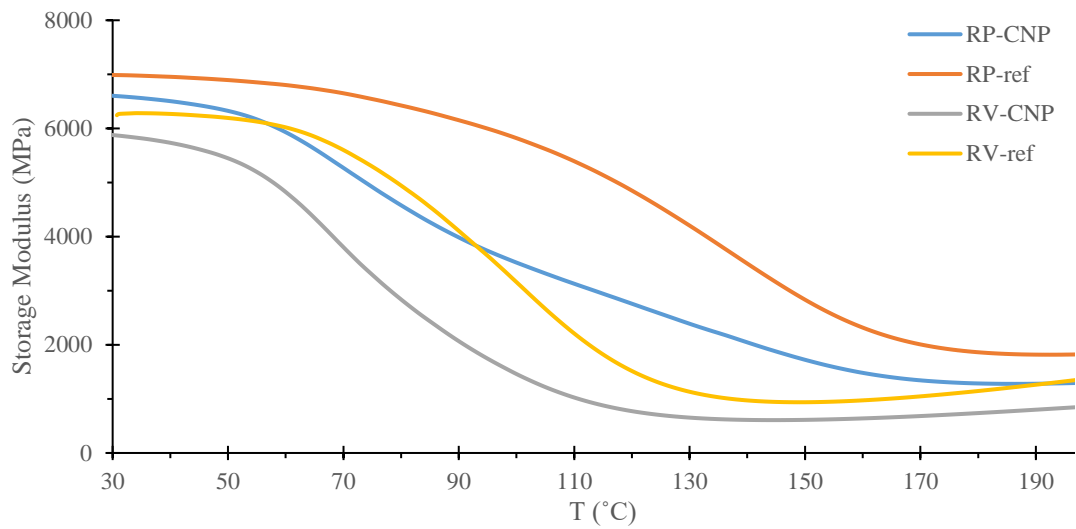
As already discussed, the mechanical properties of the ice protection system based on nanocomposite materials have not been studied yet. In this work three-point flexural strength, interlaminar shear strength (ILSS) and dynamic mechanical analysis (DMA) have been executed to further increase the knowledge on self-heating nanocomposites.

Dynamic mechanical analysis (DMA) is used to study the viscoelastic behaviour of polymers. A sinusoidal stress is applied and the strain in the material is measured, allowing one to determine the complex modulus. In typical DMA experiments stress is applied at a constant frequency (~ 1 Hz), strain is kept constant and temperature is increased at a specific rate. The outputs from the analysis are: storage modulus (E'), loss modulus (E'') and loss tangent ($\tan \delta$) versus temperature or time. Loss tangent is a measure of the “damping” or the lag between stress and strain. Storage modulus represents the elastic behaviour of the polymer, while loss modulus measures the energy dissipated as heat, representing the viscous portion of the polymer. For an elastic material, strain and stress will be in phase. For a viscous material, there will be phase lag of strain with respect to stress [218]. Each polymer has its own phase lag that will occur during DMA tests.

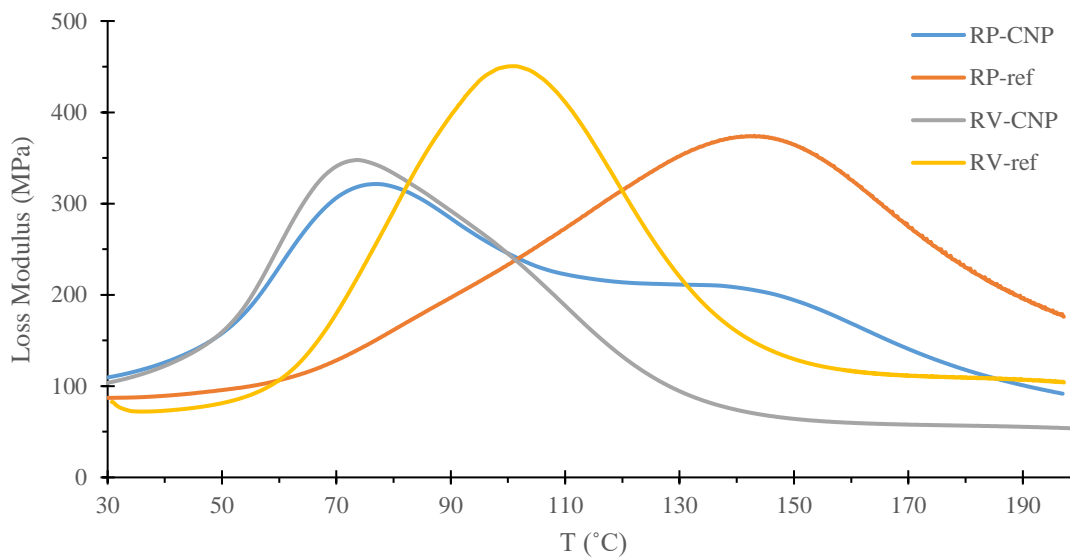
DMA can measure the glass transition temperature (T_g) of polymers. Above the glass transition temperature the polymer will have rubbery properties instead of glassy behaviour, the stiffness of the material will drop with an increase of its viscosity. At the glass transition, the storage modulus decreases dramatically and the loss modulus reaches a maximum [218]. DMA results are shown in Fig. 6.10. RP-ref and RV-ref were used for reference composite samples, while RP-CNP and RV-CNP were used for the composite samples modified with buckypapers. In Fig. 6.10b the RP-CNP and

RV-CNP curves show a peak of loss modulus, due to the glass transition temperature, at around $\sim 75^{\circ}\text{C}$. This value is lower than the respective reference one ($\sim 95^{\circ}\text{C}$ for RV-ref and $\sim 145^{\circ}\text{C}$ for RP-ref). The RP-CNP group has two peaks: the first at the T_g ($\sim 75^{\circ}\text{C}$) of the resin in which the CNPs has been soaked; the second peak is in correspondence of the T_g of RP-ref group ($\sim 145^{\circ}\text{C}$). The RV-CNP group shows only one peak. The change of phase is highlighted in Fig. 6.10a, where the RP-CNP curve presents two different gradients between $\sim 60^{\circ}\text{C}$ and $\sim 160^{\circ}\text{C}$. The first slope (between $\sim 60^{\circ}\text{C}$ and $\sim 85^{\circ}\text{C}$) is caused by the first phase transition at $\sim 75^{\circ}\text{C}$. The second slope (between $\sim 85^{\circ}\text{C}$ and $\sim 160^{\circ}\text{C}$) is caused by the second phase transition at $\sim 145^{\circ}\text{C}$. Pressure, unlike vacuum, enhanced the cross-linking between the polymers chains, causing a change in physical characteristics of the thermos-setting resin. The use of pressure during the curing cycle is the reason for microstructure change indicated by the presence of the second peak. The pressure effect is further confirmed by the two reference curves RV-ref and RP-ref. RP-ref peak is at higher temperature ($\sim 145^{\circ}\text{C}$) than the RV-ref one ($\sim 103^{\circ}\text{C}$)

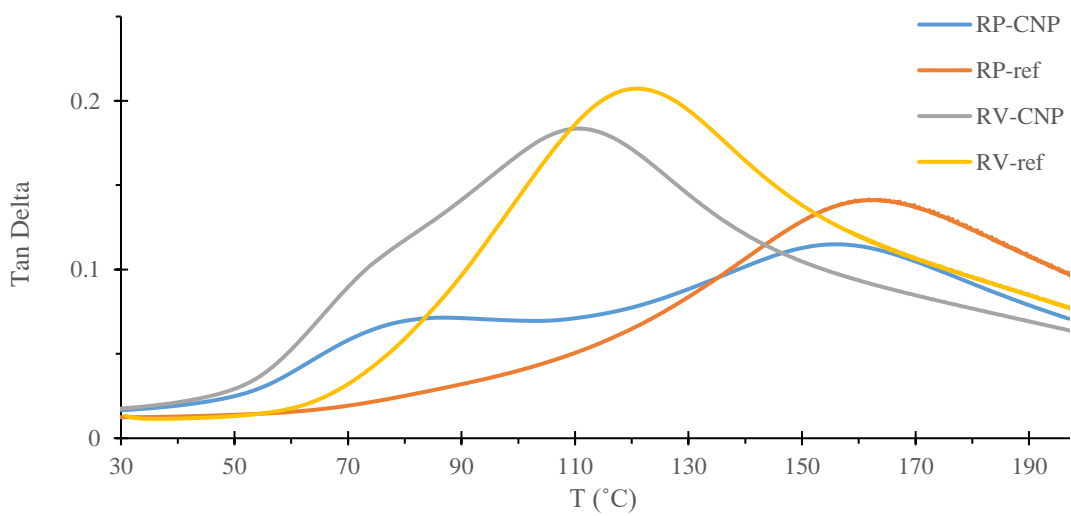
For composite materials used in ice protection systems the glass transition temperature should be as high as possible, e.g. $T_g > 100^{\circ}\text{C}$. Post-curing treatments could help to increase the glass transition temperature [219-221]. The difference between modified and reference samples could be due to the silica content in araldite MY750 resin. The buckypapers were soaked in unfilled araldite MY750. Silica content could change $\tan \delta$ value as particles cause restrictions against polymer chains motion. Mineral particles may also act as either nucleation promoters or inhibitors, which changes the polymer morphology and its thermal behaviour (e.g. T_g , glass transition temperature) [222, 223]. Pre-preg fabric without silica content could be used for a comparison test.



a)



b)



c)

Fig. 6.10 - DMA results for the different samples: a) Storage Modulus; b) Loss modulus; c) Tan Delta.

The CNP weight percentage, in the RV and RP composite samples, has been obtained by scaling the electrical resistance samples. The average weight values for RV and RP classes are 13.0 g and 14.0 g respectively (Table 6.6, the weight of the copper electrodes has been subtracted). Considering that in each sample there are two CNP buckypapers of 0.1 g each, the CNP weight percentage in the composite element is less than 1 wt%. The volume percentage of the CNPs with and without resin has been calculated dividing the CNPs thickness (2 CNP layers soaked or not in resin) by the thickness of the RV and RP composite samples. As expected the volume increase, due to resin impregnation, causes an increase of the CNP/resin vol% values. The volume percentages of the CNP layers (< 1 vol%) is lower than the volume percentage of the CNP/resin layer.

Table 6.6 - Buckypaper weight percentage in the composite structure

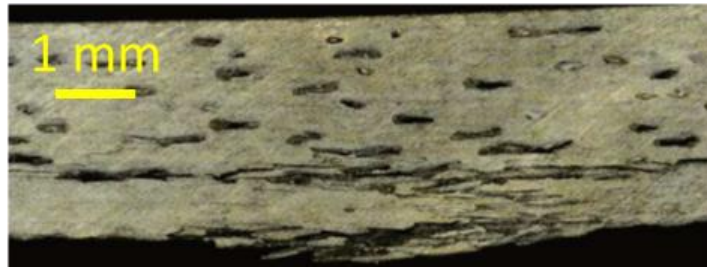
Sample	Composite Weight (g)	Weight St.dev. (g)	CNP wt% (%)	CNP vol% (%)	CNP/resin vol% (%)
RV-CNP	13.0	0.5	0.8	0.4	1.5
RP-CNP	14.0	0.3	0.7	0.5	1.6

Flexural test results are listed in Table 6.7. The RP samples have higher fracture strength values than RV ones. The pressure during curing cycle would be the main reason of the improvement. About RP fracture strength, the RP-CNP samples also have higher (about ~9 % more) values than RP-ref. Increasing the CNP wt%, consequently the CNP vol%, would lead to higher strength improvements. The buckypaper acted like a reinforcement layer for the structure. In RV samples instead, RV-CNP fracture strength is lower than that of RV-ref.

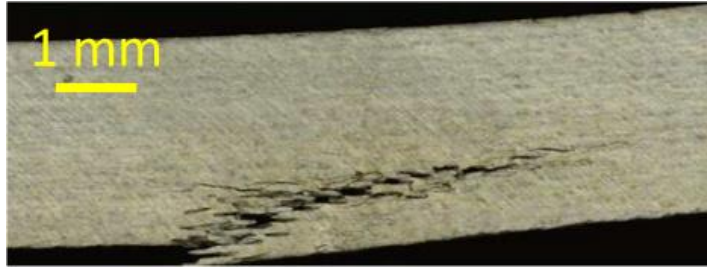
Table 6.7 – Three-point flexural tests results

Sample	Fracture Strength (MPa)	St. Dev. (MPa)	Young's modulus (GPa)	St. Dev. (GPa)	CNP wt% (%)	CNP vol% (%)	CNP/resin vol% (%)
RP-CNP	353.3	13.7	16.3	0.6	0.7	0.5	1.6
RP-ref	321.0	15.2	14.1	0.3	-	-	-
RV-CNP	231.6	10.1	11.4	0.6	0.8	0.4	1.5
RV-ref	283.6	9.3	12.8	0.4	-	-	-

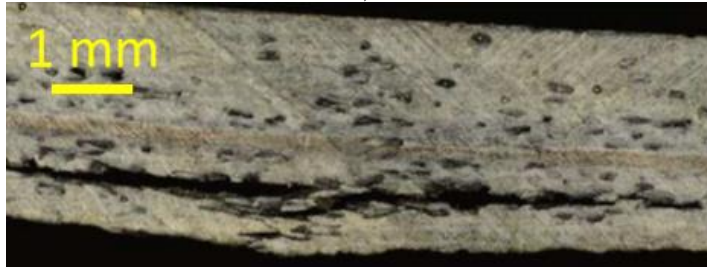
Considering the high defect concentration, RV method (Fig. 6.11a and Fig. 6.11c) seems not to be an ideal method for self-heating composite production. To avoid porosity formation, pressure should be applied during the curing cycle of the thermosetting system (resin/hardener), as it can be noticed from the porosity-free surfaces of RP samples (Fig. 6.11b and Fig. 6.11d). RP-ref (Fig. 6.11b) and RP-CNP (Fig. 6.11d) show similar fracture morphology. This indicates that the soaked CNP did not cause any changes in the fracture mechanism. Fig. 6.12 shows that the crack propagated in the CNP element. This could explain the higher fracture strength value for the RP-CNP samples.



a)



b)



c)



d)

Fig. 6.11 – Three-point flexural tested samples: a) RV-ref sample; b) RP-ref sample; c) RV-CNP sample; d) RP-CNP sample



Fig. 6.12 - Magnified image of the crack in the three-point flexural RP-CNP sample

ILSS results are listed in Table 6.8. The RP-CNP and RP-ref samples have slightly lower values than RP-ref. The buckypaper did not bring any significant changes to this characteristic. RV-CNP ILS Strength average value is lower than RV-ref (~30% lower). A typical RV-CNP fracture surface is shown in Fig. 6.13. The buckypapers

have probably weakened the structure, acting as a defect and reducing the interlaminar properties. In RV-CNP samples the crack propagated along the interface between the two CNP layers. The buckypapers interface is a weak point for the RV-CNP samples. The pressure during curing cycle may be the key reason for the different behaviours between RP and RV. Pressure enhanced the interface bond between the CNP layers. These results further highlight how the RV treatment is not appropriate for self-heating composite production.

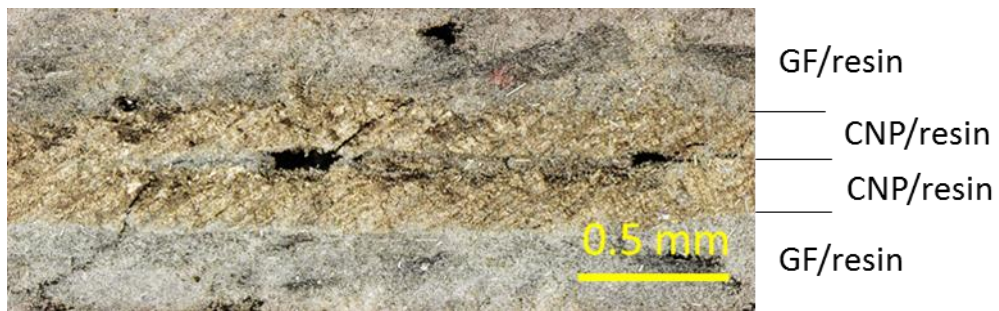


Fig. 6.13 - Laser microscope image of ILSS RV sample with crack between the two soaked CNPs. The layer configuration is described on the side

Table 6.8 - Interlaminar Shear Strength results

Sample	ILS Strength (MPa)	St. Dev. (MPa)	CNT wt% (%)
RP-CNP	45.0	2.2	0.7
RP-ref	48.1	1.1	-
RV-CNP	27.5	0.8	0.8
RV-ref	38.1	2.1	-

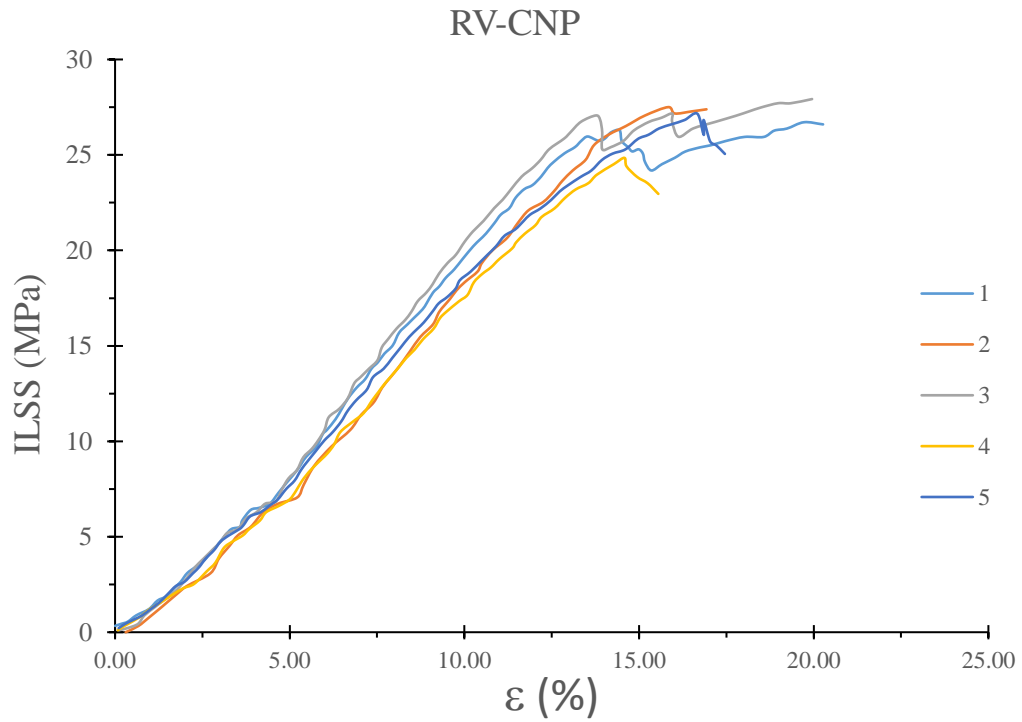
In Fig. 6.14 and Fig. 6.15, the ILSS test shows the behaviour of the different RV and RP samples. RP samples reach higher stress values than RV ones, thanks to their better microstructural characteristics. The small standard deviation of the RP samples indicates a rather homogeneous composite structure even when the CNPs were introduced. As discussed in the previous session, the pressure during the curing process would be the main reason of the mechanical performance of RP samples. The

gaps on the RV-CNP curves (for $\varepsilon > 12.5\%$, Fig. 6.14a) are caused by the fractures that were created on the sample during the test (example in Fig. 6.13). It can be noticed from the figures that all the RV-CNP samples have been damaged during the test. This is a further proof that RV is not an effective method for the preparation of self-heating CNP-based composite.

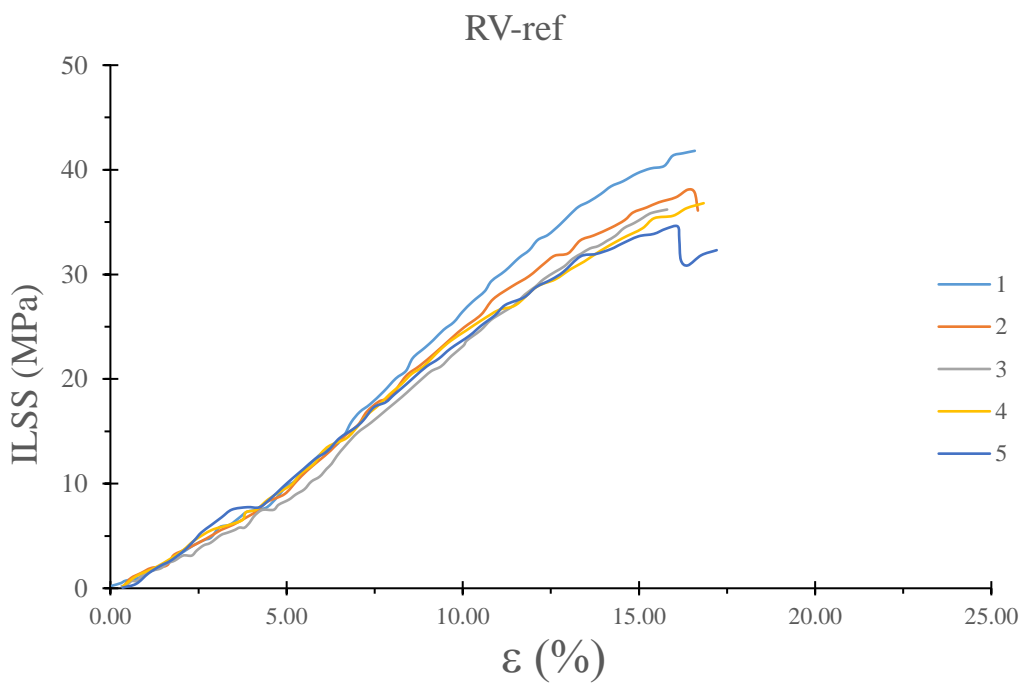
The ILSS results indicate that RP-CNP and RP-ref have similar behaviour Fig. 6.15. The regular/linear trend of the curves indicates that the samples have not been damaged during the test. The RP samples (CNP and ref) have been able to withstand up to 3kN interlaminar shear load. From Fig. 6.15 it can be noticed that the average $\varepsilon\%$ value at the end of the test is between 15%~20% for RP-CNP samples and between 20%~25% for RP-ref. These results indicate a more rigid behaviour for RP-CNP samples. The CNP/resin system has different mechanical characteristics compared to the GF/resin system. The presence of an element (CNP/resin) with different mechanical characteristics is the reason for its rigid behaviour. Reducing the thickness of the CNP/resin element should help to reduce the effect due to the different mechanical properties. The less the volume with different mechanical characteristics, the less rigid the CNP-based composite behaviour will be. Due to their reduced thickness, working with acid treated buckypaper will help to overcome the rigid behaviour issue. Moreover, the introduction of oxygen-containing groups onto the graphitic surface will enhance the interfacial adhesion. Zhu et al. [224] and Guo et al. [55] studied nanotube-reinforced epoxy composites using functionalized carbon nanotubes. Results of both works demonstrated clear enhancement in the mechanical properties as ultimate strength, elastic modulus and fracture toughness.

From the mechanical tests results (three-point flexural test and ILSS) for the RP-CNP class, it can be deduced that the CNPs did not cause a deterioration of the mechanical

characteristics of the composite structure. Moreover, the flexural tests indicate a slight improvement of the breaking stress (about 10% higher). These results indicate that the RP method is appropriate for the production of self-heating composite CNP-based. Further process optimisation may increase the interlaminar shear strengths and overcome this rigid behaviour.



a)



b)

Fig. 6.14 - Stress "ILSS" (MPa)/Extension " ε " curves of interlaminar shear strength test for Resin Impregnation Vacuum samples: (a) RV-CNP; (b) RV-ref. 1, 2, 3, 4 and 5 are three samples within one testing group

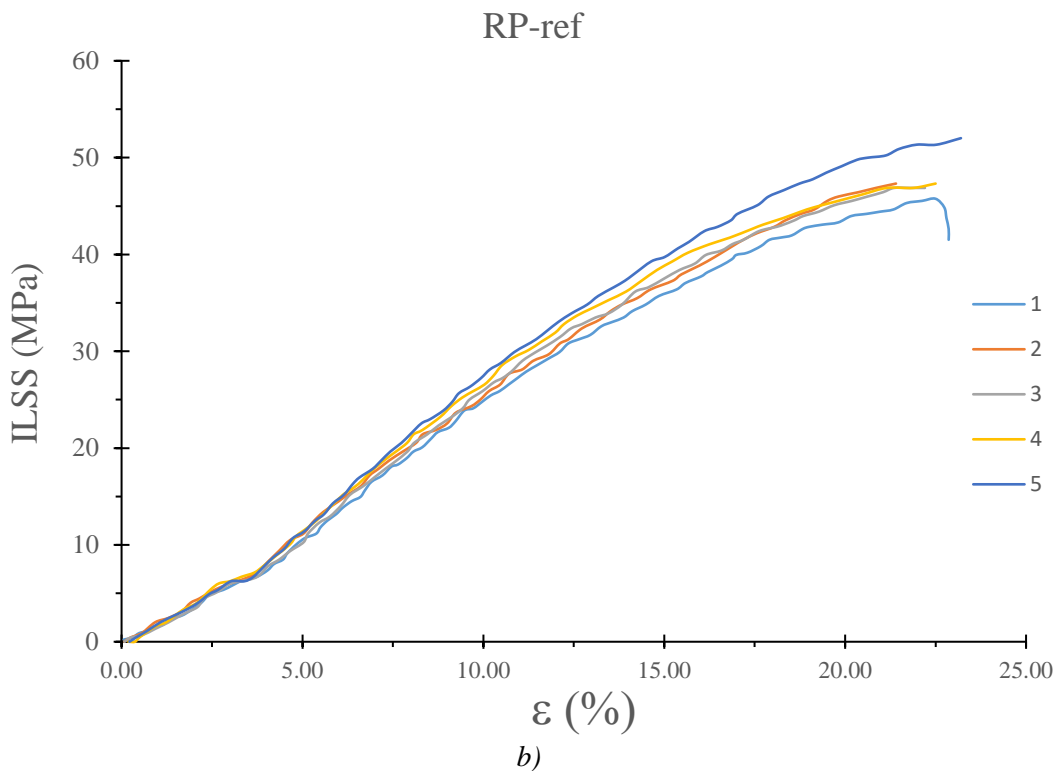
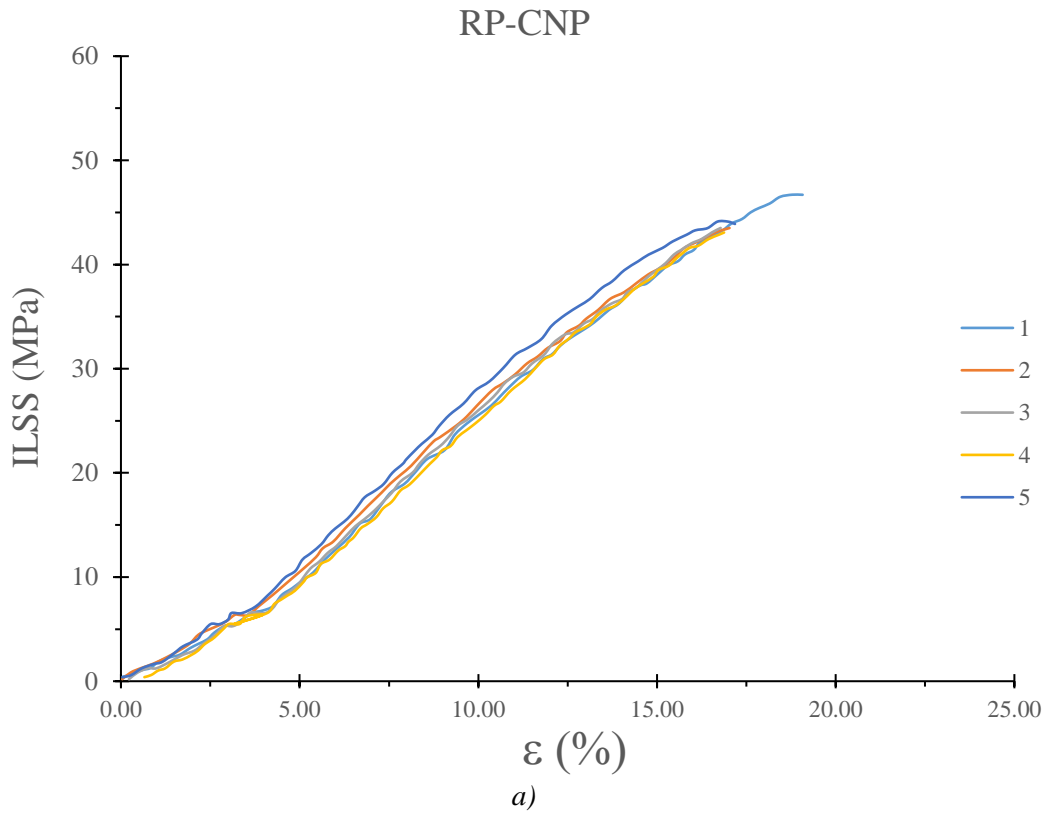


Fig. 6.15 - Stress "ILSS" (MPa)/Extension " ε " curves of the interlaminar shear strength test for Resin Impregnation Pressure samples: (a) RP-CNP; (b) RP-ref. 1, 2, 3, 4 and 5 are three samples within one testing group

6.2 Combination of super-hydrophobic resin with CNP based self-heating composites

6.2.1 Morphology and electrical characteristics

The composite samples were named based on the thermosetting resin and buckypaper utilised: EF-MWCNP (Fig. 6.16a) for untreated buckypaper soaked in Silikopon resin; EL2-MWCNP (Fig. 6.16a) for untreated buckypaper soaked in EL2 laminating resin. The same rule has been applied for NA-CNP. The thickness of the composites samples is listed in Table 6.9. To obtain the thickness of the impregnated CNP (CNP/resin column), the GF fabrics thickness has been subtracted to the composite thickness value. In these operations, the increase of the GF thickness caused by the resin impregnation has been considered null. The resin impregnation caused an increase of the CNP thickness. The reduced thickness of the nitric acid treated CNP is the reason why the thickness of NA-CNP based composites is lower than the thickness of composites made with MWCNP.

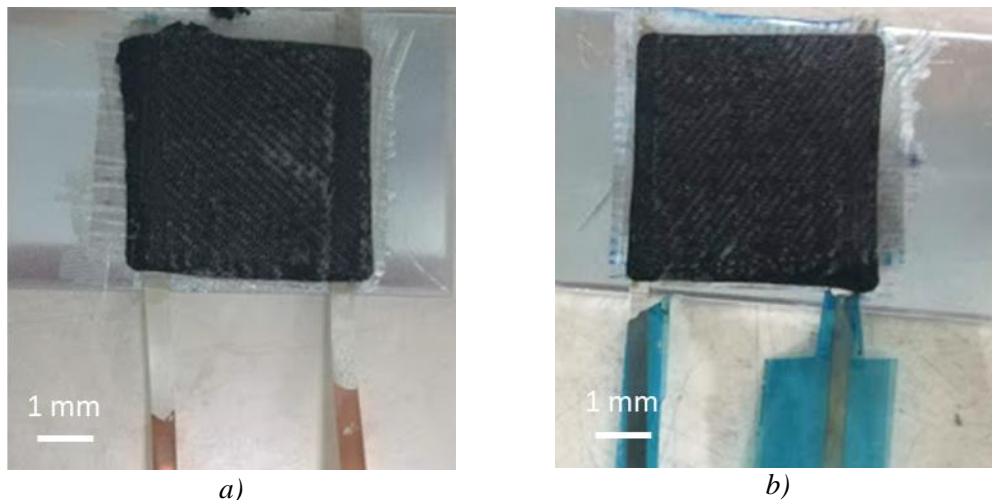


Fig. 6.16 - Examples of composite samples with one layer configuration: a) EF-MWCNP; b) EL2-MWCNP

Table 6.9 - Composite samples characteristics

Sample	Thickness				
	Composite (mm)	CNP/resin (mm)	St.dev. (mm)	MWCNP (mm)	NA-CNP (mm)
EF-MWCNP	0.618	0.248	0.019	0.120	0.081
EF-NA-CNP	0.589	0.219	0.018	0.120	0.081
EL2-MWCNP	0.645	0.275	0.020	0.120	0.081
EL2-NA-CNP	0.564	0.194	0.016	0.120	0.081

Fig. 6.17 shows SEM images of EL2-MWCNP, EL2-NA-CNP and EF-MWCNP respectively. In the magnified images, the nanotubes covered by resin are visible. For the same resin, between MWCNP (Fig. 6.17a and Fig. 6.17b) and NA-CNP (Fig. 6.17c and Fig. 6.17d) there is not any visible difference in the morphology. Even comparing two different resins (EL2-MWCNP in Fig. 6.17a and EF-MWCNP in Fig. 6.17e) there are no clear differences. The resin impregnated the CNP layer, the solidification caused a volume increase of the resin and consequently the CNP volume. The MWCNTs randomly distributed on the surface create the pathway for current flow through the CNP. Electrical characteristics variation of the CNP is caused by the electrically insulating resin around the CNT bundles. Despite the similar morphology, the composite samples have different electrical characteristics.

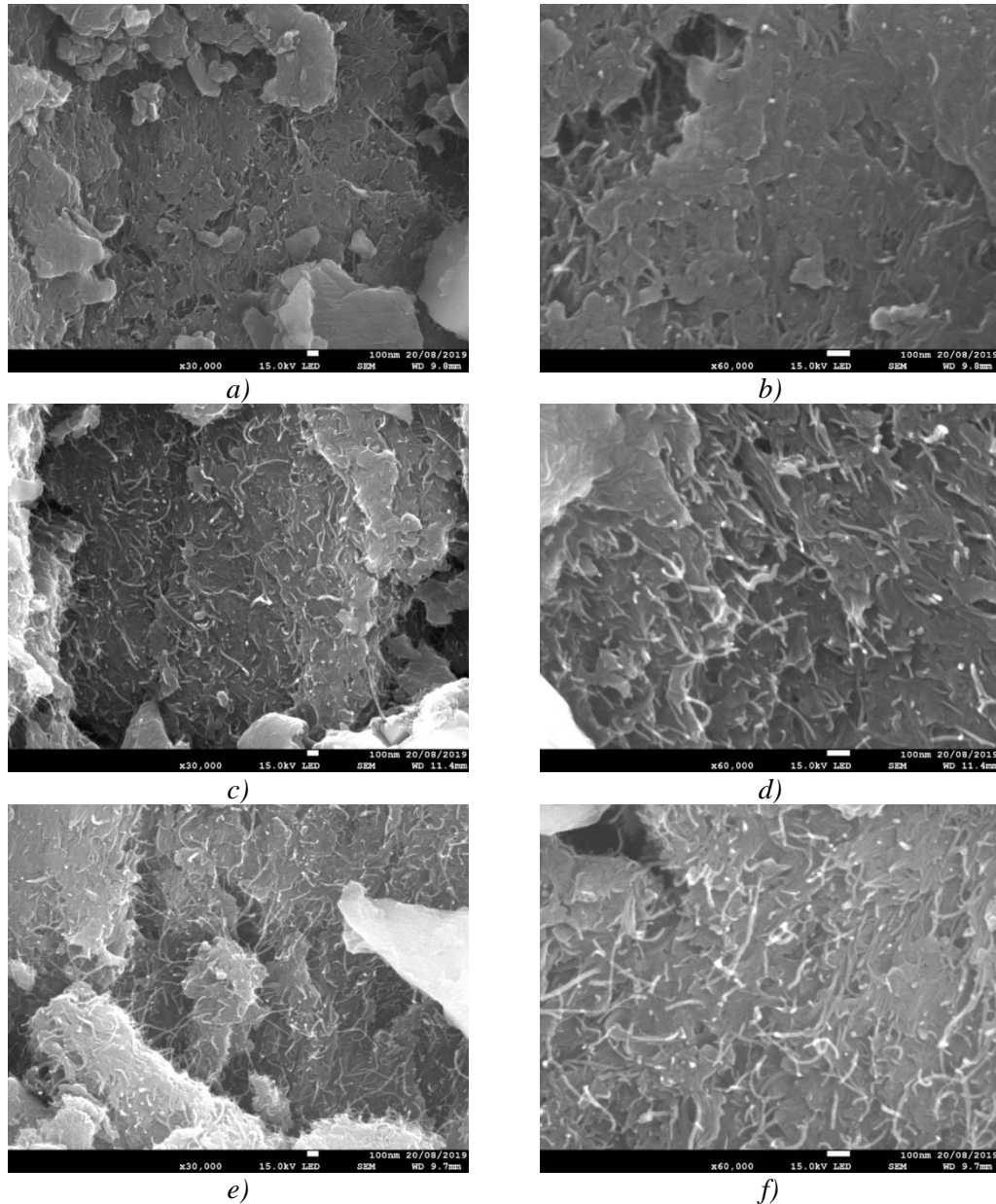


Fig. 6.17 - SEM images of cross section: a, b) EL2-MWCNP (x30000, x60000); c, d) EL2-NA-CNP (x30000, x60000); e, f) EF-MWCNP (x30000, x60000)

The electrical properties of the composite samples are listed in Table 6.10. The electrical resistance of the composite samples is higher than the CNP (MWCNP and NA-CNP). The electrical resistance comparison between the CNP and the respective composite sample is illustrated in Fig. 6.18. Contrary to the morphological results, the electrical characteristics of the composite samples show a different behaviour between each other. The resin impregnation is the cause of the increased electrical resistance value. In each group of resin, the composite samples based on NA-CNPs showed the

highest increase in electrical resistance. The conductive film is made of MWCNTs randomly distributed on the surface, which create the pathway for current flow. Electrical resistance variation is due to the fact that thermosetting resin around the CNT bundles is electrically insulating. This means the resin infiltrates into the inner space of the CNP and MWCNT bundles are packaged by the resin. The resin/CNT bundles are the reason for the electrical resistance increase. NA-CNPs were more compact than MWCNPs (demonstrated by the low thickness value). The resin penetrated with more difficulty through the NA-CNT bundles, disturbing the intra-bundle interactions and causing the formation of bigger resin/CNT bundles. This increased the electrical resistance of the respective composite sample. For every CNP group (MWCNP or NA-CNP) the electrical resistance of samples impregnated with Silikopone resin is lower than the electrical resistance of samples impregnated with EL2. The impregnation of EF resin caused the formation of CNT bundles smaller than the CNT bundles formed with EL2 resin. The smaller bundles caused the lower electrical resistance increase.

The impregnation with the icephobic resin caused the lower increase of electrical resistance. The dilution with the proper solvent, at the proper volume ratio, would improve the impregnation characteristics of the resin. A less viscous resin would penetrate through the CNP layer, forming smaller CNT bundles. The smaller the CNT bundles are, the lower the electrical resistance increase of the CNP will be.

Table 6.10 - Electrical properties of composite samples

Sample	Resistance (Ω)	St. Dev. (Ω)	ρ ($10^{-3}\Omega\text{ m}$)	σ (S/m)
MWCNP	5.5	0.5	0.7	1513.2
NA-CNP	6.0	0.8	0.5	2045.3
EF-MWCNP	11.8	1.2	2.9	345.8
EF-NA-CNP	36.7	2.5	8.0	125.0
EL2-MWCNP	15.8	1.8	6.1	190.2
EL2-NA-CNP	51.5	1.5	10.0	100.6

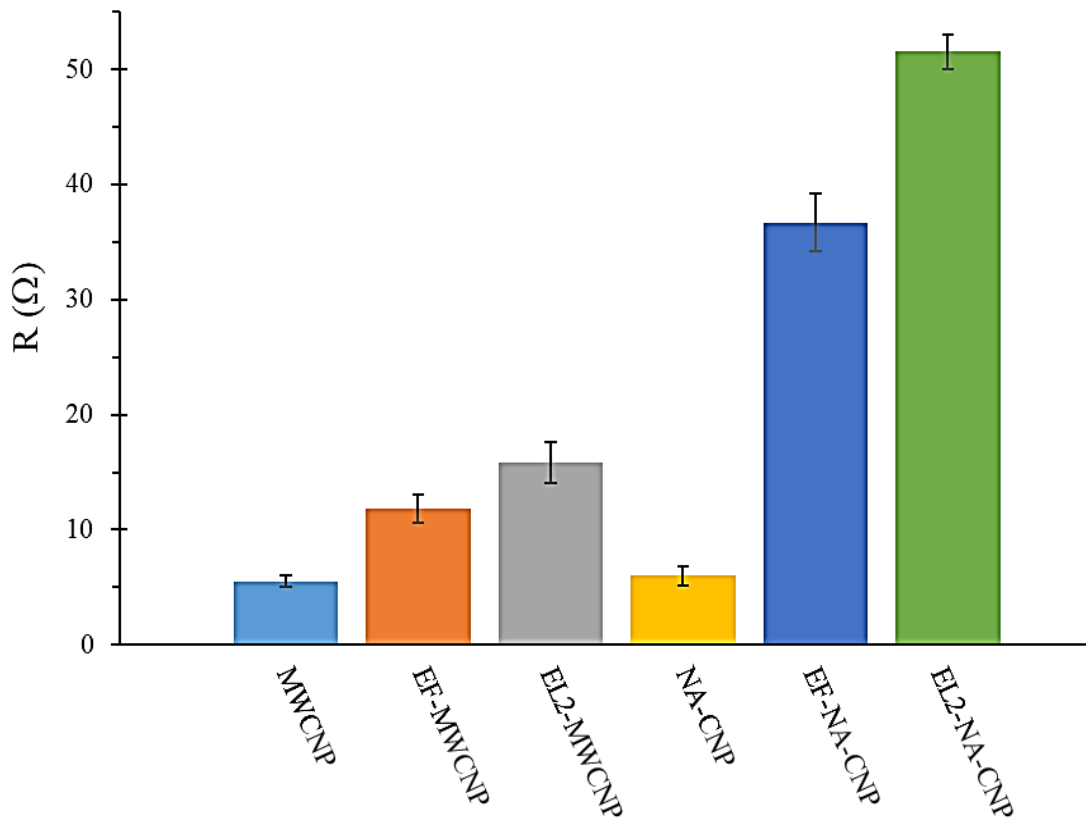


Fig. 6.18 - The electrical resistance comparison between the CNP and the respective composite sample

6.2.2 Electro-thermal test in icing environment

Fig. 6.19 shows the samples conditions and heat distribution during the ice protection test. The composite samples were covered in rime ice at -20°C and the 5 V electrical potential was applied to start the heating. This test condition was to simulate an ice protection system working in de-icing configuration. Fig. 6.19a shows the beginning of the test, when the voltage has been applied. In the IR image in Fig. 6.19d, a light orange area appears in the middle of the sample. The bright area indicates the heat generated by the current that passing through the sample (Joule effect). During the test dark dots appeared on the white ice surface, as in Fig. 6.19b. The dark dots represent the point in which the ice is turning into water. When the ice between the electrodes was completely removed, as in Fig. 6.19c, the ice melting time was ended.

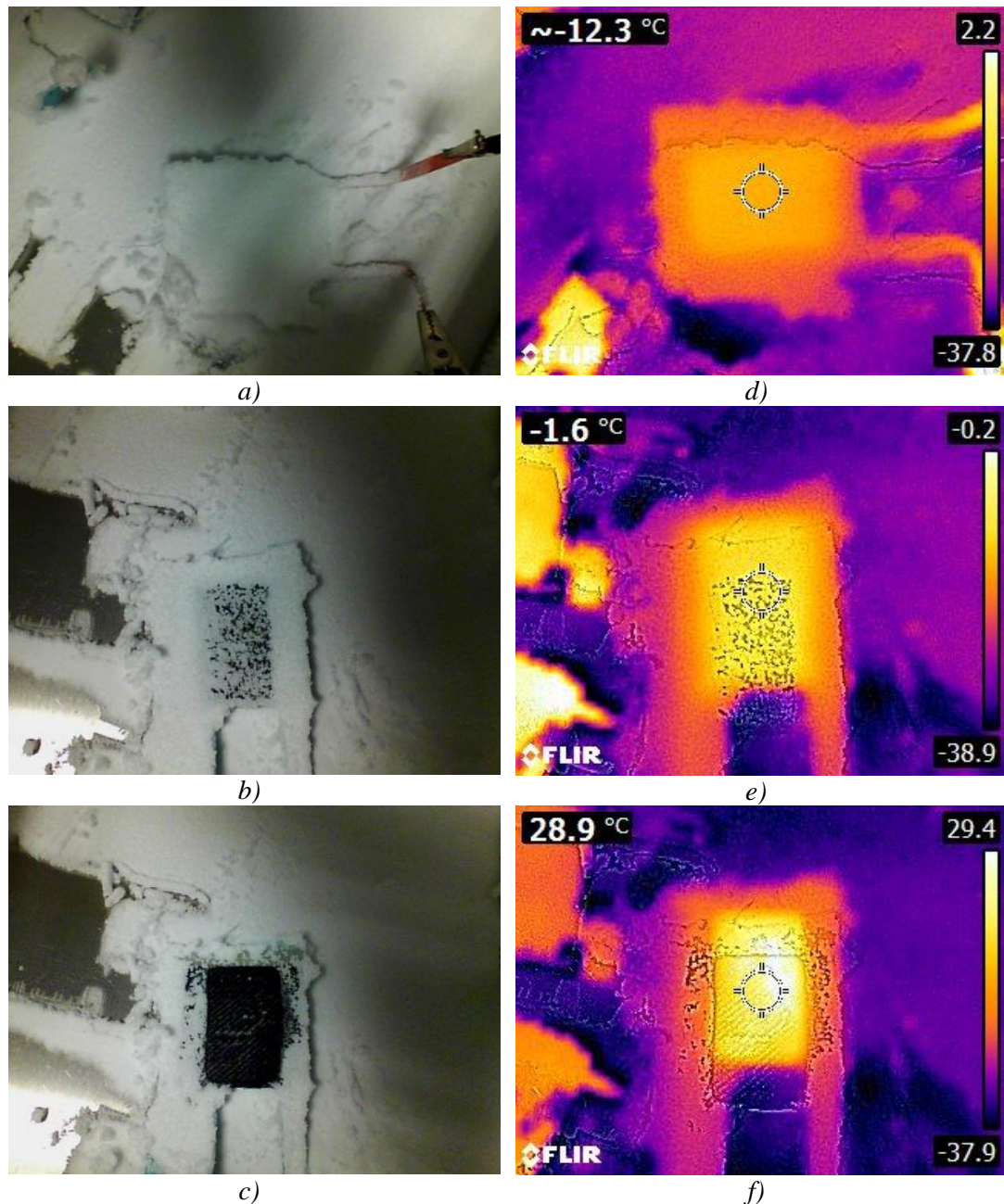


Fig. 6.19 - Photos (left column) and thermal imaging (right column) of the de-icing test for an EF-MWCNP sample: a, d) at the beginning of the heating; b, e) during the ice melting; c, f) at the end of the ice melting

Fig. 6.20 shows an example of the increase of surface temperature T of two samples (EF-MWCNP and EL2-MWCNP) during the de-icing test. The ice melting time is characterized by a plateau of temperature values; this plateau is visible in Fig. 6.20 from 50 s to 315 s. During the ice melting, the measured temperature was slightly below 0°C (around $-1^{\circ}\text{C} \sim -2^{\circ}\text{C}$). The camera was measuring the temperature in the

centre of the sample where there was an ice/water mixed phase. For this reason, the measured temperature was not exactly 0°C, as thermodynamically expected. The ice melting started when melting spots appeared on the sample, as in Fig. 6.19b. The test was completed when the ice disappeared from the surface between the two electrodes, as shown in Fig. 6.19c. EF-MWCNP average electrical resistance is lower than EL2-MWCNP one. The heat developed by electro-thermal effect is proportional to the electrical power (Eq. 6, section 3.8.2) generated by the samples. At constant voltage (5 V) samples with different electrical resistances generate different amounts of heat. The electrical power is proportional to the square value of the current. Samples with low electrical resistance (high current) will generate more heat than samples with high electrical resistance (low current). A lower amount of heat generated causes longer ice melting time. EF-MWCNP samples have lower ice melting time than EL2-MWCNP due to the lower electrical resistance of EF-MWCNP samples. This difference can be further noticed from the graph in Fig. 6.20: the plateau of EF-MWCNP samples is shorter than the EL2-MWCNP one. From the graph in Fig. 6.20, the EF-MWCNP plateau starts at ~50 s and it ends at ~200 s, so the EF-MWCNP ice melting time is ~150 s. The EL2-MWCNP plateau starts at ~50 s and it ends at ~300 s, so the EL2-MWCNP ice melting time is ~250 s.

In Table 6.11 the power consumption during the de-icing test is listed. The surface of the samples is approximately 0.003 m². At the end of the experiments, power density values were < 1 kW/m². The power density of MWCNP has been calculated for one layer with 5.5 Ω resistance with an applied voltage of 5 V. The electrical resistance increase produced by the resin infiltration caused the power density decrease. In these experiments the Silikopon EF resin offered the samples with the lowest electrical resistance and therefore the highest power density (~0.7 kW/m²). For a more efficient

ice-protection system, the electrical resistance of the CNP based composite should be reduced to increase the power density value and to reduce the ice melting time. The dilution with the proper solvent would improve the impregnation characteristics of the resin and reduce the electrical resistance increase. The icephobic characteristics of the Silikopon EF resin combined with the promising heating performances of the CNP-based self-heating composites and the optimization of the fabrication process will produce composite materials with promising characteristics for ice protection applications.

Table 6.11 - Power densities of the ice protection test

Sample	Power density (kW/m ²)	St.dev. (kW/m ²)
MWCNP	1.38	/
EF-MWCNP	0.68	0.09
EL2-MWCNP	0.52	0.05

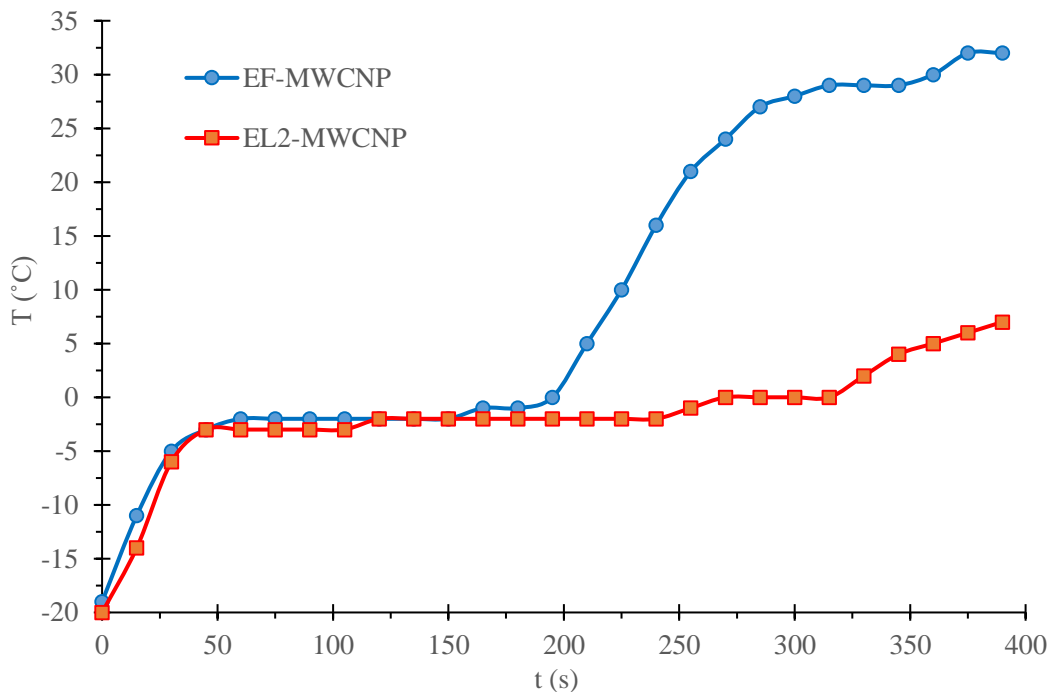


Fig. 6.20 - Example of temperature versus heating time during the de-icing test for one EF-MWCNP sample and one EL2-MWCNP sample

6.3 Summary

For the one-layer configuration experiments, CNPs (NA-CNP and MWCNP) were soaked in the resin (EL2 or Silikopon EF) and laid-up with glass fibre fabrics. Compared to the single buckypaper layer, the composite samples (with one layer of CNP) showed more than 50% increase of the electrical resistance. The electrical resistance increase is due to the insulating characteristics of the thermosetting resins. The NA-CNP based composite samples showed more than 80% electrical resistance increase, due to the formation of bigger CNT bundles increasing the electrical resistance of the respective composite samples. The electrical resistance of samples impregnated with Silikopone resin was lower than the electrical resistance of samples impregnated with EL2. The one-layer composites showed promising heating performances as self-heating composite for ice protection systems.

In the two-layer configuration experiments, different methods to fabricate a self-heating nanocomposite have been studied and characterized. In resin impregnation method the CNPs were soaked in araldite MY750 (diluted in acetone), while in the pre-preg method the buckypaper layers were layered between cyanate ester pre-preg fabrics. The pre-preg method was demonstrated to be ineffective as a production method: the resin amount was not enough to bond the layers together, therefore causing delamination.

The electrical resistance of the resin impregnation samples was around 4 ~ 5 Ω . Compared to the one-layer composite sample, for the two-layer composite samples the ruining effect of the insulating resin was lower. The resin, diluted with acetone, has been able to impregnate the 2 layers of CNP, causing a slightly electrical resistance increase.

Heating performance and ice protection tests showed power density values (2 kW/m^2) within the range reported in the literature. Flexural test and ILSS show that in RP process the buckypaper did not weaken the mechanical characteristics, as for RV samples. The overall results indicate RP method as a possible process to produce self-heating nanocomposite.

Chapter 7 Technical discussion

Different treatments have been tested to improve the electrical characteristics of the carbon nanotubes and the resulting buckypaper.

7.1 Acid treatment effects on CNT network

For the acid treatments, the nitric acid was chosen as best candidate. The treatment was effective on reducing the amorphous carbon. The SEM images indicated a low amount of CNT aggregates on NA-CNP surface, due to the effect of the MWCNTs oxidation. Nitric acid is a strong oxidizing agent, therefore some amorphous carbon would be removed [33, 141, 164], which helps to make the NA-CNP surface much flatter than MWCNP. The reduction of amorphous carbon allows a more compact (around 32% less thickness) configuration of NA-CNP, without sacrificing electrical conductivity. The 2-NA-CNP (double thickness configuration) showed a 35% reduction in electrical resistivity and 54% increase in electrical conductivity. Despite the same electrical resistance value ($\sim 6 \Omega$), the nitric acid-treated CNTs are more effective in the construction of a thin-layer electrical conducting network. Accordingly to Zhang et al. [42] work, the acid treated buckypaper showed improved electrical conductivity. The electrical conductivity increase in Zhang's work was higher ($\sim 60\%$) than in the NA-CNP sample (54%). Unlike Zhang's work, the acid treated buckypaper has not been heat treated; the heat treatment were used to remove the surfactant from the paper. Due to its non-conductive nature, the surfactant Triton X-100 could interfere with the electron transport wrapping around the tubes or accumulating at the contact area of the nanotubes, causing an increase in the electrical resistance [42]. Removing the surfactant, by heat treatment, would result in further improvements of the electrical conductivity. Promising results were obtained during the de-icing test: the power

density of the CNP based heater was around 62% lower than the power density of the traditional heater [74]. This highlight the potential application of the CNP as ice protection system.

7.2 ZnO coatings results

To improve the electrical conductivity of the nanotubes web, ZnO was used as jointing agent on CNTs coatings. In ALD samples, the zinc oxide completely covered the surface of the sample, following the morphology of the nanotubes coatings. The parameters of the reacting chamber allowed the formation of the coating around the carbon nanotubes. Each nanotube and their junction areas were covered by zinc oxide. Similar morphology were obtained in other research works (Fig. 7. 1 [225, 226]). The homogeneous morphology of the ZnO coating caused the highest reduction in electrical sheet resistance. Despite the electrical sheet resistance reduction for ALD coatings, the results indicated the ineffectiveness of the ZnO in reducing the electrical resistance of the buckypaper. The irregular distribution of the ZnO coated spots could have caused the breaking of the CNP.

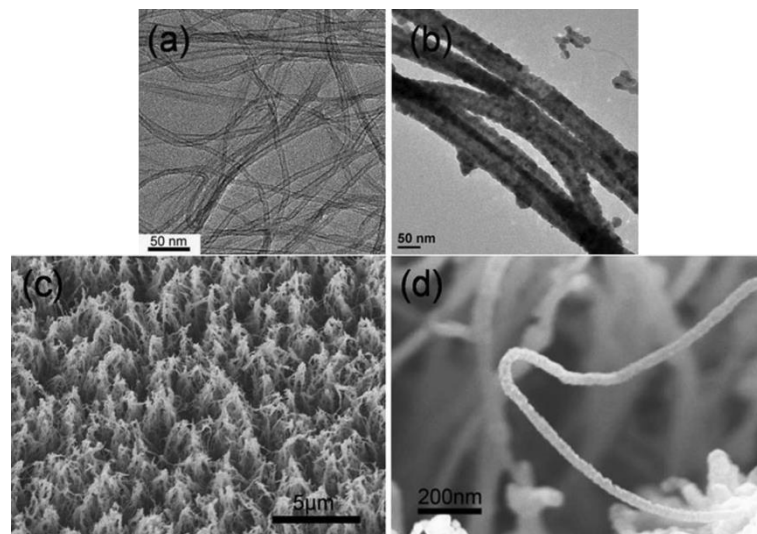


Fig. 7. 1 – a) TEM image of PECVD-grown CNTs. b) TEM image of ALD ZnO-coated CNTs. c - d) SEM images of ALD ZnO-coated CNTs [226]

Further work could be done to investigate the proper ZnO precursor solution; the precursor solution would be able to penetrate through the CNP, improving its electrical characteristics, without compromising its structural integrity.

7.3 Effects of doping agents on CNP characteristics

High electrically conductive particles were mixed with the CNTs in order to improve the electrical characteristics of the buckypaper. The efficiency of the doping particles is based on their characteristics. Such particles as graphene, with a high directional electrical conductivity (along their plane), need an aligned configuration in the CNP structure. The random orientation of the GPH particles caused no improvements of the electrical resistance and, moreover, it caused a crack resistance reduction. The aligned configuration of the GPH particles would increase the electrical resistance of the CNP, avoiding the crack resistance reduction. Patole et al. [65] obtained ~60% increase of the electrical conductivity by adding graphene to a CNT buckypaper. A possible explanation of the different result could be the sonication time. Their graphene/CNT solution was sonicated for 24 h; a higher sonication time would help to obtain a more compact configuration in the final buckypaper, avoiding its weakening and breaking.

For μ -Cu doped CNP, the powder in the samples was oxidized during the drying process of the doped CNP. The oxidation was confirmed by the XPS analysis of the Cu powder. The interaction area between the CNTs and the oxidized Cu micropowder caused a local increase of the electrical resistance. The CNP electrical conductivity was decreased by these high electrical resistance areas. In n-Cu doped CNP, CNT/Cu agglomerates were created by the interactions between CNTs and Cu nanoparticles. This agglomerated structures affected the electrical conductivity of the doped CNP (around 59% less). Byrne et al. [68] developed a Cu/CNT buckypaper with an

electrical conductivity 3.5 times higher than the pristine buckypaper. With a different process, non oxidized copper particles were deposited on the nanotube surfaces. An even distribution of copper particles would reduced the contact resistance between nanotubes, increasing the electrical conductivity of the Cu/CNT buckypaper.

The effective doping agents were silver flakes and silver nanowires. The micron size Ag flakes interacted with the carbon nanotubes, reducing the electrical resistance of the CNT/Ag web. The silver nanowires minimum amount (0.1 g) to reduce the CNP electrical resistance was around 40% lower than the silver flakes amount value (0.3g). Silver nanowires interaction with carbon nanotubes was better than silver flakes. Silver nanowires seemed to be the ideal candidates as doping agent. A combination of nitric acid treated MWCNTs and silver flakes will led to a more conductive buckypaper, with optimal electrical characteristics for integration in electro-thermal composite structure. The nanoparticles showed better improvements than micron-size ones, as indicated from the comparison between AgNWs doped CNP and Ag flakes doped ones. The improved contact between AgNWs and CNTs explains the different behaviour of the Ag particles. Similar Ag doped buckypapers (Fig. 7. 2) were produced by Oluwalowo et al. [63]. Their work reported that smaller the Ag particle higher is the electrical conductivity increase. The electrical conductivity of their AgNW/CNT buckypaper (round paper with 50 mm diameter) was ~130 S/m. The 20AgNWs-CNP electrical conductivity (2.4 kS/m) is considerably higher than the AgNW/CNT buckypaper in the literature. The difference can be explained by the higher amount of AgNWs used in these experiments.

The silver demonstrated even a non-effective behaviour. The silver decorated CNTs did not show any electrical conductivity improvements. The silver decorated CNTs by Tollen reaction demonstrated that to obtain CNP electrical resistance improvements,

a good level of nanoparticles dispersion, in the CNP structure, should be obtained. Silver would help to the electrical conductivity of the CNP only if evenly distributed in the buckypaper structure. The homogeneous distribution of the nanoparticles would avoid the electrical resistance increase of the doped CNP, due to particle agglomerates formation, and the doped CNP crack resistance reduction.

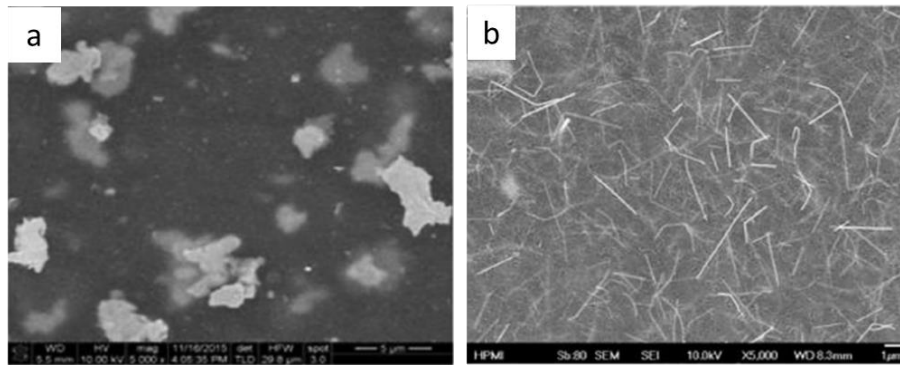


Fig. 7. 2 – a) 20 μm CNT/Ag composite. b) CNT/AgNW composite [63]

7.4 Overall results of CNP based composites

For the composite experiments with one-layer configuration, CNPs (NA-CNP and MWCNP) were soaked in the resin (EL2 or Silikopon EF) and laid-up with glass fibre fabrics. The insulating characteristics of the thermosetting resins increased the electrical resistance of the impregnated buckypapers. The NA-CNP based composite samples showed more than 80% electrical resistance increase, due to the more compact configuration of the acid treated buckypaper. The electrical resistance of samples impregnated with Silikopone resin is lower than the electrical resistance of samples impregnated with EL2. To reduce the electrical resistance increase, the viscosity of the resin should be reduced; the dilution would reduce the viscosity of the resin and facilitate the impregnation of the buckypaper.

In the two-layer configuration experiments, different methods to fabricate a self-heating nanocomposite have been studied and characterized. In resin impregnation

method the CNPs were soaked in araldite MY750 (diluted in acetone), while in the pre-preg method the buckypaper layers were layered between cyanate ester pre-preg fabrics.

Pre-preg samples (PP and PV) have almost ~50% lower electrical resistance than resin impregnation ones. The buckypaper used in pre-preg method were not previously soaked in any thermosetting resin. The low amount of resin involved in the process, coming from the pre-preg fabric, should be the reason of the nul electrical resistance increase. The silver paint, applied on the electrode surfaces, increased the electrical conductivity at the CNP/electrode interface. The delamination that occurred for PP an PV samples should be a further effect of the low amount of resin. The thermosetting resin did not infiltrate the layers and formed proper bonding. The amount of resin coming from the pre-preg fabric was not enough to completely impregnate the CNT sheets and to affect/increase their electrical resistance. The pre-preg method was demonstrated to be ineffective as a production method.

For the two-layer composite samples, the ruining effect of the insulating resin was lower. The resin, diluted with acetone, has been able to impregnate the 2 layers of CNP, causing a slightly electrical resistance increase. Heating performance and ice protection tests showed power density values (2 kW/m^2) within the range reported in the literature [69, 71, 72]. The speed of rising temperature for the RV-CNP and RP-CNP samples was $\sim 0.8^\circ\text{C/s}$. The traditional heater, studied by Zhao et al. [74], has a heating rate of 0.6°C/s . The better performance indicates the RV and the RP heater as a potential substitute of the traditional metal heater. The power density of the CNP based heater 70% lower than the power density of the traditional heater (Zhao et al. [74]). A low power density indicate a low power consumption of the ice protection

system. The CNP based heater shows an impressive energy saving result. This result highlight the potential application of the CNP based heater as ice protection system. Flexural test and ILSS show that in RP process the buckypaper did not weaken the mechanical characteristics, as for RV samples. Similar production process was used in Tarfaoui et al. [194] work and the resulting composite has similar mechanical properties (in-plane shear of 44.7 MPa). In ILSS test the average $\epsilon\%$ value at the end of the test is between $\sim 18\%$ for RP-CNP samples and between $\sim 22\%$ for RP-ref. These results indicate a more rigid behaviour for RP-CNP samples. The presence of an element (CNP/resin) with different mechanical characteristics is the reason for its rigid behaviour. Working with acid treated buckypaper will help to overcome the rigid behaviour issue, reducing the thickness of material with different mechanical charactersitics. Moreover, Zhu et al. [224] and Guo et al. [55] demonstrated clear enhancement in the mechanical properties of epoxy resins, as ultimate strength (30-70% increase) and elastic modulus (50% increase) and fracture toughness (127.8% increase of fracture strain at break[55]), using functionlised carbon nanotubes. The overall results, from ice protection performance to mechanical properties, indicate RP method as a possible process to produce self-heating nanocomposite.

Chapter 7 Conclusions

This project aim was to fabricate self-heating nanocomposites from electrical conducting nanomaterials, as an effective de-icing approach in aerospace. The nanocomposite electro-thermal structures are expected to offer enhanced mechanical and electrical properties, thanks to the natural advances of nanocomposites. Carbon nanotubes have been chosen as candidate nanomaterials in this project. The electrical conductivity of the carbon nanotubes has been improved by different treatments or applied coatings. The modified carbon nanotubes were used to produce conducting films (carbon nanotube buckypapers) by filtration approach. These films (CNPs) have been integrated into different composite structures. Heating performances, mechanical and electrical characteristics of the produced composite samples were analysed.

- Acid treatments: high temperatures treatments indicated the nitric acid as the best candidate for the room temperature treatment. Nitric acid treatment (room temperature) of the carbon nanotubes led to a more compact (around 32% thinner) configuration of the CNP layer, without sacrificing the electrical conductivity. Power densities of the CNP devices in the de-icing test were around 3 kW/m^2 , suggesting a good potential as a self-heating element that could be integrated into a composite structure for ice protection purpose.
- ZnO coatings: ALD samples showed high reduction in electrical sheet resistance reduction of the CNT layers (CNTs sprayed on glass substrates). The CNP coated with ZnO did not show the same improvements. The ZnO coating caused the embrittlement and the breaking of the coated CNP.
- Silver decoration: TEM images of Tollen samples revealed the inhomogeneous distribution of silver particles aggregated on the nanotubes, causing the

formation of CNT bundles. The NA-T-CNTs were used to produce carbon nanotube buckypaper, but failed during the peeling-off. The high concentration of the Ag/CNT agglomerates was the cause of the CNP weakening.

- Doping agents: copper and graphene were not as effective as the silver particles. The micron size Ag flakes interacted with the carbon nanotubes, reducing the electrical resistance of the CNT/Ag web. The silver nanowires minimum amount (0.1 g), to reduce the CNP electrical resistance, was around 40% lower than the silver flakes amount value (0.3g). Silver nanowires interaction with carbon nanotubes was better than silver flakes. Silver nanowires seemed to be the ideal candidates as doping agent.
- Composite fabrication (one layer configuration): CNPs (NA-CNP and MWCNP) were soaked in the resin and laid-up with glass fibre fabrics. The respective composite samples showed an increase of the electrical resistance due to the insulating characteristics of the thermosetting resins. The NA-CNP based composite samples showed the highest increase in electrical resistance; due to the more compact NA-CNP configuration, the resin would penetrate with more difficulty through the NA-CNT bundles. The formation of bigger resin/CNT bundles increased the electrical resistance of the composite samples. The MWCNP based composites showed promising heating performances as self-heating composite for ice protection.
- Composite fabrication (two layer configuration): two methods to fabricate a self-heating nanocomposite have been studied: electrical resistance test indicated that both methods produced samples with electrical resistance lower than 5Ω . In the pre-preg method, the resin did not affect the electrical resistance, but its amount was not enough to bond the layers together causing

delamination. Heating performance and ice melting tests demonstrated power density values (2 kW/m^2) within the range reported in the literature. Lower voltages could be used, which sacrifices the ice melting time, but reduces the risk of thermal damage of the composite structure. Power density values can be increased by further reduction of the electrical resistance of the CNTs composite. The flexural test and ILSS show that in RP process the buckypaper did not weaken the mechanical characteristics, as for RV samples. The pressure during curing cycle helped to create a stronger bond between buckypaper and matrix. The overall results indicate the RP method as a possible process to produce self-heating nanocomposite.

Chapter 8 Future work

For further study, a few key research directions are proposed as below.

ZnO deposited by ALD method has confirmed the effective reduction in electrical sheet resistance. Future works could be focused on optimizing the electrical characteristics of CNP using ZnO coatings or particles, with good mechanical properties.

The Ag decoration results indicated that the both silver decoration methods need improvements. More works could be conducted to improve the quantity of the deposited particles (especially for the NaOH method) and/or their distribution on the CNT surfaces and to avoid the oxidation.

The graphene particles interacted with the carbon nanotubes and formed randomly oriented GPH/CNT agglomerates. Obtaining a more GPH/CNT aligned configuration to improve the buckypaper electrical properties, without compromising its integrity, could be a future goal of research.

Cu nanoparticles interacted with CNTs and formed Cu/CNT agglomerates that increased the CNP electrical conductivity. The optimization of the process to obtain a better distribution of Cu nanoparticles may lead to improved electrical characteristics of CNP.

The oxidation of the Cu micropowder caused the CNP electrical resistance increase. Avoiding the particle oxidation during the doping process could be necessary to improve the electrical characteristics of CNP.

For the CNP based composite, the electrical characteristics of the one layer samples could be improved. The dilution of the resin in a proper solvent would help the resin

impregnation, reducing the increase of the electrical resistance. Future research works could be focused on the optimization of the solvent/resin ratio and the fabrication process.

Studies could be carried out to optimize the manufacturing process of the self-heating composite. The comprehension of the mechanical properties and behaviour of nanocomposites are a fundamental step for composites use in the applications of new generation materials.

More research could be carried out done to study and to design CNP based composite with different geometries. Furthermore, the process scale-up could be studied in order to integrate the new nanocomposite in real dimension industrial components. Theoretical analysis could be executed to be capable to predict the CNP based composite characteristics.

References

- [1] A. Amendola and G. Mingione, "On the problem of icing for modern civil aircraft," *Air & Space Europe*, vol. 3, no. 3, pp. 214-217, 2001.
- [2] P. Koivisto, "Effects of Cold Soaked Fuel Frost on Lift Degradation during Simulated Take-off," *Finnish Transport Safety Agency, Trafi Research Reports*, pp. 4-2015, 2015.
- [3] T. Vukits, "Overview and risk assessment of icing for transport category aircraft and components," in *40th AIAA Aerospace Sciences Meeting & Exhibit*, 2002, p. 811.
- [4] R. W. Gent, N. P. Dart, and J. T. Cansdale, "Aircraft icing," *Philosophical Transactions of the Royal Society of London. Series A: Mathematical, Physical and Engineering Sciences*, vol. 358, no. 1776, pp. 2873-2911, 2000.
- [5] F. A. A. U.S. Department of Transportation, "Aviation Maintenance Technician Handbook," Handbook vol. 1 - 2, 2012.
- [6] O. Parent and A. Ilinca, "Anti-icing and de-icing techniques for wind turbines: Critical review," *Cold Regions Science and Technology*, vol. 65, no. 1, pp. 88-96, 2011.
- [7] C.-C. Hung, M. E. Dillehay, and M. Stahl, "A heater made from graphite composite material for potential deicing application," *Journal of Aircraft*, vol. 24, no. 10, pp. 725-730, 1987.
- [8] O. Gohardani, M. C. Elola, and C. Elizetxea, "Potential and prospective implementation of carbon nanotubes on next generation aircraft and space vehicles: A review of current and expected applications in aerospace sciences," *Progress in Aerospace Sciences*, vol. 70, pp. 42-68, 2014.
- [9] N. Dalili, A. Edrissy, and R. Carriveau, "A review of surface engineering issues critical to wind turbine performance," *Renewable and Sustainable Energy Reviews*, vol. 13, no. 2, pp. 428-438, 2009.
- [10] H. Seifert, "Technical requirements for rotor blades operating in cold climate," in *VI BOREAS Conference, Pyhatunturi, Finland*, 2003.
- [11] Z. Goraj, "An overview of the deicing and anti-icing technologies with prospects for the future," in *24th International Congress of the Aeronautical Sciences*, vol. 29, 2004.
- [12] E. Peltola *et al.*, "Specific recommendations for the development of wind energy projects in cold climates," *Proceedings of Boreas VII, Saariselkä, Finland*, pp. 12-13, 2005.
- [13] B. Marinho, M. Ghislandi, E. Tkalya, C. E. Koning, and G. de With, "Electrical conductivity of compacts of graphene, multi-wall carbon nanotubes, carbon black, and graphite powder," *Powder Technology*, vol. 221, pp. 351-358, 2012.
- [14] M. Moniruzzaman and K. I. Winey, "Polymer nanocomposites containing carbon nanotubes," *Macromolecules*, vol. 39, no. 16, pp. 5194-5205, 2006.
- [15] S. Stankovich *et al.*, "Graphene-based composite materials," *nature*, vol. 442, no. 7100, pp. 282-286, 2006.
- [16] O. Yu, P. Jing-Cui, W. Hui, and P. Zhi-Hua, "The rehybridization of electronic orbitals in carbon nanotubes," *Chinese Physics B*, vol. 17, no. 8, p. 3123, 2008.
- [17] S. Reich, C. Thomsen, and J. Maultzsch, *Carbon nanotubes: basic concepts and physical properties*. John Wiley & Sons, 2008.
- [18] G. Peschel, "Carbon-carbon bonds: hybridization," *Obtained online from: [207](http://www.physik.fu-berlin.de/einrichtungen/ag/ag-</i></div><div data-bbox=)*

reich/lehre/Archiv/ss2011/docs/Gina_Peschel-Handout.pdf, published on, vol. 5, no. 5, 2011.

- [19] Z. Wu, Z. Chen, X. Du, J. Logan, J. Sippel, M. Nikolou, K. Kamaras, J. Reynolds, D. Tanner, A. Hebard, A. Rinzler, "Transparent, conductive carbon nanotube films," *Science*, vol. 305, no. 5688, pp. 1273-1276, 2004.
- [20] S. De and J. N. Coleman, "The effects of percolation in nanostructured transparent conductors," *Mrs Bulletin*, vol. 36, no. 10, pp. 774-781, 2011.
- [21] M. Kaempgen, G. Duesberg, and S. Roth, "Transparent carbon nanotube coatings," *Applied Surface Science*, vol. 252, no. 2, pp. 425-429, 2005.
- [22] L. f. C. SWCNTs (HiPco, Houston, USA; MWCNTs from Infineon Technologies, Munich, Germany.
- [23] A. Kaiser, G. Düsberg, and S. Roth, "Heterogeneous model for conduction in carbon nanotubes," *Physical Review B*, vol. 57, no. 3, p. 1418, 1998.
- [24] A.P.Graham, G.S.Duesberg, R.Seidel, M.LiebauE.UngerF.KreuplW.Hönlein, "Towards the integration of carbon nanotubes in microelectronics," *Diamond and related materials*, vol. 13, no. 4, pp. 1296-1300, 2004.
- [25] G. Duesberg, A.P.Graham, F.Kreupl, M.Liebau, R.Seidel, E.Unger, W.Hoenlein, "Ways towards the scaleable integration of carbon nanotubes into silicon based technology," *Diamond and related Materials*, vol. 13, no. 2, pp. 354-361, 2004.
- [26] R. R. Mitchell, N. Yamamoto, H. Cebeci, B. L. Wardle, and C. V. Thompson, "A technique for spatially-resolved contact resistance-free electrical conductivity measurements of aligned-carbon nanotube/polymer nanocomposites," *Composites Science and Technology*, vol. 74, pp. 205-210, 2013.
- [27] E. T. Thostenson, C. Li, and T.-W. Chou, "Nanocomposites in context," *Composites Science and Technology*, vol. 65, no. 3, pp. 491-516, 2005.
- [28] T.-W. Chou, L. Gao, E. T. Thostenson, Z. Zhang, and J.-H. Byun, "An assessment of the science and technology of carbon nanotube-based fibers and composites," *Composites Science and Technology*, vol. 70, no. 1, pp. 1-19, 2010.
- [29] J. N. Coleman, U. Khan, W. J. Blau, and Y. K. Gun'ko, "Small but strong: a review of the mechanical properties of carbon nanotube-polymer composites," *Carbon*, vol. 44, no. 9, pp. 1624-1652, 2006.
- [30] B. Wei, R. Vajtai, and P. Ajayan, "Reliability and current carrying capacity of carbon nanotubes," *Applied Physics Letters*, vol. 79, no. 8, pp. 1172-1174, 2001.
- [31] P. Poncharal, C. Berger, Y. Yi, Z. Wang, and W. A. de Heer, "Room temperature ballistic conduction in carbon nanotubes," ed: ACS Publications, 2002.
- [32] M. Tehrani, M Safdari, A Y Boroujeni, Z Razavi, S W Case, K Dahmen, H Garmestani and M S Al-Haik, "Hybrid carbon fiber/carbon nanotube composites for structural damping applications," *Nanotechnology*, vol. 24, no. 15, p. 155704, 2013.
- [33] V. Datsyuka, M.Kalyvaa, K.Papagelisb, J.Partheniosab, D.Tasisb, A.SiokouaI, Kallitsisac, C.Galiotisab, "Chemical oxidation of multiwalled carbon nanotubes," *Carbon*, vol. 46, no. 6, pp. 833-840, 2008.
- [34] J. Kwon and H. Kim, "Comparison of the properties of waterborne polyurethane/multiwalled carbon nanotube and acid-treated multiwalled carbon nanotube composites prepared by in situ polymerization," *Journal of*

- Polymer Science Part A: Polymer Chemistry*, vol. 43, no. 17, pp. 3973-3985, 2005.
- [35] J. Y. Kwon and H. D. Kim, "Preparation and properties of acid-treated multiwalled carbon nanotube/waterborne polyurethane nanocomposites," *Journal of Applied Polymer Science*, vol. 96, no. 2, pp. 595-604, 2005.
- [36] X. G. Luo, X. X. Huang, X. X. Wang, X. H. Zhong, X. X. Meng, and J. N. Wang, "Continuous preparation of carbon nanotube film and its applications in fuel and solar cells," *ACS applied materials & interfaces*, vol. 8, no. 12, pp. 7818-7825, 2016.
- [37] R. A. Susantyoko, Z. Karam, S. Alkhoori, I. Mustafa, C.-H. Wu, and S. Almheiri, "A surface-engineered tape-casting fabrication technique toward the commercialisation of freestanding carbon nanotube sheets," *Journal of Materials Chemistry A*, vol. 5, no. 36, pp. 19255-19266, 2017.
- [38] K. Mukai, K. Asaka, T. Sugino, K. Kiyohara, I. Takeuchi, N. Terasawa, N. Futaba, K. Hata, T. Fukushima, T. Aida, "Highly conductive sheets from millimeter-long single-walled carbon nanotubes and ionic liquids: application to fast-moving, low-voltage electromechanical actuators operable in air," *Advanced materials*, vol. 21, no. 16, pp. 1582-1585, 2009.
- [39] W. Lee, H. Koo, J. Sun, J. Noh, K. Kwon, C. Yeom, Y. Choi, K. Chen, A. Javey and G. Cho, "A fully roll-to-roll gravure-printed carbon nanotube-based active matrix for multi-touch sensors," *Scientific reports*, vol. 5, p. 17707, 2015.
- [40] D. D. Tune, A.J. Cameron, J. Shearer, K. Moore, M. Pfohl, J. Shapter, B. Flavel, "Aligned carbon nanotube thin films from liquid crystal polyelectrolyte inks," *ACS applied materials & interfaces*, vol. 7, no. 46, pp. 25857-25864, 2015.
- [41] X. He, W. Gao, L. Xie, B. Li, Q. Zhang, S. Lei, J. M. Robinson, E. H. Házroz, S. K. Doorn, W. Wang, R. Vajtai, P. M. Ajayan, W. W. Adams, R. H. Hauge & Junichiro., "Wafer-scale monodomain films of spontaneously aligned single-walled carbon nanotubes," *Nature nanotechnology*, vol. 11, no. 7, p. 633, 2016.
- [42] S. Zhang, B. E. Leonhardt, N. Nguyen, A. Oluwalowo, C. Jolowsky, A. Hao, R. Liang and J. G. Park, "Roll-to-roll continuous carbon nanotube sheets with high electrical conductivity," *RSC advances*, vol. 8, no. 23, pp. 12692-12700, 2018.
- [43] N. Behabtu, C. C. Young, D. E. Tsentelovich, O. Kleinerman, X. Wang, A. W. K. Ma, E. Amram, "Strong, light, multifunctional fibers of carbon nanotubes with ultrahigh conductivity," *science*, vol. 339, no. 6116, pp. 182-186, 2013.
- [44] Y. Zhao, J. Wei, R. Vajtai, P. M. Ajayan, and E. V. Barrera, "Iodine doped carbon nanotube cables exceeding specific electrical conductivity of metals," *Scientific reports*, vol. 1, p. 83, 2011.
- [45] I.-W. P. Chen, R. Liang, H. Zhao, B. Wang, and C. Zhang, "Highly conductive carbon nanotube buckypapers with improved doping stability via conjugational cross-linking," *Nanotechnology*, vol. 22, no. 48, p. 485708, 2011.
- [46] S. Gantayat, D. Rout, and S. K. Swain, "Mechanical properties of functionalized multiwalled carbon nanotube/epoxy nanocomposites," *Materials Today: Proceedings*, vol. 4, no. 2, pp. 4061-4064, 2017.

- [47] J. Chen, J. Han, and D. Xu, "Thermal and electrical properties of the epoxy nanocomposites reinforced with purified carbon nanotubes," *Materials Letters*, vol. 246, pp. 20-23, 2019.
- [48] N. Ferreira Braga, H. Morales Zaggo, L. Stieven Montagna, and F. Roberto Passador, "Effect of Carbon Nanotubes (CNT) Functionalization and Maleic Anhydride-Grafted Poly (trimethylene terephthalate)(PTT-g-MA) on the Preparation of Antistatic Packages of PTT/CNT Nanocomposites," *Journal of Composites Science*, vol. 4, no. 2, p. 44, 2020.
- [49] M. Carmo, V. Paganin, J. Rosolen, and E. Gonzalez, "Alternative supports for the preparation of catalysts for low-temperature fuel cells: the use of carbon nanotubes," *Journal of Power Sources*, vol. 142, no. 1-2, pp. 169-176, 2005.
- [50] P. Chen, X. Wu, J. Lin, and K. Tan, "Synthesis of Cu nanoparticles and microsized fibers by using carbon nanotubes as a template," *The Journal of Physical Chemistry B*, vol. 103, no. 22, pp. 4559-4561, 1999.
- [51] W. Chen, K. P. Loh, H. Xu, and A. T. S. Wee, "Nanoparticle dispersion on reconstructed carbon nanomeshes," *Langmuir*, vol. 20, no. 25, pp. 10779-10784, 2004.
- [52] T. M. Day, P. R. Unwin, N. R. Wilson, and J. V. Macpherson, "Electrochemical templating of metal nanoparticles and nanowires on single-walled carbon nanotube networks," *Journal of the American Chemical Society*, vol. 127, no. 30, pp. 10639-10647, 2005.
- [53] D.-J. Guo and H.-L. Li, "High dispersion and electrocatalytic properties of palladium nanoparticles on single-walled carbon nanotubes," *Journal of colloid and interface science*, vol. 286, no. 1, pp. 274-279, 2005.
- [54] D.-j. Guo and H.-l. Li, "Electrochemical synthesis of Pd nanoparticles on functional MWNT surfaces," *Electrochemistry communications*, vol. 6, no. 10, pp. 999-1003, 2004.
- [55] P. Guo, X. Chen, X. Gao, H. Song, and H. Shen, "Fabrication and mechanical properties of well-dispersed multiwalled carbon nanotubes/epoxy composites," *Composites science and Technology*, vol. 67, no. 15-16, pp. 3331-3337, 2007.
- [56] Z. He, J. Chen, D. Liu, H. Zhou, and Y. Kuang, "Electrodeposition of Pt–Ru nanoparticles on carbon nanotubes and their electrocatalytic properties for methanol electrooxidation," *Diamond and Related Materials*, vol. 13, no. 10, pp. 1764-1770, 2004.
- [57] F. Ahmadpoor, S. M. Zebarjad, and K. Janghorban, "Decoration of multi-walled carbon nanotubes with silver nanoparticles and investigation on its colloid stability," *Materials Chemistry and Physics*, vol. 139, no. 1, pp. 113-117, 2013.
- [58] Y. Liu, J. Tang, X. Chen, W. Chen, G. Pang, and J. Xin, "A wet-chemical route for the decoration of CNTs with silver nanoparticles," *Carbon*, 2006.
- [59] F. Xin and L. Li, "Decoration of carbon nanotubes with silver nanoparticles for advanced CNT/polymer nanocomposites," *Composites Part A: Applied Science and Manufacturing*, vol. 42, no. 8, pp. 961-967, 2011.
- [60] D. Langley, G. Giusti, C. Mayousse, C. Celle, D. Bellet, and J.-P. Simonato, "Flexible transparent conductive materials based on silver nanowire networks: a review," *Nanotechnology*, vol. 24, no. 45, p. 452001, 2013.
- [61] S. You, Y. S. Park, H. W. Choi, and K. H. Kim, "Properties of Silver Nanowire/Zinc Oxide Transparent Bilayer Thin Films for Optoelectronic

- Applications," *Journal of nanoscience and nanotechnology*, vol. 15, no. 11, pp. 8656-8661, 2015.
- [62] Ö. Guler, F. Yo, H. Aydin, C. Aydin, F. E. Tantawy, E. S. M. Duraia & A. N. Fouda "Electrical and optical properties of carbon nanotube hybrid zinc oxide nanocomposites prepared by ball mill technique," *Fullerenes, Nanotubes and Carbon Nanostructures*, vol. 23, no. 10, pp. 865-869, 2015.
- [63] A. Oluwalowo, N. Nguyen, S. Zhang, J. G. Park, and R. Liang, "Electrical and thermal conductivity improvement of carbon nanotube and silver composites," *Carbon*, vol. 146, pp. 224-231, 2019.
- [64] F. Su and M. Miao, "Transition of electrical conductivity in carbon nanotube/silver particle composite buckypapers," *Particuology*, vol. 17, pp. 15-21, 2014.
- [65] S. P. Patole, M. F. Arif, and S. Kumar, "Polyvinyl alcohol incorporated buckypaper composites for improved multifunctional performance," *Composites Science and Technology*, vol. 168, pp. 429-436, 2018.
- [66] Y. Hu, X. Li, J. Wang, R. Li, and X. Sun, "Free-standing graphene-carbon nanotube hybrid papers used as current collector and binder free anodes for lithium ion batteries," *Journal of power sources*, vol. 237, pp. 41-46, 2013.
- [67] S. P. Patole, M. F. Arif, R. A. Susantyoko, S. Almheiri, and S. Kumar, "A wet-filtration-zipping approach for fabricating highly electroconductive and auxetic graphene/carbon nanotube hybrid buckypaper," *Scientific reports*, vol. 8, no. 1, pp. 1-12, 2018.
- [68] M. T. Byrne, Y. R. Hernandez, T. Conaty, F. M. Blighe, J. N. Coleman, and Y. K. Gun'ko, "Preparation of buckypaper-copper composites and investigation of their conductivity and mechanical properties," *ChemPhysChem*, vol. 10, no. 5, pp. 774-777, 2009.
- [69] W. Zhao, M. Li, Z. Zhang, and H. Peng, "Carbon nanotube based composites film heater for de-icing application," in *14th European Conference on Composite Materials*, 2010.
- [70] M. Mohseni, "Development of a novel electro-thermal anti-icing system for fiber-reinforced polymer composite airfoils," University of Alberta, 2012.
- [71] H. Chu, Z. Zhang, Y. Liu, and J. Leng, "Self-heating fiber reinforced polymer composite using meso/macropore carbon nanotube paper and its application in deicing," *Carbon*, vol. 66, pp. 154-163, 2014.
- [72] X. Yao, S. C. Hawkins, and B. G. Falzon, "An advanced anti-icing/de-icing system utilizing highly aligned carbon nanotube webs," *Carbon*, vol. 136, pp. 130-138, 2018.
- [73] S. T. Buschhorn, S. S. Kessler, N. Lachmann, J. Gavin, G. Thomas, and B. L. Wardle, "Electrothermal icing protection of aerosurfaces using conductive polymer nanocomposites," in *54th AIAA/ASME/ASCE/AHS/ASC Structures, Structural Dynamics, and Materials Conference*, 2013, p. 1729.
- [74] Z. Zhao, H. Chen, X. Liu, H. Liu, and D. Zhang, "Development of high-efficient synthetic electric heating coating for anti-icing/de-icing," *Surface and Coatings Technology*, vol. 349, pp. 340-346, 2018.
- [75] C.-H. Liu and X. Yu, "Silver nanowire-based transparent, flexible, and conductive thin film," *Nanoscale research letters*, vol. 6, no. 1, p. 75, 2011.
- [76] M. W. Rowell and M. D. McGehee, "Transparent electrode requirements for thin film solar cell modules," *Energy & Environmental Science*, vol. 4, no. 1, pp. 131-134, 2011.

- [77] A. Graff, D. Wagner, H. Ditlbacher, and U. Kreibig, "Silver nanowires," *The European Physical Journal D-Atomic, Molecular, Optical and Plasma Physics*, vol. 34, no. 1, pp. 263-269, 2005.
- [78] R. Hillebrand, H. Hofmeister, K. Scheerschmidt, and J. Heydenreich, "Crystallographic HREM studies of small CdTe crystallites," *Ultramicroscopy*, vol. 49, no. 1-4, pp. 252-258, 1993.
- [79] V. Gryaznov, J. Heydenreich, A. Kaprelov, S. A. Nepijko, A. Romanov, and J. Urban, "Pentagonal symmetry and disclinations in small particles," *Crystal Research and Technology*, vol. 34, no. 9, pp. 1091-1119, 1999.
- [80] J. Kang, D. Son, G.J. Nathan, W Yuxin, J. Lopez, Y. Kim, J. Young Oh, T. Katsumata, J. Mun, Y. Lee, L. Jin, J. B.-H. Tok, Z. Bao, "Tough and water-insensitive self-healing elastomer for robust electronic skin," *Advanced Materials*, vol. 30, no. 13, p. 1706846, 2018.
- [81] M. A. Ali, R. Umer, K. A. Khan, Y. A. Samad, K. Liao, and W. Cantwell, "Graphene coated piezo-resistive fabrics for liquid composite molding process monitoring," *Composites Science and Technology*, vol. 148, pp. 106-114, 2017.
- [82] S. Gao, X. Wu, H. Ma, J. Robertson, and A. Nathan, "Ultrathin multifunctional graphene-PVDF layers for multidimensional touch interactivity for flexible displays," *ACS applied materials & interfaces*, vol. 9, no. 22, pp. 18410-18416, 2017.
- [83] J. Lee, D. H. Sin, B. Moon, J. Shin, H.G.Kim, M. Kim and K. Cho, "Highly crystalline low-bandgap polymer nanowires towards high-performance thick-film organic solar cells exceeding 10% power conversion efficiency," *Energy & Environmental Science*, vol. 10, no. 1, pp. 247-257, 2017.
- [84] C.-L. Kim, J.-J. Lee, Y.-J. Oh, and D.-E. Kim, "Smart wearable heaters with high durability, flexibility, water-repellent and shape memory characteristics," *Composites Science and Technology*, vol. 152, pp. 173-180, 2017.
- [85] Y.D. Suh, J. Jung, H. Lee, J. Yeo, S.Hong, P. Lee, D. Lee and S. Hwan Ko, "Nanowire reinforced nanoparticle nanocomposite for highly flexible transparent electrodes: borrowing ideas from macrocomposites in steel-wire reinforced concrete," *Journal of Materials Chemistry C*, vol. 5, no. 4, pp. 791-798, 2017.
- [86] I. Jeon, J. Yoon, N. Ahn, M. Atwa, C. Delacou, A. Anisimov, E. I. Kauppinen, M. Choi, S. Maruyama, Y.Matsuo., "Carbon nanotubes versus graphene as flexible transparent electrodes in inverted perovskite solar cells," *The journal of physical chemistry letters*, vol. 8, no. 21, pp. 5395-5401, 2017.
- [87] Y. Leterrier, L.Médico, F.Demarco, J.A.E.Månsona, U.Betz, M.F.Escolà, M.Kharrazi, F.Atamny, "Mechanical integrity of transparent conductive oxide films for flexible polymer-based displays," *Thin Solid Films*, vol. 460, no. 1, pp. 156-166, 2004.
- [88] M. D. Lima, M. J. de Andrade, C. P. Bergmann, and S. Roth, "Thin, conductive, carbon nanotube networks over transparent substrates by electrophoretic deposition," *Journal of Materials Chemistry*, vol. 18, no. 7, pp. 776-779, 2008.
- [89] Y. Lu and K. Chou, "Tailoring of silver wires and their performance as transparent conductive coatings," *Nanotechnology*, vol. 21, no. 21, p. 215707, 2010.

- [90] V. Scardaci, R. Coull, P. E. Lyons, D. Rickard, and J. N. Coleman, "Spray deposition of highly transparent, low-resistance networks of silver nanowires over large areas," *Small*, vol. 7, no. 18, pp. 2621-2628, 2011.
- [91] M. Majumder, M. Mainak, M. Clint, R. Michelle, L. Behabtua, J. A. Eukela, R. H. Hauge, H. K. Schmidt, M. Pasquali, "Insights into the physics of spray coating of SWNT films," *Chemical Engineering Science*, vol. 65, no. 6, pp. 2000-2008, 2010.
- [92] D. S. Hecht, L. Hu, and G. Irvin, "Emerging transparent electrodes based on thin films of carbon nanotubes, graphene, and metallic nanostructures," *Advanced materials*, vol. 23, no. 13, pp. 1482-1513, 2011.
- [93] S. De, T. M. Higgins, P. E. Lyons, E. M. Doherty, P. N. Nirmalraj, W. J. Blau, J. J. Boland, J. N. Coleman, "Silver nanowire networks as flexible, transparent, conducting films: extremely high DC to optical conductivity ratios," *ACS nano*, vol. 3, no. 7, pp. 1767-1774, 2009.
- [94] J. -Won Do, D. Estrada, X. Xie, N. N. Chang, J. Mallek, G. S. Girolami, J. A. Rogers, E. Pop, J.W. Lyding, "Nanosoldering carbon nanotube junctions by local chemical vapor deposition for improved device performance," *Nano letters*, vol. 13, no. 12, pp. 5844-5850, 2013.
- [95] T. Tokuno, M. Nogi, M. Karakawa, J. Jiu, T. Nge, Y. Aso and K. Suganuma, "Fabrication of silver nanowire transparent electrodes at room temperature," *Nano Research*, vol. 4, no. 12, pp. 1215-1222, 2011.
- [96] L. Hu, H. S. Kim, J.-Y. Lee, P. Peumans, and Y. Cui, "Scalable coating and properties of transparent, flexible, silver nanowire electrodes," *ACS nano*, vol. 4, no. 5, pp. 2955-2963, 2010.
- [97] W. Zhang, R. Shen, K. Lu, A. Ji, and Z. Cao, "Nanoparticle enhanced evaporation of liquids: A case study of silicone oil and water," *AIP Advances*, vol. 2, no. 4, p. 042119, 2012.
- [98] R. D. Deegan, O. Bakajin, T. F. Dupont, G. Huber, S. R. Nagel, and T. A. Witten, "Contact line deposits in an evaporating drop," *Physical review E*, vol. 62, no. 1, p. 756, 2000.
- [99] T. Kim, Y. W. Kim, H. S. Lee, H. Kim, W. S. Yang, and K. S. Suh, "Uniformly interconnected silver-nanowire networks for transparent film heaters," *Advanced Functional Materials*, vol. 23, no. 10, pp. 1250-1255, 2013.
- [100] J. Kang, H. Kim, K. S. Kim, S. Lee, S. Bae, J.-H. Ahn, Y.-J. Kim, J.-B. Choi, B. H. Hong, "High-performance graphene-based transparent flexible heaters," *Nano letters*, vol. 11, no. 12, pp. 5154-5158, 2011.
- [101] D. Sui, Y. Huang, L. Huang, J. Liang, Y. Ma, and Y. Chen, "Flexible and transparent electrothermal film heaters based on graphene materials," *Small*, vol. 7, no. 22, pp. 3186-3192, 2011.
- [102] A. Volk, D. Knez, P. Thaler, A. W. Hauser, W. Grogger, F. Hofer and W. E. Ernst, "Thermal instabilities and Rayleigh breakup of ultrathin silver nanowires grown in helium nanodroplets," *Physical Chemistry Chemical Physics*, vol. 17, no. 38, pp. 24570-24575, 2015.
- [103] X. Zhang, X. Yan, J. Chen, and J. Zhao, "Large-size graphene microsheets as a protective layer for transparent conductive silver nanowire film heaters," *Carbon*, vol. 69, pp. 437-443, 2014.
- [104] S. Wang, Y. Tian, C. Wang, C. Hang, Y. Huang, and C. Liao, "Chemical and thermal robust tri-layer rGO/Ag NWs/GO composite film for wearable heaters," *Composites Science and Technology*, vol. 174, pp. 76-83, 2019.

- [105] Y. Cai *et al.*, "Transparent conductive film based on silver nanowires and single-wall carbon nanotubes for transparent heating films," *Nanotechnology*, vol. 30, no. 22, p. 225201, 2019.
- [106] "Treccani Encyclopaedia."
- [107] A. K. Geim, "Graphene: status and prospects," *science*, vol. 324, no. 5934, pp. 1530-1534, 2009.
- [108] A. C. Ferrari, J. C. Meyer, V. Scardaci, C. Casiraghi, M. Lazzeri, F. Mauri, S. Piscanec, D. Jiang, K. S. Novoselov, S. Roth, and A. K. Geim, "Raman spectrum of graphene and graphene layers," *Physical review letters*, vol. 97, no. 18, p. 187401, 2006.
- [109] K. L. Sorensen, A. S. Helland, and T. A. Johansen, "Carbon nanomaterial-based wing temperature control system for in-flight anti-icing and de-icing of unmanned aerial vehicles," in *Aerospace Conference, 2015 IEEE*, pp. 1-6, 2015.
- [110] Z. Han and A. Fina, "Thermal conductivity of carbon nanotubes and their polymer nanocomposites: a review," *Progress in polymer science*, vol. 36, no. 7, pp. 914-944, 2011.
- [111] A. -R O. Raji, T Varadhachary, K Nan, T Wang, J Lin, Y Ji, B. Genorio, Y Zhu, C Kittrell, J M. Tour, "Composites of Graphene Nanoribbon Stacks and Epoxy for Joule Heating and Deicing of Surfaces," *ACS applied materials & interfaces*, vol. 8, no. 5, pp. 3551-3556, 2016.
- [112] O. Redondo, S. Prolongo, M. Campo, C. Sbarufatti, and M. Giglio, "Anti-icing and de-icing coatings based Joule's heating of graphene nanoplatelets," *Composites Science and Technology*, vol. 164, pp. 65-73, 2018.
- [113] J. Li, P.-S. Wong, and J.-K. Kim, "Hybrid nanocomposites containing carbon nanotubes and graphite nanoplatelets," *Materials Science and Engineering: A*, vol. 483, pp. 660-663, 2008.
- [114] K. Chu, W.-s. Li, and H. Dong, "Role of graphene waviness on the thermal conductivity of graphene composites," *Applied Physics A*, vol. 111, no. 1, pp. 221-225, 2013.
- [115] A. Jiménez-Suárez, M. Campo, M. Sánchez, C. Romón, and A. Ureña, "Dispersion of carbon nanofibres in a low viscosity resin by calendaring process to manufacture multiscale composites by VARIM," *Composites Part B: Engineering*, vol. 43, no. 8, pp. 3104-3113, 2012.
- [116] A. Jiménez-Suárez, M. Campo, I. Gaztelumendi, N. Markaide, M. Sánchez, and A. Ureña, "The influence of mechanical dispersion of MWCNT in epoxy matrix by calendaring method: Batch method versus time controlled," *Composites Part B: Engineering*, vol. 48, pp. 88-94, 2013.
- [117] R. Moriche, S. Prolongo, M. Sánchez, A. Jiménez-Suárez, M. Sayagués, and A. Ureña, "Morphological changes on graphene nanoplatelets induced during dispersion into an epoxy resin by different methods," *Composites Part B: Engineering*, vol. 72, pp. 199-205, 2015.
- [118] N. Karim, M. Zhang, S. Afroj, V. Koncherry, P. Potluri, and K. S. Novoselov, "Graphene-based surface heater for de-icing applications," *RSC advances*, vol. 8, no. 30, pp. 16815-16823, 2018.
- [119] E. K Akbar, A. Khatibia, S.Yooa, R Wang, N Gleizesc, C. H.Wanga, "Improving the through-thickness thermal and electrical conductivity of carbon fibre/epoxy laminates by exploiting synergy between graphene and silver nano-inclusions," *Composites Part A: Applied Science and Manufacturing*, vol. 69, pp. 72-82, 2015.

- [120] N. Yamamoto, R. G. de Villoria, and B. L. Wardle, "Electrical and thermal property enhancement of fiber-reinforced polymer laminate composites through controlled implementation of multi-walled carbon nanotubes," *Composites Science and Technology*, vol. 72, no. 16, pp. 2009-2015, 2012.
- [121] S.Y. Yang, W.N. Lin, Y.-L. Huang, H.-W. Tien, J. Yu, W.C. Chi, M.M.S.-MingLi, Y.S. Wang, "Synergetic effects of graphene platelets and carbon nanotubes on the mechanical and thermal properties of epoxy composites," *Carbon*, vol. 49, no. 3, pp. 793-803, 2011.
- [122] I. Zaman, H-C. Kuan, Q A Michelmore, N Kawashima, T Pitt, L Zhang, S Gouda, L Luong, J Ma, "A facile approach to chemically modified graphene and its polymer nanocomposites," *Advanced Functional Materials*, vol. 22, no. 13, pp. 2735-2743, 2012.
- [123] I.Zaman, H.C. Kuan, J. Dai, N.Kawashima, A.Michelmore, A.Sovi, S.Dong, L.Luonga and J. Ma, "From carbon nanotubes and silicate layers to graphene platelets for polymer nanocomposites," *Nanoscale*, vol. 4, no. 15, pp. 4578-4586, 2012.
- [124] I. Zamana, T Thanh, PH-Chiang, K Qingshi, M Ly, T Bao, L L Luong, O Youssf, J Ma, "Epoxy/graphene platelets nanocomposites with two levels of interface strength," *Polymer*, vol. 52, no. 7, pp. 1603-1611, 3/23/ 2011.
- [125] <http://www.compositesworld.com/articles/787-integrates-new-composite-wing-deicing-system>, (last access 28/06/2017).
- [126] D. C. Lawson and G. Wiese, "Electrically conductive composite heater and method of manufacture," ed: Google Patents, 1999.
- [127] M. J. Giamati, "Electrothermal de-icing system," ed: Google Patents, 1997.
- [128] https://www.lbf.fraunhofer.de/en/projects-products/iceprotection_strukturintegriertes-nanomaterial.html, "last access 16/05/2017."
- [129] <https://www.imeche.org/news/news-article/smart-de-icing-aircraft-wing-completes-%27crucial%27-nasa-wind-tunnel-tests>, (last access 16/05/2017).
- [130] D. Y. Choi, H. W. Kang, H. J. Sung, and S. S. Kim, "Annealing-free, flexible silver nanowire-polymer composite electrodes via a continuous two-step spray-coating method," *Nanoscale*, vol. 5, no. 3, pp. 977-983, 2013.
- [131] E. Sheka, A. Morozova, and E. Sheka, "Spectroscopy of Molecular Crystals: A Bibliography for 1972," 1974.
- [132] C. Wagner, "Auger lines in x-ray photoelectron spectrometry," *Analytical Chemistry*, vol. 44, no. 6, pp. 967-973, 1972.
- [133] S. Gaarenstroom and N. Winograd, "Initial and final state effects in the ESCA spectra of cadmium and silver oxides," *The Journal of Chemical Physics*, vol. 67, no. 8, pp. 3500-3506, 1977.
- [134] M. Satta and G. Moretti, "Auger parameters and Wagner plots," *Journal of Electron Spectroscopy and Related Phenomena*, vol. 178, pp. 123-127, 2010.
- [135] M. C. Biesinger, "Advanced Studies of Transition Metal X-ray Photoelectron Spectra," University of South Australia, 2012.
- [136] P. S. Arora and R. S. C. Smart, "Formation of Silicate Structures in Oxidized Nickel Surfaces Using Low-temperature Plasma Reaction," *Surface and interface analysis*, vol. 24, no. 9, pp. 539-548, 1996.
- [137] M. Steveson, P. S. Arora, and R. S. C. Smart, "XPS studies of low-temperature plasma-produced graded oxide-silicate-silica layers on titanium," *Surface and Interface Analysis: An International Journal devoted to the development and*

- application of techniques for the analysis of surfaces, interfaces and thin films*, vol. 26, no. 13, pp. 1027-1034, 1998.
- [138] J. Mejias, V. Jiménez, G. Lassaletta, A. Fernández, J. Espinós, and A. González-Elipe, "Interpretation of the binding energy and auger parameter shifts found by XPS for TiO₂ supported on different surfaces," *The Journal of Physical Chemistry*, vol. 100, no. 40, pp. 16255-16262, 1996.
- [139] C. Wagner, A. Naumkin, A. Kraut-Vass, J. Allison, C. Powell, and J. Rumble Jr, "NIST standard reference database 20, Version 3.4 (Web version)," *National Institute of Standards and Technology: Gaithersburg, MD*, vol. 20899, 2003.
- [140] P. Curtis, "CRAG (Composite Research Advisory Group) Test Methods for the Measurement of the Engineering Properties of Fibre Reinforced Plastics," royal aerospace establishment farnborough (United Kingdom), 1988.
- [141] I. D. Rosca, F. Watari, M. Uo, and T. Akasaka, "Oxidation of multiwalled carbon nanotubes by nitric acid," *Carbon*, vol. 43, no. 15, pp. 3124-3131, 2005.
- [142] M. S. Strano, C A. Dyke, M L. Usrey, P W. Barone, M J. Allen, H Shan, C Kittrell, R.H. Hauge, J M. Tour, R E. Smalley, "Electronic structure control of single-walled carbon nanotube functionalization," *Science*, vol. 301, no. 5639, pp. 1519-1522, 2003.
- [143] M. S. Dresselhaus, A. Jorio, M. Hofmann, G. Dresselhaus, and R. Saito, "Perspectives on carbon nanotubes and graphene Raman spectroscopy," *Nano letters*, vol. 10, no. 3, pp. 751-758, 2010.
- [144] A. C. Ferrari and D. M. Basko, "Raman spectroscopy as a versatile tool for studying the properties of graphene," *Nature nanotechnology*, vol. 8, no. 4, p. 235, 2013.
- [145] M. S. Dresselhaus, G. Dresselhaus, R. Saito, and A. Jorio, "Raman spectroscopy of carbon nanotubes," *Physics reports*, vol. 409, no. 2, pp. 47-99, 2005.
- [146] A. C. Ferrari, "Raman spectroscopy of graphene and graphite: disorder, electron-phonon coupling, doping and nonadiabatic effects," *Solid state communications*, vol. 143, no. 1-2, pp. 47-57, 2007.
- [147] S. Lebedkin, C. Blum, N. Stürzl, F. Hennrich, and M. M. Kappes, "A low-wavenumber-extended confocal Raman microscope with very high laser excitation line discrimination," *Review of Scientific Instruments*, vol. 82, no. 1, p. 013705, 2011.
- [148] C. Thomsen and S. Reich, "Raman scattering in carbon nanotubes," in *Light Scattering in Solid IX*: Springer, 2006, pp. 115-234.
- [149] G. Katagiri, H. Ishida, and A. Ishitani, "Raman spectra of graphite edge planes," *Carbon*, vol. 26, no. 4, pp. 565-571, 1988.
- [150] R. Graupner, "Raman spectroscopy of covalently functionalized single-wall carbon nanotubes," *Journal of Raman Spectroscopy: An International Journal for Original Work in all Aspects of Raman Spectroscopy, Including Higher Order Processes, and also Brillouin and Rayleigh Scattering*, vol. 38, no. 6, pp. 673-683, 2007.
- [151] J. L. Blackburn, C. Engtrakul, T. J. McDonald, A. C. Dillon, and M. J. Heben, "Effects of surfactant and boron doping on the BWF feature in the Raman spectrum of single-wall carbon nanotube aqueous dispersions," *The Journal of Physical Chemistry B*, vol. 110, no. 50, pp. 25551-25558, 2006.
- [152] A. M. Rao, E. Richter, S Bandow, B Chase, P. C. Eklund, K. A. Williams, S. Fang, K. R. Subbaswamy, M. Menon, A. Thess, R. E. Smalley, G. Dresselhaus,

- M. S. Dresselhaus, "Diameter-selective Raman scattering from vibrational modes in carbon nanotubes," *Science*, vol. 275, no. 5297, pp. 187-191, 1997.
- [153] S. Gupta, M. Hughes, A. Windle, and J. Robertson, "Charge transfer in carbon nanotube actuators investigated using in situ Raman spectroscopy," *Journal of applied Physics*, vol. 95, no. 4, pp. 2038-2048, 2004.
- [154] P. M. Ajayan, "Nanotubes from carbon," *Chemical reviews*, vol. 99, no. 7, pp. 1787-1800, 1999.
- [155] S. Reich and C. Thomsen, "Raman spectroscopy of graphite," *Philosophical Transactions of the Royal Society of London. Series A: Mathematical, Physical and Engineering Sciences*, vol. 362, no. 1824, pp. 2271-2288, 2004.
- [156] P. Knoll, M. Marchl, and W. Kiefer, "Raman-spectroscopy of microparticles in laser-light traps," *INDIAN JOURNAL OF PURE & APPLIED PHYSICS*, vol. 26, no. 2-3, pp. 268-277, 1988.
- [157] N. P. Zschoerper, V. Katzenmaier, U. Vohrer, M. Haupt, C. Oehr, and T. Hirth, "Analytical investigation of the composition of plasma-induced functional groups on carbon nanotube sheets," *Carbon*, vol. 47, no. 9, pp. 2174-2185, 2009.
- [158] N. Zhang, J. Xie, and V. K. Varadan, "Functionalization of carbon nanotubes by potassium permanganate assisted with phase transfer catalyst," *Smart materials and structures*, vol. 11, no. 6, p. 962, 2002.
- [159] P. C. Ma, J.-K. Kim, and B. Z. Tang, "Functionalization of carbon nanotubes using a silane coupling agent," *Carbon*, vol. 44, no. 15, pp. 3232-3238, 2006.
- [160] M. E. Lipińska, S. L. Rebelo, M. F. R. Pereira, J. Gomes, C. Freire, and J. Figueiredo, "New insights into the functionalization of multi-walled carbon nanotubes with aniline derivatives," *Carbon*, vol. 50, no. 9, pp. 3280-3294, 2012.
- [161] T. Okpalugo, P. Papakonstantinou, H. Murphy, J. McLaughlin, and N. Brown, "High resolution XPS characterization of chemical functionalised MWCNTs and SWCNTs," *Carbon*, vol. 43, no. 1, pp. 153-161, 2005.
- [162] N. Sezer and M. Koç, "Oxidative acid treatment of carbon nanotubes," *Surfaces and Interfaces*, vol. 14, pp. 1-8, 2019.
- [163] L. Zhang, Q.-Q. Ni, Y. Fu, and T. Natsuki, "One-step preparation of water-soluble single-walled carbon nanotubes," *Applied Surface Science*, vol. 255, no. 15, pp. 7095-7099, 2009.
- [164] F.-H. Ko, C.-Y. Lee, C.-J. Ko, and T.-C. Chu, "Purification of multi-walled carbon nanotubes through microwave heating of nitric acid in a closed vessel," *Carbon*, vol. 43, no. 4, pp. 727-733, 2005.
- [165] M. C. Biesinger, L. W. Lau, A. R. Gerson, and R. S. C. Smart, "Resolving surface chemical states in XPS analysis of first row transition metals, oxides and hydroxides: Sc, Ti, V, Cu and Zn," *Applied surface science*, vol. 257, no. 3, pp. 887-898, 2010.
- [166] P. J. Cumpson and M. P. Seah, "Elastic scattering corrections in AES and XPS. II. Estimating attenuation lengths and conditions required for their valid use in overlayer/substrate experiments," *Surface and Interface Analysis: An International Journal devoted to the development and application of techniques for the analysis of surfaces, interfaces and thin films*, vol. 25, no. 6, pp. 430-446, 1997.
- [167] D. Briggs, *Surface analysis of polymers by XPS and static SIMS*. Cambridge University Press, 1998.

- [168] T. Ghodselahi, M. Vesaghi, A. Shafiekhani, A. Baghizadeh, and M. Lameii, "XPS study of the Cu@ Cu₂O core-shell nanoparticles," *Applied Surface Science*, vol. 255, no. 5, pp. 2730-2734, 2008.
- [169] S. Poulston, P. Parlett, P. Stone, and M. Bowker, "Surface oxidation and reduction of CuO and Cu₂O studied using XPS and XAES," *Surface and Interface Analysis: An International Journal devoted to the development and application of techniques for the analysis of surfaces, interfaces and thin films*, vol. 24, no. 12, pp. 811-820, 1996.
- [170] G. Wee, W F. Mak, N Phonthammachai, A Kiebele, M. V. Reddy, B. V. R. Chowdari, G Gruner, M Srinivasan and S G. Mhaisalkar, "Particle size effect of silver nanoparticles decorated single walled carbon nanotube electrode for supercapacitors," *Journal of The Electrochemical Society*, vol. 157, no. 2, pp. A179-A184, 2010.
- [171] S. Xiaoming and L. Yadong, "Colloidal Carbon Spheres and Their Core/Shell Structures with Noble-Metal Nanoparticles," *Angewandte Chemie International Edition*, vol. 43, no. 5, pp. 597-601, 2004.
- [172] V. E Ronald, J.Mascarenhas, Ashis K.Satpatic, SDZine, MJoseph, DA.Dhasone, "Sensitive detection of Ferulic acid using multi-walled carbon nanotube decorated with silver nano-particles modified carbon paste electrode," *Journal of Electroanalytical Chemistry*, vol. 806, pp. 22-31, 2017.
- [173] H. Gaminian and M. Montazer, "Decorating silver nanoparticles on electrospun cellulose nanofibers through a facile method by dopamine and ultraviolet irradiation," *Cellulose*, vol. 24, no. 8, pp. 3179-3190, 2017.
- [174] X. Sun and Y. Li, "Colloidal carbon spheres and their core/shell structures with noble-metal nanoparticles," *Angewandte Chemie International Edition*, vol. 43, no. 5, pp. 597-601, 2004.
- [175] C.-W. Hsu, Z.-Y. Lin, T.-Y. Chan, T.-C. Chiu, and C.-C. Hu, "Oxidized multiwalled carbon nanotubes decorated with silver nanoparticles for fluorometric detection of dimethoate," *Food chemistry*, vol. 224, pp. 353-358, 2017.
- [176] V. Pifferi, G. Facchinetti, A. Villa, L. Prati, and L. Falciola, "Electrocatalytic activity of multiwalled carbon nanotubes decorated by silver nanoparticles for the detection of halothane," *Catalysis Today*, vol. 249, pp. 265-269, 2015.
- [177] M. Shivakumar, G. Krishnamurthy, C. Ravikumar, and A. S. Bhatt, "Decoration of silver nanoparticles on activated graphite substrate and their electrocatalytic activity for methanol oxidation," *Journal of Science: Advanced Materials and Devices*, 2019.
- [178] M. Montazer, F. Alimohammadi, A. Shamei, and M. K. Rahimi, "In situ synthesis of nano silver on cotton using Tollens' reagent," *Carbohydrate Polymers*, vol. 87, no. 2, pp. 1706-1712, 2012.
- [179] L. Qu and L. Dai, "Novel silver nanostructures from silver mirror reaction on reactive substrates," *The Journal of Physical Chemistry B*, vol. 109, no. 29, pp. 13985-13990, 2005.
- [180] T. Textor, M. M. Fouda, and B. Mahltig, "Deposition of durable thin silver layers onto polyamides employing a heterogeneous Tollens' reaction," *Applied Surface Science*, vol. 256, no. 8, pp. 2337-2342, 2010.
- [181] L. Chen, H. Xie, and W. Yu, "Multi-walled carbon nanotube/silver nanoparticles used for thermal transportation," *Journal of Materials Science*, vol. 47, no. 14, pp. 5590-5595, 2012.

- [182] W. M. Daoush and S. H. Hong, "Synthesis of multi-walled carbon nanotube/silver nanocomposite powders by chemical reduction in aqueous solution," *Journal of Experimental Nanoscience*, vol. 8, no. 5, pp. 742-751, 2013.
- [183] J. Safari and S. Gandomi-Ravandi, "Silver decorated multi-walled carbon nanotubes as a heterogeneous catalyst in the sonication of 2-aryl-2, 3-dihydroquinazolin-4 (1 H)-ones," *RSC Advances*, vol. 4, no. 23, pp. 11654-11660, 2014.
- [184] R. Dondi, W. Su, G. A. Griffith, G. Clark, and G. A. Burley, "Highly Size-and Shape-Controlled Synthesis of Silver Nanoparticles via a Templated Tollens Reaction," *Small*, vol. 8, no. 5, pp. 770-776, 2012.
- [185] S. Pal, R Varghese, Z Deng, Z Zhao, A Kumar, H Yan, Y Liu, "Site-Specific Synthesis and In Situ Immobilization of Fluorescent Silver Nanoclusters on DNA Nanoscaffolds by Use of the Tollens Reaction," *Angewandte Chemie International Edition*, vol. 50, no. 18, pp. 4176-4179, 2011.
- [186] N. X. Dinh, N. V. Quy, T. Q. Huy, and A.-T. Le, "Decoration of silver nanoparticles on multiwalled carbon nanotubes: antibacterial mechanism and ultrastructural analysis," *Journal of Nanomaterials*, vol. 16, no. 1, p. 63, 2015.
- [187] S. Huang and A. W. Mau, "Selective growth of aligned carbon nanotubes on a silver-patterned substrate by the silver mirror reaction," *The Journal of Physical Chemistry B*, vol. 107, no. 15, pp. 3455-3458, 2003.
- [188] M. Barberio, P. Barone, V. Pingitore, and A. Bonanno, "Optical properties of TiO₂ anatase – Carbon nanotubes composites studied by cathodoluminescence spectroscopy," *Superlattices and Microstructures*, vol. 51, no. 1, pp. 177-183, 2012/01/01/ 2012.
- [189] T. Theivasanthi and M. Alagar, "Electrolytic synthesis and characterizations of silver nanopowder," *arXiv preprint arXiv:1111.0260*, 2011.
- [190] X. Pan and X. Bao, "The effects of confinement inside carbon nanotubes on catalysis," *Accounts of chemical research*, vol. 44, no. 8, pp. 553-562, 2011.
- [191] P. Serp and E. Castillejos, "Catalysis in carbon nanotubes," *ChemCatChem*, vol. 2, no. 1, pp. 41-47, 2010.
- [192] J Zheng, X Duan, H Lin, Z Gu, H Fang, J Li, Y Yuan, "Silver nanoparticles confined in carbon nanotubes: on the understanding of the confinement effect and promotional catalysis for the selective hydrogenation of dimethyl oxalate," *Nanoscale*, vol. 8, no. 11, pp. 5959-5967, 2016.
- [193] E J Koop, M J Iqbal, F Limbach, M Boute, B J van Wees, D Reuter, A D Wieck, B J Kooi and C H van der Wall, "The annealing mechanism of AuGe/Ni/Au ohmic contacts to a two-dimensional electron gas in GaAs/AlGaAs heterostructures," *Semiconductor Science and Technology*, vol. 28, 09/05 2008.
- [194] M. Tarfaoui, A. El Moumen, M. Boehle, O. Shah, and K. Lafdi, "Self-heating and deicing epoxy/glass fiber based carbon nanotubes buckypaper composite," *Journal of materials science*, vol. 54, no. 2, pp. 1351-1362, 2019.
- [195] X. Liu, H. Chen, W. Kou, and D. Zhang, "Robust anti-icing coatings via enhanced superhydrophobicity on fiberglass cloth," *Cold Regions Science and Technology*, vol. 138, pp. 18-23, 2017.
- [196] C. Peng, S. Xing, Z. Yuan, J. Xiao, C. Wang, and J. Zeng, "Preparation and anti-icing of superhydrophobic PVDF coating on a wind turbine blade," *Applied Surface Science*, vol. 259, pp. 764-768, 2012.

- [197] S. D. Bhagat and M. C. Gupta, "Superhydrophobic microtextured polycarbonate surfaces," *Surface and Coatings Technology*, vol. 270, pp. 117-122, 2015.
- [198] H. H. Ipekci, H. H. Arkaz, M. S. Onses, and M. Hancer, "Superhydrophobic coatings with improved mechanical robustness based on polymer brushes," *Surface and Coatings Technology*, vol. 299, pp. 162-168, 2016.
- [199] S. Zheng, C Li, Q Fu, T Xiang, W Hu, J Wang, S Ding, P Liu and Z Chen, "Fabrication of a micro-nanostructured superhydrophobic aluminum surface with excellent corrosion resistance and anti-icing performance," *RSC Advances*, vol. 6, no. 83, pp. 79389-79400, 2016.
- [200] Y. Liu, X. Li, Y. Yan, Z. Han, and L. Ren, "Anti-icing performance of superhydrophobic aluminum alloy surface and its rebounding mechanism of droplet under super-cold conditions," *Surface and Coatings Technology*, vol. 331, pp. 7-14, 2017.
- [201] C. Antonini, M. Innocenti, T. Horn, M. Marengo, and A. Amirfazli, "Understanding the effect of superhydrophobic coatings on energy reduction in anti-icing systems," *Cold Regions Science and Technology*, vol. 67, no. 1-2, pp. 58-67, 2011.
- [202] S. Kulinich and M. Farzaneh, "Ice adhesion on super-hydrophobic surfaces," *Applied Surface Science*, vol. 255, no. 18, pp. 8153-8157, 2009.
- [203] I. D. Rosca and S. V. Hoa, "Highly conductive multiwall carbon nanotube and epoxy composites produced by three-roll milling," *Carbon*, vol. 47, no. 8, pp. 1958-1968, 2009.
- [204] Y. S. Song and J. R. Youn, "Influence of dispersion states of carbon nanotubes on physical properties of epoxy nanocomposites," *Carbon*, vol. 43, no. 7, pp. 1378-1385, 2005.
- [205] K. R. Reddy, B. C. Sin, K. S. Ryu, J.-C. Kim, H. Chung, and Y. Lee, "Conducting polymer functionalized multi-walled carbon nanotubes with noble metal nanoparticles: synthesis, morphological characteristics and electrical properties," *Synthetic Metals*, vol. 159, no. 7-8, pp. 595-603, 2009.
- [206] Y. Zhou, P. Wu, Z. Cheng, J. Ingram, and S. Jeelani, "Improvement in electrical, thermal and mechanical properties of epoxy by filling carbon nanotube," *Express polymer letters*, vol. 2, no. 1, pp. 40-48, 2008.
- [207] Z. Spitalsky, D. Tasis, K. Papagelis, and C. Galiotis, "Carbon nanotube-polymer composites: chemistry, processing, mechanical and electrical properties," *Progress in polymer science*, vol. 35, no. 3, pp. 357-401, 2010.
- [208] X. F. Sánchez-Romate, A. Jiménez-Suárez, J. Molinero, M. Sánchez, A. Güemes, and A. Ureña, "Development of bonded joints using novel CNT doped adhesive films: Mechanical and electrical properties," *International Journal of Adhesion and Adhesives*, vol. 86, pp. 98-104, 2018.
- [209] Q. Wang, J. Dai, W. Li, Z. Wei, and J. Jiang, "The effects of CNT alignment on electrical conductivity and mechanical properties of SWNT/epoxy nanocomposites," *Composites science and technology*, vol. 68, no. 7-8, pp. 1644-1648, 2008.
- [210] A. Oliva-Avilés, F. Avilés, and V. Sosa, "Electrical and piezoresistive properties of multi-walled carbon nanotube/polymer composite films aligned by an electric field," *Carbon*, vol. 49, no. 9, pp. 2989-2997, 2011.
- [211] J.-M. Zhu, Y. Zare, and K. Y. Rhee, "Analysis of the roles of interphase, waviness and agglomeration of CNT in the electrical conductivity and tensile modulus of polymer/CNT nanocomposites by theoretical approaches,"

- Colloids and Surfaces A: Physicochemical and Engineering Aspects*, vol. 539, pp. 29-36, 2018.
- [212] A. Sharma, B. Tripathi, and Y. Vijay, "Dramatic improvement in properties of magnetically aligned CNT/polymer nanocomposites," *Journal of Membrane Science*, vol. 361, no. 1-2, pp. 89-95, 2010.
- [213] H. Zhang, G. Zhang, M. Ting, L. Zhou, J. Li, X. Fan, X. Shi, J. Qin, "Synergistic effect of carbon nanotube and graphene nanoplates on the mechanical, electrical and electromagnetic interference shielding properties of polymer composites and polymer composite foams," *Chemical Engineering Journal*, vol. 353, pp. 381-393, 2018.
- [214] Z. Liu, W. Peng, Y. Zare, D. Hui, and K. Y. Rhee, "Predicting the electrical conductivity in polymer carbon nanotube nanocomposites based on the volume fractions and resistances of the nanoparticle, interphase, and tunneling regions in conductive networks," *RSC advances*, vol. 8, no. 34, pp. 19001-19010, 2018.
- [215] M. T. Byrne and Y. K. Gun'ko, "Recent advances in research on carbon nanotube-polymer composites," *Advanced materials*, vol. 22, no. 15, pp. 1672-1688, 2010.
- [216] Y. J. Kim, T. S. Shin, H. Do Choi, J. H. Kwon, Y.-C. Chung, and H. G. Yoon, "Electrical conductivity of chemically modified multiwalled carbon nanotube/epoxy composites," *Carbon*, vol. 43, no. 1, pp. 23-30, 2005.
- [217] Y. Su, S. Zhang, X. Zhang, Z. Zhao, and D. Jing, "Preparation and properties of carbon nanotubes/carbon fiber/poly (ether ether ketone) multiscale composites," *Composites Part A: Applied Science and Manufacturing*, vol. 108, pp. 89-98, 2018.
- [218] M. A. Meyers and K. K. Chawla, *Mechanical behavior of materials*. Cambridge university press, 2008.
- [219] F. Meyer, G. Sanz, A. Eceiza, I. Mondragon, and J. Mijović, "The effect of stoichiometry and thermal history during cure on structure and properties of epoxy networks," *Polymer*, vol. 36, no. 7, pp. 1407-1414, 1995.
- [220] R. Carbas, L. Da Silva, E. Marques, and A. Lopes, "Effect of post-cure on the glass transition temperature and mechanical properties of epoxy adhesives," *Journal of Adhesion Science and Technology*, vol. 27, no. 23, pp. 2542-2557, 2013.
- [221] J.-C. Munoz, H. Ku, F. Cardona, and D. Rogers, "Effects of catalysts and post-curing conditions in the polymer network of epoxy and phenolic resins: Preliminary results," *Journal of Materials Processing Technology*, vol. 202, no. 1-3, pp. 486-492, 2008.
- [222] S. A. Awad and E. M. Khalaf, "Investigation of improvement of properties of polypropylene modified by nano silica composites," *Composites Communications*, vol. 12, pp. 59-63, 2019.
- [223] S. Ilangoan, S. S. Kumaran, A. Vasudevan, and K. Naresh, "Effect of silica nanoparticles on mechanical and thermal properties of neat epoxy and filament wounded E-glass/epoxy and basalt/epoxy composite tubes," *Materials Research Express*, 2019.
- [224] J. Zhu *et al.*, "Reinforcing epoxy polymer composites through covalent integration of functionalized nanotubes," *Advanced Functional Materials*, vol. 14, no. 7, pp. 643-648, 2004.

- [225] L. P. Bakos *et al.*, "Photocatalytic and Gas Sensitive Multiwalled Carbon Nanotube/TiO₂-ZnO and ZnO-TiO₂ Composites Prepared by Atomic Layer Deposition," *Nanomaterials*, vol. 10, no. 2, p. 252, 2020.
- [226] X. Li, C. Li, Y. Zhang, D. Chu, W. Milne, and H. Fan, "Atomic layer deposition of ZnO on multi-walled carbon nanotubes and its use for synthesis of CNT–ZnO heterostructures," *Nanoscale research letters*, vol. 5, no. 11, pp. 1836-1840, 2010.